Nuclear Magnetic Resonance Studies of Disorder and Local Structure in Borate and Germanate Materials

Vladimir K. Michaelis

A thesis submitted to the Faculty of Graduate Studies of

the University of Manitoba

in partial fulfillment of the requirements for the degree of

Doctor of Philosophy

Department of Chemistry

University of Manitoba
Winnipeg, Canada

UNIVERSITY OF MANITOBA

for Lindsey

Table of Contents

List of Tables

List of Figures

Abstract

Glass materials surround us, impacting our lives on a daily basis, whether geologically deposited by volcanic activity or synthesized in large volume by industry. These amorphous oxide materials are vastly important due to their variety of applications including solid electrolytes, cookware, and storage of high-level nuclear waste. Although they are used for different applications, one common characteristic of these materials is the absence of long-range periodic order. This makes it difficult to use traditional solid-state characterization methods such as x-ray and neutron diffraction to study glass structure. Nuclear magnetic resonance (NMR), is ideally suited to study materials that exhibit short-range non-periodic order as it probes directly at a nucleus of interest and is sensitive to its local structural environment. This ability of solid-state NMR is illustrated by revealing local structural features in various oxide materials presented in this thesis. Within is a compilation of studies looking at basic borates, followed by borovanadates and complex borosilicate glasses. A multinuclear application of using quantum chemical calculations, single and double resonance methods and charge-balance models are discussed to deconvolute the complex structures of these disordered materials. This is followed by a study of a difficult low-gamma nucleus, ^{73}Ge, (once considered "impossible" for solid-state NMR) which is explored for future material studies by looking at ^{73}Ge NMR of crystalline and glassy germanates. ^{73}Ge chemical shifts were related to coordination environments and quadrupolar coupling constants were related to bond length distortions.

Acknowledgement

A structure is only as strong as the foundation it is built upon. Throughout my time completing this PhD, I have been very fortunate for the crew that I have been exposed to, providing me with the materials for this task. Throughout one's life there are many influences. Here are those that have made this contribution possible. Most notable is my supervisor Professor Scott Kroeker, who has provided endless scientific guidance, patience, and opportunity. He has taught me many valuable skills to become a successful, careful and thoughtful researcher, and I hope to master many more of these traits in the coming years. I will always be indebted to Scott as I continue my path, wherever it should take me. I thank Dr. Pedro Aguiar for taking me under his wing while in the Kroeker group. Pedro is responsible for teaching me NMR, methods for attacking problems, and how to alleviate stress when research is not going as planned. I will never forget the great times at the gym, especially discussing half-squats. Dr. Kirk Marat has provided me with endless discussions regarding experiments, spectrometer issues and endless modifications to SpinWorks that I needed throughout my time here. I am most grateful however, for him sharing his knowledge on probe design and repair that he bestowed onto me. I am grateful to Dr. Charlotte Martineau, Dr. Paul Sidhu, Mr. Brandon Greer and Mr. John Wren for many helpful and constructive comments regarding manuscripts, posters, talks, etc. which eventually managed to become a part of this thesis. All the undergrads that I have been fortunate to work alongside while within the Kroeker group must also be

acknowledged. These include Amy, Christine, Carolyn, Lawson, Nick, Palak, and Stan. You have all contributed in a variety of ways and I will never forget the great summers and friendships we have made.

I have been fortunate to have amazing collaborators who have provided various materials and knowledge in order to solve many scientific problems. I would like to begin with Dr. Steve Feller and Dr. Mario Affatigato (Coe College, Cedar Rapids) who have provided me with unique, difficult and intriguing glass samples for NMR analysis. They have also provided me with a plethora of samples, especially with regards to vanadium based glass oxides. The work with Dr. Frank Hawthorne and Mr. Aaron Lussier (Department of Geology, University of Manitoba) has been very fruitful and fascinating, examining coordination environments in a variety of minerals collected from all corners of the world. To Dr. Daniel Leznoff and Dr. Michael Katz (Simon Fraser University, British Columbia), thank you for synthesizing a variety of heavy metal coordination polymers, in addition to the excellent times at the *Inorganic Mixers*. Thank you Dr. John Greedan and Ms. Tomoko Aharen for synthesizing and enabling me to study various paramagnetic double perovskites. Last but not least, I would like to thank my comrade at the ultrahigh field NMR facility for solids, Dr. Victor Terskikh (NRC, Ottawa) whose wide-range knowledge of quadrupolar based nuclei, high-field expertise and comments has made me a stronger researcher.

I would also like to recognize the members of my PhD advisory committee. Professors Sean Cadogan, Peter Budzelaar and Joe O'Neil for providing advice, suggestions and interest during this degree. I am extremely grateful to the generous funding that I have received over the years including the Natural Sciences and

Engineering Research Council of Canada for a Post-Graduate Scholarship, Duff Roblin Graduate Fellowship, Manitoba Graduate Fellowship, Faculty of Science Scholarship, Department of Chemistry (Anderson, Bock, Centennial, Rodewald, etc.) awards and the various travel support received from Department of Chemistry, Faculty of Science, Faculty of Graduate Studies, Chemistry Graduates Student Association and Graduate Students Association.

Finally, there are no words that can express my gratitude for my family. My parents provided me with the work ethic, means and determination enabling me the tools to get to this point. My parents-in-law for providing the endless methods to decompress, whether by fishing or cruising for farm parts. In memory of my grandfather, Де́душка, who taught me to always: *"Think, man".* Mostly, Lindsey for being by me in the highs and lows during this process and always being there for me with an open ear, a loving heart and words of encouragement – I am truly thankful.

1. INTRODUCTION

Glasses are extensively used products within our industrialized society. To the reader, it may seem as a fairly bold statement but in an age where we are surrounded by the notion of being "green", i.e., using recyclable energy efficient materials, one will see how glass is widely used in many areas and its uses continue to expand. Let us take a moment and think about a typical morning and what items one may see or use that incorporate glass science. For example, brushing one's teeth while looking at a mirror (silica glass with a backing of Ag- or Al-film), perhaps turning on the television (alkali-Ba-silicate) for local news or checking one's iPad® (e.g., Gorilla Glass®, Alkali aluminosilicate) for a weather update. While enjoying a good breakfast you pour a glass (soda-lime glass) of orange juice and you may see a hummingbird drinking nectar outside the kitchen window (Ca-Na-borosilicate). The vehicle you use to get to the office is engineered with impact resistant (shatterproof) windows. Sitting at one's desk reading email, the connection to the cyber world is made possible by fiber optics (SiO_2), perhaps one of the most significant discoveries of this past century. There are many other applications, some of which are definitely not everyday occurrences; glass science and technology is vast, versatile and will continue to grow in all aspects of civilization. The basic physical properties that make these materials viable are their unique structural properties, which can be tuned, creating endless possibilities. However, the structural properties are difficult to probe and comprehend due to the inherent absence of periodic long-range order within these materials. This thesis is

written to provide tools and methods that can be used in determining local structure for a variety of amorphous oxide materials. Two particular applications, which will be explored and discussed, include ionic conducting materials and high-level nuclear waste sequestering using borosilicate glasses. We will begin by defining what is a glass.

1.1. What is a Glass?

A glass is a solid that in general terms is obtained from a supercooled liquid, whereby the onset of crystallization is by-passed (Figure 1.1). In principle, any material (inorganic or organic) can be considered a glass if its structure is as follows: "A state of matter that possesses most of the macroscopic and thermodynamic properties of a solid while retaining the structural disorder and isotropic behaviour of a liquid".[1] An alternate definition is "an amorphous solid completely lacking in long-range, periodic atomic structure and exhibiting a region of glass transformation behaviour (temperature range and time where the liquid by-passes crystallization forming a glass)".[2] One distinguishing property of a glass is that it has a glass transition temperature, T_g (T_g, is the region where the onset of glass transformation occurs). The values are typically determined using differential scanning calorimetry (DSC); an endothermic response is T_g, continued heating is the onset of crystallization, T_c (which exhibits exothermic behaviour) other properties of interest include refractive index, density and hardness that can vary with composition.[2] One of the most commonly found class of glasses is oxide glass. Oxide glasses are typically characterized by local-

(<5 Å) and medium-range order (5-10 Å) while long-range periodic order is absent (Figure 1.2).

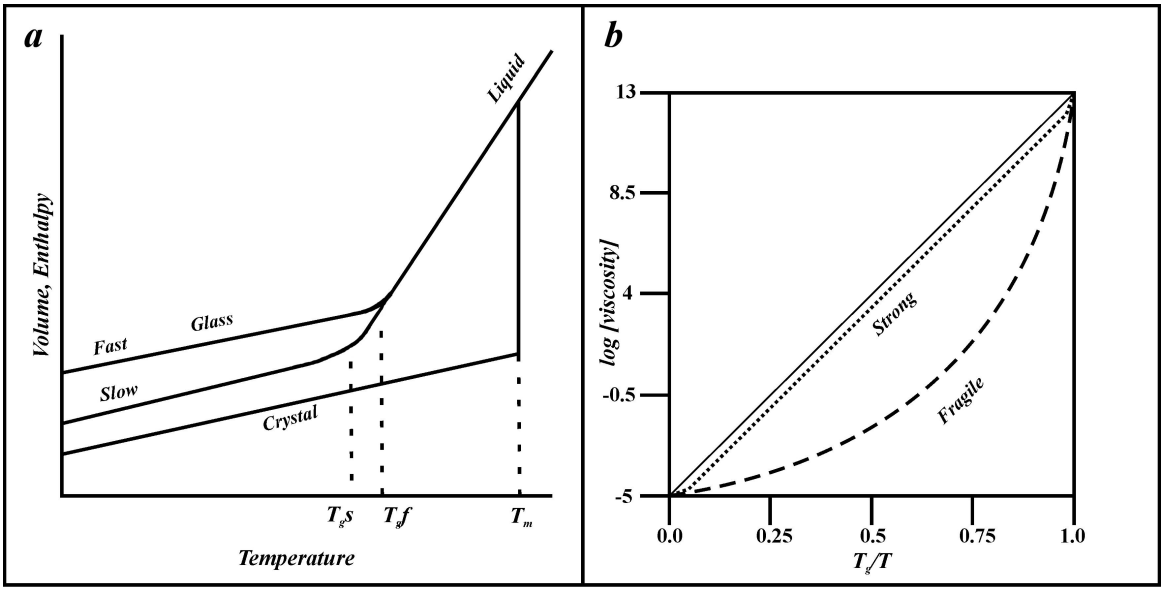

Figure 1.1. (a) The temperature dependence of the enthalpy during glass and crystal formation. Cooling of a melt slowly allowing the system to reach a thermodynamic equilibrium will allow the formation of a crystalline material. As this material is further cooled the overall enthalpy will continue to decrease due to the heat capacity of the crystal. If we can rapidly cool a melt, by-passing the on-set of crystallization, a supercooled liquid is obtained. As this liquid continues to cool, very little change in enthalpy occurs (little change in structure) but the viscosity increases. This liquid eventually becomes so viscous that rearrangment cannot occur within the network and a glass is formed. (b) Arrhenius plot illustrating both strong and fragile glass formers. This shows how the viscosity of a glass is affected by sample temperature. For a strong liquid with discrete local-structural units the viscosity increases linearly as the temperature decreases, while a curved line indicates a fragile (poor) glass former, with viscosity changing in a non-linear manner.

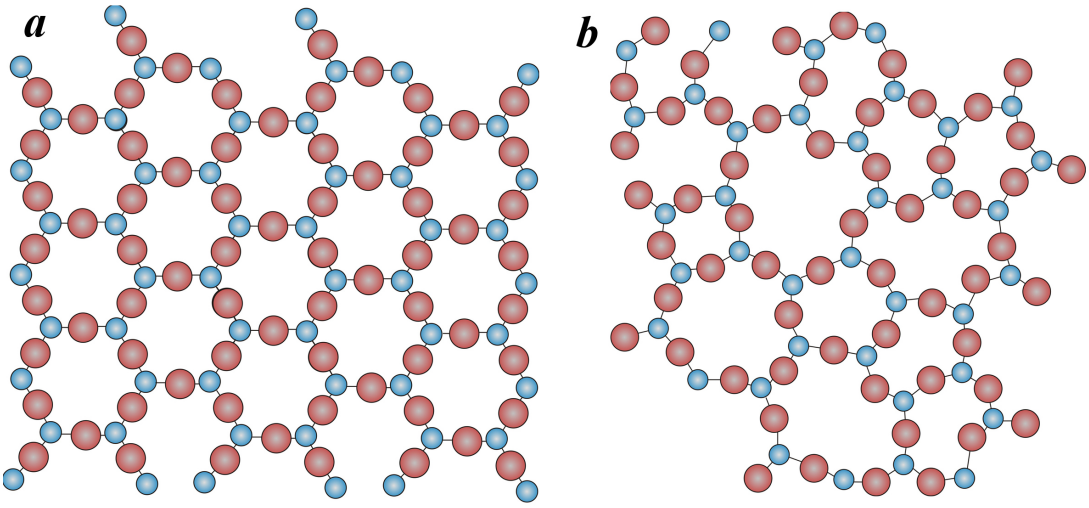

Figure 1.2. Two-dimensional representation of (a) crystalline-SiO_2 and (b) vitreous-SiO_2.

These oxides are typically excellent solvents; that is, they have the ability to incorporate a variety of elements while maintaining their glass formation region. The ability to mix with a diversity of other oxides at various concentrations causes structural changes to the glass forming oxide. The added oxide potentially provides the ability to tune and in theory create a material with the desired physical properties.

There is a balance between the melt, crystallization tendencies, and nucleation sites that determine the ease of vitrification. In addition, one must also contend with volatility, melting temperatures, concentrations, and quench rates in determining possible glass formation. Materials that form good glasses are those that exhibit liquid-like behaviour (i.e., the solid is a good representation of the liquid) while in a solid form. Speciation and connectivity can be determined in the solid phase, which can provide information regarding the properties in the melt.

Amorphous oxides are typically categorized into one of two categories, as a strong-liquid or as a fragile-liquid. These terms are assigned on the basis of the viscosity behaviour for oxides as the temperature is decreased from the melt to the solid (known as Angell plots, Figure 1.1). If oxides display Arrhenius behaviour (linear-relationship), they are considered strong liquids, indicating good candidates for glass formation. Strong-liquids (good glass-formers) are species that will exhibit similar properties in the solid-state as they do in the liquid-state, with comparable heat capacities, a high degree of short-range order, and a tendency towards covalent bonding.[2] Fragile-liquids on the other hand are the opposite in nature. As the melt is cooled the viscosity exhibits non-linear behaviour resulting in larger changes in heat capacity, poorly defined short-range order, and ionic bonding. This non-Arrhenius behaviour causes these materials to be less favorable as it is more difficult to relate the structure-property relationships between the solid and liquid. This behaviour is typically found in weak inter-molecular interactions (such as hydrogen bonding or van der Waals forces) often occurring in organic-based glasses. Moderately-strong liquids fall between the two extremes mentioned above (e.g., MgO, Al_2O_3 and TiO_2). These materials do not form glasses generally on their own but can be added to strong-liquids, enabling a glass to form. These species are often referred to as intermediate glass forming oxides. To create a glass typically a combination of strong, moderate and fragile liquids are melted together followed by a quench. The oxide species combined will exhibit either network forming or network modifying characteristics.

1.1.1. What is a Network Former

The terminology of a network former was coined by Zachariasen[3] in 1932, and it is the most common method used today for describing glass structure. For oxides, a network former, A_mO_n must exhibit four structural behaviours.

1. Oxygen atoms are linked to no more than two atoms A,
2. The oxygen coordination around A is small (i.e., 3 or 4),
3. Oxygen polyhedra share corners but not edges or faces,
4. At least three corners are shared

If the oxide in question meets these requirements, it provides a strong indication that it will act as a network former in a three-dimensional array. Typical oxide formers include B_2O_3, SiO_2, P_2O_5 and GeO_2. Generally, these four conditions are first considered when looking at a system to determine whether or not a species is involved in the formation of the network. Network formers are cations that have a fractional ionic character near 50% when forming a bond with oxygen.

Intermediate network formers such as Al_2O_3, Ga_2O_3, and TiO_2 do not obey the Zachariasen rules. However, when added to a strong glass former in moderate amounts, glass formation will occur typically causing a stronger material, as they can assist in increasing polymerization (i.e., inhibiting the formation of non-bridging oxygens). These oxides become an integral part of the glass-forming network, increasing connectivity. Higher levels of intermediate oxides (not considered here) may inhibit glass formation altogether, as this will typically induce crystallization or solid-solid phase separation (i.e., crystalline and amorphous phases).

1.1.2. What is a Network Modifier?

Modifiers are ionic cations that are added to a former, thereby introducing a charge differential. Since the system must maintain charge neutrality they cause the formers to change, modifying the glass network. In other words, cations that exhibit very low electronegativity will not act as formers. Instead, these highly ionic oxide species contribute indirectly to the connectivity. They are added to provide a desired physical property; such as increased strength or higher refractive indices. Common modifiers include: alkali and alkaline earth metal oxides, as well as oxides of the heavier elements such as, Ag_2O, PbO, Bi_2O_3 or As_2O_3.

1.2. Short Range Order of Common Glass Formers

A variety of short-range structural units are known to occur in a wide range of oxide glasses. Silicates, borates, vanadates, germanates are network formers of particular importance as are intermediate network forming additives, like aluminates and gallates. Figures 1.3 to 1.8 display the local structural building units within these materials (with the associated abbreviations) that may occur with an appropriate modifier.

1.2.1. Silicates

SiO_2 is an archetypal glass former comprised of silicon cations interconnected covalently with oxygen anions throughout a 3D web of Si-O-Si bonds. Silicates have the ability to form five local structures (all of which are four-coordinate) as modifiers are added. Silicates sit in a pseudo-tetrahedral arrangement with the concise notation,

Q. Q is used as it represents a quaternary species. A superscripted number (x) is added to identify the number of bridging oxygens (BO), whereby the balance (4-x) is the number of non-bridging oxygens (NBO). The five silicate species include four BOs (Q^4), three BOs (Q^3), two BOs (Q^2), one BO (Q^1) and all NBOs (Q^0).[2,4] Excluded from this discussion due to their observation typically only in extreme cases (i.e., high temperature and/or high pressure), are those silicates with five- and six-coordinate environments ($^{[5]}$Si and $^{[6]}$Si).[5,6]

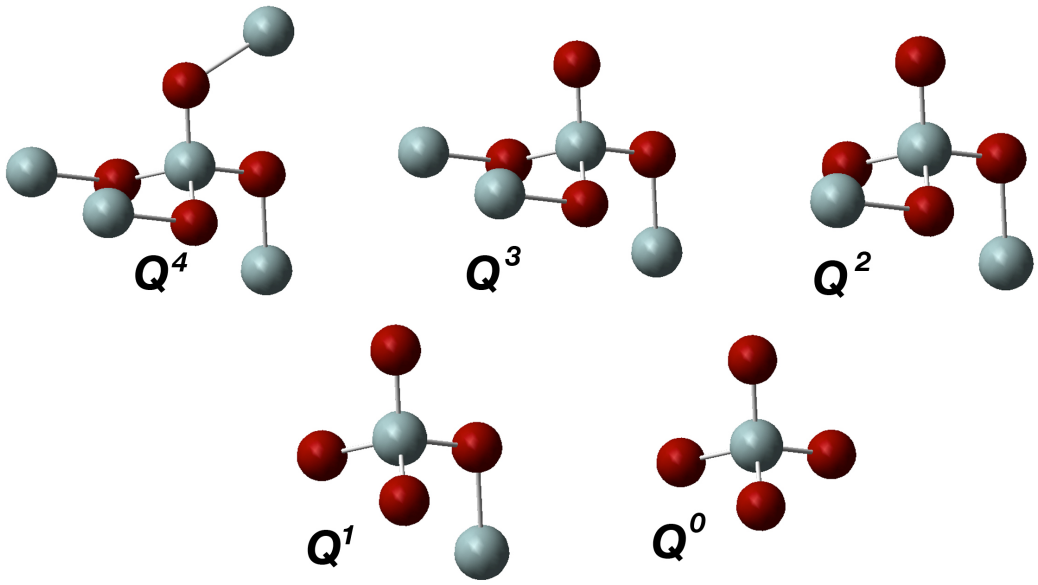

Figure 1.3. Short-range order species found in silicate-containing glasses, grey circles are silicon while red circles are oxygen.

1.2.2. Borate Speciation

Borate glass is connected into a 3D array of B-O-B bonds but differs from the silicates in that boron is three-coordinate and contains a high fraction of borate rings (~70%, B_3O_3) while the balance is comprised of non-ring BO_3 units (~30%).[7] Borates exhibit

five possible short-range order structural units and two different coordination environments.[4,8,9] The ring and non-ring structures in B_2O_3 are three-coordinate boron ($^{[3]}B$); both exhibiting three bridging oxygens (BO). These structures are referred to as T^3 units (T represents trigonal and the superscript gives the number of bridging oxygens). $^{[3]}B$ with two BOs, and one non-bridging oxygen (NBO) is denoted as T^2, while $^{[3]}B$ with a single BO and two NBOs is abbreviated as T^1 and $^{[3]}B$ with three NBOs is called a T^0 unit. A four-coordinate boron with four BOs also exists, with a negative charge delocalized over the borate unit ($^{[4]}B$), due to boron being trivalent, B^{3+}. Ring structures will be discussed below as they are medium, not short-range ordered structures. The local structure for the three-coordinate species are pseudo-trigonal planar while the four-coordinate boron is pseudo-tetrahedral (Figure 1.4).

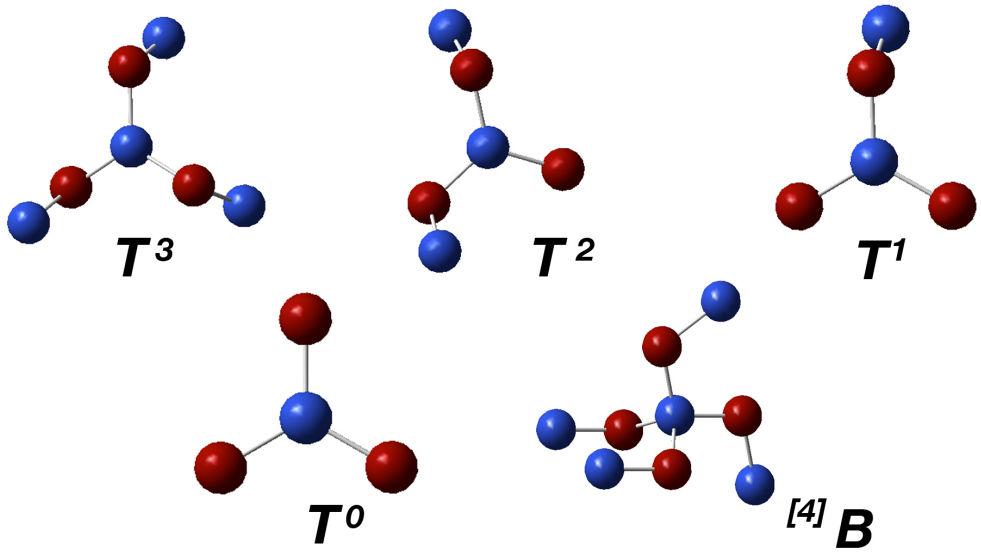

Figure 1.4. Short-range order species found for borate-containing glasses, blue circles are boron and red circles are oxygen.

1.2.3. VANADATE SPECIATION

V_2O_5 is a unique glass former as it is a transition metal oxide glass former that is difficult to vitrify. It contains a doubly bound oxygen that does not participate directly in network formation (non-covalent interactions), unlike the silicates where all oxygens are covalently bound. The structural units are comprised of V^{5+}, forming five local structures. The five local structures include a five-coordinate species ($VO_{5/2}$) and four, four-coordinate pseudo-tetrahedral vanadium environments ($VOO_{3/2}$), similar to a phosphate group (PO_4) in terms of structure. Vanadium can have a variety of oxidation states (3^+, 4^+ and 5^+) in crystalline systems but oxide-glasses typically contain diamagnetic V^{5+}.[10] The four-coordinate vanadium oxide species comprises one oxygen doubly-bound to vanadium and three oxygens that can participate in a network formation as either BOs or NBOs. The five possible structures are: five-coordinate vanadium (in a square pyramid structure)[11,12] with five BOs ($^{[5]}V$), and four pseudo-tetrahedral vanadates; three BOs (Q^3); two BOs and one NBO (Q^2); one BO and two NBOs (Q^1); and three NBOs (Q^0). As in the case for silicates, the notation Q is used and the superscript number represents the number of BO species (Figure 1.5).[10,13]

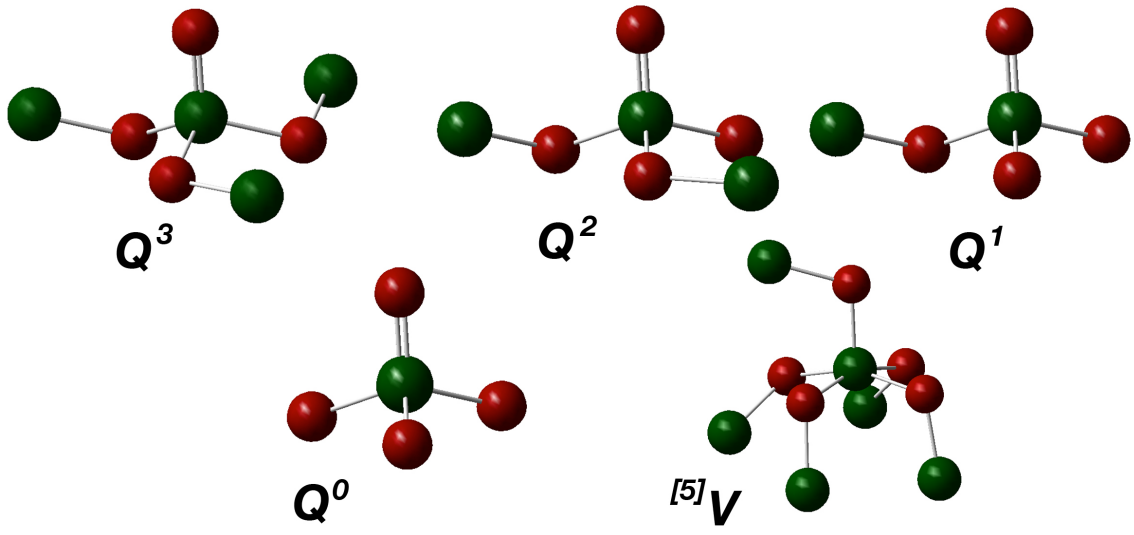

Figure 1.5. Short-range order species found in vanadate-containing glasses, green circles are vanadium and red circles are oxygen.

1.2.4. ALUMINATE AND GALLATE SPECIATION

Aluminium and gallium oxides are treated together as glassy materials due to their similar behaviour and coordination environments. Even though they do not conform to the rules set out by Zachariasen (and are thus not glass formers on their own) they are used as additives to good glass formers because both species typically increase polymerization. The local coordination surrounding these cations is four, similar to that seen in $^{[4]}$B where four oxygens are bridging with a negative charge delocalized around the species. The short-hand notations are $^{[4]}$Al and $^{[4]}$Ga. Certain glasses contain environments of five- and six-coordinate metal centres ($^{[5],[6]}$Al/Ga);[2,14] the resulting local structure is pseudo-trigonal bipyramidal and pseudo-octahedral. Glasses that exhibit these higher coordination numbers can be thought of as a four-

coordinate bridging species (covalent) with either one or two oxygens coordinating at a longer (i.e., more ionic bonding) interaction whereby the charge is maintained as -1, delocalized over the aluminium or gallium cation (Figure 1.6).

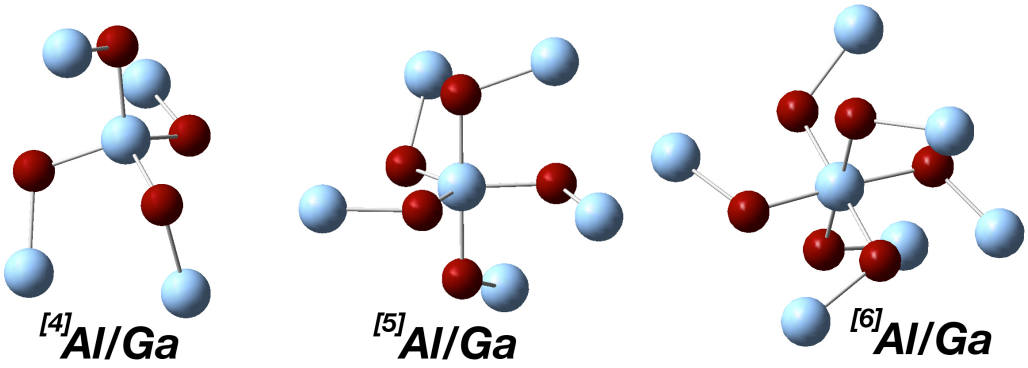

Figure 1.6. Short-range order species found in aluminate- and gallate-containing glasses, light blue are Al (Ga) and red are oxygen atoms.

1.2.5. GERMANATE SPECIATION

Germanium is below silicon within group 14 of the periodic table. As a result of the similar characteristics seen within a group, similar quaternary (four-coordinate) structures as those seen in silicates are observed. The notations for germanates are similar to those used in silicates, with Q^4 denoting four BOs, Q^3 consisting of one NBO and three BOs, and so forth until Q^0 occurs with four NBOs (Figure 1.7). Higher-coordinate (five and six) environments could also exist because germanium is a larger cation (the "germanate anomaly", Chapter 6). The six-coordinate environment contains six BOs and is abbreviated as $^{[6]}$Ge.[2,15] The five-coordinate environment would be in a pseudo-trigonal bipyramidal structure as seen for the aluminum and gallium species above (Figure 1.6).

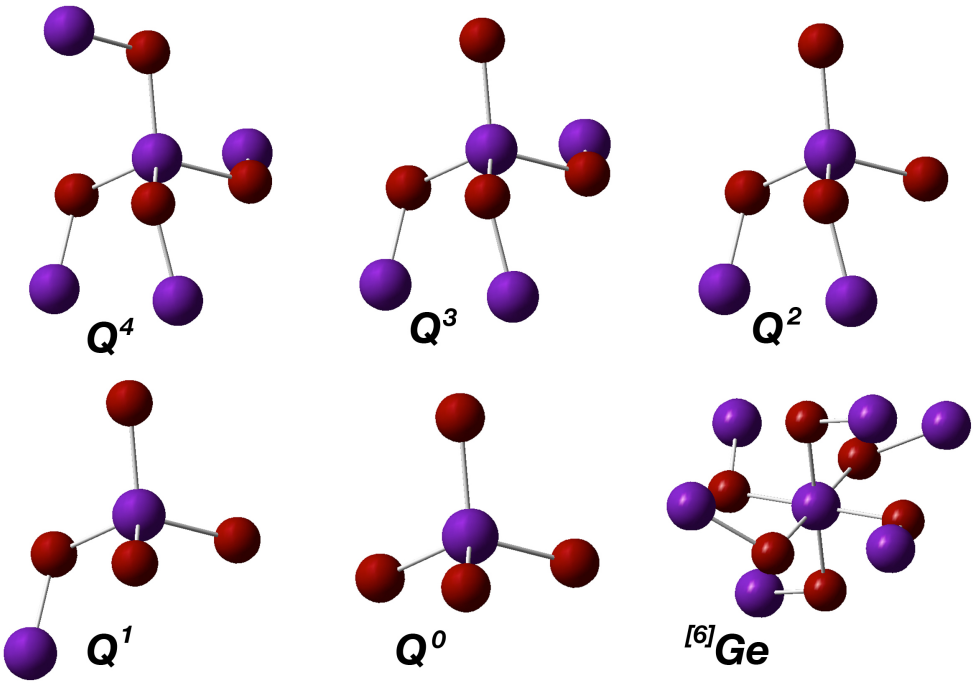

Figure 1.7. Short-range order species found for germanate-containing glasses, purple are Ge atoms and red represent O atoms.

1.3. How Local Structural Units Form

For a given network former, oxygens will be bridging in a three-dimensional array (or be doubly bound to the cation as in the case of V_2O_5 and P_2O_5). Incorporation of a network modifier will introduce excess positive charge, creating an imbalance. To maintain charge neutrality within the network, formers must break oxygen linkages to either form NBOs and/or increase their coordination number. The changes in the structure will affect the physical properties (i.e., melting temperature, density and refractive index). Considering how each compensates the new charge, one can see that SiO_2 and B_2O_3 are two examples of how the starting oxide is modified by alkali

(modifier) addition (Example 1.1 and Example 1.2). Knowing the structural changes that govern these properties proves a difficult task due to the lack of long-range periodic order.

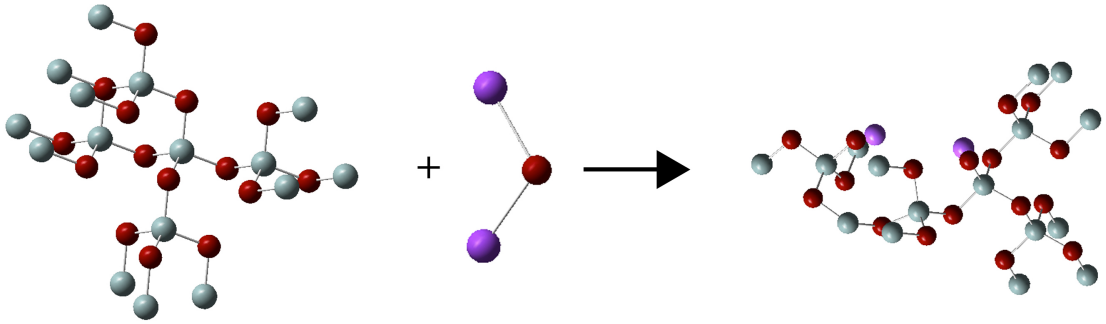

Example 1.1. Na_2O added to *v*-SiO_2 causes Q^3 speciation, decreasing network polymerization. As the Na^+ adds to the Q^4 units, Q^3 (bearing a single NBO) forms to maintain charge balance. Note the Na^+ (purple) ions are adjacent to a NBO (red) that are connected to Si (grey).

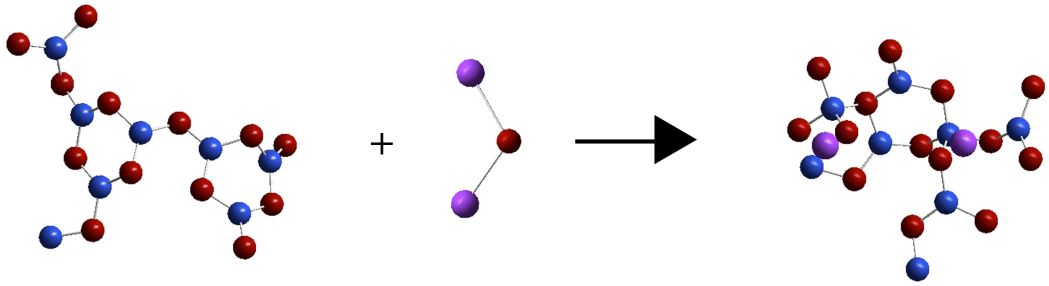

Example 1.2. K_2O added to *v*-B_2O_3 causes $^{[4]}B$ speciation, increasing polymerization in the network. Addition of K^+ causes the $^{[3]}B$ to change to $^{[4]}B$ (increase in coordination number) where the delocalized negative charge neutralizes the K^+. Both K^+ ions (purple) interact with $^{[4]}B$ (blue) that are surrounded by O (red).

Boron is an excellent glass former and B_2O_3 is a favoured oxide due to its abundance and low melting point (T_m = 450°C).[16] Borates are unique when compared to other formers such as the silicates, as boron undergoes a change in coordination environment over a large modifier range prior to the formation of NBOs. This unique behaviour will be discussed further in later chapters.

1.4. Structure Determination Methods for Glasses

Determining short- and medium-range structure in glasses is a difficult task. Traditional methods employed for studying crystalline solids such as x-ray and neutron diffraction cannot be performed easily for amorphous solids. When they are, often only limited information can be extracted. Amorphous materials that lack long-range periodic order do not provide well defined diffraction peaks. This occurs as glasses comprised of short-range order do not have well defined periodic structure causing diffraction peaks to broaden and essentially coalesce into a broad, low intensity diffraction peak spanning many degrees. Other areas where x-ray diffraction struggles is lighter elements (e.g., H, Li and B), due to the low electron density and differentiation between similar elements (e.g., Mg, Al and Si) when mixing occurs. The latter situation exists due to the electron environments (12 vs. 13 vs. 14 electrons) being similar, position mixing creates difficulties in identifying unique positions.[17] Other methods used for studying disordered materials include vibrational spectroscopy (IR, Raman), x-ray absorption fine structure (EXAFS), molecular dynamics (MD) and nuclear magnetic resonance (NMR).

1.4.1. VIBRATIONAL SPECTROSCOPY

Vibrational spectroscopy is based on measuring a change in energy as the atoms vibrate, creating transitions in energy states. IR and Raman spectroscopy provide vibrational spectra which exhibit a spectral signature from atomic vibrations in the region of 0 to 4000 cm^{-1}.[18] Vibrational spectroscopy is an attractive method in Chemistry due to its inherent sensitivity to the response of molecular vibrations.[17] This method is ideal for organic molecules which typically have resonances which span a range of ~ 4000 cm^{-1} and this spectroscopy is commonly used to determine characteristic functional groups such as, $-NH_2$, -OH, -CN and -CO. Inorganic materials are typically heavier than organic materials with reduced stiffness and longer bonds causing the vibrational mode to decrease in energy (lower wave number). As the mass of the atoms is inversely related to frequency (ν, cm^{-1}) and the spring constant (k) is related to the stiffness of the bond, inorganic vibrations are typically compressed into a narrower spectral range, i.e., 0 to 1000 cm^{-1}.[10] For example, this narrow region causes difficulties when differentiation is required between B-O, Si-O and Al-O stretches. The resolution of sites (bond-stretches) and identification of particular species is often difficult, and a quantitative analysis is nearby impossible in many cases. Further drawbacks associated with Raman and inorganic materials is that fluorescence can occur, causing the detector to become saturated.[17] Two aspects that are attractive for this method are the sensitivity and ability to identify hydroxyl groups (i.e., -OH and H_2O), and the possibility of identifying medium-range order such as rings (ring breathing modes). Larger structural units (superstructures) can be

identified using characteristic shifts, such as borate rings (808 cm^{-1}) and other rings like triborate (770 cm^{-1}).[19]

1.4.2. X-ray Absorption Spectroscopy

X-ray absorption fine structure spectroscopy uses the photoelectric effect from x-rays to interact with an atom of interest to retrieve local structural information.[18] There are two slightly different methods used to study glasses that are under the scope of XANES (near edge) and EXAFS (extended).[17] These techniques measure the absorption of x-rays as they interact with the material. If the energy of the x-ray is comparable to the energy needed to eject an electron, a response is recorded, giving rise to an absorption energy, this is typically called an absorption edge.[10,17] Because each element and local structure has a characteristic "edge" (in theory), structural information can be extracted from this behaviour. Relating these data to the sample, the atom(s) and local environment(s) can be determined based on recorded energies. It is most often used to study interatomic distances, coordination, and chemical nature (short-range order) in heavier elements (greater electron density). Certain disadvantages do exist, including insensitivity to light atomic species and the difficulty in fitting these spectra quantitatively and reliably. Small (light) atoms (Li to S) suffer from low intensity back scatter, which is due to their low electron density.[17] Electron ejection is also easier (i.e., lower energy required to eject an electron) which causes the scale for materials bearing many light atoms (Li, B, O, Si, etc.) to be compressed within a small region (few eV). This small region could potentially create difficulty in distinguishing between similar environments (e.g., T^2 vs. T^1) or similar sized element compositions (e.g., $MgAlSiO_x$ and $CaTiVSiO_x$).[17] Furthermore, acquiring quantitative

data can be challenging, requiring a large set of crystalline materials as standards to determine accurate and precise values for a proposed structural model.

1.4.3. Molecular Dynamic Calculations

For the study of dynamics and local structures governing dynamics, quantum and ab-initio based molecular dynamic (MD) calculations are often used. This method encompasses a large series (100's) of atoms in a given space. These clusters of ions are typically treated at elevated temperatures (3,000 to 4,000 K) and allowed to move throughout space in a predetermined volume randomly generating a disordered phase while the convergence energy is accomplished in about 10,000 steps (varies with system size).[20] At certain points in time the fictitious temperature is decreased (in large steps) until the system is "frozen", that is, it becomes glassy. The results of MD calculations reveal dynamic information based on the overall random structure, which in turn provides theoretical information on the system of interest. Advantages of MD simulations are that large scale systems can be calculated, including ionic and metallic glasses, that are typically difficult (nearly impossible) to synthesize. It also provides a good visual basis for cation mobility within a disordered lattice. A few drawbacks do exist, one being the unrealistic quench rates, typically on the order of 10^{11} K/s, whereas conventional laboratory and industrial quench rates are 10 to 10,000 K/s. Computational codes are also optimized for ionic and metallic glasses, often hindering at times the proper treatment of covalent oxide systems.[10]

1.5. Nuclear Magnetic Resonance

Nuclear magnetic resonance (NMR) is one of the most widely used methods for studying local structure within amorphous materials. Sensitivity can be an issue for certain nuclei in a system, but the structural information that can be gathered cannot be matched by the other methods discussed above. NMR is quantitative, sensitive to the local environment and is selective to a particular nucleus of interest. In addition, modern technology and pulse sequences developed in the past 20 years enable secondary coordination (medium-range order) to be probed, providing a better understanding of these (disordered short-range ordered) materials.

NMR is a spectroscopic method that uses a static magnetic field and a rotating magnetic field to study local environments in a variety of nuclei. Within the periodic table almost every element has at least one isotope that contains the intrinsic physical property of nuclear spin. The nuclear spin number is determined by the number of protons and neutrons within the nucleus. This spin is denoted as I, the spin quantum number and can vary from 0 (not NMR active) to I=9/2 for non-integer, non-radioactive nuclei.

All NMR active nuclei (I>0) have a magnetic moment, μ. This can be described by the interaction between the spin-quantum number, I, and another intrinsic nuclear property, the gyromagnetic ratio (γ).

$$\mu = \gamma \hbar I \qquad \textbf{(1.1)}$$

For example in a I=1/2 system (e.g., ^{1}H), the magnetic moments (i.e., nuclear spins) within a sample are introduced into a strong magnetic field (B_o), these will orient themselves with respect to B_o and precess around an axis (which we will define

as the z-axis) at a characteristic frequency, known as the Zeeman interaction. This is the simplest spin system considered (i.e., isolated spin system in a static field with no other interactions). The precessing spins can only take a certain number of states (2I+1) for a given field. Since these states have different energies this forces the degeneracy to be lifted, causing evenly spaced energy spin-states (see below, 1.3). If we use the quantum mechanical description of the Zeeman interaction we can define this as the Zeeman Hamiltonian, $\hat{H}_z$ as shown in equation 1.2.[21]

$$\hat{H}_z = -\mu \bullet B_o = -\hbar\gamma\hat{i}_z B_o \qquad \textbf{(1.2)}$$

The most commonly studied nucleus, ^{1}H, has a spin of 1/2, which gives rise to two degenerate states and allows for a single transition (1/2 to -1/2). The energy splitting of these levels is directly proportional to the field (Figure 1.8). When quadrupolar nuclei such as, ^{23}Na (I=3/2), ^{17}O (I=5/2), ^{45}Sc (I=7/2) and ^{93}Nb (I=9/2), (which respectively contain four, six, eight and ten degenerate energy levels), are introduced into a magnetic field, multiple splittings will occur (i.e., multiple single-quantum transitions). The number of energy levels of a given nucleus is given by

$$\text{Number of energy levels} = 2I+1 \qquad \textbf{(1.3)}$$

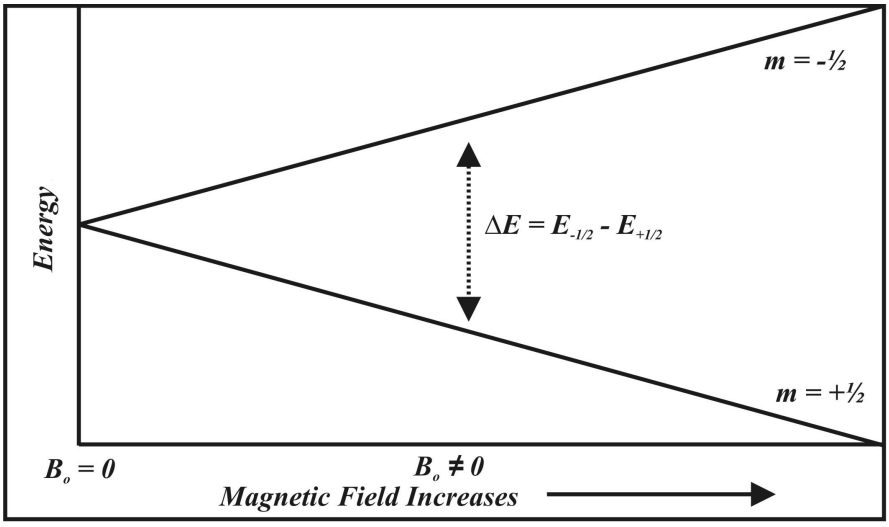

Figure 1.8. Zeeman interaction of an I=1/2 nucleus (e.g., ^{1}H, ^{13}C, ^{31}P, etc.) as the magnetic field strength increases.

The magnetic moment precesses around the magnetic field at some rate, which is known as the Larmor frequency, ν_o.

$$\nu_o = \gamma B_o/2\pi \qquad \textbf{(1.4)}$$

The Larmor frequency falls into the radiofrequency range (MHz) and is therefore a low energy method within the electromagnetic spectrum. The splitting caused by the Zeeman interaction can be expressed as an energy term, ΔE. The energy difference is proportional to the magnetic field.

$$\Delta E = \gamma \hbar B_o \qquad \textbf{(1.5)}$$

In the absence of a magnetic field, the nuclear spins occupy degenerate energy levels. The Zeeman interaction imparts a change in the population distribution of the nuclear spins, based on two energy levels (I=1/2). The difference in population will be proportional to B_o, where a stronger field causes a greater population of the lower level. The population difference between the energy levels can be described by the

Boltzmann distribution. This allows the probability of the relative populations to be determined between the two energy states.

$$\frac{N_{-1/2}}{N_{1/2}} = e^{\frac{-\Delta E}{kT}} \tag{1.6}$$

For an I=1/2 spin, the total number of spins must equal the sum of the two energy levels. Thus $N = N_{1/2} + N_{-1/2}$, and the difference is $n = N_{1/2} - N_{-1/2}$. Combining these equations, the value of $N_{1/2}= (N+n)/2$ and for $N_{-1/2}=(N-n)/2$. The Boltzmann equation then becomes:

$$\frac{N-n}{N+n} = e^{\frac{-\Delta E}{kT}} \rightarrow n = N\left[\frac{1-e^{\frac{-\Delta E}{kT}}}{1+e^{\frac{-\Delta E}{kT}}}\right] \tag{1.7}$$

In NMR it is appropriate to make the high temperature approximation, $\Delta E/kT<<1$, resulting in $n=N(\Delta E/2kT)$, where $\Delta E = E_{-1/2}-E_{1/2}=\gamma\hbar B_o$.[4,21] Therefore one can increase the sensitivity by increasing B_o and/or decreasing temperature. Only a small proportion of spins will contribute to the signal, on the order of 1/1000 to 1/10000.[22]

This population difference is what enables NMR to be performed on a given nucleus. The energy difference(s) between the levels is small, causing the population difference to be small, requiring many spins for a signal to be observed. Applying a pulse at a specific Larmor frequency causes a perturbation of those nuclear spins to the higher energy level. After the pulse, these promoted spins will precess about B_o generating a measureable magnetic field as the system relaxes back to equilibrium.

This new albeit small generated rotating magnetic moment, induces an electro-magnetic field in the receiver coil (μV, typically) which is recorded as a free induction decay.[21,23] This magnetic field that is generated by the precessing magnetic moments is related to an induced electric field according to Maxwell's equations.[23] Strong pulses and higher fields are favoured to promote more nuclear spins into higher energy levels. This results in a stronger and more sensitive signal. For I>1/2 nuclei the same approach is taken, but one must deal with more energy levels and different population distributions. This could result in fewer "observable" spins as a variety of transitions between spin populations could occur including various coherences decreasing sensitivity even further. The magnetization that we record is governed by two relaxation rates, spin-lattice (T_1) is the time for the Boltzmann distribution to develop (time required between pulses), and spin-spin (T_2), which is the coherence life-time (i.e., the signal that is detected).

1.6. Anisotropic Interactions in Solids

Above we introduced the Zeeman interaction (H_z), which causes an energy splitting when magnetic moments are introduced into a magnetic field. To express any system one needs to consider the total internal nuclear electromagnetic interaction ($H_{internal}$) that is experienced within a sample. These interactions include J-coupling (H_J), dipolar coupling (H_D), chemical shielding (H_{CS}), Knight shift (H_{KS}), paramagnetic interaction (H_P) and quadrupolar interaction (H_Q[1,2]). The magnitudes of these interactions vary and range from a few Hz to MHz. Three internal interactions that are of particular importance to solid state NMR include: i) chemical shielding, ii) dipolar coupling and

iii) quadrupolar coupling. The anisotropic portions of these interactions have no effect on the observed frequencies in liquids and gases (in most cases). Rapid rotation and free-motion averages the chemical shielding anisotropy (CSA) and dipole-dipole interaction but becomes slightly more complex for the quadrupolar interaction as T_2 (defined below) can become very short, potentially causing the sites to become "invisible". In some cases it can be easier to study quadrupolar nuclei in the solid state as the lack of motion in the solid can lengthen T_2. A description of these interactions follows:

$$H_{internal} = H_J + H_D + H_{CS} + H_{KS} + H_P + H_Q^1 + H_Q^2 \quad \textbf{(1.8)}$$

1.6.1. Chemical Shielding Interaction

The chemical shielding interaction involves the local electron density within a system and the effect it has on the nucleus. The interaction is expressed below where σ is the shielding tensor.

$$H_{CS} = \gamma_I h I \bullet \sigma \bullet B_o \quad \textbf{(1.9)}$$

The shielding felt by a nucleus is based on their electronic environment, giving rise to a resonance frequency. To understand shielding, let us focus on a bare nucleus (i.e., no electrons), this would have a characteristic Larmor frequency.[24] Since a nucleus is not free of electrons, electronic coupling with the surrounding field (B_o) causes a new transition frequency, υ (although small). This effect changes the field at the nucleus, which is defined as shielding (i.e., the effect on the nucleus caused by surrounding electrons).

$$\upsilon = (1 - \sigma)\left[\frac{B_o|\gamma|}{2\pi}\right] \quad \textbf{(1.10)}$$

As the electronic interaction for a nucleus is three dimensional, one can describe the orientation of a nucleus (within a B_o) using a 3 x 3 tensor. This tensor provides information of the electronic environment of the nucleus and B_o.[25]

$$\sigma = \begin{bmatrix} \sigma_{11} & \sigma_{12} & \sigma_{13} \\ \sigma_{21} & \sigma_{22} & \sigma_{23} \\ \sigma_{31} & \sigma_{32} & \sigma_{33} \end{bmatrix} = \sigma_{iso} + \sigma_{sym} + \sigma_{anti} \qquad \textbf{(1.11)}$$

This potentially allows up to nine independent components to be used in the description of the chemical shielding interaction within the surrounding field. The tensor is comprised of three contributing terms, isotropic, symmetric and anti-symmetric. The anti-symmetric component of the tensor has no measurable effect on the lineshape at conventional fields. Because of this we can remove it from our discussion (the anti-symmetric portion of the tensor affects higher order terms, since the Zeeman interaction is always larger than any contribution from shielding for a system).[25,26]

$$\sigma = \begin{bmatrix} \sigma_{11} & \sigma_{12} & \sigma_{13} \\ \sigma_{12} & \sigma_{22} & \sigma_{23} \\ \sigma_{13} & \sigma_{23} & \sigma_{33} \end{bmatrix} = \sigma_{iso} + \sigma_{sym} \qquad \textbf{(1.12)}$$

The isotropic matrix provides the position of the centre of the spectrum, while the symmetric tensor will provide the lineshape for the system. If we operate in the principal axis system, PAS (coordinate system in which the tensor is diagonalized) we can form a diagonal matrix with three diagonal elements, these are used to define the

chemical shift tensor, where $\sigma_{11} \leq \sigma_{22} \leq \sigma_{33}$. The remaining three elements are the Euler angles (α, β and γ) that provide the directions of the PAS in the molecular frame.[25,26]

$$\sigma_{PAS} = \begin{bmatrix} \sigma_{11} & 0 & 0 \\ 0 & \sigma_{22} & 0 \\ 0 & 0 & \sigma_{33} \end{bmatrix} \quad \textbf{(1.13)}$$

Within an experimental scenario we rarely refer to actual shieldings. Instead one often uses the term chemical shift. This creates the chemical shift convention where $\nu_{unknown}$ is the frequency of your sample and ν_{ref} is the frequency of your reference.

$$\delta_{unknown} = \left[\frac{\nu_{unknown} - \nu_{ref}}{\nu_{ref}} \right] \bullet 10^6 \quad \textbf{(1.14)}$$

The relationship between chemical shift and chemical shielding is simply

$$\delta_{unknown} = \left[\frac{\sigma_{ref} - \sigma_{unknown}}{1 - \sigma_{ref}} \right] \bullet 10^6 \quad \textbf{(1.15)}$$

This is further simplified since $\sigma_{ref} \approx 0$ (for most systems) and the chemical shift is

$$\delta_{unknown} = \left[\sigma_{ref} - \sigma_{unknown} \right] \bullet 10^6 \quad \textbf{(1.16)}$$

Therefore the shielding tensor in equation 1.13 can be recast in terms of chemical shift

$$\delta_{PAS} = \begin{bmatrix} \delta_{11} & 0 & 0 \\ 0 & \delta_{22} & 0 \\ 0 & 0 & \delta_{33} \end{bmatrix} \quad \textbf{(1.17)}$$

By convention these three components are ordered as $\delta_{11} \geq \delta_{22} \geq \delta_{33}$. Three useful parameters are typically reported: average shift (isotropic shift, δ_{iso}), full breadth of the anisotropy (span, Ω) and the 'shape-factor' of the anisotropy (skew, κ).

$$\delta_{iso} = \left(\delta_{11} + \delta_{22} + \delta_{33}\right)/3 \quad \textbf{(1.18)}$$

$$\Omega = \delta_{11} - \delta_{33} \quad \textbf{(1.19)}$$

$$\kappa = \frac{3\left(\delta_{22} - \delta_{iso}\right)}{\Omega} \quad \textbf{(1.20)}$$

The chemical shift anisotropy interaction is typically found to be on the order of a few ppm to 100's of ppm. At higher fields this interaction increases linearly, i.e., 10 ppm CSA for ^{1}H at 100 MHz is 100 Hz versus 10 ppm CSA for ^{1}H at 800 MHz is 800 Hz. To minimize this interaction (in Hz) lower B_o fields are preferred.

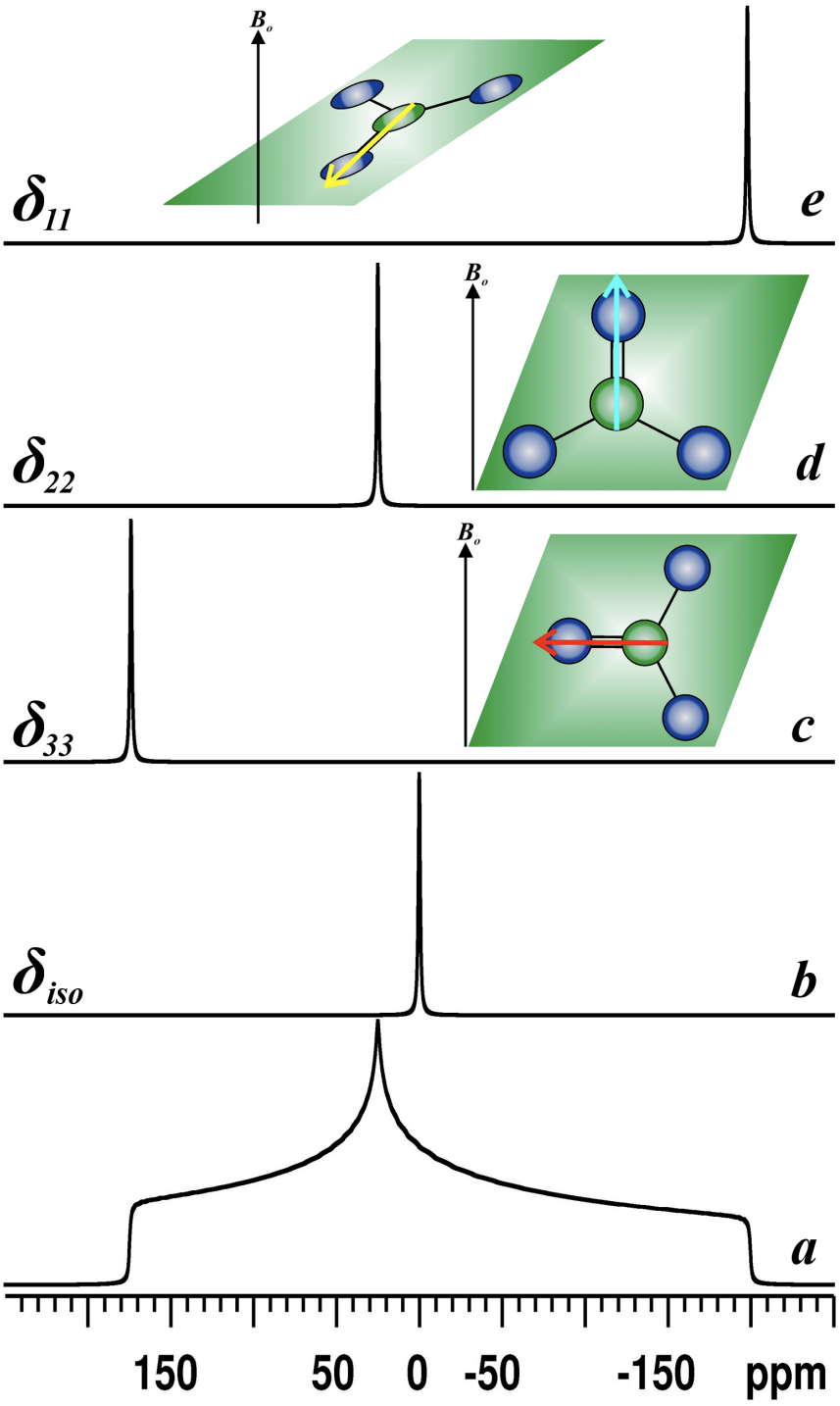

Figure 1.9. Chemical shift anisotropic interaction: (a) powder pattern, (b) isotropic shift, δ_{iso} and the three chemical shift tensors (c) δ_{33}, (d) δ_{22} and (e) δ_{11}. The simple molecule is shown in different orientations with respect to the magnetic field. These

three orientations represent the principal tensor components, while the whole powdered sample pattern is shown in (a). As the orientation of the molecule is now a distribution within the field a different shielding will be observed giving rise to the anisotropic powder spectrum.

1.6.2. DIPOLAR COUPLING INTERACTION

The dipolar coupling interaction in its simplest form can be viewed as two bar magnets. If these approach each other either an attraction or repulsion force occurs. We can express the interactions between these two magnets as magnetic dipoles μ_1 and μ_2 as

$$U = \left(\frac{\mu_o}{4\pi}\right)\left\{\frac{\mu_1 \cdot \mu_2}{r^3} - 3\frac{(\mu_1 \cdot r)(\mu_2 \cdot r)}{r^5}\right\} \tag{1.21}$$

where r is the distance between dipoles, U is the energy of the interacting dipoles and μ_o is the vacuum permeability constant.

Nuclear spins contain an intrinsic nuclear magnetic moment (μ, above) that will precess around a strong magnetic field. These nuclear spins (I and S) can interact through space (Figure 1.10) just as in the case of the bar magnets, causing a small splitting to the Zeeman interaction.

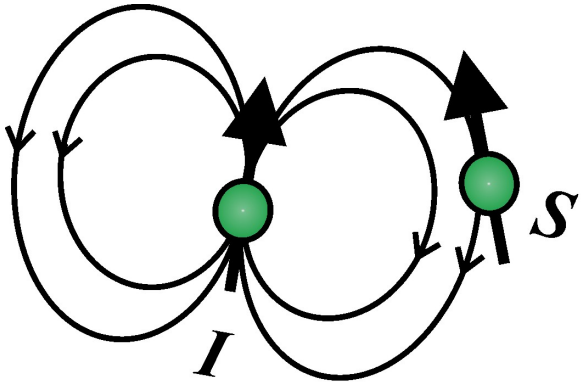

Figure 1.10. Two spin-1/2 nuclei interacting with one another in space, showing the effect of the dipolar interaction.

This small splitting in energy is caused by the dipole-dipole interaction and is observable as an broadening in a spectrum. If this interaction occurs between the same nuclear spins, I=S (e.g., ^{1}H-^{1}H or ^{7}Li-^{7}Li), this is known as a homonuclear dipolar coupling, whereas a heteronuclear coupling occurs when I≠S (e.g., ^{1}H-^{31}P).[13,27] The dipolar interaction (H_D) is shown in equation 1.22.

$$H_D = \left[\left(\frac{\mu_o}{4\pi}\right)\left(\frac{\gamma_I \gamma_S \hbar}{r^3}\right)\right]\{A + B + C + D + E + F\} \qquad \textbf{(1.22)}$$

Where γ_I and γ_S are the gyromagnetic ratio terms for nuclear spins I and S. The six alphabetic terms (A-F) that contribute to the dipolar interaction are defined below.

$$
\begin{aligned}
A &= I_{1Z}I_{2Z}\left(3\cos^2\theta - 1\right) \\
B &= -\frac{1}{4}\left[I_{1+}I_{2-} + I_{1-}I_{2+}\right]\left(3\cos^2\theta - 1\right) \\
C &= -\frac{3}{2}\left[I_{1+}I_{2Z} + I_{1Z}I_{2+}\right]\left(\sin\theta\cos\theta\right)\exp(-i\phi) \\
D &= -\frac{3}{2}\left[I_{1-}I_{2Z} + I_{1Z}I_{2-}\right]\left(\sin\theta\cos\theta\right)\exp(+i\phi) \\
E &= -\frac{3}{4}\left[I_{1+}I_{2+}\right]\sin^2\theta\exp(-2i\phi) \\
F &= -\frac{3}{4}\left[I_{1-}I_{2-}\right]\sin^2\theta\exp(+2i\phi)
\end{aligned}
\qquad \textbf{(1.23)}
$$

Of these six terms we can conveniently remove four (C to F) as these are time-dependant terms known as the non-secular portion of the dipolar Hamiltonian. These contribute to the relaxation behaviour however their effect on the spectrum or energy splitting is negligible, enabling us to neglect these terms.[4,23] The A and B terms comprise the secular portion of the dipolar interaction, which are time-independent. These cannot be set to zero and can contribute to homonuclear (A and B terms) and heteronuclear (A term only) dipolar interactions.

1.6.2.1. Homonuclear Dipolar Coupling

The homonuclear dipolar interaction occurs between two spins of the same nuclear species (e.g., ^{1}H-^{1}H or ^{7}Li-^{7}Li). The two most important terms within H_D are the distance (r^{-3}) and the gyromagnetic ratio, γ. As shown in equation 1.22, if γ becomes smaller and/or the distance between the nuclei increase, the overall dipolar interaction will decrease. Therefore high-γ nuclei (e.g., ^{1}H, ^{7}Li, ^{19}F and ^{31}P) cause a larger concern for homonuclear dipolar interactions than lower-γ nuclei (e.g., ^{25}Mg, ^{89}Y and ^{109}Ag). Both the A and B terms have a '$3\cos^2\theta$-1' term, which further can be

used to remove or alleviate the dipolar interaction, vide infra. However, the B-term complicates this for the homonuclear (but not the heteronuclear) case as it also contains the 'flip-flop' operator. This 'flip-flop' term allows transitions between different spin-states for coupled nuclei. For example, if we have two coupled spins (I=1/2), the αα(1/2,1/2) and βα (-1/2,1/2) levels are linked, which can flip back and forth. As this allows for the coupled spins to change-states over time (e.g., 1/2 to -1/2 or α -> β) reaching an isotropic value can be difficult using conventional averaging methods.

1.6.2.2. Heteronuclear Interaction

Since the highest probability of the flip-flop process occurring is when no external energy is required; the heteronuclear dipolar coupling interaction (i.e., I≠S) is less of an issue due to the effects of the B term becoming negligible. In the heteronuclear case the energies of spins I and S are different (i.e., requiring external energy), preventing the 'flip-flop' operator to change in the B term. The A term, however will cause broadening depending on the orientation of the two spins with respect to B_o.

The dipolar Hamiltonian presents one crucial feature, (absent from all the other NMR interactions) which is the relation between dipolar coupling and inter-atomic distance. This opens up the opportunity to determine atomic distances between spins.

1.6.3. Quadrupolar Interaction

The quadrupolar interaction is present within ~74% of NMR active nuclei in the periodic table, meaning they possess an electric quadrupole moment (eQ). All spin-

active nuclei with I > 1/2 have a non-spherical nuclear charge distribution (Figure 1.11).

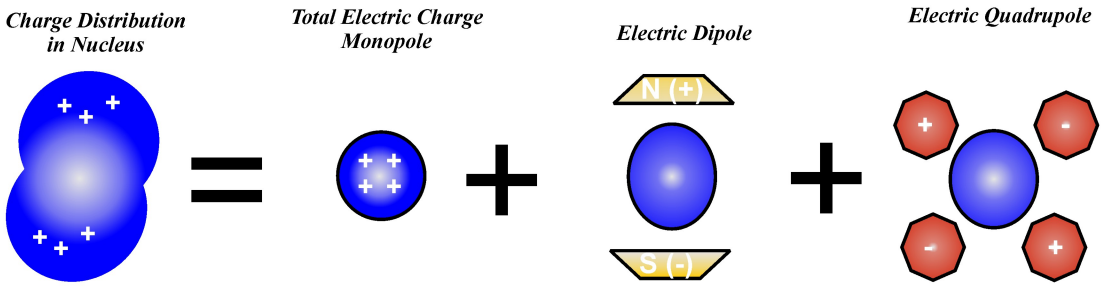

Figure 1.11. Overall charge distribution caused by the electric monopole, dipole and quadrupole interactions for a I>1/2 nucleus. Note: Physicists have shown that the electric dipole is zero and does not exist.

This interaction is observed in spectra when the electric quadrupolar moment (intrinsic to the nucleus, eQ) interacts with the electric field gradient (**V**) from the surrounding atomic environment causing a change in the energy levels.

The electric field gradient **V** is of interest as it can relate information of the local environment in which the nucleus is situated. If we think of this charge distribution in an electrostatic potential (ρ(r)), the energy will be defined by E and the volume surrounding the nucleus is *V(r)*. We can describe the electrostatic potential using a Taylor expansion (1.26).[4]

$$E = \int \rho(r) \bullet V(r) d\tau$$
$$V(r) = V(0) + \sum_{i=x,y,z} i \frac{\partial V}{\partial i}\Big|_{r=0} + \frac{1}{2!}\sum_{i,j} ij \frac{\partial^2 V}{\partial_i \partial_j}\Big|_{r=o} + \ldots$$
$$V_i = \frac{\partial V}{\partial i} \qquad \textbf{(1.24)}$$
$$V_{ij} = \frac{\partial^2 V}{\partial_i \partial_j}$$

Where V_{ij} is the Cartesian components of the electric field gradient at the origin, ***V***. Here, ***V*** is a second-rank symmetrical tensor. Within the PAS ***V*** is diagonal with $|V_{ZZ}| \geq |V_{YY}| \geq |V_{XX}|$, with the largest component defined as V_{ZZ} and $V_{XX}+V_{YY}+V_{ZZ}=0$.[28,29]

$$\boldsymbol{V} = \begin{bmatrix} V_{XX} & 0 & 0 \\ 0 & V_{YY} & 0 \\ 0 & 0 & V_{ZZ} \end{bmatrix} \qquad \textbf{(1.25)}$$

The quadrupolar interaction within the PAS is defined below where operator $\hat{I}$ is the angular spin momentum, $\hat{I}_Z$ is the Z-component of the angular momentum and the raising and lowering operators are $\hat{I}_+ = \hat{I}_X + i\hat{I}_Y$ and $\hat{I}_- = \hat{I}_X - i\hat{I}_Y$.[30]

$$\hbar \hat{H}_Q = \frac{C_Q}{4I(2I-1)}\left[3\hat{I}_Z^2 - I(I+1) + \frac{\eta}{2}(\hat{I}_+^2 + \hat{I}_-^2)\right] \qquad \textbf{(1.26)}$$

This interaction is described by the quadrupolar coupling constant (C_Q) and the asymmetry parameter (η) defined below.

$$C_Q = \frac{eQV_{ZZ}}{h} \qquad \textbf{(1.27)}$$

$$\eta = \frac{V_{XX} - V_{YY}}{V_{ZZ}} \quad \textbf{(1.28)}$$

It is this interaction between V_{ZZ} and the quadrupolar moment (eQ) that causes an effect in the spectrum as described by C_Q and η (where C_Q can typically range from 0 Hz to 100's of MHz and η is between 0 and 1).

The three tensor components, V_{XX}, V_{YY} and V_{ZZ} describe the electric field gradient (arising from the charge distribution outside the atom). The coupling between the eletric field gradient and the quadrupole moment will manifest in the observed spectrum and be accompanied by a characteristic shape based on the local symmetry at the nucleus (Figure 1.12).

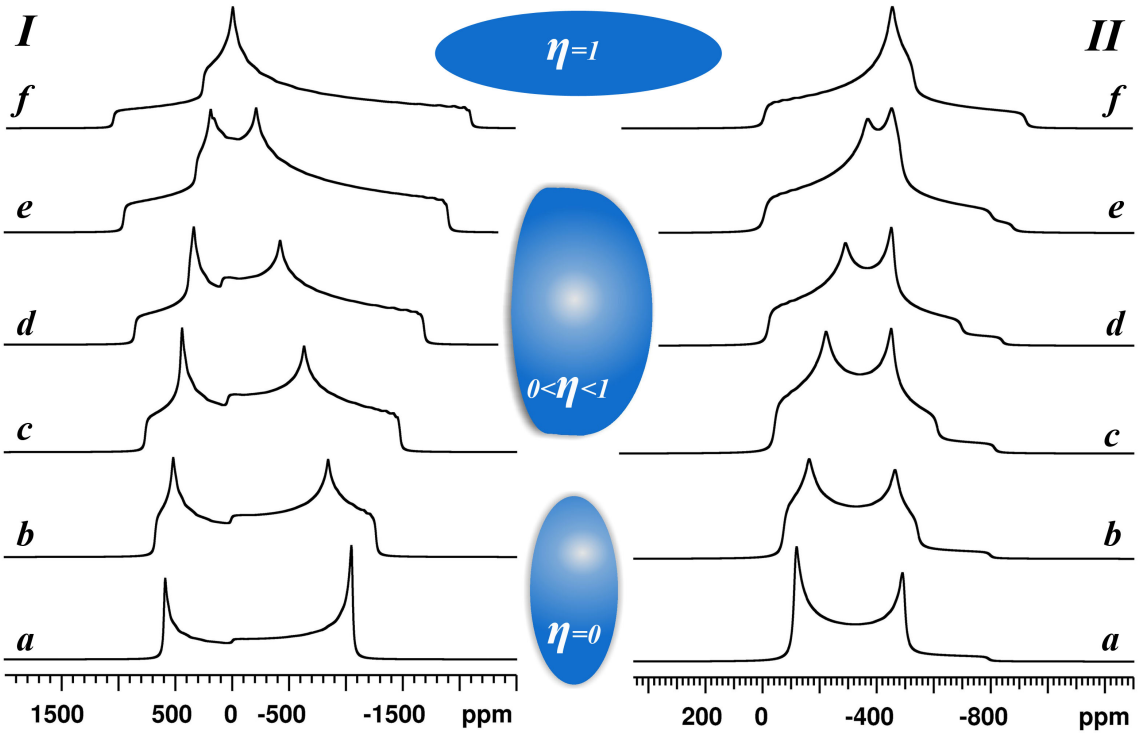

Figure 1.12. Second order quadrupolar lineshape of the central transition as the three EFG tensors change. I: non-spinning and II: magic angle spinning (discussed below) with (a) η=0, (b) 0.2, (c) 0.4, (d) 0.6, (e) 0.8, (f) 1.0.

1.6.3.1. Quadrupolar – Zeeman Interaction

The quadrupolar interaction acts as a perturbation of the Zeeman interaction (when in a high field scenario), thus enabling the quadrupolar Hamiltonian (H_Q) to be split into first- and second-order contributions ($H_Q = H_Q^1 + H_Q^2$).[4,26,30]

$$H_Q = \frac{eQh}{4I(2I-1)}\left\{\sqrt{\frac{3}{2}}\left[3\hat{I}_Z^2 - \hat{I}^2\right]V_o + \left[\hat{I}_Z\hat{I}_+ + \hat{I}_+\hat{I}_Z\right]V_{-1} - \left[\hat{I}_Z\hat{I}_- + \hat{I}_-\hat{I}_Z\right]V_1 + \hat{I}_+^2V_{-2} - \hat{I}_-^2V_2\right\} \quad \textbf{(1.29)}$$

$$H_Q^1 = \frac{eQh}{4I(2I-1)}\sqrt{\frac{3}{2}}\left[3\hat{I}_Z^2 - \hat{I}^2\right]V_o \quad \textbf{(1.30)}$$

$$H_Q^2 = -\frac{2}{\upsilon_o}\left(\frac{eQ}{4I(2I-1)}\right)^2\left\{V_1V_{-1}\hat{I}_Z(4\hat{I}^2 - 8\hat{I}_Z^2 - 1) + V_2V_{-2}\hat{I}_Z^2(2\hat{I}^2 - 2\hat{I}_Z^2 - 1)\right\} \qquad \textbf{(1.31)}$$

Where υ_o is the spectrometer frequency, V_0, V_1, V_{-1}, V_2 and V_{-2} are

$$V_0 = 3\sqrt{\frac{1}{6}V_{ZZ}}$$
$$V_1 = -V_{XZ} - iV_{YZ}$$
$$V_{-1} = V_{XZ} - iV_{YZ}$$
$$V_2 = \frac{1}{2}(V_{XX} - V_{YY}) + iV_{XY}$$
$$V_{-2} = \frac{1}{2}(V_{XX} - V_{YY}) - iV_{XY}$$

Within the PAS the elements simplify to $V_o = \sqrt{3}/2 \bullet V_{ZZ}$, $V_{\pm1} = 0$ and $V_{\pm2} = (V_{ZZ} \bullet \eta)/2$.[4]

It is important to note that the central transition (1/2 to -1/2) is unaffected by the first-order interaction (it only experiences the second-order and higher symmetric terms) and the satellite transitions (all transitions other than 1/2 to -1/2) are mostly affected by first order interactions, with slight effects from higher order terms (Figure 1.13).

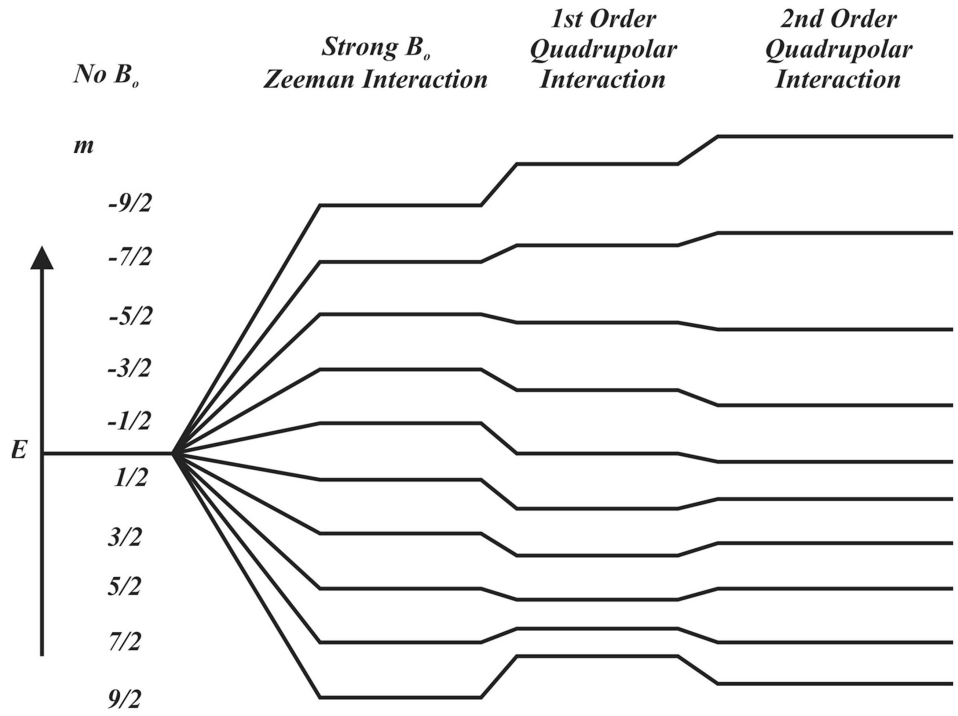

Figure 1.13. The Zeeman+Quadrupolar interaction for a I=9/2 nucleus illustrating the effects of the Zeeman interaction and the 1st and 2nd order quadrupolar interactions on the nuclear energy levels.

The first-order interaction causes the former evenly spaced energy levels resulting from the Zeeman interaction to become unevenly split causing a change in the peak shape. The satellite transitions either increase or decrease under first order, creating a new energy difference between the single-quantum transitions, however the central transition is unaffected to first order. The energy differences between analogous spin states (i.e., ±3/2, ±5/2, ±7/2 and ±9/2) stay the same. The second-order interaction affects all the energy levels, although the effect is greater for the CT, as it is unaffected to first-order (Figure 1.13).

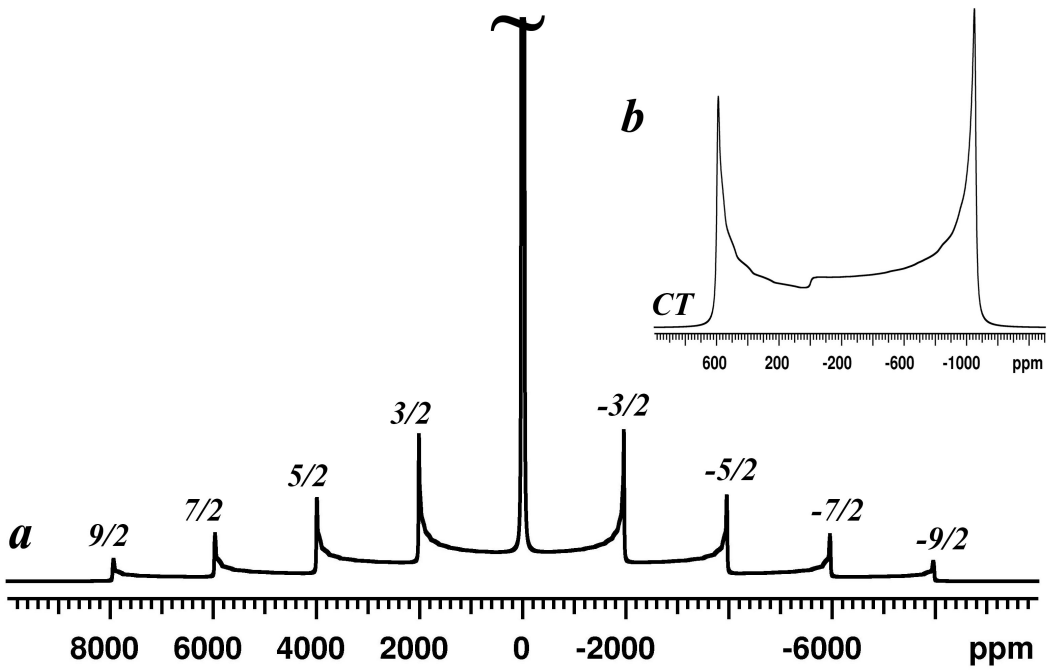

Figure 1.14. (a) powder spectrum of all nine single quantum transitions for an I=9/2 nucleus, (e.g., ^{73}Ge or ^{93}Nb). The "~" represents the CT that is off-scale due to increasing the scaling for the satellite transitions. Each satellite transition is labeled accordingly, with each satellite caused by a single quantum transition (i.e., 9/2<-> 7/2 or -5/2 <-> -7/2) and (b) Enlargement of the central transition (1/2 to -1/2) from the powder spectrum in (a), showing the effect of the second-order quadrupolar interaction.

Determining C_Q, η and δ_{iso} parameters from a spectrum can be difficult when they span many kHz to MHz. The magnitude of the quadrupolar coupling can be estimated by measuring the total breadth of the spectrum ($\Delta\nu_{full}$ in Hz),

$$\Delta\nu_{full} = |1-2m|\upsilon_Q \qquad \textbf{(1.32)}$$

$$\upsilon_Q = \frac{3C_Q}{2I(2I-1)} \qquad \textbf{(1.33)}$$

where m is the satellite transition of interest ±3/2, ±5/2, ±7/2 or ±9/2 and ν_Q is the quadrupolar frequency (Figure 1.15).

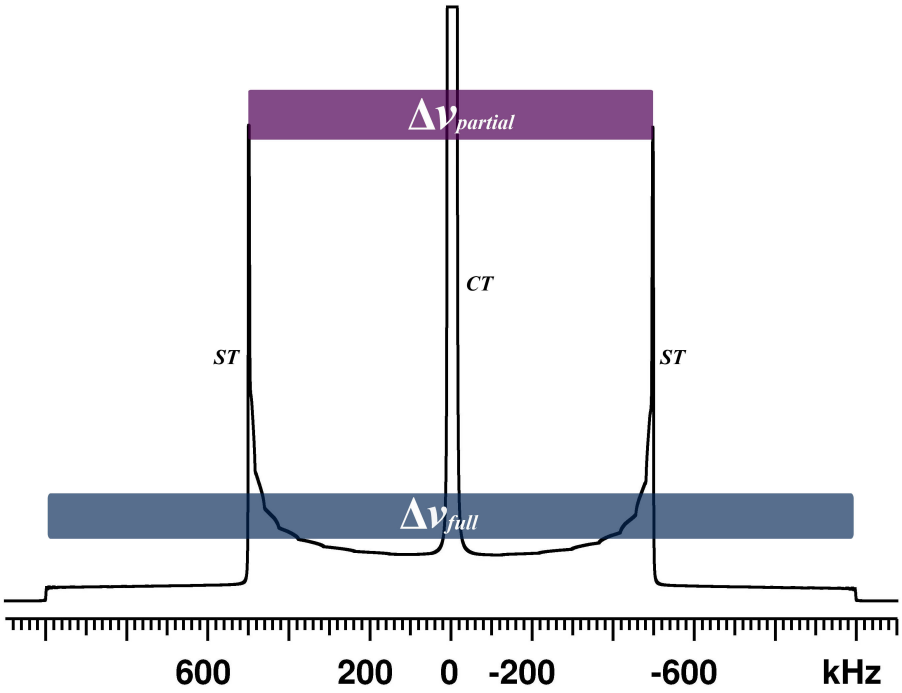

Figure 1.15. The full separation ($\Delta\upsilon_{full}$) measured in Hz is used to calculate the quadrupolar coupling interactions. The breadth of the satellites ($\Delta\upsilon_{partial}$) provides a way to measure the asymmetry parameter as discussed below.

The asymmetry parameter can be measured from the breadths of the satellite transitions and breadths of the horns using,

$$\Delta\nu_{partial} = \Delta\nu_{full}\left[\frac{1-\eta}{2}\right] \qquad \textbf{(1.34)}$$

Since the CT is broadened by the second-order quadrupolar interaction, determining the isotropic shift requires a little more effort. One needs to take into account the field dependence of the second-order interaction and the inherent

relationship to the isotropic shift. From the spectrum, one can easily determine the centre-of-gravity shift (δ_{cgs}) and knowing the C_Q and η, we can determine the isotropic shift (δ_{iso})

$$\delta_{iso} = \delta_{cgs}^{EXP} + \frac{1}{30}\left(1+\frac{1}{3}\eta^2\right)\left[I(I+1)-\frac{3}{4}\right]\frac{3(C_Q)^2}{2I(2I-1)\nu_o} \qquad \textbf{(1.35)}$$

The second-order quadrupolar broadening based on the quadrupolar coupling constant can also be calculated. This is useful in determining what sort of contributions to linewidths are expected for systems that have a small quadrupolar interaction, such as encountered in ^{7}Li, ^{9}Be and ^{133}Cs NMR. We will abbreviate the second-order quadrupolar effect as SOQE and ν_o as the Larmor frequency (Figure 1.16).

$$SOQE = \frac{1}{30}\left(I(I+1)-\frac{3}{4}\right)\left(1+\frac{2}{3}\eta\right)\left[\frac{\nu_Q^2}{\nu_o}\right] \qquad \textbf{(1.36)}$$

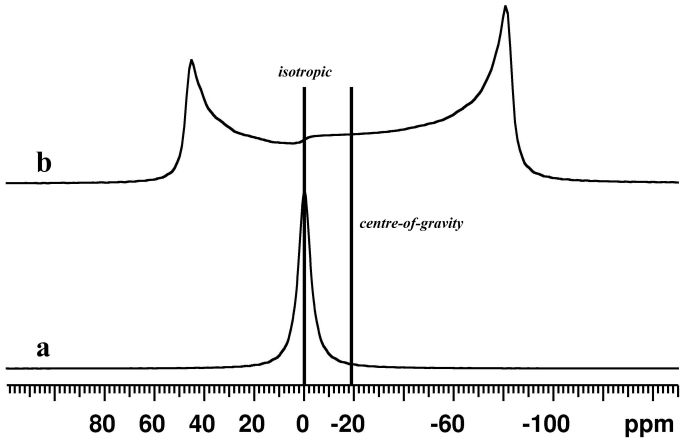

Figure 1.16. (a) Isotropic shift (δ_{iso}) and (b) full second order quadrupolar lineshape of the central transition. Note the centre-of-gravity in (b) does not correspond to the isotropic shift.

1.6.4. Solution versus Solid NMR

Although one or more of these anisotropic interactions exist they are typically only observed in solids. Solution NMR is identical to solid-state NMR in terms of the theory. However, the inherent anisotropic interactions that broaden solid spectra typically do not occur in solutions due to the molecules' ability to rotate freely within a liquid phase.[31] The rapid motion in solution averages these interactions leaving behind the isotropic component, which is the isotropic shift. However, with averaging one loses vital information regarding local structure. This information is retained in solids and solid-state NMR spectroscopists have other methods to get "solution-like" spectra while maximizing the local structural information from a solid.

1.7. The "Magic" in Magic Angle Spinning

Solid spectra traditionally were collected under non-spinning conditions. The powdered samples are comprised of millions of tiny 'crystallites' representing the material with their orientation in the field being arbitrary. Each crystallite has a slightly different resonance frequency based on the orientation, resulting in a powder spectrum (powder pattern). This powder pattern would contain all the information on the system with any and all relevant anisotropic interactions already mentioned. This method is functional but suffers from multiple interactions that broaden the signal, creating challenges in determining the magnitudes of each interaction. In addition, most solids have multiple sites, which cause further overlap, impeding the deconvolution of the individual anisotropic contributions. Dissolving these in solution is not a possible route either for determining isotropic chemical shift as many inorganic solids will decompose, change structurally when introduced into a solvent, or are insoluble. A method would need to be developed in order to overcome these inherent drawbacks, other than solution state NMR where only the isotropic shift can be observed.

In the late 1950's Andrew[32] and Lowe[32,33] independently suggested a ground-breaking concept with their introduction of a new tool for the solid state spectroscopist. Their concept was to rotate a solid powder at a fixed angle at a high rate (typically hundreds to thousands of hertz). They realized that many of the larger anisotropic interactions had a common spatial term that existed when the powder was placed in a field, namely $P_2(\cos\theta)$.

$$P_2(\cos\theta) = \frac{3\cos^2\theta - 1}{2} \quad \textbf{(1.37)}$$

Although θ within the magnetic field can vary from 0^0 (perpendicular to B_o) to 90^o (parallel to B_o), only one angle (54.73^o) causes this term to be zero under spinning conditions. In theory, if one were able to spin the sample infinitely quickly, many of the anisotropic terms would be zero. This was the creation of magic angle spinning (MAS) and is the most common application for solid state NMR today.

Spinning infinitely quickly is obviously impossible. Therefore MAS often reduces these interactions and at times can remove them completely depending on their magnitude. Generally, the spinning frequency has to be in the order of the interaction (or faster) for the interaction effect to be removed. For example, ^{207}Pb (I=1/2) bearing material under non-spinning conditions has a span of 40 kHz at a magnetic field of 14 T. The sample should be spinning at a frequency >40 kHz, for one to observe a "solution-like spectrum", which is the isotropic peak (Figure 1.17).

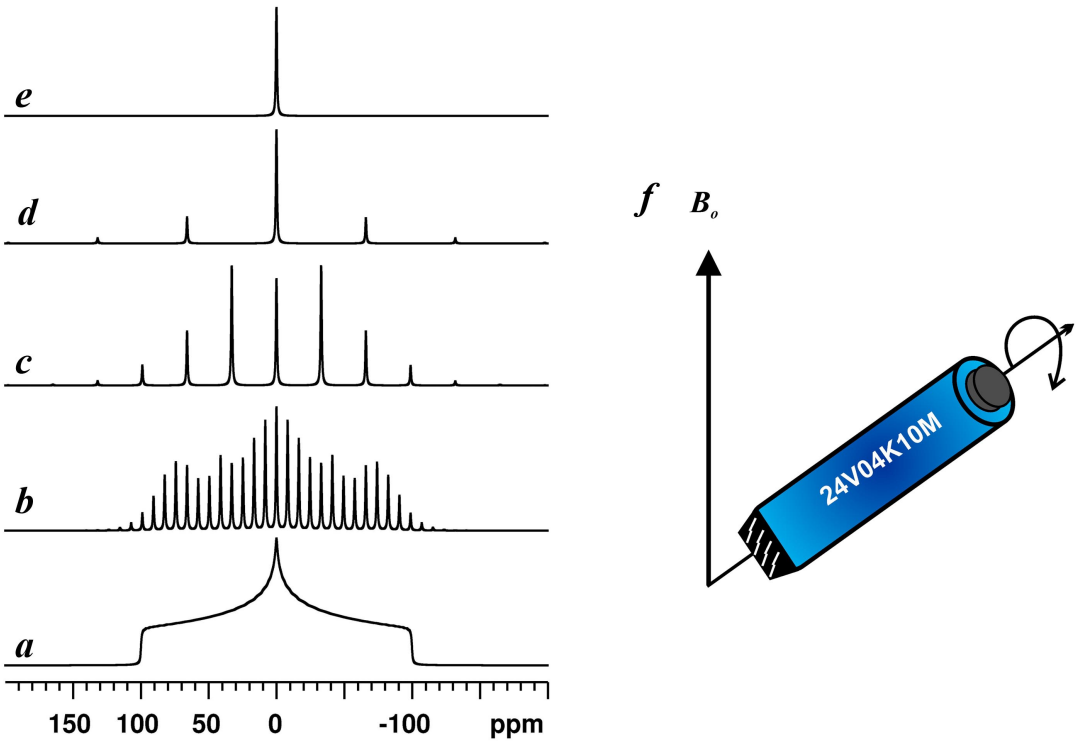

Figure 1.17. Chemical shift anisotropy interaction, (a) non-spinning, (b-d) increasing spinning speeds, (e) infinite spinning at the magic angle and (f) MAS rotor at the magic angle with respect to the magnetic field. Slow spinning maintains the overall line shape of the non-spinning spectrum however compresses the signal into narrower peaks, increasing signal to noise. Increasing the spinning frequency causes the spinning side bands to be removed and leaves behind the isotropic resonance (e).

Spinning not only improves resolution but provides another significant contribution to solid-state NMR by improving sensitivity. The spinning causes a broad spectrum to be compressed into a series of smaller lines thereby focusing the intensity into smaller packets. Using a combination of non-spinning and MAS, the extraction of various interactions can be performed. For example, the isotropic shift can be

determined by collecting MAS data at various spinning rates. The various rates enable the identification of spinning side bands (ssb) and the true isotropic shift (which will not change position with spinning frequency, unless temperature dependent).

The quadrupolar interaction is dependent on two different spatial terms $P_2(\cos\theta)$ and $P_4(\cos\theta)$. The P_2 term is removed by MAS, whereas the $P_4(\cos\theta)$ term is only partially averaged (Figure 1.18).

$$P_4(\cos\theta) = \frac{1}{8}(35\cos^4\theta - 30\cos^2\theta + 3) \qquad \textbf{(1.38)}$$

The spinning axis required for this term to be averaged can be either, $\theta = 30.6^0$ or 70.1^0.[4] The MAS angle does not remove this interaction completely, but does however decrease the magnitude by approximately 60% (Figure 1.17).

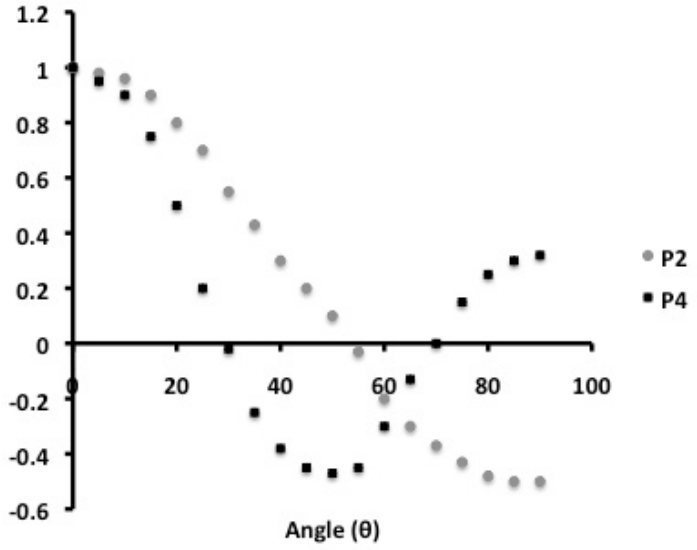

Figure 1.18. Angular dependence of the P_2 and P_4 terms; P_4 is of concern only for the second-order quadrupolar interaction.

Figure 1.19 shows how the breadth of the CT changes between a non-spinning and spinning quadrupolar nucleus. It is clear that the breadth changes drastically as we partially average the P_4 term. The centre-of-gravity also changes. The non-spinning spectrum (Figure 1.19) is approximately split 40/60 at 0 ppm whereas the left-edge of the MAS spectrum is located at that position. MAS enables us to measure or estimate more accurately the isotropic chemical shift for quadrupolar nuclei. Although the second-order quadrupolar interaction still exists, there are two probe designs that allow it to be removed. This is achieved using double angle spinning (DAS) or double rotation (DOR) probes that can spin a sample at two different angles, averaging both the P_2 and P_4 terms. DAS involves a two-dimensional experiment where we have evolution of two different angles. This switching of angles allows for an isotropic dimension to be achieved. DOR employs a double rotor device that spins the sample at both angles simultaneously, enabling the P_2 and P_4 terms to be averaged, resulting in an isotropic spectrum.[4] DOR probes however have limited spinning frequencies due their inherent design (they have a large outer rotor that limits the spinning speed).

Commercial MAS probes have spinning speeds up to 70 kHz and have improved significantly in the past ten years when the limit was on the order of 30 kHz. This has allowed major advancements to be made in the solids community where work continues. Recently (within the past four years) a homebuilt probe within Ago Samosons NMR group was recorded to spin at 100 kHz, thereby paving the way for future advancements in NMR.

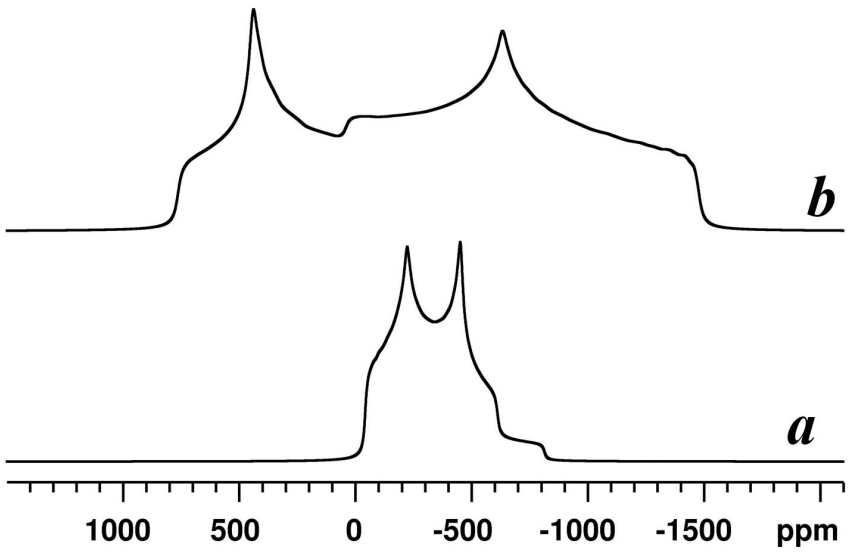

Figure 1.19. Effect of MAS on the breadth of the second-order quadrupolar interaction; (a) MAS and (b) non-spinning.

1.8. NMR in Glasses

The anisotropic interactions described above occur in both crystalline and amorphous (disordered) solids. However, due to the inherent nature of the disordered solid (lack of long-range periodic order), we do not observe the distinct NMR powder patterns depicted above. The inherent disorder causes a range of anisotropic interactions, with a slightly different powder pattern for each powdered 'crystallite' (Figure 1.20). Glasses typically display a statistical distribution of sites. This distribution occurs because glasses are comprised of 1,000's of slight variations of some local structure. In other words crystalline species are a single defined unit that is periodically ordered whereas glasses contain many similar units however each exhibiting slightly different distortions in their polyhedron. This distribution is often observed as a Gaussian peak

shape due to the range of bond angles and bond lengths in the amorphous material. Structural information for these systems can still be gathered regarding the chemical shift, quadrupolar interaction and other potential interactions. By combining MAS methods and various magnetic fields, (recall, chemical shielding anisotropy (in Hz) increases with magnetic field, whereas the second-order quadrupolar interaction decreases with field) local speciation can be teased out if one has competing interactions. This is a common approach for crystalline materials where the interactions can be more easily defined. In certain instances, resonance lineshapes do not exhibit a Gaussian distribution, and instead a broad peak with a low frequency asymmetric tail occurs. This is known as a Czjzek distribution[34] and is caused by a distribution of quadrupole interactions within the system (often observed when the quadrupolar moment is large).

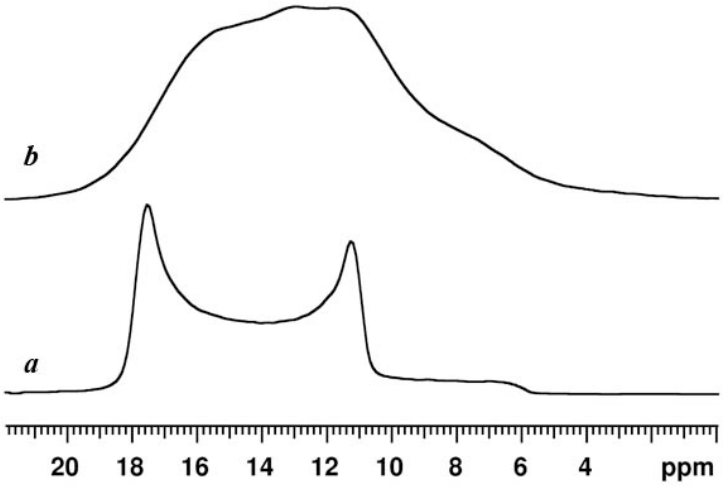

Figure 1.20. An example of a central transition for a (a) crystalline and a (b) glass sample.

2. Synthesis and Methods

2.1. Glass and Crystalline Formation

All solid materials presented in this thesis were formed from traditional solid-state synthesis methods. Starting materials such as oxides, hydroxides and carbonate powders were mixed in stoichiometric quantities using an agate mortar and pestle (without the use of liquid solvents) followed by a variety of heat treatments unique to each material. Common heat treatments for starting materials include a decarbonation process, between 500 and 750°C and dehydration or re-crystallization process between 400 and 900°C. Samples were subsequently weighed to confirm proper decarbonation and to ensure that no other components have evaporated. Powders or melts were re-ground to ensure homogeneity, then placed into crucibles of platinum/gold(5%) or alumina (Al_2O_3). Treatments follow one of two approaches, either crystalline synthesis or amorphous quenching. Crystalline samples were treated at temperatures just below their respective melting temperatures and allowed to sit in the furnace for one to seven days. During that time, certain heat treatments (systematically lowering the temperature) may be applied. The crystals were re-ground and placed back into the furnace for 24 to 48 hours, promoting an increase in crystalline purity, followed by slow cooling (either in the furnace or simply by air). The amorphous samples are heated until the melting temperatures were reached (borates and borovanadates ~850 to 1150°C, borosilicates, silicates and germanates

~1250 to 1550°C), and samples were left to mix homogeneously for 20 to 180 minutes. The melt was then quenched rapidly by dipping the crucible in deionized water. Other methods used to form glasses from melts included plate-quenching (cold steel plates) or roller-quenching (two large spinning steel cylinders). Plate-quenching involves a large steel plate with a large surface area, as this is used to induce vitrification as the melt was poured onto the plate. In some instances a second plate is used. It will be placed on top of the poured melt, increasing the cooling efficiency of the melt. Roller-quenching entails pouring the melt between steel cylinders that are rotating. The large surface area and narrow space between rollers allows for very fast cooling, by-passing the onset of crystallization. These latter two methods are typically used for difficult glasses (e.g., borovanadates and high-R compositions). Two furnace options are possible; for moderate temperatures (T < 1100°C) a Thermolyne® 1300 box furnace was chosen, for elevated temperatures (T < 1700°C) and specified heat treatments a Deltech® vertical-tube furnace was required.

2.2. Structure Determination of Crystals and Glasses

Three NMR spectrometers were used for the study of the materials presented in this thesis, employing a variety of pulse methods (section 2.3). The "work horse" (whereby 80% of the materials described were studied) is the Varian UNITYINOVA 600 (14.1 T) spectrometer. These experiments employed a variety of probes, each with unique features that were individually selected based on the property under investigation. All experiments done on this spectrometer used 3.2 mm double and triple resonance, 5

mm double resonance and 1.6 mm triple resonance Varian-Chemagnetic and Varian MAS probes. The 5 mm experiments were performed using 5 mm o.d. (160 μL fill volume) ZrO_2 or Si_3N_4 rotors with maximum spinning frequency of 12.4 kHz. The 3.2 mm probes use ZrO_2 3.2 mm o.d. rotors, with varying fill volumes (11, 22 and 36 μL), and a maximum spinning frequency of 24 kHz (11 & 22 μL), while the 36 μL rotors were limited to 16 kHz. The 1.6 mm probe uses ZrO_2 rotors with a sample volume of ~ 8 μL (~ 8 to 15 mg) and maximum spinning frequency of 40 kHz.

The Bruker Avance II 900 (21.1T) spectrometer at the National Ultrahigh-Field NMR Facility for Solids at the NRC in Ottawa, Canada, was used for all ultrahigh-field experiments. The experiments were performed using double resonance MAS probes with stator sizes of 1.2 mm, 2.5 mm, 4 mm and 7 mm. Rotors are constructed from ZrO_2 and have maximum spinning frequencies of 65 kHz, 35 kHz, 18 kHz and 7 kHz (using a thick walled rotor) respectively. Certain non-spinning experiments were carried out with a 7mm MAS probe and thin walled rotors, providing a larger sample volume (~ double).

The moderate-field Bruker AMX 500 (11.7 T) spectrometer was used to acquire certain spectra that could not be recorded on the Varian spectrometer. The intermediate frequency (I.F.) for the Inova spectrometer is at ^{73}Ge Larmor frequency. These experiments involved two solution based probes (a 10 mm broadband probe and a 5 mm inverse probe) and a 5 mm home-built non-spinning low gamma broadband solids probe with replaceable coils, designed specifically for the project outlined in Chapter 6.[35]

2.3. Description of NMR Pulse Sequences

Over the past 60 years there has been significant work in the development of pulse sequences for the manipulation of spins. Pulse sequences are used to manipulate spins in a variety of ways, however in its most basic form, a RF pulse is turned on for some period of time, then shut off, allowing the collection of an NMR signal. Recall in Chapter 1, when a sample is introduced into a strong magnetic field the magnetic moments will orientate and precess about B_o. For an NMR signal to be recorded, a pulse will be applied to tip the precessing spins away from the z-axis into the xy plane. If the applied pulse causes the spins to rotate by 90^o then this is termed a $\pi/2$ pulse. The spins will now dephase in the xy plane (relaxation time, T_2) and eventually return to precessing along the z-axis (relaxation time, T_1).[23] The transverse magnetisation induces a very small voltage into a coil, which is recorded over some period of time, commonly known as a free induction decay (FID).[4,22] This section will outline key features and pulse sequences used within this thesis to study a variety of materials.

2.3.1. Bloch Sequence

The Bloch decay (single pulse) sequence, named for Felix Bloch,[36,37] is a basic and widely-used method. The sequence (Figure 2.1a) is comprised of a single $\pi/2$ (90^0) pulse. The pulse length can be adjusted to place any amount of magnetization into the observable plane, typically 10^o to 90^o. The rf-pulse will cause the z-magnetization to be tipped towards the xy plane, enabling the receiver to detect a signal.

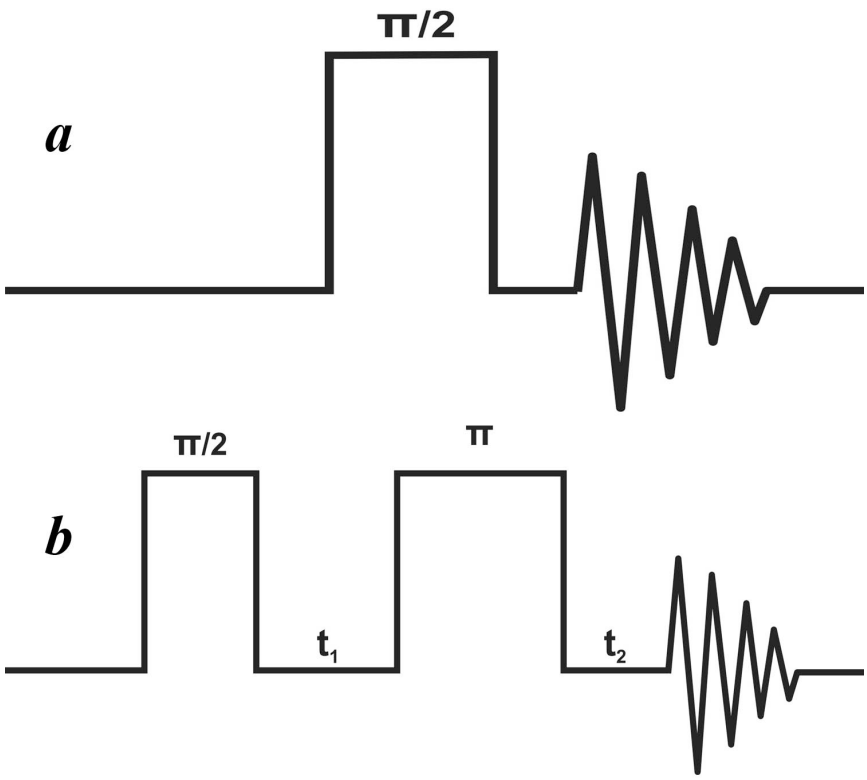

Figure 2.1. Schematic (a) Bloch and (b) Echo pulse sequences.

2.3.2. Echo Sequence

The next pulse sequence, developed in 1950 by Erwin Hahn,[38] included the addition of a second pulse following the Bloch pulse. The Hahn-echo sequence (or spin-echo), is a π/2 pulse, followed by a delay (t_1), then a second pulse (typically π) followed by acquisition after some delay, t_2 (Figure 2.1b). The first pulse places the magnetization into the xy plane. As the spin coherence dephases (after some time, t_1 (μs)), the second pulse flips the spin coherence forcing the magnetization to refocus when t_2=t_1 and the data are detected. This sequence is often required for studying low-γ nuclei to alleviate baseline imperfections and artifacts, since these species often suffer from

probe ringing. The echo is also used when some component in the probe (a stator, screws or rotor) are constructed from materials that contain the same element of interest. These components typically have broad resonances, which can be removed or minimized by using an echo. This sequence is also commonly employed for T_2 relaxation measurements due to the removal of any inhomogeneous broadening caused by the magnetic field.[23] In solids, a common modification to the echo is to apply a π/2 pulse instead of the π pulse. This sequence also depends on a different phase shift for the two pulses. This gives better lineshapes of broad central transitions. This latter sequence is referred to as a solid-echo or quadrupolar-echo.[22,39,40]

2.3.3. Inversion Recovery

The inversion recovery sequence is employed to study T_1 (spin-lattice) relaxation for a particular nucleus. This method is similar to the Hahn-echo, incorporating two pulses and a single varied delay. However, the pulses are reversed with the π/2-pulse following the initial π pulse (π-t_a-π/2). The π-pulse flips the magnetization (along +Z) onto –Z (spins inverted). A delay follows (t_a), allowing a certain amount of longitudinal relaxation to occur. The π/2 pulse causes the magnetization in z to precess in the transverse (xy) plane, enabling a signal to be observed. The sequence is repeated numerous times using several t_a values (Figure 2.2a). As t_a increases, the observed resonance intensity will change until full relaxation occurs. These intensities can be measured as a function of the delay time, typically showing a single exponential response. Fitting this response allows the extraction of the spin-lattice relaxation constant, T_1 *(or rate,* $R_1 = 1/T_1$*)*.

A drawback of this sequence is that full inversion of the magnetization must be preceded by a delay, $d_1 \geq 5 \times T_1$ to ensure that steady-state equilibrium has been reached (requiring an educated guess, which is difficult for long T_1 systems).[23,41]

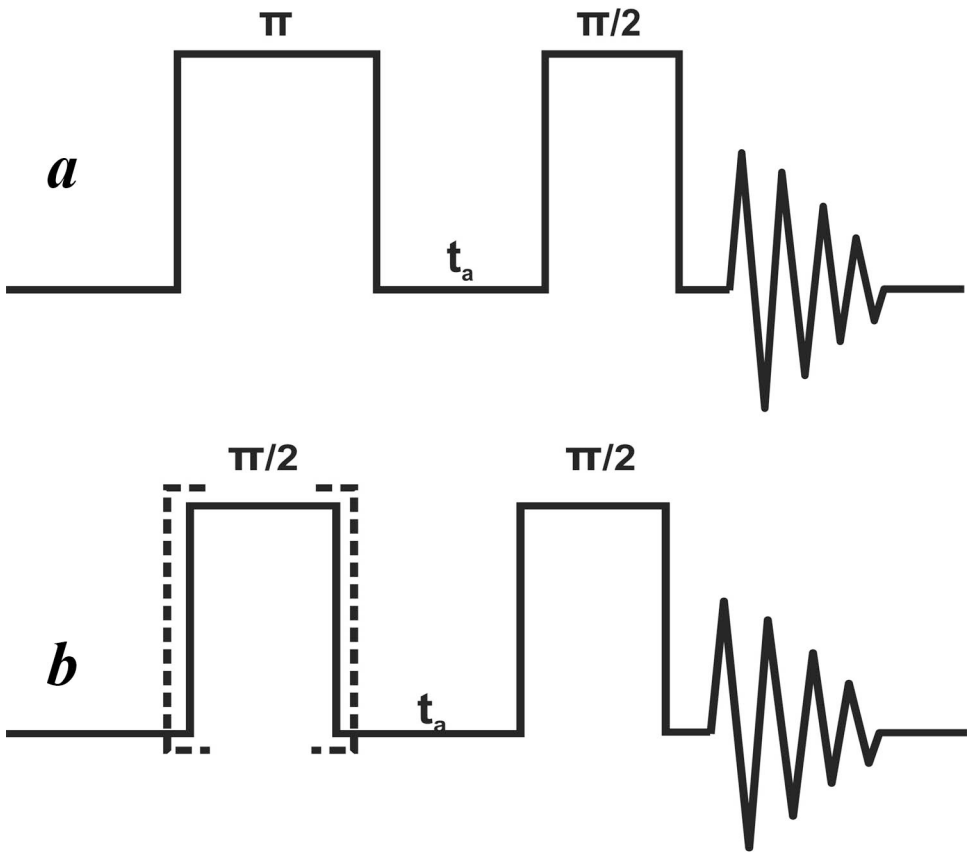

Figure 2.2. Pulse sequence schematic for (a) inversion recovery and (b) saturation recovery.

2.3.4. Saturation Recovery

A method that can by-pass the issue of beginning from equilibrium is the saturation recovery experiment (Figure 2.2b). This involves a train of π/2 pulses, which saturate the spin populations (i.e., steady-state). This comb of π/2 pulses is then followed by a

delay t_a, and an observation pulse, $(90^o)_n - t_a - 90^o$. The delay is varied over a range of values until a consistent maximum is obtained (as in the inversion recovery method). Acquisition should commence immediately after the second π/2 pulse, to avoid potential loss of signal. Processing the spectral intensities versus the delay time t_a will reveal an exponential recovery from which T_1 can be determined. The advantage of this sequence is that the repetition rate of the experiment can be less than 5 x T_1 (unlike inversion recovery) due to the 90^o pulse comb saturating the spins, and it is useful for species with long T_1 relaxation. A drawback is that the separation between the saturating pulses must be less than T_1, but longer than T_2 to impede spin-locking.

2.3.5. Carr-Purcell-Meiboom-Gill

A modification of the spin-echo pulse sequence, known as the Carr-Purcell-Meiboom-Gill (CPMG) sequence, utilizes a spin-echo followed by a train of echo-acquisition pulses (Figure 2.3a). Although this is commonly called the QCPMG sequence or spikelet experiment for quadrupolar nuclei, it has the same basis as the more traditional CPMG.[42-44] The FID signal decays in a systematic exponential method whereby T_2 can be measured from the observed echoes within. The sequence behaves identically to the echo, however the series of echo-acquisition steps keep refocusing the magnetization within the xy plane until all of the transverse magnetization is gone (i.e., spin-spin relaxation). Quadrupolar solids suffer from low receptivity due to the resonance being dispersed over a large spectral range. CPMG causes the overall envelope of the powder pattern (normally determined from an echo or single pulse), to become a series of narrow spikelets (narrow lines) that are evenly separated. These spikelets maintain the same overall powder pattern (observed from an echo) but force

the signal intensity into sharper lines, increasing sensitivity, improving S/N and decreasing acquisition times. The gain in signal-to-noise is dramatic for low-γ species or systems with large quadrupolar coupling constants where sensitivity is lacking.[43,45,46]

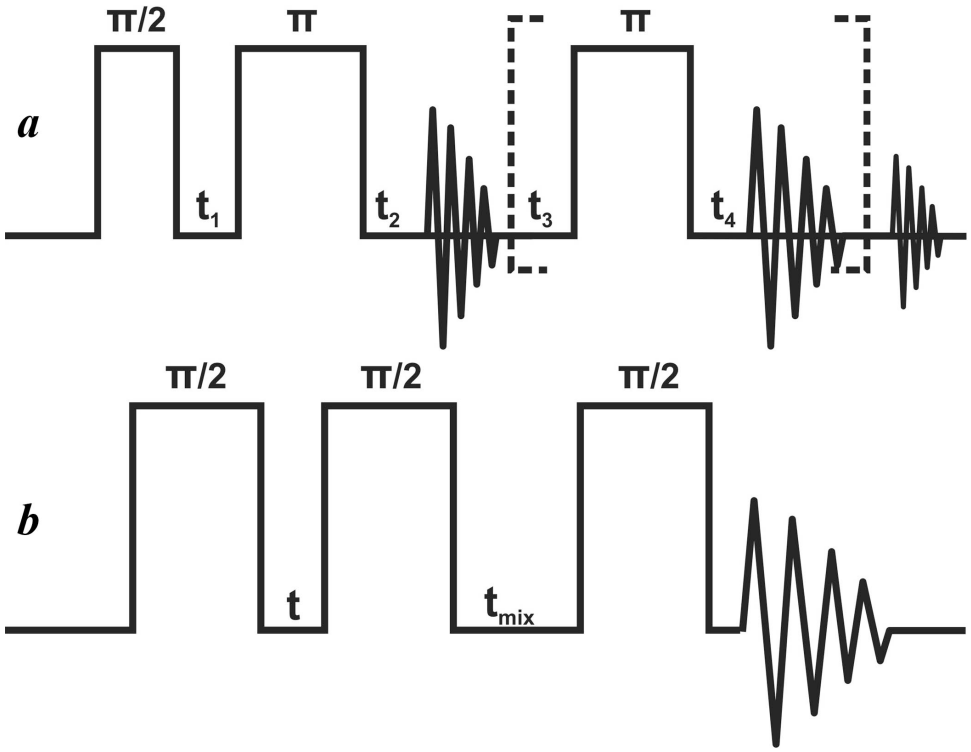

Figure 2.3. Schematic for (a) Carr-Purcell-Meiboom-Gill, CPMG and (b) exchange spectroscopy, EXSY pulse sequences.

2.3.6. EXchange SpectroscopY

Two dimensional exchange spectroscopy, EXSY[47] is a method that can be used to determine positional exchange (i.e., dynamics) between sites, usually in the range of μs to s. It involves three π/2 sequences and a mixing time, t_{mix} between the 2nd and 3rd π/2 pulses. The first two pulses allow the spins to "talk" to each other, setting up and

identifying their initial positions or environments (Figure 2.3b). After the second pulse transfers the magnetization back onto the –Z axis, a mixing time allows the species of interest to exchange positions from one site to another. The third pulse transfers this mixing time coherence and records the new environment for these spins. Since this is a two-dimensional technique, one needs to consider their evolution time (that is the number of slices defining the second dimension, typically rotor synchronised when using MAS). A diagonal response is observed in the spectrum when there is no mixing (i.e., single pulse experiment is observed). If site exchange and/or mixing occurs a cross peak will develop within the two-dimensional spectrum and will display which sites are exchanging. For glasses the diagonal will begin to spread into a circular shape as the disordered solid does not have discrete "isolated" sites in most cases. The mixing time can be varied from zero (no-mixing) to T_1 depending on the system and type of dynamics present. It is best applied when the exchange rates are on the same order as the relaxation time T_1 or slower.[26,48]

2.3.7. Rotational Echo DOuble Resonance

In order to study proximity and spatial arrangement of a system, one can often employ the Rotational Echo DOuble Resonance (REDOR) method.[49,50] This double resonance experiment depends on the manipulation of the dipolar coupling interaction present between two nuclear spins I and S. This interaction is removed under MAS and may be re-introduced using the REDOR sequence (Figure 2.4).[4,26]

REDOR is collected under MAS conditions with a Hahn-echo pulse sequence on I, acquiring a spectrum without the existence of dipolar interactions. The S portion of the sequence contains two π pulses, one timed to be at ½ a rotor cycle, $T_R/2$ and

another at a full rotor cycle, T_R. The second spectrum is collected by re-introducing the dipolar interaction using intermittent S pulses. These π-pulses cause the net-spin magnetization to be inverted whereby I and S spins become anti-parallel (Figure 2.4b). This flipping effectively re-introduces the dipolar interaction that was initially removed by the MAS, resulting in two spectra, one with no dipolar interaction and one with the interaction re-introduced. The difference between these spectra can be used in conjunction with others in a series of measurements to establish a relationship for the strength of the dipolar interaction between I and S, and extend this relationship to include distance (equation 2.1). If disorder exists, bond lengths cannot be determined and this technique is used for proximity and potentially slow-range mobility.

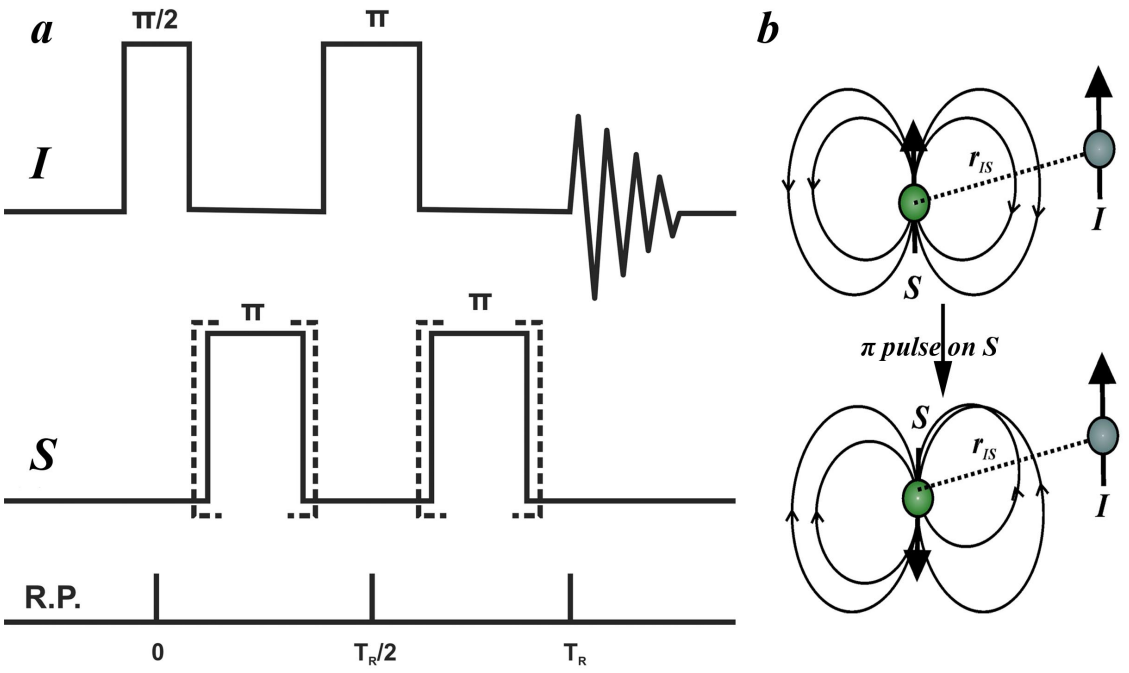

Figure 2.4. (a) REDOR pulse sequence, where I is the observed nucleus and S is nucleus where recoupling occurs during the rotor synchronized period (R.P.). Under MAS, the dipolar interaction between I and S (b) is averaged out, but applying a π-pulse on channel S causes the net dipole vector to change, reintroducing the dipolar interaction. A two-spin model (green=S and grey=I) can be probed to determine the average interaction between I and S.

$$R_{DD} = \left(\frac{\mu_o}{4\pi}\right)\left(\frac{\hbar}{2\pi}\right)\left(\frac{\gamma_I \gamma_S}{r_{IS}^3}\right) \qquad \textbf{(2.1)}$$

2.3.8. MULTIPLE-QUANTUM MAGIC ANGLE SPINNING

The multiple-quantum magic angle spinning (MQMAS) sequence was developed approximately 15 years ago, revolutionizing the study of quadrupolar nuclei. MQMAS

is a two dimensional method by which an "isotropic" spectrum for quadrupolar nuclei can be obtained with a simple MAS probe. This sequence uses the fact that symmetric transitions (i.e., 1/2 to -1/2, 3/2 to -3/2, etc.) are unaffected to first-order by the quadrupolar interaction. Also, the second-order quadrupolar interactions are correlated in some manner between these symmetric transitions. Under MAS conditions, all symmetric transitions are only affected by the second-order quadrupolar interaction and a correlation in quadrupolar frequencies exists between a triple-quantum (3/2 to -3/2) and single-quantum transition (1/2 to -1/2). A spectrum is comprised of an isotropic and anisotropic part whereby the anisotropic portion causes broadening and can be potentially removed. The 1Q and 3Q coherences evolve at different time intervals, thereby a time exists where the anisotropic interactions can be removed, and an isotropic spectrum can be measured. Half-integer quadrupolar nuclei can be studied using this method, typically using two pulses and two delays. The first pulse (p_1) causes triple quantum (5Q, 7Q and 9Q are possible as well) population transfer (3/2 to -3/2) and evolves during t_1. The application of a 2^{nd} pulse and the transfer of 3Q to 1Q are needed in order to observe the coherence. After a second delay, t_2 ($t_2=k*t_1$, where k depends on the spin quantum number and coherence pathway) the top of the echo can be collected, this will be an isotropic component (i.e., no broadening observed from the second order quadrupolar interaction). The consequence is that the whole echo is comprised of both components with the tops being isotropic. To obtain an isotropic spectrum, we collect a 2D data set with a series of experiments, which are carried out at different evolution times with the echo maximum containing no second order anisotropy. These tops can be selected

to create a two-dimensional spectrum where f_1 is the isotropic dimension and f_2 is the standard MAS dimension.

A variety of sequences and modifications exist on the MQMAS experiment that will not be discussed here. However, one commonly applied sequence is the three pulse shifted-echo sequence, in which three pulses are applied in total, two of the pulses are hard (high power) pulses that transfer the spin magnetization to a higher order quantum coherence and to single quantum coherence. The third pulse (soft selective π refocusing pulse) creates a pure absorption lineshape with no phase correction required.[4,26,51]

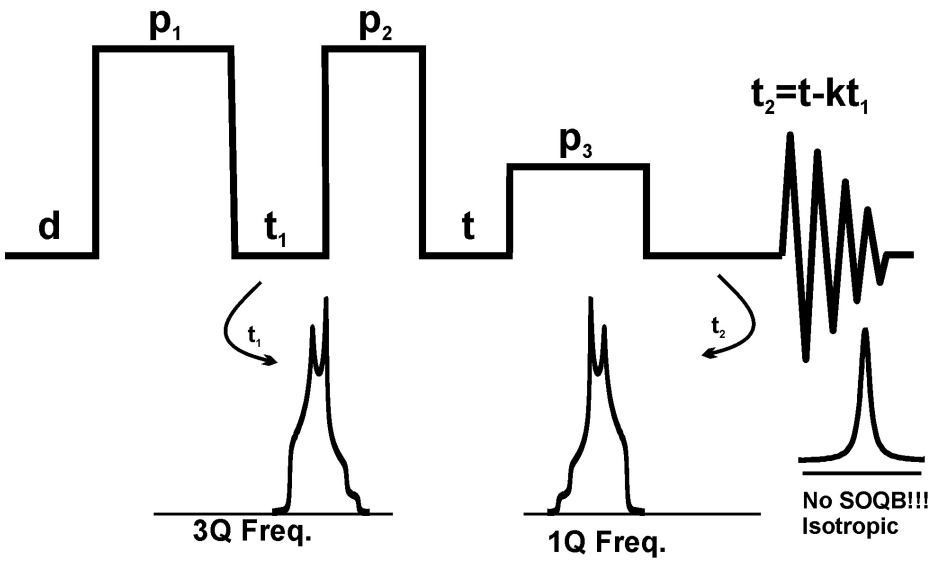

Spin I	3/2	5/2	7/2	9/2
k	7/9	19/12	101/45	91/36

Figure 2.5. MQMAS pulse sequence with two hard pulse (p_1 & p_2) and a soft refocusing third pulse (p_3). The associated coherence table with depicted refocusing times (mirror images) show how the second order quadrupolar broadening (SOQB) interaction can be removed. The k-values are shown for a triple-quantum transition.

2.4. Quantum Chemical Calculations

Quantum chemical calculation methods are used to study the theoretical interactions inherent to chemical structure and to confirm experimental results for both amorphous and crystalline materials. The particular interactions of interest are chemical shieldings and electric field gradients, as these can be used to connect measurements to structure and local environment. As our interest lies in calculating NMR interactions, density functional theory (DFT) is used in three programs Gaussian03, CASTEP and WIEN2k.

Density functional theory calculates the energy and properties of a many-electron system by using functionals of electron density (correlation-exchange functional) unlike ab-initio methods, which calculates them from the full wave-function.[20,52] We use these calculations in turn to extract EFGs and shieldings from an energy minimized structure and compare these calculated results with those measured experimentally. Other levels of theory are available such as molecular mechanics (e.g., Amber), semi-empirical (e.g., AM1, PM3) and ab-initio (e.g., Hartree-Fock). DFT provides us with a method that is more advanced and efficient for studying larger solid based clusters, and is more reliable and accurate than the "simple" ab-initio Hartree-Fock method. DFT[53] is more efficient at larger scale calculations than ab-initio because it allows the many-electron problem to be treated as one involving independent particles, instead of requiring a full N-electron wavefunction. This also replaces the explicit electron exchange and repulsion terms (found within ab-initio) by global exchange and correlation terms, which results in considerable savings. This allows DFT to scale $N^2 – N^3$ whereas ab-initio (HF) scales $\sim N^3 - N^4$.

2.4.1. Gaussian03

Gaussian03 is a commercially available electronic-structure modeling program with the capacity to perform energy minimizations, geometry optimizations and calculate NMR interactions.[54] A variety of levels of theories are available including molecular mechanics, semi-empirical, ab-initio and DFT. For calculating NMR interactions we generally use B3LYP,[55] which is a hybrid-DFT method in combination with higher-level basis sets as these are found to be the most accurate in reproducing experimental trends in NMR. First, the clusters for amorphous models are calculated at lower basis sets (i.e., 3-21g and 6-31g*)[56,57] for geometry optimizations. Glasses are disordered structures by definition; therefore the same structure for one polyhedron to the next is not expected, this can allow for lower level optimizations. However, one should take care with this statement as this is not always the case and higher-level calculations are required at times for optimizing prior to moving forward to the next step. For reliable NMR calculations (e.g., EFGs and shieldings) the lower level optimized clusters (exact clusters will be defined later) are submitted for high-level triple-zeta basis set NMR calculations (i.e., 6-311g++(d,p) and aug-cc-PVTZ).[58-63] The "d,p" terms (also known as, "**") are polarization functions that are added to the basis set (e.g., 6-311g) while the "++" represent diffuse functions. Basis sets have by default s, p or d functions appropriate to the atom, but including additional functions grant a larger basis set space, for improved description of the system. Properties derived from the electronic structures of the model (e.g., IR, Raman, NMR, etc.) depend on high-level calculations. Polarization functions grant the system greater electronic flexibility.[20,52,64] Diffuse functions are added to allow for more spatial flexibility near

the edges of the computational space preventing unnatural breaks.[20,52,65] The limiting factor for a chosen basis set is the trade-off in the calculated result and computational cost on the servers. B3LYP is typically chosen as it allows us to calculate a high-level basis set in a reasonable period of time with accurate results.[20] These calculations typically confirm experimental trends however often poorly match the experimentally determined values for solids.

2.4.2. CASTEP

CASTEP is a newer computational program that has recently been commercialized for quantum chemical calculations.[66] We have used CASTEP to model NMR interactions (EFGs and shieldings) in crystalline materials. It is attractive because it was designed specifically to model solids that exhibit long-range periodicity. The theory implemented for our calculations was DFT-based and treats the low-lying electrons (core) via pseudopotentials. CASTEP is also efficient as it has incorporated a phase factor and makes use of cell periodicity. This simplifies the calculation since the phase factor can be described as a plane-wave, and as a linear combination of reciprocal lattice vectors or as orthogonal wave-vectors.[67] Parameters for CASTEP included implementing the Perdew, Burke and Ernzerhof (PBE) functional under the generalized gradient approximation (GGA).[68,69] Three basis set levels were used including medium, fine and ultrafine. Shieldings were calculated using the gauge included projector-augmented wave method (GIPAW) and scalar relativistic effects were included using the zeroth-order regular approximation (ZORA)[70] implemented within CASTEP.[71,72] For heavier elements pseudopotentials are used to model the chemically most inert core electrons and help account for relativistic effects. As NMR

interactions are most sensitive to their local structure and the shieldings affected by the electron environments we often incorporate ZORA into NMR calculations of heavier atoms.[20,52]

2.4.3. WIEN2k

WIEN2k is a software program that employs DFT-based theory to calculate a variety of interactions. We use this program to calculate NMR parameters (EFGs only) for crystalline systems. The same method used for CASTEP was employed for WIEN2k; Perdew, Burke and Ernzerhof (PBE) functional under the generalized gradient approximation (GGA).[68,69] The periodic boundary space chosen for most calculations varied between 15,000 and 100,000 kpoints, defining the grid-space for the periodic boundary condition (i.e., a supercell). These were increased until an appropriate convergence was achieved (i.e., changes in quadrupolar couplings were only observed in the third decimal place, XX.xx**x**).[73] The energy convergence criterion was set to 10^{-4} to 10^{-6}. RKMAX determines the matrix size convergence where KMAX is the plane wave cut-off and R is the smallest of all atomic sphere radii, one typically uses a value between 5 to 10.[73] For our calculations this was set between 7 to 9. WIEN2k calculations provided the best agreement with experimental results. This can be explained by its ability to combine an all electron structure calculation (i.e., no pseudopotentials) and periodic boundary conditions for solids. Unfortunately the ability to calculate shieldings has not been implemented at this time.

2.5. Powder X-Ray Diffraction

Powder x-ray diffraction is employed to study both crystalline and amorphous materials. Glass samples can be verified using x-ray diffraction to indicate the presence of crystalline phases. In addition it can provide evidence of any possible crystalline inclusions or impurities that are invisible to the eye or polarized light microscope. Amorphous materials will resemble broad featureless peaks indicating complete vitrification. If a small crystalline impurity exists, sharp diffraction peak(s) will be present.

Crystalline reference materials may need to be synthesized during certain stages of the study to interpret amorphous structure. These crystals are then characterized by x-ray diffraction to identify purity. Samples are ground into a fine powder and mounted on quartz slides using grease. The samples were assessed using a PANAlytical X'Pert Pro Bragg-Brentano powder x-ray diffractometer employing a Cu K_α radiation source, an X'Celerator detector and a Ni-filter diffracted beam. Data were typically collected at room temperature using a 2θ range of 10^o to 90^o at 0.0167^o increments with a 65-75s step time. These parameters can change, depending on the materials and the questions needing to be answered.

2.6. Simulation Software

NMR data require further treatment to extract information regarding the interactions that are contributing to the observed spectra and their respective parameters. This is often done using a variety of software applications that allow a user to analyze and

simulate experimental data. There are four such methods that are of interest and include: WSolids®, STARS®, SpinWorks® and SIMPSON®.

2.6.1. WSolids®

WSolids is a frequency based software program that is used to simulate common solid-state NMR interactions. This software can be used with both Bruker and Varian data to visualize and analyze one-dimensional spectra.[74] It is written in C++ and operates on any Windows® machine employing a multiple document interface (MDI), which allows for multiple screens. This is a numerical simulation program where the user inputs the suspected NMR interactions, enabling the parameters to be extracted.

2.6.2. STARS®

STARS® is a time-domain density matric program that can simulate NMR interactions and can be used for analysis on spectra that are collected on Varian® spectrometers. This program is based on the Alderman algorithm and optimized using the MINUIT© program, which enables fast and efficient simulations of CSA and quadrupolar interactions. In addition, it has the ability to fit various interactions on different sites and enables quantitative results to be obtained from the simulations.[75-79] A key feature of STARS® is its ability to simulate spectra under MAS conditions and identify the artifacts that may develop if the magic angle is poorly set.

2.6.3. SpinWorks®

SpinWorks® is a processing software that can Fourier transform a variety of spectroscopic data formats. For solids it provides a method for peak fitting, integrating and iterative analysis of larger data sets. It also has the ability to process

2D experiments such as MQMAS. Although MAS and quadrupolar nuclei are not supported in the simulation code, it is useful when the line shape is Gaussian (i.e., no SOQE is observed) as only the CT is of concern for peak fitting or measuring chemical shifts. This software has been developed and designed by Dr. Kirk Marat in house at the University of Manitoba.[80]

2.6.4. SIMPSON®

SIMPSON (SIMulation Program for SOlid-state NMR spectroscopy) treats calculations based on a "virtual spectrometer" that utilizes an input file containing the particular interactions of concern together with the experimental parameters (B_0, spinning rate, pulse width, etc.). One selects the nuclear spins of interest and the interactions for simulations. Simulations are based on the Liouville-von-Neumann equation of motion, and employ a series of density matrices to describe the spin system.[81] The result is delivered in a variety of formats including raw and a FID option that will illustrate the calculated spectrum. However, since this is based on a density matrix system and quadrupolar nuclei are described by large matrices, the calculations can become quite complex (i.e., time-consuming) when many quadrupolar spins are introduced.

3. Binary Borates

B_2O_3 is an excellent glass former that can incorporate a variety of network modifiers. Vitreous B_2O_3 (*v*-B_2O_3) is a unique structure that is composed of a series of three-coordinate boron ($^{[3]}B$) with bridging oxygens, forming both ring ($^{[3]}B^{R}$) and non-ring ($^{[3]}B^{NR}$) T^3 units (Figure 3.1). The properties are tuned by the addition of a modifier (e.g., Li_2O), which will cause the formation of four-coordinate boron and eventually lead to non-bridging oxygens (NBO) on the three-coordinate units (Figure 1.3). When a single network modifier is added to B_2O_3, the resulting composition is termed a *binary borate*. Binary borates in the form of glasses, crystals and minerals are vast. The mineral Borax, $Na_2B_4O_7 \bullet 10H_2O$, is a common additive in glasses for its flux (lower working temperature) ability.[2] Other uses include flame-retardants, agricultural micro-nutrients and a variety of ceramic applications.[82-84] Crystalline lithium borates have ionic conducting ability. Vycor®, a porous silicate used in filtration applications, is formed from a phase-separated borosilicate which is washed to remove the borate phase.[2,10]

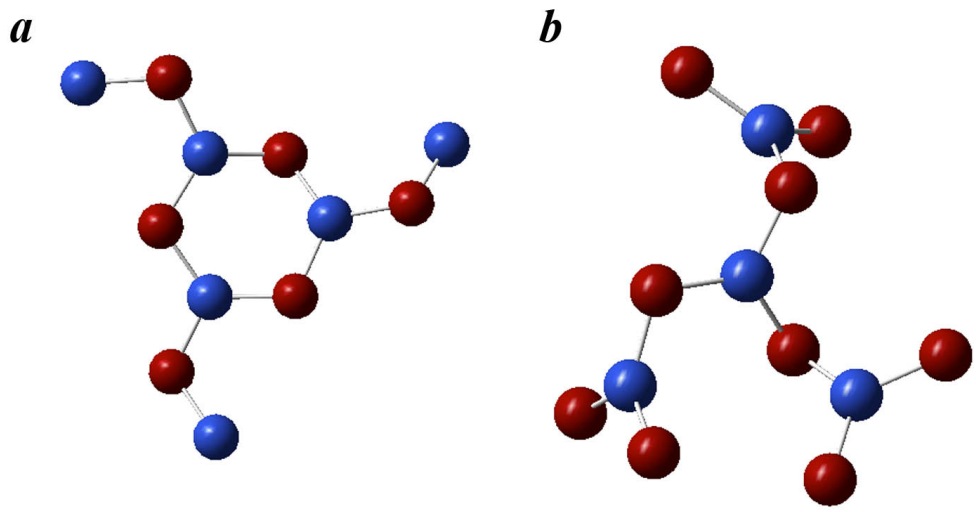

Figure 3.1. B_2O_3 structural units (a) ring comprised of T^3 units and (b) $^{[3]}B$ non-ring T^3 units. Boron (blue) and oxygen (red); excess oxygens and boron were removed for clarity.

NMR is an ideal means of determining boron speciation, as both $^{[3]}B$ and $^{[4]}B$ species can be resolved and quantified at moderate field strength, because they have a large chemical shift difference (~15 to 20 ppm). Furthermore, the quadrupolar coupling constants for both species are different, providing an additional tool for local structure elucidation.[8,9,85-91]

Alkali speciation can also be informative, but it is not as commonly studied. In this section, we will discuss a variety of techniques used to obtain qualitative and quantitative information regarding network-forming species (B) and alkali modifier cations (Li, Na, K, Rb and Cs) probed by NMR. Emphasis is placed on developing higher resolution methods, the role of the alkali modifiers in borate glasses and new methods for probing slow cation mobility.

3.1 Crystalline Lithium Borates

B_2O_3 is an excellent glass former and very difficult to crystallize on its own, but the addition of alkali oxide enables a variety of crystal structures to be formed. Three structures of particular interest, include lithium meta-, pyro- and orthoborate, with lithium to boron ratios of 1:1, 2:1 and 3:1 respectively. These crystal compositions (cause B to) contain NBO environments. ^{11}B MAS NMR was used to verify the crystalline species through measurement of the chemical shifts and quadrupolar interactions, which will also be used as a basis for characterization of amorphous materials further on. The lithium environment(s) were studied using $^{6/7}$Li MAS NMR, where ^{7}Li is the preferred NMR nucleus of the two due to its high gyromagnetic ratio (10.39 rad/T s), high natural abundance (93%) and relatively small quadrupolar interaction (typically on the order of a few 100 kHz). The other NMR active nucleus, ^{6}Li, also has a small quadrupolar interaction but suffers from a low natural abundance (~7%) and a low gyromagnetic ratio (3.93 rad/T s), limiting its receptivity for studies in NMR. Relaxation of ^{6}Li in non-paramagnetic materials is also less efficient, causing further difficulty. As such, many studies use ^{6}Li MAS NMR for spectral resolution, while sacrificing signal-to-noise and sensitivity. An alternative method involving ^{6}Li enrichment will be discussed below that allows for better sensitivity, good resolution and ease of acquisition for both crystalline and amorphous systems.

3.1.1. Materials and Methods

3.1.1.1. Synthesis

Three sets of crystalline lithium borates and five sets of amorphous lithium borates were synthesized using typical solid-state chemistry. Stochiometric amounts of B_2O_3 (from dehydrated boric acid: $2H_3BO_3 \rightarrow B_2O_3 + 3H_2O$) and lithium carbonate (Li_2CO_3) were mixed together. Each material was made in duplicate: naturally abundant (N.A.) samples were synthesized from regular Li_2CO_3, while the ^{7}Li-depleted (D) samples were synthesized using isotopically enriched $^6Li_2CO_3$ (^{6}Li - 95% / ^{7}Li - 5%). Crystalline borates were synthesized by heating the samples in platinum/gold(5%) crucibles between 600 to 800°C with periodic grinding over 48 hours. Amorphous borates were synthesized by heating the powders in platinum/gold(5%) crucibles at 900°C for 20 minutes and then quenching in deionized H_2O (deionized water prevents mineral deposits on the bottom of the crucibles).

Crystalline lithium metaborate undergoes compression from a 3D framework to a 2D sheet when it is packed or compressed (i.e., by placing into a sample rotor).[9] This can be observed in the ^{11}B spectrum where the powder pattern contains rounded corners resembling a disordered structure (not shown). Mixing the crystalline metaborate (N.A. and D) with quick-set epoxy helps in minimizing this compression; the sample is allowed to harden, then sanded to a fine powder.

3.1.1.2. Powder X-Ray Diffraction

Crystalline compositions were confirmed using a PANalytical X'Pert Pro Bragg-Brentano powder X-ray diffractometer. The radiation source was Cu-K_α with an

X'Celerator detector and a Ni-filter diffracted beam. Data were acquired at room temperature (21°C) over a 2θ range of 15^0 – 75^0 with a 0.0075^0 step size. Powder crystalline samples were mounted on a zero-background quartz sample holder using grease. Diffraction patterns were matched using the PANalytical X'Pert Highscore Plus software® to confirm lithium borate phases.

3.1.1.3. Nuclear Magnetic Resonance

MAS NMR spectra were acquired using a 3.2 mm double resonance (H/F-X) Varian-Chemagnetics probe on a Varian ^{UNITY}INOVA spectrometer equipped with a 14.1 T magnet (Oxford). Powdered samples ranging from 20 to 35 mg were packed into 3.2 mm o.d. (22 μL fill volume) ZrO_2 rotors and spun from 6.000 (± 0.001) to 20.000 (± 0.005) kHz. ^{11}B was referenced using boric acid (0.1 M) at 19.6 ppm while $^{6/7}$Li used aqueous lithium chloride (9.7 M & 1 M, respectively).[4,92]

3.1.1.3.1. Boron-11 & Lithium-6/7 MAS NMR

^{11}B MAS NMR spectra were acquired on all the samples using a Bloch sequence with a pulse width of 0.7 μs (~17° tip angle). Spectra were acquired with 16 to 4,000 co-added transients and recycle delays between 10 to 1,000 seconds. ^{7}Li MAS NMR spectra were obtained using 4 to 1,640 co-added transients and recycle delays between 15 to 3,000 s. The Bloch sequence was used with a pulse width of 0.5 μs (~13^0 tip angle). ^{6}Li MAS NMR spectra were acquired with 4 to 64 co-added transients, and recycle delays between 60 to 15,000 seconds. The pulse width was 0.5 μs with appropriate power to match the 13^0 tip angle used in the ^{7}Li experiments.

3.1.1.3.2. Lithium-6/7 Orthoborate Resolution and S/N

^{6}Li versus ^{7}Li resolution (and S/N per spin) data were acquired using a spinning speed of 6 kHz, 4 co-added transients, with 360 to 15,000 second recycle delays and appropriate power levels to obtain an ν_{rf} of 36 kHz.

3.1.1.3.3. Lithium Spin-Lattice Relaxation

^{7}Li relaxation measurements employed the saturation recovery pulse sequence with a 24-pulse comb to ensure complete saturation of the crystalline samples. Sample rotation was maintained at 16.000 ± 0.002 kHz, with recycle delays of 1s. The pulses were optimized at 3.75 μs (solid 90^{o}) with 20 ms delays between pulses and τ-delays varying from 1 to 20,000 seconds. ^{6}Li relaxation measurements were also performed on the natural abundant and depleted orthoborate samples using identical parameters.

3.1.2. Results

3.1.2.1. Boron-11 MAS NMR

^{11}B MAS NMR for the three sets of lithium borate phases (Meta ($LiBO_2$), Pyro ($Li_4B_2O_5$) and Ortho (Li_3BO_3)), allow us to determine (i) whether $^{[4]}$B was present as an impurity (these samples should contain no four-coordinate boron according to their crystal structures) and (ii) evidence that depleting the sample of ^{7}Li caused no observable spectroscopic change (i.e., the N. A. and D ^{11}B spectra were identical). Spectra for the lithium borate glasses confirmed appropriate compositions based on the fraction of four-coordinate boron (N_4) when compared to previous studies.[90,93]

^{11}B MAS NMR for the three samples (three N.A. and three D) revealed $^{[3]}$B spectrum (Figure 3.2) of pure orthoborate species. The meta- and pyroborate seem to have an impurity, although powder x-ray diffraction indicates a single pure crystalline phase for both species. The central transition of the orthoborate has a quadrupolar coupling of 2.6 ± 0.1 MHz as seen in similar alkali borate crystals.[9] Each $^{[3]}$B resonance displays a systematic increase (higher frequency) as one goes from T^2 (meta) to T^0 (ortho) species, confirming the borate assignments. The asymmetry parameter, η, provides information on the local symmetry for each borate, as the boron site changes from pseudo-C_{2v} (meta & pyro) to pseudo-D_{3h} (ortho). η is zero for the orthoborate, which indicates that the B unit has axial symmetry (V_{xx} and V_{yy} are within the plane of the BO_3 unit, while the V_{zz} is orthogonal to this plane). The shift is caused by bridging-oxygens (BO) breaking down and forming non-bridging oxygens (NBO).[9] The pyroborate is hygroscopic and readily picks up water during packing of the sample. The ^{11}B MAS NMR spectrum for pyroborate suggests an impurity of $B(OH)_3$, or this particular crystal contains two $^{[3]}$B resonances (the atomic coordinates are not known for this crystal), although powder x-ray diffraction indicated a clean phase with no evidence of impurities.

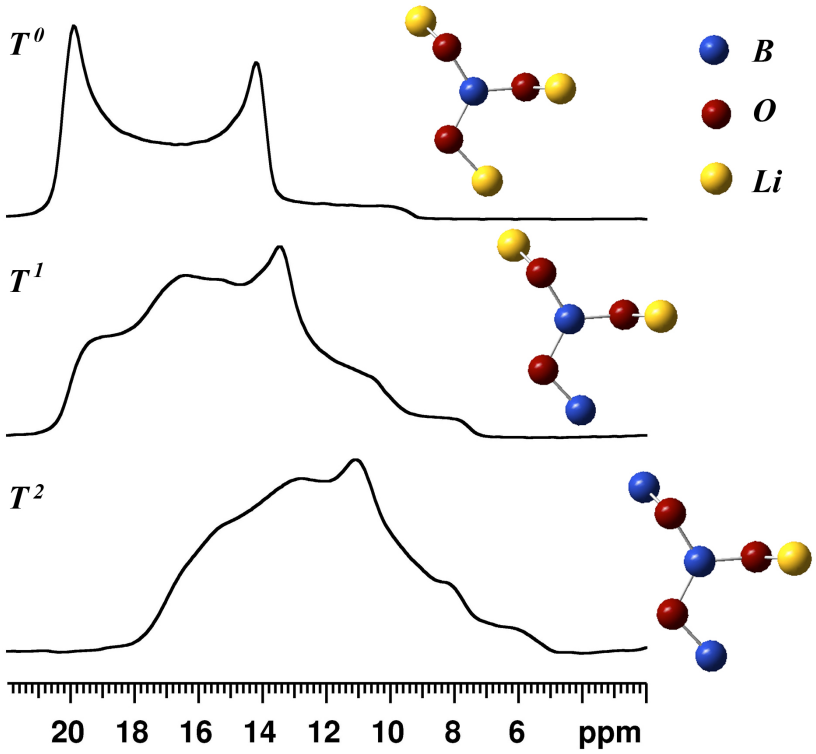

Figure 3.2. ^{11}B MAS NMR of the metaborate (T^2), pyroborate (T^1) and orthoborate (T^0). The orthoborate is a pure phase with no evidence of impurity. The pyroborate seems to contain an impurity or more than a single boron site as the shape of the CT does not conform to traditional T^1 units. The metaborate is pure however affected by imperfect crystal packing, which results in a poorly defined powder pattern.

3.1.2.2. Lithium-7 MAS NMR

3.1.2.2.1. Lithium Metaborate

The crystalline metaborate contains a single lithium environment.[94] The quadrupolar coupling constant is 70 ± 10 kHz (both N.A. and D measured from the spinning sideband (ssb) manifold), with δ_{iso} = 0.1 ppm (N.A.) and 0.49 ppm (D) and full-width at half maximum intensity (FWHM) of 1030 Hz (N.A.) and 150 Hz (D), Figure 3.3.

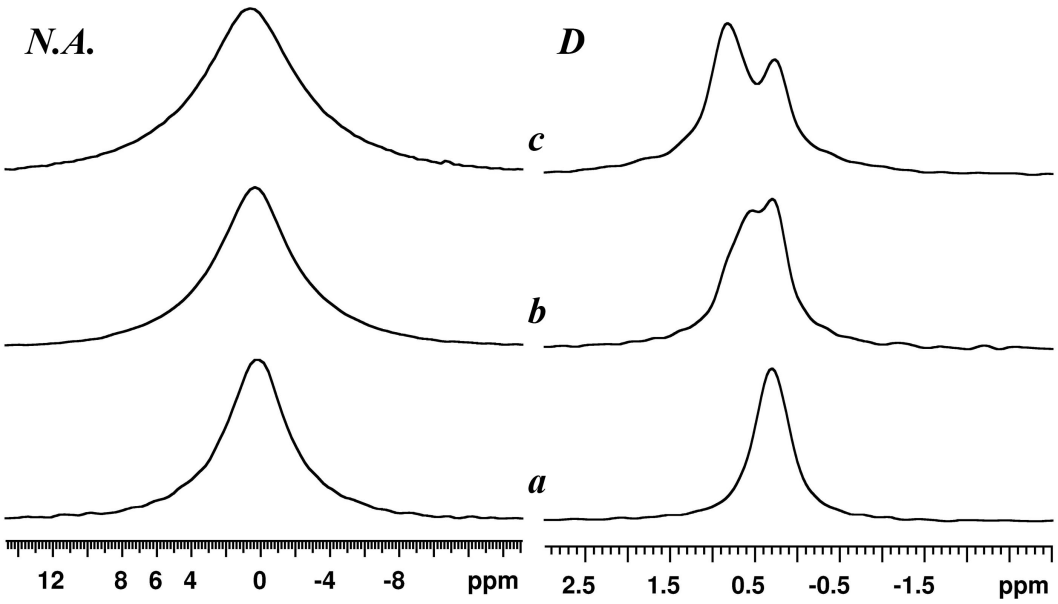

Figure 3.3. Central transition of ^{7}Li MAS NMR of the (a) meta, (b) pyro and (c) orthoborate crystals. (N.A.) Natural abundance samples and (D) depleted samples.

3.1.2.2.2. Lithium Pyroborate

The pyroborate crystalline atomic positions are not known. Powder x-ray diffraction was used for phase identification and the space group for $Li_4B_2O_5$ has been previously determined to be orthorhombic, Pb21a.[95] According to the International Tables for Crystallography[96], the pyroborate contains two to eight crystallographically distinct lithium sites. The δ_{iso} is 0.6 (N.A.) and 0.59 and 0.22 ppm (D), revealing two maxima with an approximate 1:1 ratio. This suggests two distinct lithium environments for this structure. The quadrupolar interactions were 200 ± 10 kHz (N.A.) and 180 ± 10 kHz (D), determined by measuring the extent of the ssb manifold (Figure 3.6). The difference in the quadrupolar couplings is not significant. The cause of this difference is thought to occur due to the decrease in signal from depleting ^{7}Li (i.e., fewer ^{7}Li spins

in the depleted sample cause lower S/N if identical number of acquisitions are used). Longer acquisition times would be required to observe the total breadth of the satellites.

3.1.2.2.3. LITHIUM ORTHOBORATE

Orthoborate contains three different lithium environments but a single resonance is observed at 0.6 ppm for the N.A. sample. The D sample yields two sites (0.81 ppm and 0.3 ppm) in the ratio of ~2:1. Resolution of the three sites is hampered due to the narrow chemical shift region however the integrated intensities support the crystal structure of three distinct lithium sites (Figure 3.3 and Table 3.1).[97] The FWHM is also drastically reduced from 1290 Hz (N.A.) to 230 Hz (D), while comparable quadrupolar couplings of 150 ± 10 kHz (N.A.) and 140 ± 10 kHz (D) are determined (from the ssb manifold).

Table 3.1. ^{7}Li MAS NMR parameters for N.A. and D crystalline lithium borates

Sample	δ_{iso} N.A. (ppm) (± 0.1)	FWHM N.A. (Hz) (± 10)	C_Q N.A. (kHz) (±10)	δ_{iso} D (ppm) (± 0.05)	FWHM D (Hz) (± 10)	C_Q D (kHz) (±10)
Meta	0.10	1030	70	0.49	150	70
Pyro	0.60	1190	210	0.59 & 0.22	190	180
Ortho	0.60	1290	150	0.81 & 0.3	230	140

3.1.3. Discussion

3.1.3.1. Lithium-7 MAS NMR

The three N.A. (93% ^{7}Li) samples revealed a central transition (CT, -½ – +½) characteristic of a single resonance, with no site resolution (Figure 3.3). The widths (FWHM) of the central transition are between 4 and 5 ppm (1,000 and 1,300 Hz). These measured breadths were obtained using a spinning frequency of 20 kHz, believed to average out most of the anisotropic interactions with the exception of the second-order quadrupolar interaction. Unfortunately, these measured breadths almost span the known chemical shift region for lithium oxides, preventing the resolution of multiple lithium sites.[92]

The anisotropic interactions that would affect the observed linewidth include: relaxation (T_2), field inhomogeneities, dipolar couplings, CSA and quadrupolar interactions. Lithium oxides have small quadrupolar couplings (< 300 kHz)[13,84,90,94] so the broadening resulting from the second-order quadrupolar interaction is rather small (< 10 Hz, eqn. 31)[98] when using moderately high fields (e.g., 14 T). The CSA interaction is small for lithium species and will not contribute significantly to the observed linewidth under MAS.[84] The relaxation times (T_1 and T_2^*) indicate long T_2's (with contributions in breadth on the order of ~100 to 300 Hz), which therefore, contribute very little to the breadth of the CT for the N.A. samples. Due to the narrow breadths of these lineshapes, shimming (~ 9 Hz), fluctuations in spinning rate (< 5 Hz) and proper magic angle adjustment (< 10 Hz) are important points to consider when minimizing linewidths. Accepting these statements and measuring the interactions above provides clear evidence for a major contribution from the homonuclear dipolar

coupling interaction. Dipolar coupling often causes a broad unresolved lineshape as seen in Figure 3.3.[13,84,98] To confirm our hypothesis, the dipolar coupling interaction must be minimized or removed. The strength of the homonuclear dipolar interaction will decrease if one lowers the occurrence of neighbouring ^{7}Li atoms. This is accomplished by depleting the samples (N.A. – 93% vs. D - 5%) via ^{6}Li to decrease the ^{7}Li-^{7}Li interactions, while maintaining the crystal structure (i.e., by diluting the ^{7}Li spins, using 95% $^{6}Li_2CO_3$). Our work on the depleted ^{7}Li borates (5% ^{7}Li) exhibited higher resolution providing evidence that the main broadening feature in these borates is in fact the dipolar coupling interaction. Depletion also enabled multiple lithium sites to be resolved for both the pyro- and orthoborate species, providing evidence that at least two lithium sites are present in the unknown pyroborate structure. The efficiency of isotopic depletion was tested further using variable spinning rates (6 kHz to 20 kHz) for the depleted samples. The spectrum acquired at 20 kHz did narrow slightly (<5 Hz), indicating the isotopic depletion method averages the dipolar interaction even at slow spinning. The change in linewidth by 5 Hz could be due to residual dipolar coupling but is most likely due to sample heating, possibly causing an increase in lithium mobility. The remaining breadth will be the sum of the interactions indicated above, T_2 and the field inhomogenity. The depletion method seems to be ideal for measuring ^{7}Li isotropic chemical shift and quadrupolar information without a contribution from the dipolar interaction. Additionally, accurate quadrupolar coupling constants can be measured due to the ability to spin slowly, enabling a very well defined ssb manifold. The satellite transitions (ST) are affected by first-order quadrupolar interactions, with broadening from (10's to 100's

kHz). Under MAS, the same manifold that makes up the satellite transitions develops into spinning sidebands, concentrating the signal into a series of sharp lines, providing the ability to observe the broad ST. Therefore, to measure the quadrupolar coupling constant, non-spinning is more accurate but more difficult, while slow MAS provides adequate measurements that are much easier to accomplish. The dipolar interaction for these borate crystals accounts for 850 to 1100 Hz of the broadening on the central transition even at fast spinning rates (~23 kHz) for non-isotope depleted samples.

3.1.3.2. Lithium-6 vs. Lithium-7 MAS NMR

Analysis of the N.A. samples was carried out using ^{6}Li MAS NMR. The ^{6}Li results can be compared with the depleted ^{7}Li results to determine the effectiveness of this method. The resolution and speed attained using isotopic depletion seems to be a good alternative to traditional ^{6}Li MAS NMR, alleviating longer relaxation times, low N.A. and difficulty in extracting the quadrupolar interaction (as few ssbs are seen with ^{6}Li). The lithium metaborate sample (in epoxy) was not studied by ^{6}Li MAS NMR because it was already diluted (from epoxy treatment) significantly, thereby reducing the ^{6}Li signal. Additionally there is only one crystallographic site so further resolution enhancement is not required. Lithium pyroborate data were acquired for three days (with long recycle delays), but no observable signal was detected. We believe the relaxation process is inefficient (with T_1's longer than 3000 s) and therefore the system was saturated, resulting in no signal being observed. The orthoborate sample revealed better resolution (two signals in a ratio of ~2:1) using ^{6}Li MAS NMR (Figure 3.4), although they required three days of acquisition and did not reveal enough information to extract any quadrupolar coupling constants.

The lower receptivity (difficult to obtain a signal due to the nucleus being low-γ and low natural abundance) for ^{6}Li NMR, combined with the long relaxation times intrinsic to these compounds necessitates long acquisition times for both crystals and glasses. The ^{6}Li MAS NMR spectra of the depleted sample (95%-^{6}Li) would be a natural choice as the spin-active nuclei (^{6}Li) are now abundant (95%). Although multiple field experiments are not often required for lithium NMR, the frequency difference between $^{6/7}$Li allows one to do this artificially. Specifically, the gyromagnetic ratio of ^{6}Li is about 40% that of ^{7}Li, so one can use a single magnet to confirm parameters by acquiring signals from both nuclei. This can be useful when dealing with competing interactions such as CSA and C_Q. $^{6/7}$Li MAS NMR using depleted samples showed similar resolution but determining which sample can be acquired most efficiently with regards to S/N and acquisition time per active spin is required to further validate isotopic depletion.

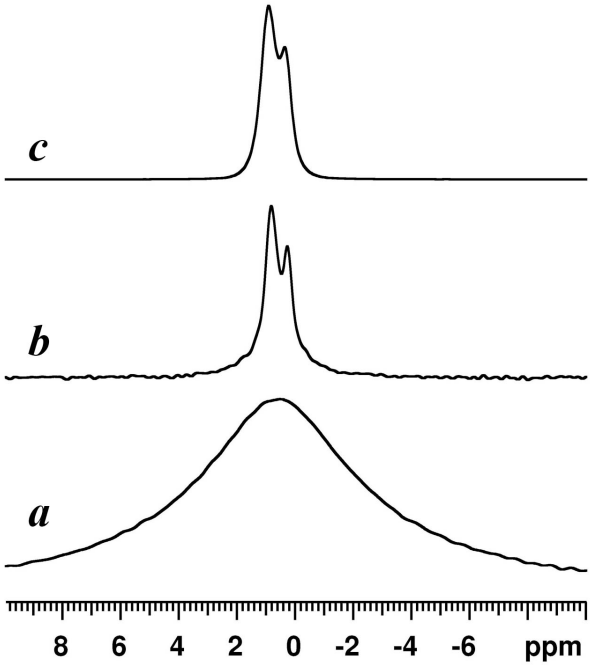

Figure 3.4. $^{6/7}$Li MAS NMR of the orthoborate sample; (a) ^{7}Li MAS NMR of N.A., (b) ^{6}Li MAS NMR of N.A. and (c) ^{7}Li MAS NMR of D samples.

3.1.3.3. Lithium-7 Spin Counting

The orthoborate sample is ideal for spin counting. It is the most lithiated species (containing three Li for every B), has a favourable relaxation rate (discussed below) and displays multiple lithium site resolution. The four combinations of interest for NMR are: ^{7}Li-93% (N.A.), ^{7}Li-5% (D), ^{6}Li-95% (D) and ^{6}Li-7% (N.A.). The NMR acquisition of these four samples was carefully controlled, using identical pulse durations/power, number of scans, appropriate relaxation delays, spinning frequency and sample masses. This provided four spectra that can be rated for sensitivity, resolution and signal obtained in the same amount of time per NMR spin-active nucleus.

The strongest signals were observed using ^{7}Li MAS NMR on the N.A. sample and ^{6}Li MAS NMR on the D sample (as one could expect due to each containing 93% and 95% NMR active spin, respectively). If we consider the acquisition time, the ^{7}Li-5% depleted sample (^{7}Li MAS NMR) is the more obvious choice with a recycle delay on the order of 3000 s. The second choice is the ^{6}Li-95% depleted sample (^{6}Li MAS NMR), although it is better resolved between the two sites, the recycle delays are one of the worst, being in the order of hours, d_1 > 15,000 s (d_1 > 4 hrs.). The ^{7}Li-93% natural abundant (^{7}Li) is third, while the least favourable is the 7% ^{6}Li (N.A.) sample (Table 3.2). The S/N is based on the maximum signal strength recorded divided by the number of spin active nuclei present within the sample. These were determined from the sample masses, working down to the number of atoms based on Avogadro's number. The resolution is rated by the degree of separation for the two resonances; all samples showed two resolved peaks with the exception of the N.A. ^{7}Li spectrum.

Table 3.2. ^{6}Li and ^{7}Li MAS NMR spin-counting for N.A. and D. lithium orthoborate crystal.

Sample	S/N	# Li spins X 10^{21}	Mass (g)	Delay (s)	Resonances
Li_3BO_3-NA-^{7}Li	1540	~3.8	0.0259	3,000	1
Li_3BO_3-D-^{7}Li	620	~0.20	0.0259	3,000	2
Li_3BO_3-NA-^{6}Li	220	~0.12	0.0226	15,000	2
Li_3BO_3-D-^{6}Li	5175	~3.9	0.0226	15,000	2

3.1.3.4. Lithium-7 Relaxation

^{7}Li relaxation was studied on the N.A. and D samples using the saturation recovery method. Peak intensities were fitted to a bi-exponential function as shown in Figure 3.5 (single exponential fits gave a poor representation of the data). Bi-exponential behaviour can be explained by two different responses (a slow and fast) occurring within these crystals (Table 3.3). The bi-exponential relaxation seen in these crystals can be explained by three potential pathways, a.) lithium dynamics, b.) multiple relaxation mechanisms or c.) various coherence transfer pathways. If two motion pathways were involved, this could be seen in the lithium dynamics, although this is highly unlikely as lithium mobility in borates is known to be ionic hopping.[84] Furthermore, since multiple sites are observed for two of the depleted samples, lithium hopping at room temperature cannot be occurring because one would expect to observe coalescence of these peaks in this instance. Variable temperature saturation recovery may be able to reveal more in this regard; however, for our purposes here these are not necessary. Both quadrupolar and dipolar interactions are strong in ^{7}Li materials and would display the two relaxation mechanisms involved. The relaxation data reveal very similar T_1*'s* for both the N.A. and D samples, providing evidence that the quadrupolar mechanism dominates. If the relaxation mechanism involved a significant contribution from the dipolar interaction, the spin-lattice relaxation times should increase for the D samples.[84] Therefore, the observation of slow and fast relaxation processes is best explained by various coherences (transitions) that can take place when studying quadrupolar nuclei, I=3/2.

Saturation recovery on the depleted orthoborate (95% ^{6}Li) sample using ^{6}Li MAS NMR revealed similar bi-exponential relaxation with a T_1 longer than 60 minutes. The ^{7}Li value for the same sample was ~ 5 minutes (T_1 = 320 s), over an order of magnitude less. Another benefit of isotopic depletion presents itself when a contribution from dipolar relaxation exists or is thought to exist as one can study its behaviour on the lithiated material by acquiring both a N.A. sample (where the interaction is present) and a D sample (where the interaction is minimized). If dipolar relaxation made a significant contribution to the relaxation in the N.A. sample, the relaxation time of the D sample should increase. Although the meta- and orthoborate seem to have similar $T_1^{(1)}$ values, the lack of a pyroborate crystal structure prevents us from saying more regarding the differences observed in T_1 measurements for the three crystals.

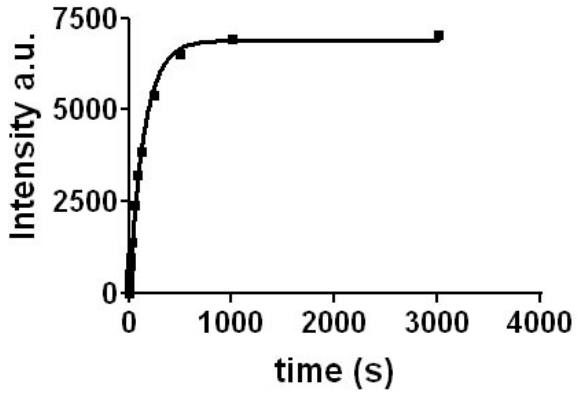

Figure 3.5. ^{7}Li MAS NMR saturation recovery data fitted using a bi-exponential curve for N.A. lithium orthoborate.

Table 3.3. ^{7}Li MAS NMR bi-exponential spin-lattice relaxation parameters for N.A. and D samples

Crystal	N.A. - $T_1^{(1)}$ (s)	N.A. - $T_1^{(2)}$ (s)	D - $T_1^{(1)}$ (s)	D - $T_1^{(2)}$ (s)
Meta	90 ± 10	900 ± 40	130 ± 15	1060 ± 180
Pyro	40 ± 6	510 ± 70	10 ± 5	625 ± 40
Ortho	90 ± 10	250 ± 20	90 ± 10	310 ± 35

3.1.3.5. Lithium-7 in Borate Glasses

The decrease in broadening interactions using isotopic depletion was successfully achieved in crystalline materials. In an effort to improve resolution in glass speciation, lithium borate glasses were also attempted. For amorphous materials, the distribution of sites introduces a new broadening mechanism. For example, a crystalline material with one distinct lithium site has the same local geometry and interactions throughout the periodic cell. Glasses are comprised of many lithium cations all exhibiting small differences in local geometry (bond length and bond angle), causing a statistical distribution of environments. Lithium borates are an ideal system for this test as one can modify speciation in the glass based on lithium concentration. Possible lithium environments include $^{[4]}$B, T^3, T^2 and T^1 speciation. Five lithium borates (both N.A. and D) were selected, spanning the compositional range R=0.1 to 2 ($R = Li_2O/B_2O_3$). These compositions were chosen as they contain the four distinct borate environments mentioned above.

Figure 3.6 shows that the overall breadth of the resonances for these borates decreases due to a reduction in homonuclear dipolar coupling that occurs upon

isotopic depletion. The isotropic chemical shift and quadrupolar coupling constant results for these glasses are given in Table 3.4. Unfortunately, the small chemical shift range and distribution of sites masks any evidence of multiple lithium sites, although lithium motion may contribute also at room temperature. If this were the case, two distinct lithium sites could coalesce into one, thereby inhibiting resolution. Lower temperature experiments (< -40^{o}C) might solve this issue, with the ability to slow down the lithium mobility. The depletion technique in glasses does provide narrower line-widths, allowing a more accurate isotropic chemical shift to be recorded, and may provide details in multi-component glasses at higher fields combined with lower temperatures. The higher field enables an increase in spectral resolution, thus providing better site resolution. Higher fields can also prevent further resolution as the distribution of sites will also broaden due to the variance in geometry; finding a balance would be optimal.

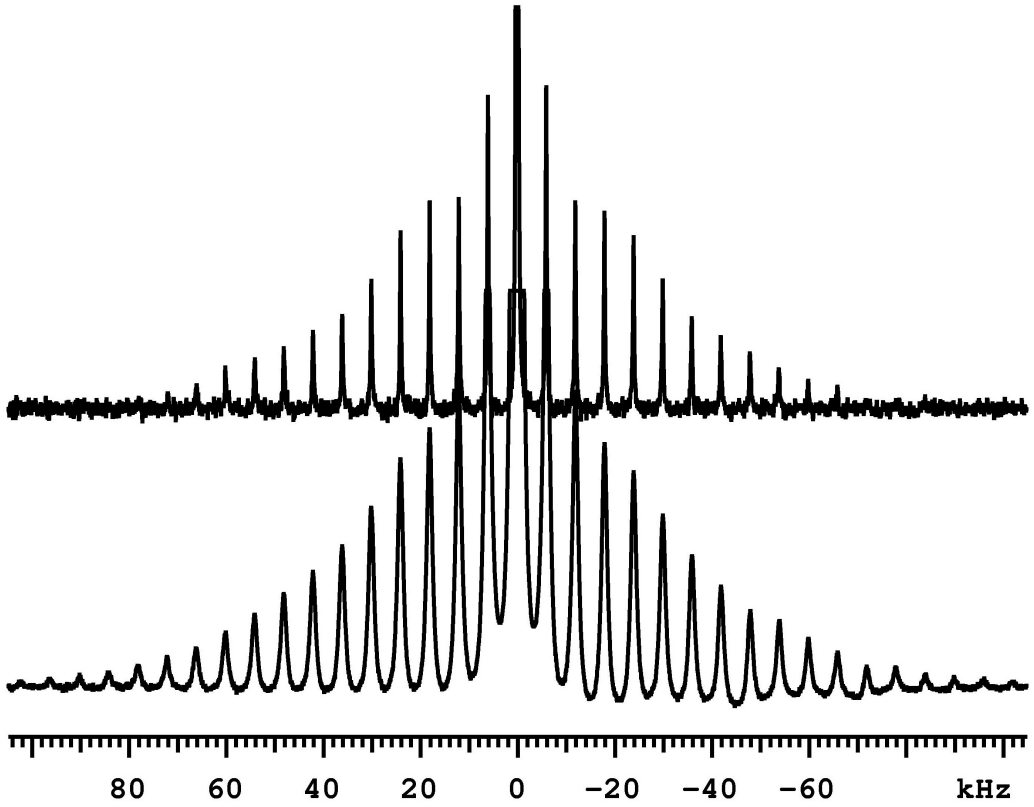

Figure 3.6. ^{7}Li MAS NMR of LiB R=2.0 glass showing (top) depleted spectrum and (bottom) natural abundant spectrum with the full breadth of the spinning sideband manifold.

Table 3.4. ^{7}Li MAS NMR N.A. and D NMR parameters for glass samples

Sample, R	δ_{iso} N.A. (ppm) (±0.1)	FWHM N.A. (Hz) (±10)	C_Q N.A. (kHz) (±10)	δ_{iso} D (ppm) (±0.01)	FWHM D (Hz) (±10)	C_Q D (kHz) (±10)
0.1	-0.4	350	150	-0.43	270	150
0.5	-0.2	570	222	-0.16	300	220
0.8	0.1	690	222	0.10	280	200
1	0.1	790	220	0.13	280	200
2	0.5	1100	216	0.56	200	190

3.1.4. Summary

Lithium-containing crystalline phases and glasses were studied in an effort to obtain multiple site resolution using isotopic dilutions. Enriching the samples with 95% ^{6}Li causes the dipolar interaction to be essentially removed (similar to the way ^{2}H is used to replace ^{1}H in organic solids) for both crystalline and glassy materials. In addition, this may also prove to be useful in studies where the relaxation mechanism is uncertain (i.e., whether it is predominantly quadrupolar or dipolar) and can be determined in an easy and inexpensive (<$10/g) manner. The identification of different lithium environments still seem to elude us in amorphous oxides. However, similar line-narrowing advantages are seen. Isotopic dilution provides an alternative to the use of expensive fast MAS probes and circumvents complex decoupling sequences (e.g., Dumbo, eDumbo, etc.), which can be difficult to optimize for quadrupolar nuclei that contain long delay times.[4]

3.2. Amorphous Alkali Borates

Alkali borate glasses have been extensively studied due to their potential importance as fast ion conductors[99-102] and alkali borosilicates as model systems for highly durable nuclear waste-forms.[103,104] One of the most valuable techniques for probing short-range structure in glasses is NMR spectroscopy.[1,105-107] ^{11}B NMR has been used for decades to quantify the types of borate polyhedra in borate glasses[1,85,108,109] and has played an important role in developing structural models of borate-based glasses.[9,110-113] Less widely studied are the alkali modifier cations. This is partly because the low field strengths characteristic of network modifiers result in highly

disordered and irregular local environments. This leads to large distributions in chemical shifts and quadrupole parameters, resulting in NMR peaks that are generally broad and featureless, making precise assignments difficult. The heavier alkali cations (K, Rb, Cs) have also traditionally been considered 'difficult' nuclei to probe because of their unfavourable NMR characteristics. ^{39}K (93.3% N.A., Q of 5.85 fm^2 and γ of 1.25 × 10^7 rad/T s) has a very low gyromagnetic ratio, and hence suffers from low sensitivity and practical acquisition problems.[114] ^{87}Rb (27.3% N.A., Q of 13.35 fm^2 and γ of 8.78 × 10^7 rad/T s) can have very large quadrupole couplings for low-symmetry sites, resulting in extremely broad peaks, if observable at all. ^{133}Cs (100% N.A., Q of -0.34 fm^2, and γ of 3.53 × 10^7 rad/T s) is highly polarisable and thus gives rise to a very broad range of chemical shifts, which can be difficult to disentangle from the spinning sidebands of the satellite transitions. However, improvements in NMR instrumentation have made it much easier to observe these nuclei in amorphous materials. The use of higher magnetic fields reduces the effect of quadrupole interactions on spectral appearance.[115-117] Faster-spinning MAS probes facilitate separation of central peaks from satellite transitions. Moreover, the chemical shift ranges of some of these nuclei (e.g., ^{133}Cs and ^{87}Rb) are sufficiently large to be sensitive to subtle structural changes. Valuable NMR studies of alkali cations, including those by Eckert[111,118-120] and Stebbins[121,122], allow the determination of the coordination environment. Common to all these studies is that structural information is inferred from spectral changes as a function of cation concentration.

We report the direct NMR observation of alkali cations in five binary alkali-borate glass systems with an emphasis on ^{133}Cs composition dependence. Spectral

changes are interpreted in terms of changes in the alkali coordination sphere. In addition to providing a systematic comparison of the group I modifiers, we extend the known regime of study to glasses with higher alkali content.

3.2.1. Materials and Methods

3.2.1.1. Synthesis

Stoichiometric amounts of alkali carbonate (M_2CO_3, M = Li, Na, K, Rb & Cs) were mixed with diboron trioxide and heated in a platinum/gold(5%) crucible from 450°C - 700°C for decarbonation. The decarbonated samples were heated between 900 - 1050°C to obtain the melt phase. The melt phase was maintained at these temperatures for 20 to 25 minutes, ensuring homogenous mixing. Quenching of the melt is achieved by immersing the crucible in deionized water (or liquid nitrogen) forming a clear, bubble-free, homogenous glass. A few higher-alkali-content glasses required the faster quench rate afforded by the use of liquid nitrogen. Glasses were checked visually for crystallinity using a polarized light microscope.

3.2.1.2. Nuclear Magnetic Resonance

NMR experiments were conducted on a Varian ^{UNITY}INOVA 600 spectrometer with a 3.2 mm double resonance MAS probe (^{11}B, ^{6,7}Li, ^{23}Na, ^{87}Rb, ^{133}Cs) and a 5.0 mm double-resonance MAS probe (^{39}K). Spectral acquisition details are given in Table 3.5. Samples were ground to a fine powder with an agate mortar and pestle, and packed into 22 µL (3.2 mm) or 90 µL zirconia rotors (5 mm). Sample amounts were 20-50 mg (3.2 mm) and ~170 mg (5 mm). High-cesium borates (R > 0.6) are rather hygroscopic, requiring the samples to be ground and packed using a glove box (dry-N_2

environment). All spectra were acquired at regulated temperatures. ^{11}B populations of the central transition were corrected for satellite transition contributions as described by Massiot et al.[123]

High field 21.1 T data (^{39}K and ^{87}Rb) were acquired on a Bruker Avance II spectrometer equipped with a 2.5 and 4 mm double-resonance probe. A 90^{o}-τ-180^{o}-τ (ν_{rf} of 83 kHz) Hahn-echo sequence was employed with the interpulse delays synchronized with spinning rates of 30 and 17 kHz.

Table 3.5. NMR experimental parameters for alkali borate glasses

Nucleus	ν_L (MHz)	Sequence	ν_R (kHz)	ν_{RF} & Pulse Width	Delay (S)	Collected Transients	Reference PPM
^{11}B	192.4	Bloch	16	50 kHz, 0.5 µs	10-15	32-64	0.1M H_3BO_3 (19.6)
^{6}Li	88.2	Bloch	16	50 kHz, 1 µs	60	32	9.7 M LiCl (0.0)
^{7}Li	233.0	Bloch	16	41.6 kHz, 0.6 µs	20-30	32	9.7 M LiCl (0.0)
^{23}Na	158.6	Bloch	17	50 kHz, 0.8 µs	5-15	64	1 M NaCl (0.0)
^{39}K	27.9	Echo	10	25 kHz, 5 µs	1-5	12k	1 M KCl
	42.0		17.241	33.3 kHz, 3.8 µs	5-10	6k – 10k	(0.0)
^{87}Rb	196.2	Echo	18	62.5 kHz, 2 µs	5	2k	1 M RbCl
	294.5		30	83.3 kHz, 1.5 µs	1-2	15k - 19k	(0.0)
^{133}Cs	78.6	Echo	18-19	31.25 kHz, 4µs	60	64	0.5 M CsCl (0.0)

3.2.2. RESULTS

3.2.2.1. BORON-11 MAS NMR

^{11}B MAS NMR spectra were acquired and analyzed in order to determine the fraction of four-coordinate boron (N_4). Figure 3.8 shows the spectral resolution of the three-coordinate boron (5 to 20 ppm) and the four-coordinate boron (-4 to 4 ppm). The breadth of the $^{[3]}$B reflects a sizable quadrupole coupling constant, $C_Q \approx 2.6$ MHz, typical of three-coordinate borons in borates.[9,105] The tetrahedral boron peak ($C_Q \approx$ 400 kHz) is much narrower because of its high site symmetry. In contrast to the BO_3 region where the apparent doublet lineshape is due to the second-order quadrupole effect, the two peaks in the BO_4 region for rubidium and cesium borates are due to two distinct BO_4 species arising from medium-range order.[87] Such an observation is clearly made for rubidium and cesium from R=0.03 to 0.7. For comparison, Figure 3.7 shows the deconvolution of the spectrum for pure B_2O_3 into ring and non-ring T^3 units.

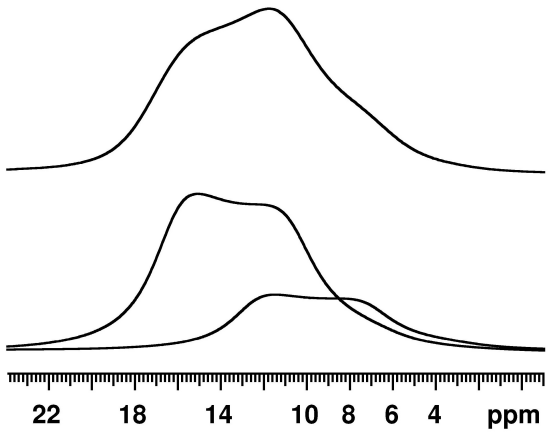

Figure 3.7. Vitreous B_2O_3 contains two sites, (top) experimental and (bottom) simulation of ring (10 to 18 ppm) and non-ring (6 to 14 ppm) T^3 units.

Figure 3.8 illustrates that the BO_4 fraction, N_4, increases linearly with R to nearly R=0.5. As is well known,[9,87,108] $^{[3]}B$ converts to $^{[4]}B$ in order to maintain charge balance with the addition of positive cations. Above about R=0.48, two processes serve to charge-compensate the alkali ions: formation of tetrahedral boron and non-bridging oxygens (NBOs) on trigonal borons. The deviation from the straight line (above R=0.5) can be interpreted as the onset of NBOs. This deviation is less pronounced for the lighter (Li and Na) alkalis than for the heavier (K, Rb and Cs) alkalis, implying that the latter prefer NBO over BO_4 at higher alkali content. N_4 values change significantly above R=0.48, where lithium seems to prefer the presence of four-coordinate species observed as a slow decrease in N_4 with R. The larger alkalis (Na, K, Rb, & Cs) display fewer $^{[4]}B$ than lithium beyond R=0.48, indicating a preference for NBOs.

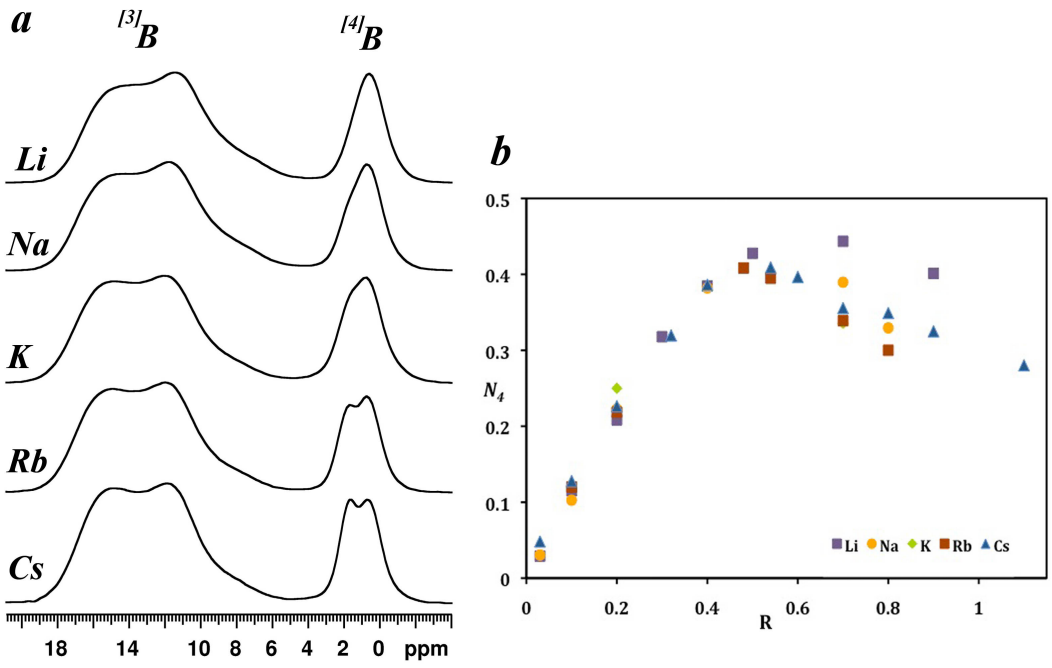

Figure 3.8. ^{11}B MAS NMR spectra of (a) R=0.2 alkali borate glasses with R=0.2 and (b) boron N_4 fractions.

3.2.2.2. ALKALI ENVIRONMENTS

3.2.2.2.1. LITHIUM MAS NMR

^{6}Li (I=1, Q of -0.0808 fm^2, N.A. of 6.5%) and ^{7}Li (I=3/2, Q of -4.01 fm^2, N.A. of 93.5%) nuclei were investigated. As expected, the observed changes in shielding of the nuclei are the same for both isotopes, revealing a subtle shift to higher frequency as R increases (Table 3.6). The ^{6}Li spectra consist of a single, narrow peak for all glasses (Figure 3.9). The satellite transitions of ^{7}Li appear as a sideband manifold extending over 600 ppm (Figure 3.6). The extent of the satellite transition envelope allows an estimation of the ^{7}Li C_Q of 190 ± 10 kHz. This small value would produce a negligible second-order shift (<10 Hz) of the central transition, hence the peak maxima are taken as the isotropic shifts (Figure 3.10). The central transition of ^{7}Li shows a somewhat larger full width at half maximum than ^{6}Li due to more extensive homonuclear dipolar interactions at 92.5% natural abundance. However the peak shift with lithium concentration is identical to that of ^{6}Li.

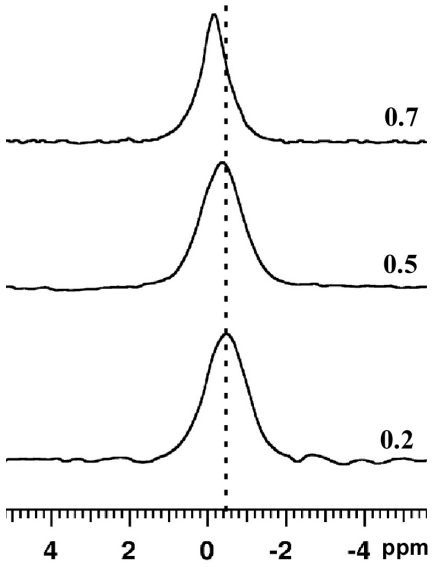

Figure 3.9. ^{6}Li MAS NMR spectra of R=0.2, 0.5, and 0.7 lithium borate glasses.

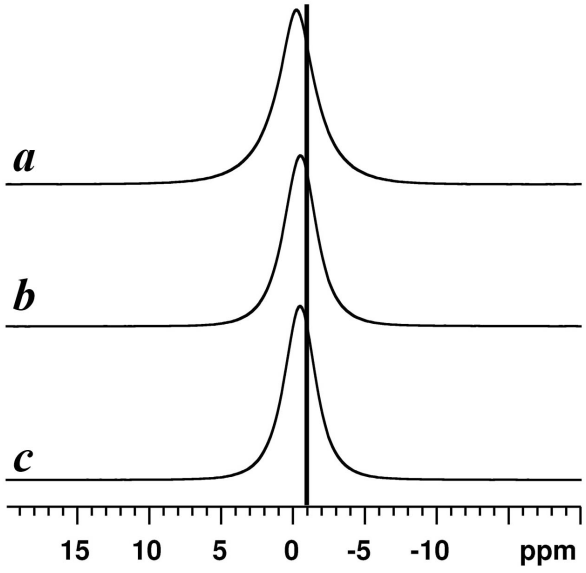

Figure 3.10. ^{7}Li MAS NMR of lithium borate glass with (a) R=0.7, (b) R=0.5 and (c) R=0.2. The vertical line is provided as a visual guide, indicating a shift to higher frequency as alkali concentration increases.

3.2.2.2.2. SODIUM-23 MAS NMR

Figure 3.11 displays typical ^{23}Na MAS NMR spectra for the sodium borate glasses. The symmetrical peak shapes indicate that distributions in the quadrupolar coupling constants do not dominate the chemical shift distribution. Nevertheless, the quadrupolar parameters are known to be too large to permit the peak maxima to reliably approximate the isotropic chemical shifts.[119] A likely variation of P_Q from 1.5 to 2.5 MHz[119] ($P_Q = C_Q (1+\eta^2/3)^{1/2}$) results in quadrupole couplings causing a variation of ca. 1 ppm in the second-order quadrupole induced shift. Nevertheless, the fact that the peak shapes and widths change little with alkali loading suggests that the shift in the peak maximum represents the true *change* in the isotropic chemical shift. The ^{23}Na peaks shift to higher frequency with increasing sodium content (Table 3.6), as

previously observed[111,118,119] for low alkali loadings. In addition, we have measured shifts at higher Na-loadings and find that this trend continues.

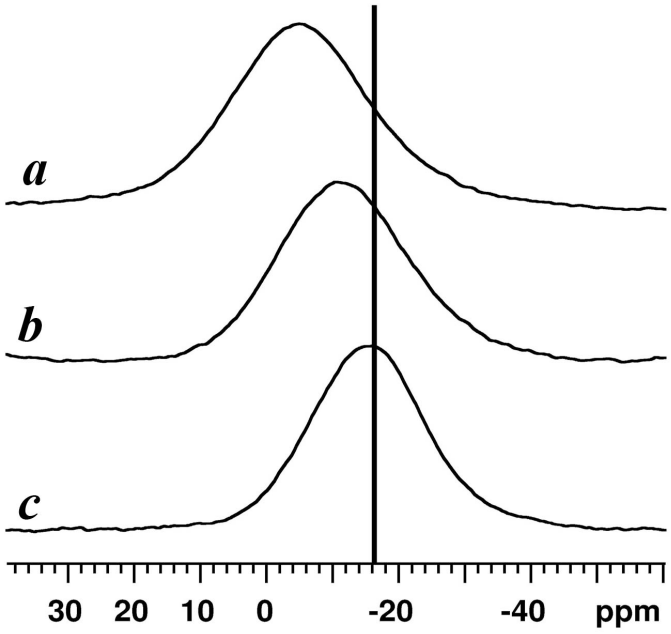

Figure 3.11. ^{23}Na MAS NMR of sodium borate glass with (a) R=0.7, (b) R=0.5 and (c) R=0.2. The vertical line is provided as a visual guide, indicating a shift to higher frequency as alkali concentration increases.

3.2.2.2.3. Potassium-39 MAS NMR

^{39}K possesses a moderate quadrupole moment (Q of 5.75 fm^2) but a very low gyromagnetic ratio (γ of 1.250×10^7 rad/Ts)[124] making it notoriously difficult to acquire spectra even in crystalline samples. Due to the low sensitivity, a larger sample-spinning rotor was used. This choice entails a trade off in the maximum spinning speed, making it impossible to resolve the broad central peak from the spinning sidebands. Consequently, the spectra consist of a broad asymmetrical peak atop a broader undifferentiated signal (Figure 3.12). This, in connection with the large

quadrupole interaction (C_Q of 2.5 ± 0.5 MHz) estimated from the second-order broadening of the central transition, makes it nearly impossible to measure the isotropic chemical shift from the MAS spectrum. Nevertheless, a direct comparison of the spectra reveals a shift of the central peak to higher frequency with potassium loading. Although the shift appears subtle against the backdrop of 400 ppm broad peaks, the peak maximum shifts nearly 40 ppm (^{23}Na shifts by only 10 ppm over the same composition) from R=0.2 to 0.7 (Table 3.6). Note that a crystalline impurity too small to be detected optically overlaps with the R=0.7 peak, but because of its sharpness, it does not interfere with the analysis.

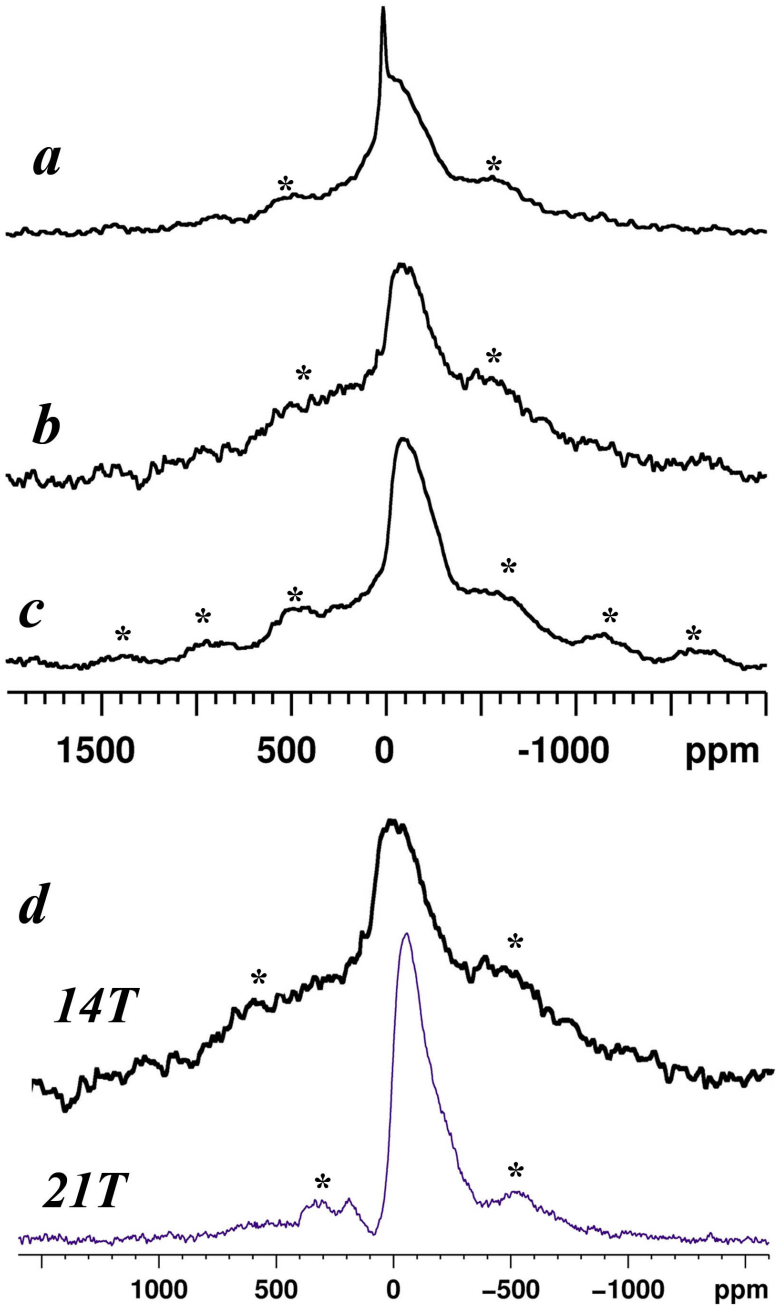

Figure 3.12. ^{39}K MAS NMR of potassium borate glass (a) R=0.7, (b) R=0.48 and (c) R=0.2. Ultrahigh-field data (21 T) for (d) R=0.54 reveals higher S/N and a narrower CT with some asymmetry to lower frequency (14 T).

3.2.2.2.4. Rubidium-87 MAS NMR

^{87}Rb has a moderately high γ, but suffers from very large C_Q values which, like ^{39}K, make it impossible to resolve the central peak from the spinning sidebands at conventional magnetic fields and spinning speeds. While some common rubidium salts have small C_Q's (e.g., RbCl, $RbClO_4$, $RbNO_3$, $RbSO_4$ and $RbCrO_4$) [125,126] we have acquired the ^{87}Rb spectrum of the more relevant α-RbB_3O_5 and found a C_Q=15.3 ± 0.3 MHz and η=0.55 ± 0.1 (Figure 3.12). Observed linewidths at 14.1 and 21.1 T were inconsistent with the range of quadrupole coupling constants available for simple rubidium salts (C_Q of 2.3 – 9.4 MHz).[125,126] In order to verify that much larger quadrupole couplings could be present to explain the observed spectra, rubidium triborate crystal was synthesized to probe the magnitude of the quadrupole coupling in boron oxide materials. A ^{87}Rb NMR spectrum of rubidium diborate crystal was also acquired. Although the presence of four crystallographically distinct sites limits precise extraction of all parameters, the C_Q's are of the same magnitude as the triborate crystal. At 14.1 T we estimate that spinning speeds in excess of 60 kHz would be required to obtain reasonable resolution of the isotropic peak from the second-order quadrupolar broadened central transition and spinning sidebands. In rubidium borate glasses, differentiation between the centre band and the spinning sidebands is very subtle (Figure 3.13), even at 21.1 T, the highest commercially available magnetic field at the time of this study. Due to all of these issues with ^{87}Rb MAS NMR, we are the first to report rubidium NMR on an oxide glass. However, as in the case with ^{39}K, a direct spectral comparison shows a clear peak shift to higher frequencies with increased rubidium loading (Table 3.6). Spectra collected at higher

field are narrower due to the improved suppression of the second-order quadrupole broadening by the Zeeman interaction; but the shift in the peak maximum is identical to that observed in data collected at lower field.

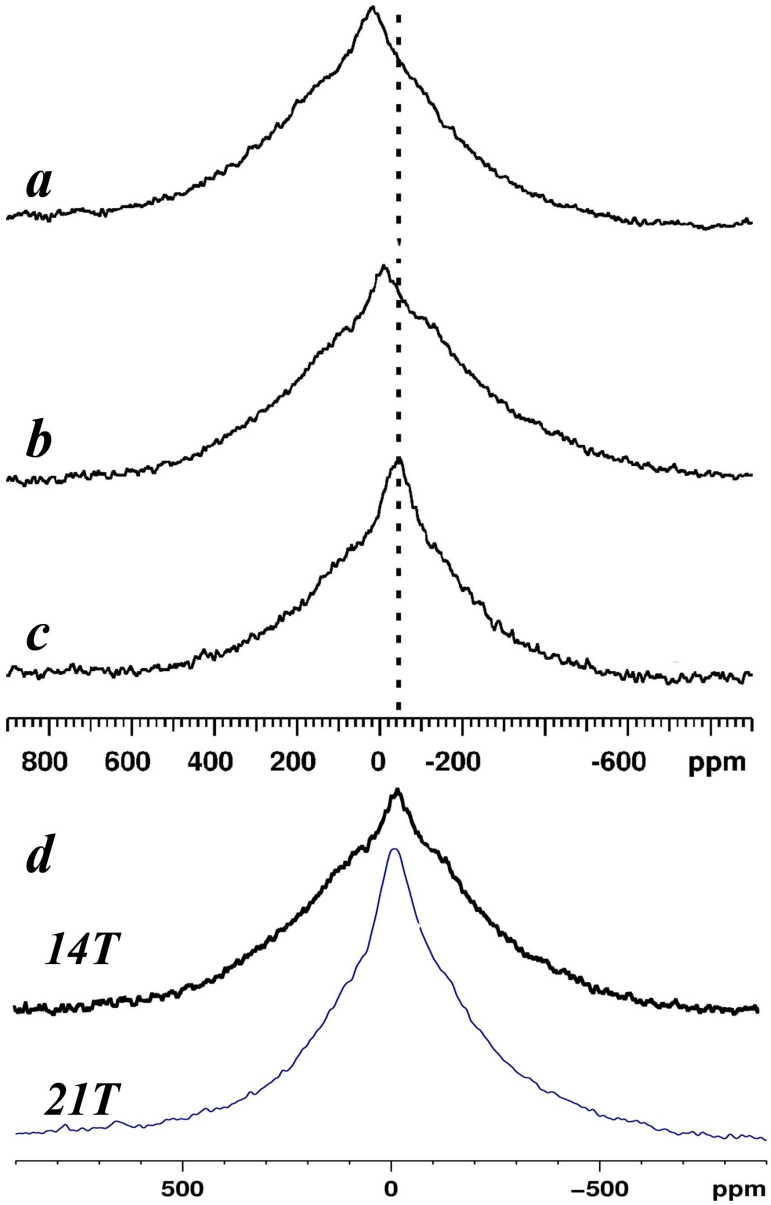

Figure 3.13. ^{87}Rb MAS NMR of rubidium borate glass (a) R=0.7, (b) R=0.48 and (c) R=0.2. Ultrahigh-field data (21 T) for (d) R=0.54 reveals higher S/N and a narrower CT than at lower field (14 T).

Table 3.6. Centre of gravity chemical shifts (δ_{cgs}) for all alkali borate glasses collected at 14.1 T.

R (M_2O/B_2O_3)	^{7}Li c.g.s. (ppm) ± 0.05	^{23}Na c.g.s. (ppm) ± 0.5	^{39}K c.g.s. (ppm) ± 10	^{87}Rb c.g.s. (ppm) ± 10	^{133}Cs c.g.s. (ppm) ± 5
0.03	n.d.	-16.6	n.d.	n.d.	-25
0.1	-0.62	n.d.	n.d.	-52	-14
0.2	-0.56	-16	-48	-50	9
0.3	-0.5	n.d.	n.d.	n.d.	39
0.4	-0.52	-10.3	n.d.	-9[a]	51
0.5	-0.41	n.d	-26	3[b]	89[b]
0.7	-0.21	-5.7	-9	16	122
0.8	n.d.	-1.4	n.d.	20	115
0.9	0.02	n.d.	n.d.	n.d.	121
1.1	n.d.	n.d.	n.d.	n.d.	121
2.5	0.56	n.d.	n.d.	n.d.	n.d.

(a) R=0.48 and (b) R=0.54, n.d., not determined

3.2.2.2.5. Cesium-133 MAS NMR

^{133}Cs (I = 7/2) has a small quadrupole moment and a moderate γ, making NMR spectra relatively easy to acquire for this receptive nucleus. ^{133}Cs also has a large chemical shift range, with correspondingly high sensitivity to small changes in local structure. Accordingly, the broad NMR peaks shown in Figure 3.14 are dominated by a

distribution of chemical shifts. The spinning sideband envelope yields an estimated C_Q of 540 ± 20 kHz. This small C_Q corresponds to a second-order quadrupole shift of 11 ± 2 Hz, hence the peak maxima are taken as the isotropic chemical shifts. Among all the alkali cations, ^{133}Cs shows the strongest chemical shift correlation with concentration, with a shift to high frequency of 122 ppm increasing upon the cesium content from R=0.03 to 0.6 (Table 3.6). Above R=0.7 the ^{133}Cs shifts plateau at 121 ± 5 ppm.

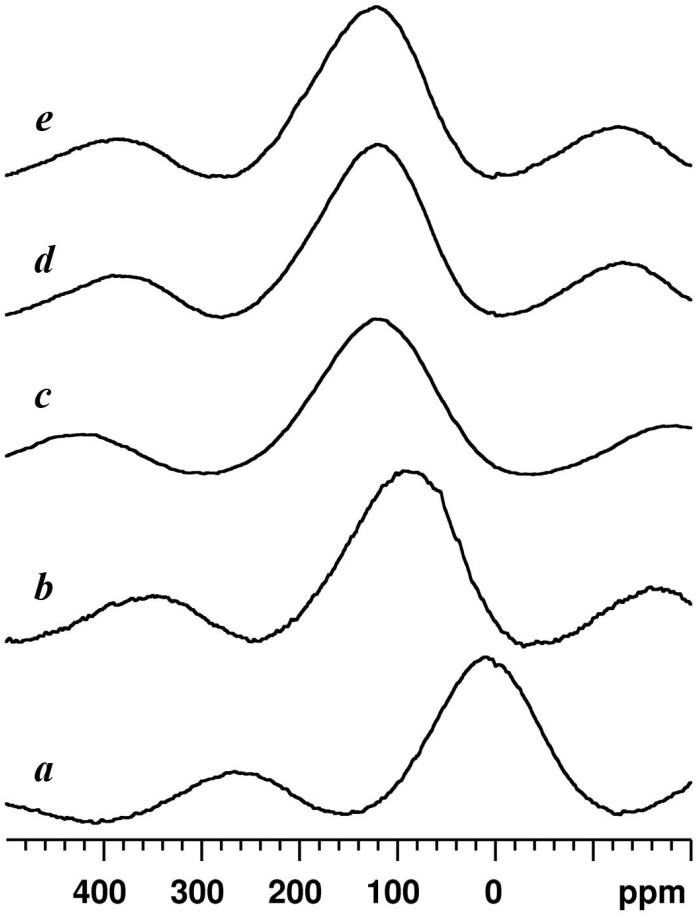

Figure 3.14. ^{133}Cs MAS NMR of cesium borate glasses, (a) R=0.2, (b) R=0.54, (c) R=0.7, (d) R=0.9 and (e) R=1.1.

3.2.3. Discussion

3.2.3.1. Boron Speciation

The four-coordinate boron population is independent of the type of alkali up to about R=0.48, as previously documented.[87,127] Beyond this alkali loading, the heavier-alkali borate glasses preferentially generate trigonal boron environments with non-bridging oxygens, whereas lithium borates continue to form a higher proportion of tetrahedral boron in response to increasing modifier content.[110] In fact, the data at R=0.7 clearly indicate that the balance of tetrahedral boron and NBOs is strongly dependent on the nature of the alkali modifier at high alkali content. Heavier alkali ions appear to stabilize NBOs, whereas lighter alkalis – particularly lithium – appear to stabilize tetrahedral boron. These results are in qualitative agreement with recent molecular dynamic simulations of cesium and lithium borate glasses which reveal smaller numbers of NBO-bearing borons for lithium borates.[128,129] This preference may be related to the size of the ions: the sum of the van der Waals radii of Li^+ and O^{2-} readily permits one lithium to interact with two bridging oxygens of a single tetrahedron, with reasonable bond angles. The larger alkalis are too big to fit between oxygens associated with a single tetrahedron, and may prefer to interact with oxygens with a larger partial negative charge, such as a non-bridging oxygen. In other words, much smaller lithium cations could fit "better" between two (and three) oxygens on a single edge (or face) of a $BO_{4/2}$ tetrahedron than larger cations. An alternative consideration is attempting to account for the electropositive character of Li^+ and Cs^+. Cs^+ is more electropositive than Li^+ causing the delocalized negative charge on a $^{[4]}B$ polyhedron to become more localized, possibly forcing NBOs to form (i.e., localizing the negative

charge onto a single oxygen). Li^+ being less electropositive can easily accommodate the delocalized negative charge on the BO_4^- polyhedra, allowing a higher fraction of $^{[4]}B$.

$$NBOs = R - N_4 \quad \textbf{(3.1)}$$

Consistent with earlier work on alkali borates[87,127], multiple tetrahedral boron sites are observed for rubidium and cesium borate glasses. However, selected potassium and sodium borate glasses (e.g., R=0.2) also exhibit an asymmetric tetrahedral boron lineshape, and a peak breadth comparable to the heavier alkalis (Figure 3.8). These observations have been interpreted in terms of medium-range order persisting throughout the entire glass-forming range of alkali borates. The observation of multiple BO_4 sites in sodium, potassium, rubidium and cesium borate glasses presents the possibility that medium-range order is the rule in low-alkali borate glasses, not the exception. The fact that no such evidence is seen in the lithium borates may be attributable to mobility of Li^+ at room temperature resulting in the observation of an average peak position for all possible sites or it may relate to a unique role for this small alkali in network-forming glasses. Another plausible argument is that lithium may behave drastically differently from the heavier alkali oxides, causing a unique borate network that contains bridging $^{[4]}B$ species for example. A more plausible explanation for this can be deduced from the Shannon radii and alkali coordination environments. Alkali cations (Na^+ to Cs^+) can accommodate up to 12 neighbours within the first coordination sphere. Lithium is limited to a maximum of eight and most crystalline species occur with coordination numbers of four to six.[130]

3.2.3.2. Alkali Environment

All of the alkali nuclei studied here via MAS NMR display a shift to higher frequency with increasing alkali oxide concentration. It is well known that high-frequency shifts accompany a reduction in cation coordination number for ionic solids. Common examples of this effect include network formers ^{29}Si [131], ^{27}Al [131], ^{31}P [114], ^{11}B [9], and network modifiers ^{6}Li [121], ^{23}Na [132], ^{25}Mg [133,134] and ^{133}Cs [135]. While it is difficult to identify precisely the discrete coordination numbers for alkali modifiers in oxide glasses, the trend to high frequency indicates that the average coordination number – and hence, the "size" of the site – decreases with higher loadings. At low alkali loadings (i.e., $R < 0.5$) this can be explained by the increasing concentration of anionic tetrahedral boron units providing partially charged oxygens for local charge balance. Indeed, double-resonance NMR methods have shown that Cs^+ preferentially associates with tetrahedral boron at low alkali concentrations.[85] With the onset of appreciable trigonal borons possessing non-bridging oxygens (i.e., $R > 0.5$), the negative charge localized on non-bridging oxygens interacts more strongly with the modifier cations. Simple bond valence arguments dictate that this results in shorter and fewer alkali-oxygen bonds, hence decreasing the coordination sphere, consistent with the NMR data.

The total ranges of the chemical shift variations differ greatly among the nuclei studied. To facilitate a direct comparison of the changes in chemical shifts, we have normalized the data by accounting for the vastly different chemical shift ranges of the alkali nuclei. We have re-referenced all shifts with respect to the R=0.2 glasses (because data for all five series were available at this composition), and divided by the

known chemical shift ranges (Figure 3.15)[114,136] to generate *relative* chemical shifts. Although the known ranges of chemical shifts for more difficult nuclei such as ^{87}Rb and ^{39}K are likely underestimated by the limited literature, this approach provides a convenient estimate of the relative changes in peak position for all alkali borate glasses (Figure 3.15). Visualizing the data in this way reveals that the relative chemical shift changes are qualitatively larger for the heavier alkali cations than they are for lithium. This is consistent with the unique behaviour of lithium in generating tetrahedral boron at compositions where the heavier alkalis generate large proportions of non-bridging oxygens (*vide supra*). Tetrahedral boron units possess a single negative charge distributed over all four bridging oxygens, conferring a lower partial negative charge on the oxygens than the more localized charge on non-bridging oxygens. Hence, with the balance shifted toward tetrahedral borons in the lithium borates, the size of the Li^+ site would be expected to be larger and change less sharply than for the heavier alkalis, where the balance is shifted toward non-bridging oxygens. Closer inspection of the relative chemical shifts show that the degree of composition-dependent shifts correlates with the size of the cation. Again, this general trend appears to follow the cation-dependent dispersion in the N_4 data, although experimental uncertainty obscures a detailed comparison of the behaviour amongst sodium, potassium, rubidium and cesium glasses.

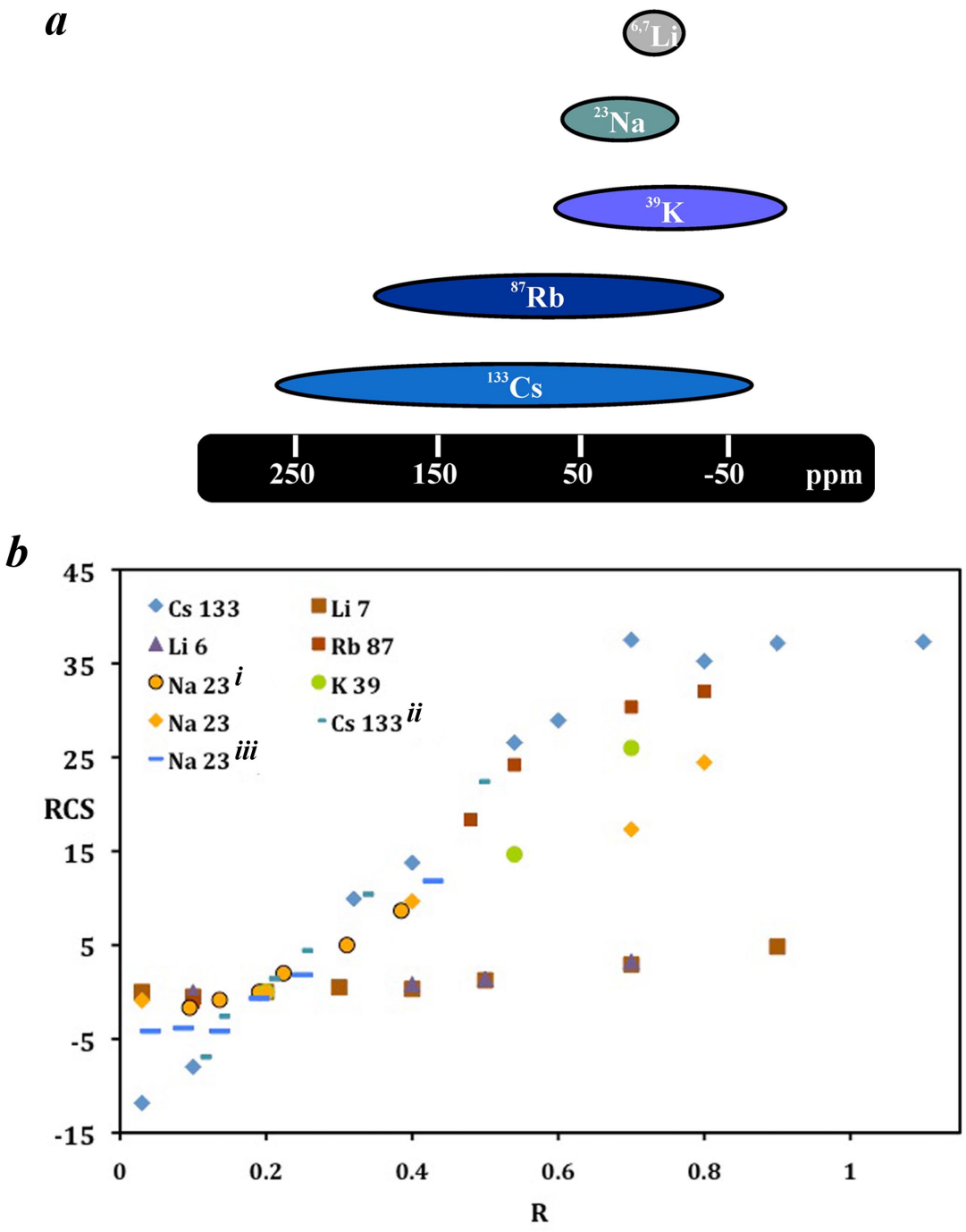

Figure 3.15. (a) Known chemical shift scales for alkali oxide species and (b) relative chemical shift as a function of alkali composition. Note additional Na and Cs data within the graph are from references ^{23}Na(i and iii)[118] and ^{133}Cs(ii)[119].

The ^{133}Cs MAS NMR data exhibit a plateau in their chemical shift above R=0.7, implying that the Cs^+ sites reach a limiting size. At this composition, 35% of the borons are present as tetrahedral boron, requiring that about half of the remaining (trigonal) borons must possess at least one non-bridging oxygen for charge balance. Increasing the cesium content further reduces N_4 marginally (see Figure 3.8) and generates additional trigonal borons with one or more non-bridging oxygens. It is difficult to rationalize this asymptotic behaviour in terms of the available anionic units, except to suggest that an intrinsic lower limit to the Cs^+ coordination number is reached at this composition. We were unable to prepare pure-phase glasses for the other alkali borates in this compositional range with a view to determining whether a similar plateau also occurs for these materials.

3.2.4. SUMMARY

Direct NMR observation of alkali metal modifier cations in borate glasses provides a valuable complement to NMR studies of network cations. In this way, we are able to monitor the coordination environments of the network modifying alkali cations in alkali borate glasses and infer a decrease in the coordination number with alkali loading. A comprehensive comparison of all alkalis in parallel provides valuable insight into the different behaviour of lithium vis-à-vis the other, heavier alkali. Moreover, significantly extending the known range of the cesium borate glasses to 53 mol% from 33 mol%[118] reveals that the early trend of a linear change in the Cs^+ coordination environment does not continue but reaches a minimum size at 41 mol%. At elevated loadings the heavier cations show a strong preference for the onset of

NBOs whereas lithium maintains a higher N_4, enabling a higher degree of polymerization for these glasses (greater degree of connectivity). The application of moderately-high fields (14.1 T) and ultrahigh-fields (21.1 T) in combination with very fast sample spinning are used to obtain the first MAS spectra of ^{87}Rb in an oxide glass.

3.3. Lithium and Cesium Mobility in Borate Glasses

Cation mobility is a property with significance in several areas. One is the possibility of alternative energy sources including solid ionic-conducting materials. Another involves the negative implication of radioactive cation mobility in nuclear waste materials, possibly leading to enhanced leaching into the environment. Although the second topic is not as well known, radioactive decay produces energy in the form of heat, which can promote cation mobility and potentially lead to degradation of waste-containing materials. The distinct structural differences that exist between the light and heavy alkali borates provide an ideal system for study, laying a foundation for understanding more complex systems in the future.

$^{135/137}$Cs is a common radioactive isotope found within high-level liquid waste (HLW) and is thought to be immobile. Although this is likely valid for materials at room temperature, the amount of thermal energy produced during decay can reach a few hundred degrees, promoting mobility. This could degrade the system or promote the onset of crystallization, creating a serious concern regarding water supplies and general health if the crystallized products are water soluble or enter the environment.[137,138] To better understand the nature and extent of mobility associated

with light and heavy alkali cations, lithium and cesium borates were studied by probing the effects on the NMR properties that result from moderate temperature increases.

3.3.1. Relaxation Theory and Glass

Relaxation measurements are commonly employed in NMR to probe molecular motion.[139,140] A common measurement (section 3.1) is that of longitudinal (spin-lattice) relaxation (T_1), which is caused by the interaction between a nucleus (e.g., ^{7}Li or ^{133}Cs) and its surroundings (i.e., the neighbouring network, the lattice).[99,141-145] Although there are six common relaxation mechanisms[23,41] (quadrupolar, dipolar, paramagnetic, chemical shift, scalar and spin-rotation) the two principal mechanisms that could contribute to the rate of relaxation (that is, the strength of the interaction and fluctuations at ν_L) in alkali borate systems are the dipolar and quadrupolar.[84] In section 3.1, we demonstrated how the quadrupolar relaxation dominates ^{7}Li, as it was unaffected by the dipolar interaction. ^{133}Cs has a larger quadrupolar moment and a smaller gyromagnetic ratio (~1/3) than ^{7}Li, suggesting that the homonuclear dipolar interaction would contribute less than in the ^{7}Li case. For these studies we consider the quadrupolar interaction to be dominating the relaxation behaviour.

If alkali hopping occurs within an amorphous system, T_1 will decrease (shorter relaxation times). If the motion is fast and randomly moving within the network, the quadrupolar interaction could decrease and even average to zero (i.e., a solution peak results). T_1 measurements in solids with quadrupolar nuclei can be difficult, as the nuclear spins contain more than two Zeeman energy levels (2I+1). ^{7}Li (I=3/2) has three single-quantum transitions, while ^{133}Cs (I=7/2) has seven. Energy levels with

different spin populations can be difficult to excite evenly, especially when large quadrupolar couplings are present. The measured response can be complex with a variety of T_1's (i.e., multi-exponential relaxation, not single-exponential) as quadrupolar relaxation is the sum of all relaxations between all transitions.[139]

Spin-lattice relaxation time measurements of quadrupolar nuclei in solids are very common, such as deuterium (^{2}H) in organic solids,[146,147] and lithium ($^{6/7}$Li) in various glasses[141,148] and battery materials.[149,150] In disordered systems, the measurements are simplified by the existence of a distribution of sites. When fitting the data to determine T_1 of a glass at a particular temperature, it is often represented as a relaxation time of the average motion displayed by the whole sample, providing an easier treatment of the data. $^{6/7}$Li and ^{133}Cs have small quadrupolar couplings (150 ± 50 kHz and 550 ± 50 kHz respectively), further simplifying these issues as their behaviour is similar to a liquid. NMR data can therefore be fitted using a single-exponential function in borate glasses and in most other oxide glasses.[84,151]

In principle, activation energies can be determined by the Bloembergen, Pound and Purcell theorem.[151] Unfortunately, the temperature range of most common probes is restricted to ~120°C, which is not high enough to reach the T_1 minimum. Hence, our determination of accurate activation energies is limited.[152-155]

Spin-spin relaxation (T_2) is another relaxation measurement that can be used to extract information from a material. This interaction accounts for the precession of nuclear spin magnetization within the xy plane.[23] This coherence of nuclear magnetic moments will begin to decay over time due to interactions and inhomogeneities in B_o (i.e., loss of magnetization within the transverse plane). T_2* is the combination of T_2

(decay due to the interactions) and T'_2 (decay due to the effect of inhomogeneities in the field). We can easily measure T_2* from the breadth of the central transition, enabling further information regarding motion as linewidth is typically sensitive to dynamics on the order of 10^{-2} to 10^{-4} s.[99] Linewidths can be measured at varying temperatures to determine whether a change is occurring. Since both the dipolar and quadrupolar interactions contribute some breadth to a central transition, a decrease would suggest some averaging of the interaction is occurring (in our case the SOQE is almost negligible). For these interactions to average, some type of mobility or rattling must be occurring. For very slow motion (1 to 10^{-2} s) we can use REDOR to measure the average dipolar coupling between two spins.

3.3.2. Mobility Mechanisms in Glasses

For our glasses, two mechanisms can be considered to describe cation dynamics, depending on the local environments found within the material; ionic hopping and percolation channels (Figure 3.16). Mobility depends on the size, charge and amount of kinetic energy available. Ionic hopping involves cations moving (hopping) from one negatively charged site or hole (e.g., $^{[4]}$B or NBO) to another. The hopping rate in other lithium oxides can be found between 0.1 and 1000 kHz,[84,99,142] and one can use T_1 relaxation measurements to probe changing hopping rates (10^4 to 10^6 Hz).[99] The less common *percolation channel* requires many anionic sites (NBOs) near one another to form a channel in which the alkali cation(s) may diffuse. The overall idea is that the material has an anionic “roadway” that contains many negatively charged species lining both sides, through which a cation is allowed to 'flow' freely. Percolation has been observed in silicates.[156]

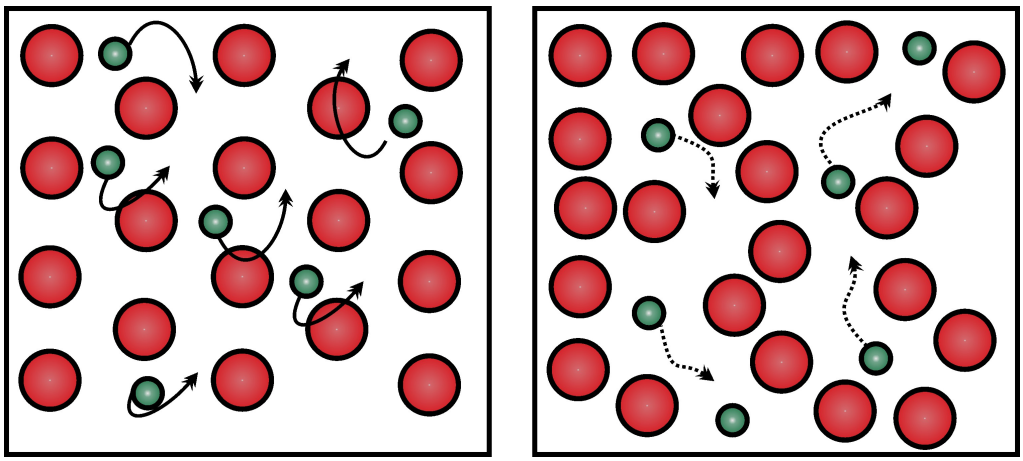

Figure 3.16. Diagrams of dynamic mechanism pathways, alkali hopping, left and alkali percolation, right. Note that the red spheres represent the glass network while the teal spheres represent the cations.

3.3.3. MATERIALS AND METHODS

3.3.3.1. SYNTHESIS

Lithium and cesium carbonate (M_2CO_3) were added to diboron trioxide, mixed using an agate mortar and pestle for 3-5 minutes, then transferred to platinum/gold(5%) crucibles. Two heat treatments ensued: decarbonation (500 to 700°C) between two an four hours followed by melting the alkali borates between 900 and 1050°C. The melt temperatures were maintained for 20-25 minutes, followed by immersion of the bottom of the crucibles in deionized water. Glasses were inspected for crystallization using a polarized light microscope. Compositions are denoted by R, where R = M_2O/B_2O_3.

3.3.3.2. Nuclear Magnetic Resonance

3.3.3.2.1. Single Resonance MAS NMR

MAS NMR experiments were conducted on a Varian ^{UNITY}INOVA 600 (14.1 T) spectrometer using a 3.2 mm H(F)/X MAS double resonance probe (Varian-Chemagnetics). Samples were ground using an agate mortar and pestle, and packed into 3.2 mm (o.d.) zirconia rotors (22 μL) with sample amounts of 30-50 mg. High alkali content cesium borates ($R \geq 0.6$) are hygroscopic, requiring manipulation in a glove box under a dry N_2 environment. All spectra were acquired at regulated temperatures using $Pb(NO_3)_2$ to calibrate for frictional heating (heating caused by sample rotation).[157] For verification of sample composition, ^{11}B (192.4 MHz) MAS spectra (not shown) were acquired using a single pulse (Bloch decay) sequence, 12° tip angle (υ_{rf} of 50 kHz) and a spinning frequency of 16.000 ± 0.002 kHz, with 16 co-added transients collected.

Spin-lattice measurements were collected for ^{7}Li (233.1 MHz) and ^{133}Cs (78.6 MHz) using an inversion recovery (180 -τ-90) pulse sequence, with υ_{rf} of 83 kHz and 61 kHz, respectively. The number of co-added transients collected for lithium borates was between 8 and 16, with a spinning frequency of 16.000 ± 0.002 kHz and a temperature range of -46 to +114°C. Cesium borates were collected using between 4 and 16 co-added transients, a spinning frequency of 20.000 ± 0.005 kHz and temperature range of +18 to +118°C. Chemical shifts were referenced to 0.1 M H_3BO_3 (19.6 ppm), 9.7 M LiCl (0 ppm) and 0.5 M CsCl (0 ppm) aqueous solutions for ^{11}B, $^{6/7}Li$ and ^{133}Cs, respectively.

3.3.3.2.2. Double Resonance Method

$^{11}B\{^{133}Cs\}$ REDOR experiments were done on four cesium borates (R=0.1 to 0.9) over a temperature range of -11 to +104 ^{o}C. The pulse sequence employed was the Hahn-echo variant,[49] with a single π-pulse on the observe channel (Figure 2.4). A spinning frequency of 6.250 ± 0.001 kHz was used for all experiments. The difference in quadrupolar couplings for $^{[3]}B$ and $^{[4]}B$ results in a variation of their nutation frequencies. This necessitates the acquisition of separate experiments with pulse lengths optimized for both $^{[3]}B$ and $^{[4]}B$. The applied π-pulse lengths were 9 μs for ^{133}Cs (υ_{rf} of 45.5 kHz), while ^{11}B used 5.2 μs for $^{[3]}B$ (υ_{rf} of 47.6 kHz) and 7.5 μs for $^{[4]}B$ (υ_{rf} of 47.6 kHz). The SIMPSON software package[81] was used to simulate the REDOR dephasing curves. Dipolar interactions were simulated at frequencies ranging from 40 to 260 Hz and fitted to the early portion of the REDOR profiles to obtain overall average field interactions between the Cs^{+} and borate polyhedra.

3.3.4. Results

3.3.4.1. Boron-11 MAS NMR

^{11}B MAS NMR spectra were acquired on all eight glasses to quantify the fraction of four-coordinate boron and confirm their compositions. Quantitative percentages of each species were obtained through integration over the $^{[3]}B$ and $^{[4]}B$ sites. To correct for the difference in quadrupolar interactions, the method described by Massiot *et al.* was used and the N_4 values were determined.[158] These results mirrored those determined from section 3.2 and confirmed that the final glass composition did not deviate from the batch composition.

3.3.4.2. Lithium-7 Relaxation Measurements

Relaxation measurements were performed on three glasses, R = 0.2, 0.5 and 0.9, over a temperature range of -46 to 114°C. The T_2^* values were determined from the CT breadth, while ln(T_2^*) was plotted versus the inverse of the temperature (Figure 3.17). ^{7}Li MAS NMR data show an increase in T_2^* as temperature increases. Above 100°C, all the glasses exhibit similar linewidths, irrespective of composition. As each composition contains different lithium concentrations the breadths of a line at any given temperature cannot be compared. A low lithium borate glass will naturally have narrower linewidths due to a smaller homonuclear dipolar coupling interaction. To determine how these materials behave differently in regards to lithium hopping, we must compare the effect on linewidth with heating time (Figure 3.17). The R=0.2 glass shows a very small change in T_2^* as one goes from -60 to 100°C. The R=0.9 glass shows a drastic increase in T_2^* over the same temperature range, this indicates a greater degree of ion mobility as the sample temperature is increased. The minimal change occurring for R=0.2 suggests very little change in mobility for Li^+ with temperature. As mobility in glasses increases, averaging of the internal interactions (e.g., dipolar and quadrupolar) will occur, lengthening T_2^*. Recall that a broad resonance is caused by a short T_2^* whereas a sharp resonance is caused by a longer T_2^*, thus removing these interactions will enable the magnetic moments of the spins within the xy plane to stay in coherence longer, increasing the time domain (free induction decay) and resulting in a narrower line upon fourier transforming.[23,84] The increase in cation motion for these borate glasses is not only affected by an increase in temperature but also with lithium concentration. An increase in Li^+ causes the borate

network to contain many more negative charges, increasing the number of sites in which Li^+ can be accommodated. Another possible effect is lithium clustering at higher lithium loadings. Although not known to occur in borate glasses, this has been seen in silicate glasses.[159]

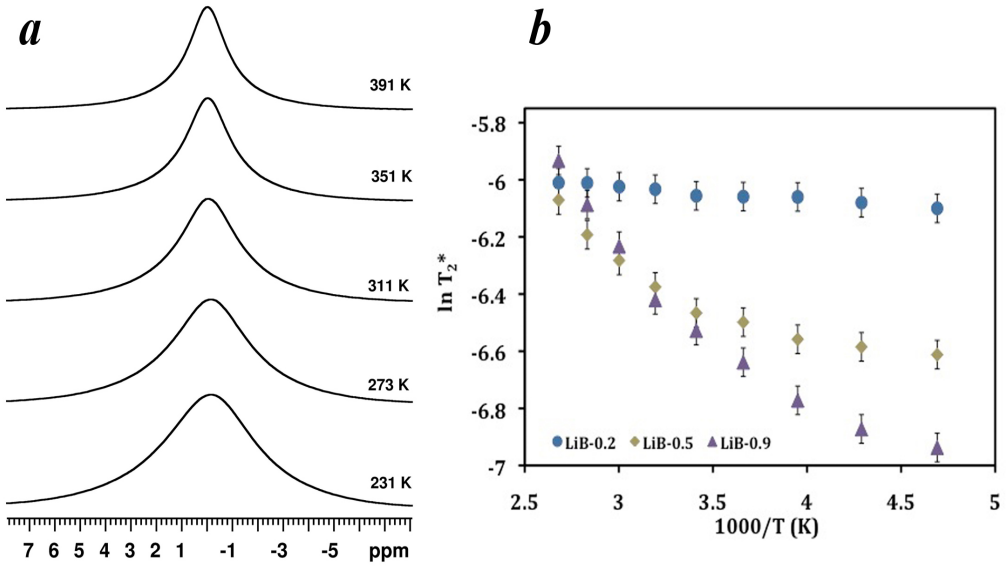

Figure 3.17. ^{7}Li MAS NMR of (a) lithium borate R=0.9 depicting the decrease in breadth of the central transition as temperature is increased and (b) lnT_2* as a function of inverse temperature, showing an increase in T_2* (decrease in FWHM) with increasing temperature.

Table 3.7. ^{7}Li T_2^* values determined from the central transition linewidth.

Temp. (K)	LiB-0.2 (ms)	LiB-0.5 (ms)	LiB-0.9 (ms)
227	2.25± 0.05	1.34± 0.05	0.97± 0.05
257	2.29± 0.05	1.38± 0.05	1.04± 0.05
287	2.33± 0.05	1.42± 0.05	1.15± 0.05
291	2.34± 0.05	1.51± 0.05	1.31± 0.05
307	2.34± 0.05	1.56± 0.05	1.46± 0.05
311	2.40± 0.05	1.70± 0.05	1.63± 0.05
347	2.42± 0.05	1.87± 0.05	1.97± 0.05
351	2.45± 0.05	2.05± 0.05	2.27± 0.05
387	2.45± 0.05	2.30± 0.05	2.65± 0.05

T_1's were also measured over the same temperature range (Figure 3.18 and Table 3.8) to further our understanding of lithium mobility. These relaxation measurements are used to study the interaction of the spin with its surroundings. The measured T_1's decrease with increasing temperature, however R=0.5 and 0.9 show a stronger temperature dependence than R=0.2. Each glass at a particular temperature should have a different T_1 value since each glass will have a network comprised of

varying degrees of polymerization. Measuring T_1 over a range of temperatures may allow us to comment on the relaxation behaviour.

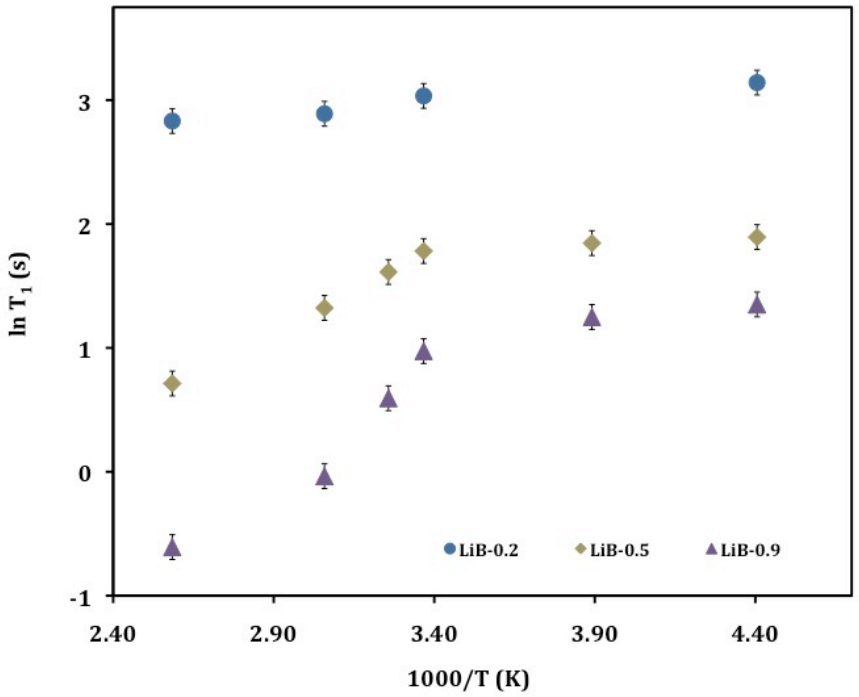

Figure 3.18. Effect on ^{7}Li spin-lattice values as a function of inerse temperature. The T_1 values decrease as the material is heated.

These data provide evidence that higher loadings of Li^{+} (more ionic environment) cause faster relaxation, and are affected to a greater extent at elevated temperatures. According to the BPP model, slopes can be measured from the low or high temperature side to determine activation energies. If we do this for these species we get values ranging from 1 to 8 kJ/mol. Unfortunately these activation energies are not reliable from our data as our available temperature range is not high enough to bring us into the more accurate high temperature curve (-'ve slope region). We would

need to go above 450°C for these data to provide valid activation energies, although the low temperature side could be used, a distribution of potential wells will cause an underestimation on the activations energies.

Table 3.8. ^{7}Li and ^{133}Cs T_1 values determined from inversion-recovery experiments.

Temp. (K)	LiB-0.2 (s)	LiB-0.5 (s)	LiB-0.9 (s)	CsB-0.2 (s)	CsB-0.5 (s)	CsB-0.9 (s)
227	28 ± 1	8.2 ± 0.5	4.4 ± 0.5	n.d.	n.d.	n.d.
257	n.d.	7.9 ± 0.5	4.2 ± 0.5	n.d.	n.d.	n.d.
287	25 ± 1	7.6 ± 0.5	3.4 ± 0.5	n.d.	n.d.	n.d.
291	n.d.	n.d.	n.d.	8.1 ± 0.8	9.5 ± 0.5	3.9 ± 0.4
307	n.d.	6.6 ± 0.5	2.3 ± 0.5	n.d.	n.d.	n.d.
311	n.d.	n.d.	n.d.	6.1 ± 0.8	7.7 ± 0.5	3.1 ± 0.4
347	23 ± 1	4.9 ± 0.5	1.2 ± 0.5	n.d.	n.d.	n.d.
351	n.d.	n.d.	n.d.	3.9 ± 0.8	5.0 ± 0.5	1.8 ± 0.4
387	21 ± 1	2.7 ± 0.5	0.7 ± 0.5	n.d.	n.d.	n.d.
391	n.d.	n.d.	n.d.	3.4 ± 0.8	3.0 ± 0.5	0.7 ± 0.4

*n.d. – not determined

3.3.4.3. Cesium Relaxation Measurements

3.3.4.3.1. Cesium-133 MAS NMR

The measured T_1 values for three cesium borate glasses (R=0.2, 0.5 and 0.9) were determined using an inversion recovery experiment and temperature between +3 and +118°C (Figure 3.19 and Table 3.8). Relaxation times for all three glasses were affected by an increase in temperature, although the effect on the R=0.2 and 0.5 glass was less than the R=0.9 glass. This can be explained by the increase in depolymerisation with higher alkali content, facilitating an increase in ionic conductance.[160] The concentration of Cs^+ does not seem to affect the relaxation times until the cesium concentration is beyond 30 mol% (R > 0.5). From section 3.2, we know the onset of NBOs form above this point within the network-forming borate glass. Using what we know occurs in the network allows us to speculate that low-loading cesium glasses exhibit little evidence of any mobility. However, at higher loadings where NBOs are present, changes do occur in the spin-lattice relaxation time, potentially providing a material that would allow for Cs^+ mobility. Cesium relaxation seems to depend more heavily on the degree of depolymerisation, than does the lithium relaxation.

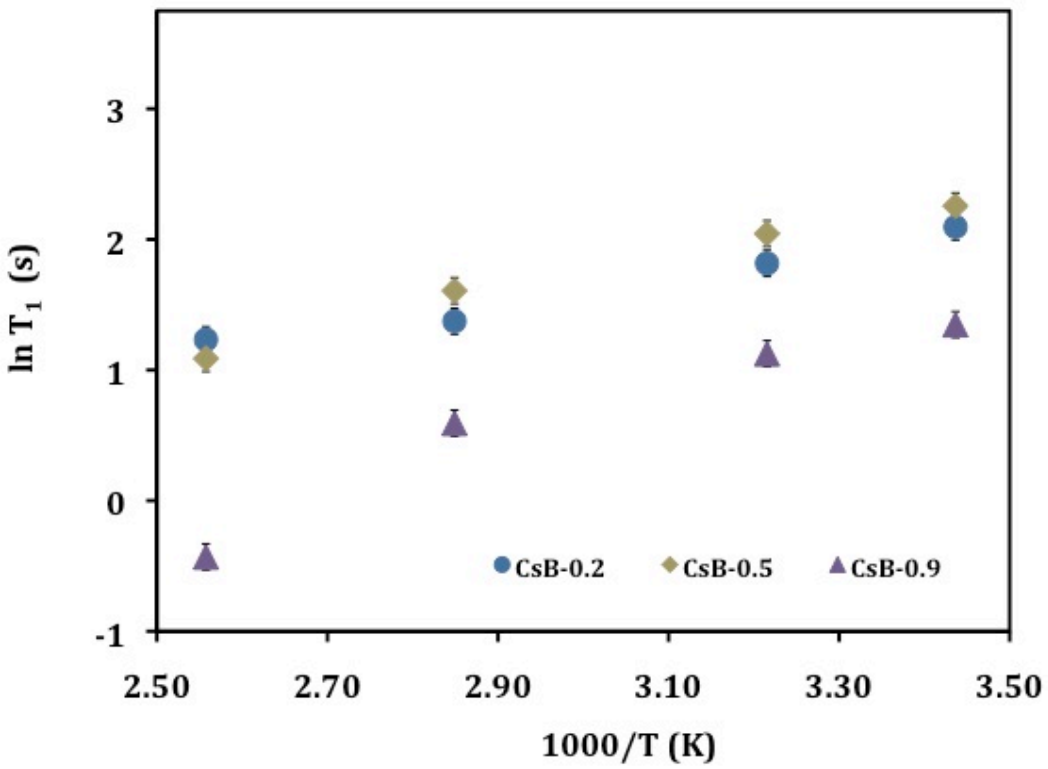

Figure 3.19. ^{133}Cs spin-lattice values, the measured T_1*s* decrease as the temperature of the material increases.

3.3.4.3.2. $^{11}B\{^{133}Cs\}$ REDOR

REDOR measurements on four cesium borate glasses (R=0.1, 0.5, 0.7 and 0.9) were acquired between -11 and 105°C (Figure 3.20). The overall extent of REDOR dephasing ($\Delta S/S_o$) is found to increase with increasing alkali content. This observation is expected due to the increasing interactions between cesium and boron, as the increasing cesium concentration causes more Cs^+ to be closer to BO_x neighbours. Furthermore, an increase in cesium creates many more anionic environments in which cesium and boron will interact (i.e., Cs^+ and $^{[4]}$B or NBO (T^2, T^1)) causing a greater interaction. The ability to differentiate between $^{[3]}$B and $^{[4]}$B dephasing data

(i.e., proximity) is limited above 42 mol% Cs_2O (R=0.7). Although experimentally $^{[3]}B$ and $^{[4]}B$ can be distinguished, the dephasing data are essentially identical (within error) because there is such a high concentration of cesium and negatively charged borate units. The REDOR curves were simulated using SIMPSON®, where we implemented a simple two-site model (Cs-B) with appropriate quadrupolar couplings, spinning rates and Larmor frequencies to simulate the REDOR curves.[161] SIMPSON simulations were calculated for varying degrees of dipolar couplings, ranging from 40 to 260 Hz, corresponding to a Cs-B interaction, r_{CsB} of 5.03 to 2.69 Å, respectively. The simulated REDOR curves (Figure 3.20) are fitted to the first few ms of the experimental curves to approximate the *average* dipolar interaction between Cs^+ and BO_X. These types of models are shown only to be sufficiently reliable for the first few ms of dephasing as we are dealing with a multiple site interaction but only have the ability to simulate a two-site model.

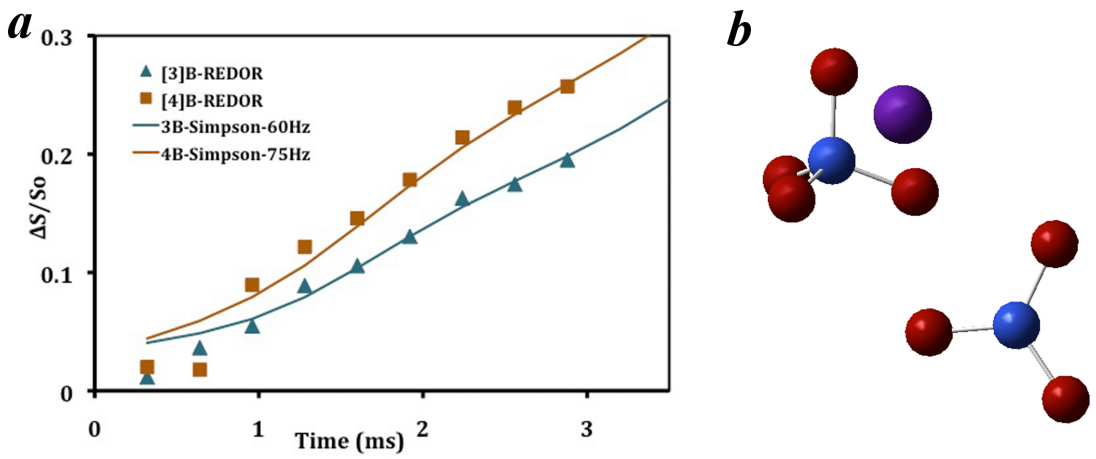

Figure 3.20. (a) CsB R=0.1 REDOR curve (points, square-$^{[4]}$B and triangle-$^{[3]}$B) with SIMPSON simulated interaction (line) and (b) polyhedra model for the cation (purple) sitting closer to $^{[4]}$B than a $^{[3]}$B as determined from the REDOR curve. Errors are within the size of the points within the graph.

Figure 3.21 shows the average dipolar interaction that each boron species "feels" as the temperature is increased, as determined from SIMPSON calculations and the REDOR dephasing curves (as shown above). At low cesium concentrations, the only anionic species is $^{[4]}$B, with a delocalized negative charge over the four-coordinate unit. At elevated cesium concentrations both $^{[4]}$B and NBOs are present.

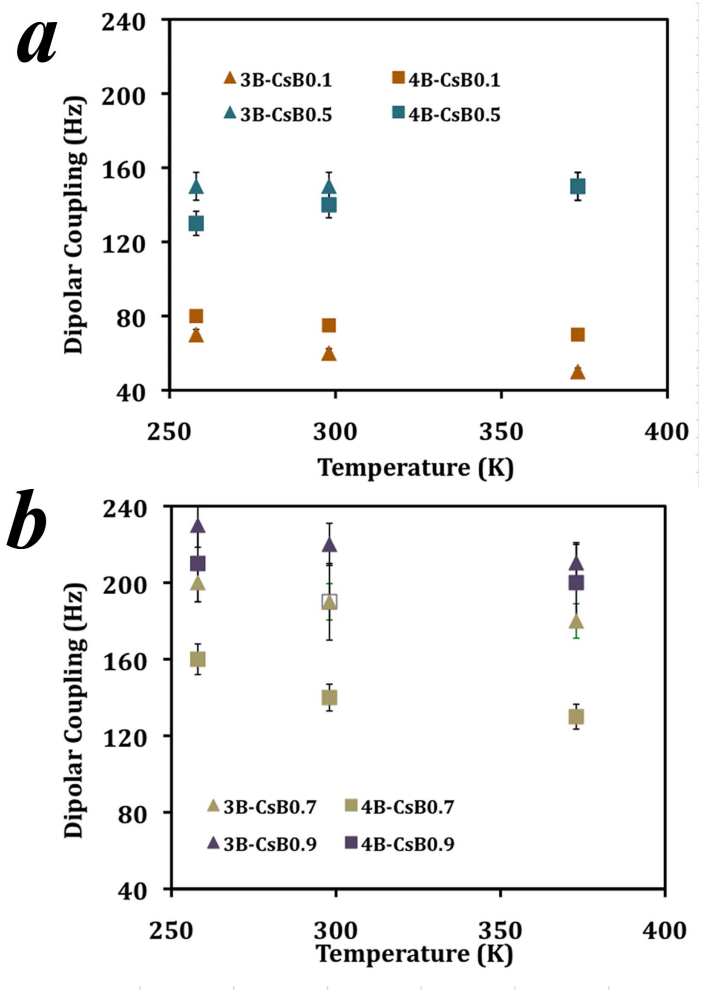

Figure 3.21. Dipolar couplings estimated from REDOR curves as temperature is increased for (a) R=0.1 and 0.5 and (b) R=0.7 and 0.9.

At lower cesium concentrations, the REDOR data indicate that the $^{[4]}$B signal is more strongly coupled to cesium and dephases more rapidly, indicating a preferential interaction with cesium at this site. This is reasonable and expected as the only anionic species present would be $^{[4]}$B. Higher cesium loaded glasses display a different behaviour in that the $^{[3]}$B signal dephases more rapidly than $^{[4]}$B. Indeed, NBOs are the significant species contributing to the structure of these high-R cesium borates, and

assuming that only T^3 and T^2 sites are available, the fraction of NBOs is between 45 to 55%. Because NBO contains a localized charge on an anionic oxygen, one would expect a stronger interaction between the NBO ($^{[3]}$B) and Cs^+ than a $^{[4]}$B, as observed here. Although these dipolar coupling constants do not provide a "real" distance due to the presence of other interacting spins and disorder, they do provide a qualitative measure of the overall dipolar field experienced by the ^{11}B nucleus.

Figure 3.21a displays the results for cesium borate glasses R=0.1 and 0.5. The R=0.1 glass exhibits an overall decrease in dipolar coupling as temperature increases. The R=0.5 glass that is on the cusp where $^{[4]}$B begin to breakdown and form NBOs behaves slightly different. The majority (>95%) of the Cs^+ are charged balanced by $^{[4]}$B, however as temperature increases the average dipolar interaction increases, indicating no evidence of motion. Although counter-intuitive, the glass network is more polymerized at this point than for the R=0.1 glass, potentially inhibiting the mobility of cesium to average out the dipolar interaction (this will be further discussed below). Figure 3.21b shows the average dipolar coupling interaction for the higher-R cesium borates (0.7 and 0.9). Both of these glasses will contain $^{[4]}$B and NBOs, these glasses show an overall decrease in dipolar coupling for both sites as temperature is increased. The R=0.7 glass has a stronger $^{[3]}$B-Cs interaction due to NBOs causing the Cs^+ to sit closer to the boron whereas the $^{[4]}$B-Cs lies further, therefore containing a smaller average dipolar interaction. The R=0.9 glass is at a point where the ratio of Cs:B is almost 1, causing cesium and boron to interact more closely and being the most anionic glass, where both $^{[4]}$B and $^{[3]}$B behave similarly. These data suggest that cesium may be mobile on the REDOR time scale (slow motion,

100s ms to s) as the average dipolar coupling decreases with temperature. The high-R cesium borates seem to be most affected as their slopes are steeper (m = -0.24 and -0.17) than the low-R glasses (m = -0.084 and +0.16). This result agrees with the observations in the T_1 measurements, where the R=0.9 glass exhibited the largest changes in T_1.

3.3.5. Discussion

3.3.5.1. Lithium-7 MAS NMR

The lithium borates were strategically chosen, representing (1) a $^{[4]}$B species (R=0.2), (2) a maximum amount of $^{[4]}$B with a smaller amount (2 to 4 %) of NBO (R=0.5) and (3) a higher-R glass where T^2 NBOs are presents as an anionic species (R=0.9). The observed changes in T_2* and T_1 as a function of temperature provide insight into lithium mobility. Relaxation times for all three glasses begin to change as the temperature increases. Unfortunately, the maximum heating temperature for our probe was not able to reach the T_1 minima in this study. Other studies on similar borate and silicate glasses reached T_1 minima at $1/\nu_L$ (10^{-8} s) in temperature regions between 600 and 900^{o}C.[17,99,162] As mentioned above, the activation energies could not be calculated from these data using the T_1 measurements.

The T_2^* data however were used to obtain an estimate. Waugh and Fedin[163] proposed that an estimate of the activation energy for lithium dynamics can be obtained using the equation E_A(kJ/mol) = $0.156T_{onset}$. The term, T_{onset} is the temperature in Kelvin when the lithium spectrum begins to narrow from a non-mobile lattice.[84,163] From our ^{7}Li T_2* measurements we can calculate an activation

energy range between 40 kJ/mol (~0.4 eV, R = 0.9) and 50 kJ/mol (~0.5 eV, R = 0.2). These experimentally determined data are reasonable for these types of materials with other groups finding activation energies between 45 and 65 kJ/mol for similar lithium borates.[99,142,154] The increase in motion with temperature indicates that very little thermal energy is required for lithium dynamics to occur in these systems. The system can be thought of in terms of potential energy, where an increase in temperature provides the Li^+ enough energy to leave and propagate along the material. The increase in anionic species within the borate network from high loadings allows Li^+ mobility to occur more easily (lower activation energy). This can be explained by the potential wells being shallower for higher loading lithium borates and provide a robust temperature range for lithium dynamics.[99,143]

In regards to forming solid ionic-conducting materials, this is beneficial for synthesis as one can tune the properties of the lithium dynamics in two discrete ways, the lithium loading and the operating temperature. Although conductivity data were not acquired, the activation energies of these glasses are comparable to studies by Matsuo et al., who studied lithium borate crystals and glasses. They found the lithium atoms in glasses similar to ours having hopping rates on the order of 10 to 10^2 Hz and electrical conductivities, $\sigma < 10^{-5}$ S/m depending on concentration and temperature.[162,164]

3.3.5.2. Cesium-133 MAS NMR

Cesium borates reveal similar, although reduced effects compared with lithium borate glasses. The R=0.9 glass contains a larger amount of NBO (compared to LiB), indicating a difference in network and anionic species (section 3.2).[90] The T_1

measurements for cesium borate glasses, R=0.2 and 0.5 (Figure 3.19) are similar over the temperature range studied. This similarity in spin-lattice relaxation behaviour may be caused by the sole anionic species being $^{[4]}$B. As $^{[4]}$B increases, the overall connectivity (polymerization) increases, limiting (or inhibiting) the ability for the large Cs^+ to move freely. The spin-lattice relaxation time for R=0.9 cesium borate glass displays a stronger temperature dependence. This suggests a change in which Cs^+ is interacting with its surrounding borate network. The large population of three-coordinate borons with NBOs comprise 85% of the three-coordinate species and statistically 74% of these are bridging to $^{[4]}$B (i.e., T^2-O-$^{[4]}$B). This amount of depolymerisation and charge will provide a more attractive environment for the larger cation to exhibit potential mobility, enabling relaxation to be more efficient (faster T_1s).

The relaxation behaviour for the lower-R cesium borate glasses seem largely dependent upon the structure of the borate network, as these are highly polymerized with $^{[4]}$B and display little to no cesium concentration dependence. Placed in the context of these two anionic species ($^{[4]}$B and NBO) and the Barrier Height Distribution (BHD) model[145,165-167], the lower-R glasses would seem to have deeper potential wells, whereas the higher-R glasses are characterized by shallower wells. These lower-R glasses require higher temperatures (>100^{o}C) for the relaxation times to decrease drastically (i.e., increase mobility, cage rattling, etc.). With regards to the lithium and cesium borate network, a plausible difference in the motion mechanism may occur. We could suggest that percolation channels for cesium borates, where localized negative charges on NBO species (creating channels) are required for cesium

mobility. Conversely, the smaller lithium cation becomes mobile as soon as sufficient charge-bearing species ($^{[4]}$B) are present. Although studies at elevated temperatures (>150^{o}C) would be required to prove this, it seems reasonable to propose percolation (as seen in silicates), which only contains NBOs (Q^3, Q^2, etc.) as their anionic units.[156]

3.3.5.3. Probing Medium Range Order and Dynamics

Variable temperature REDOR measurements can provide information about slow mobility. REDOR is also site-specific ($^{[3]}$B and $^{[4]}$B) unlike the global T_1 measurements. This provides us with a tool to probe the location and nature of the Cs-B interactions as a function of temperature and cesium loading. The R=0.1 glass possesses 13 % $^{[4]}$B and 0 % NBO units. This is reflected in the REDOR results (Figure 3.21), where a stronger interaction is seen for the $^{[4]}$B species that has the negative charge delocalized over the boron unit. Since the overall interaction decreases as temperature increases, one can see that mobility causes the decrease in the dipolar interaction. As the cesium content increases (R=0.5), the concentration of NBO (~10%) increase and a significant amount of $^{[4]}$B (40%) makes it difficult to differentiate which boron species are preferentially interacting. Both the Cs-$^{[3]}$B and Cs-$^{[4]}$B average dipolar interaction seem to increase with increasing temperature. The slight increase in the average dipolar interaction could be attributed to the increased polymerization, actually preventing cesium mobility.

The R=0.7 glass shows some interesting behaviour, which could be caused by the formation of multiple charged species, bearing many NBOs. T^2 species comprise 34 % of the $^{[3]}$B in the glass and have the strongest cesium interaction, as they are more dephased than $^{[4]}$B (which are at 36 %). This stronger interaction is caused by

the high amounts of cesium present within the glass, causing an overall stronger Cs-B average dipolar coupling. Additionally, there is a potential for shorter Cs-B internuclear distances, as seen in minerals[130,168] and borosilicates[169] where NBO-Cs^+ interactions are smaller than Cs-$^{[4]}$B. This can be explained using simple attraction/repulsion arguments, where a localized negative charge should interact more strongly than a delocalized charge ($^{[4]}$B), as the electrostatic interactions will be stronger. Both $^{[3]}$B and $^{[4]}$B REDOR curves (CsB, R=0.7) show a decrease in average dipolar coupling with increasing sample temperature, which may suggest the onset of cesium mobility, either as hopping or rattling.

The R = 0.9 cesium borate glass contains an excessive amount of modifier (almost 50 mol% cesium oxide), creating a scenario where almost every boron has a cesium associated with it. This large loading causes both $^{[3]}$B and $^{[4]}$B species to essentially have the same Cs-B interaction. The overall trend however is a decreased dipolar coupling with an increase in temperature. Boron speciation for this glass quickly reveals why one achieves this result, as it contains ~10% T^3, ~58% T^2 and ~32% $^{[4]}$B, assuming no T^1 units are present, although a few may exist.[93] As Cs^+ can interact with potentially up to three negatively charged polyhedra ($^{[4]}$B, T^2 and T^1), differentiating between these sites can no longer be simply explained.

3.3.6. SUMMARY

Spin-lattice and spin-spin relaxation measurements for three lithium borates glasses provided evidence for lithium mobility in all three cases over an extended temperature range. Although T_1 minima could not be obtained, estimates of the activation energies for these species were achieved from T_2* measurements to be on

the order of 40 to 50 kJ/mol, comparable to other lithium borate materials of this nature. Two variables, lithium concentration and working temperature, can be adjusted in order to optimize a lithium dynamic behaviour for possible applications such as solid ionic-conducting materials. The heavier cesium borate glasses also exhibited decreases in T_1 as heating temperature increased. The high-R cesium and lithium glasses showed appreciable decrease in T_1 over the lower-R glasses. These results appear to show alkali dynamics (at elevated temperatures, ~100°C) for both alkali metals, however for the larger cesium cation effects could be attributed to simple cage rattling.

To probe this further, REDOR is implemented as a slow dynamic experiment for the cesium cation. $^{11}B\{^{133}Cs\}$ indicated a decrease in dipolar coupling as temperature increased. This suggests some type of slow cesium mobility, either by cage rattling or alkali hopping/percolation. Variable temperature REDOR was a successful measure for site-specific mobility, whereas T_1 measurements in glasses display global averages in cation dynamics. The concentration of cesium (R > 0.7) is too high to allow one to distinguish between $^{[3]}B$ and $^{[4]}B$ dephasing curves, as they overlap and prevent us from commenting on the small changes measured with increasing temperature. The increase in cesium concentration appears to decrease the energy required for cation mobility. In regards to how this would relate to long-term storage of waste materials; the actual cesium concentration is much lower (~1 to 4 %) but a variety of other cations (mixed) are present, creating a similar high cation environment. Furthermore, higher sample temperatures have to be contended with (200 and 300°C) over extended periods of time suggesting that some concern is

warranted. As well large efforts are currently being investigated to enable higher waste loadings in glasses, which would increase the alkali concentration even further.

4. Borovanadates

Current cathode materials designed for a variety of applications involve $LiCoO_2$ or some modification of this material.[170] $LiCoO_2$ is the chosen material for a variety of battery based applications because of its good cycling ability, stability, long lifetimes and high energy density.[171] However, certain limitations exist, including cobalt being a heavier element, difficult to recycle (or reprocess) and there are issues regarding its long-term cycling ability.[170,171] Possible alternatives are vanadium-containing materials such as lithium metavanadate ($LiVO_3$). $LiVO_3$ has good conductivity and the onset of local disorder within the crystal structure causes an increase in conductivity, believed to be caused by VO_4 distortion.[172] This association of disorder with increased conductivity has led to the development and characterization of ionic conducting glasses.

Another modification that should be considered involves the incorporation of V_2O_5, a poor glass former, into B_2O_3 which is a good glass former, potentially enabling a new generation of lighter weight, better cycling and optimized cathode materials that vitrify more easily. Amorphous borovanadate materials have received attention for their electrical properties.[173-179] As these cathode materials require high current density, research into lithium-based crystalline[180-183] and polymer composites[184,185] has also received much attention for battery based applications (i.e., as a solid electrolyte medium), unlike traditional $LiCoO_2$ materials.[186,187] Lithium-borate-based materials are also prominent cathode sources.[188,189] Although the properties of these

systems are understood, the local structure that causes these properties is poorly characterized. Lithium and cesium borovanadates were studied using ^{11}B and ^{51}V MAS NMR to better understand the local speciation, while ^{7}Li and ^{133}Cs dynamics was studied using two-dimensional exchange spectroscopy.

4.1. Lithium Borovanadates

The foundation for binary borate systems will be extended in this chapter, as the glass systems will incorporate a second glass-forming oxide. B_2O_3 can be easily modified with network modifiers, while maintaining its glass forming ability. The ability to incorporate a third component (V_2O_5) will produce a ternary glass with added complexity. The behaviour of the boron environment is of interest when vanadium is added. With regard to vanadium, the interest lies in the coordination environment, crystallization and charge sharing with boron.[90,106,190,191]

Crystalline V_2O_5 comprises edge- and corner-sharing five-coordinate species in a distorted square-pyramidal ($^{[5]}V$) structure.[192] V_2O_5 by itself is rather difficult to vitrify, although we have been able to do so with careful roller quenching. However, incorporation with a good network-former (i.e., B_2O_3) alleviates the onset of crystallization.[193] As a borovanadate, the system would be composed of bridging oxygens in a fully polymerized environment. As charge build-up occurs from alkali oxide loading, the framework will need to compensate for this charge by forming four-coordinate boron (pseudo-tetrahedral) species. As for the vanadium unit, the coordination number should decrease, forming four-coordinate VO_4 units, where three oxygens can participate as BOs while one oxygen is doubly bound (Figure

1.5).[194] In regard to connectivity, three different bridging oxygen types are expected; B-O-B, V-O-V and V-O-B, assuming homogeneous mixing. Any medium-range order observed in borates and vanadates, such as boroxol rings and vanadate chains, has been shown to break down upon formation of borovanadate glasses, and such order is not expected to form in considerable concentrations for these materials.[178,179]

The structural variations that occur between the three series designated by the parameter K ($K = V_2O_5/B_2O_3$) ranging from 0.2 to 0.6, with a range of lithium concentrations, R ($R = Li_2O/B_2O_3$) between 0 and 2.2 (16.6 to 68.8 mol % of Li_2O), will be discussed below. We have studied the effects on both network forming and modifying cations using solid-state NMR.

4.1.1. Materials and Methods

4.1.1.1. Synthesis

Glasses were synthesized from commercial grade vanadium oxide (V_2O_5), boric acid (H_3BO_3) and lithium carbonate (Li_2CO_3). B_2O_3 was synthesized by dehydrating boric acid by heating to 650°C. Stochiometric quantities of V_2O_5, B_2O_3 and Li_2CO_3 were ground together in an agate mortar and pestle, then placed in a platinum crucible and heated between 800 and 1000°C for 20 minutes, where decarbonation of Li_2CO_3 to Li_2O occurred. These are then weighed to verify decarbonation was completed. A second heat treatment was performed at 1000°C, held for 5 minutes to ensure a homogeneous melt, and quenched using a metal plate or roller-quencher. Plate quench involves pouring the melt onto a large steel plate, followed by dropping a second large metal plate. This cools the glass quickly and is often used for glasses that

are more difficult to quench. Roller quenching is used for difficult glass forming compositions, i.e., those that do not want to vitrify, high-R and high-K glasses. This device uses two cylinders that spin with a narrow gap (25 microns for these glasses, but can be adjusted) where the melt is poured and cooled very quickly. As these glasses need special handling and processing; they were supplied by Dr. Steve Feller and Dr. Mario Affatigato from Coe College, Cedar Rapids, Iowa.

4.1.1.2. Nuclear Magnetic Resonance

4.1.1.2.1. Boron-11 MAS NMR

^{11}B MAS NMR spectra were acquired using a 3.2 mm double-resonance T3 MAS probe (Varian-Chemagnetics) on a Varian ^{UNITY}INOVA 600 (14.1 T) spectrometer operating at 192.4 MHz. A single-pulse experiment using a short tip angle (0.5 μs, *ca.* 9°) and a spinning rate of 16,000 ± 2 Hz was used to minimize errors in quantification. Final integrated intensities were corrected to obtain central-transition intensities as described by Massiot *et al.* [195] ^{11}B 3QMAS of the R = 1.8, K = 0.2 lithium borovanadate was acquired using a shifted-echo MQMAS sequence with a FAM-1 conversion pulse. The ν_{rf} nutation frequency for the excitation (5 μs) and conversion pulses (1.7 μs, 1 loop) was *ca.* 155 kHz. The soft central-transition selective π-pulse was 20 μs in duration. Simulation were done under the approximation of infinite spinning speed, using WSolids.[196] Spectra were referenced with 0.1 M boric acid at 19.6 ppm as a secondary reference to $BF_3 \bullet Et_2O$ (0.0 ppm).

4.1.1.2.2. VANADIUM-51 MAS NMR

^{51}V MAS NMR spectra were acquired using the same 3.2 mm double resonance probe and spectrometer operating at 157.8 MHz. Experiments were carried out at MAS rates of 20,000 – 23,000 ± 5 Hz, using a rotor-synchronized Hahn-echo (υ_{rf} of 50 kHz) or Bloch sequence. ^{51}V MAS NMR spectra were also acquired using a 2.5 mm double resonance MAS probe (Bruker) on a 900 MHz Bruker Avance II spectrometer (21.1 T) operating at 236.7 MHz. A Bloch sequence with a spinning rate of 30,000 ± 5 Hz and a pulse of 0.5 μs (20° tip angle) was used to examine four of the higher-R, K=0.2 glasses. Spectra were referenced with respect to 0.16 M $NaVO_3$ (-574 ppm).

4.1.1.2.3. LITHIUM-7 MAS NMR

^{7}Li MAS NMR spectra were collected using a 3.2 mm double resonance MAS probe operating at 233.1 MHz (14.1 T). Bloch pulse experiments were acquired using between 16 and 64 co-added transients, spinning rates of 6,000 ± 1 to 20,000 ± 5 Hz and recycle delays of 3 to 5 s. EXSY experiments were acquired using 3 μs solid 90's (ν_{rf} of 67 kHz), mixing times between 2 μs and 500 μs and with sample temperatures between 273 and 343 K. Recycle delays of 5 seconds, spinning rate of 20,000 ± 5 Hz, 16 co-added transients and 256 increments were implemented for all experiments. Shifts were referenced to 1 M LiCl (0.0 ppm).

4.1.2. Results

4.1.2.1. Boron-11 MAS NMR

4.1.2.1.1. K=0.2

The ^{11}B MAS NMR spectra for the K=0.2 series are displayed in Figure 4.1. These six samples show a $^{[3]}$B resonance that exhibits a lineshape characteristic of an asymmetry parameter near that of axial symmetry ($\eta \approx 0$), suggesting the majority of $^{[3]}$B have T^3 local structure. The resonance is similar to that observed in other borate glasses, suggesting the $^{[3]}$B is mainly composed of $^{[3]}$B non-ring species. The increase in lithium concentration does cause a very slight shift of the $^{[3]}$B edge (R>1.8) accompanied by a slight change in lineshape reminiscent of an asymmetry parameter, η>0.5, suggesting the onset of NBOs (T^2).[9,197] Analysis of the $^{[4]}$B population with lithium content shows a near-linear increase in population, even at low-R (Figure 4.1). When comparing these data to alkali borates, they show a slower increase in the fraction of $^{[4]}$B and a higher maximum in the fraction of four-coordinate boron.[106] Alkali borosilicates have also shown similar increases of $^{[4]}$B, reaching an N_4 of 0.60 at R=0.7 and K=0.2.[198] These ternary lithium borovanadates reach a maximum N_4 of 0.5 at R=1.0 for the K=0.2 lithium borovanadate.

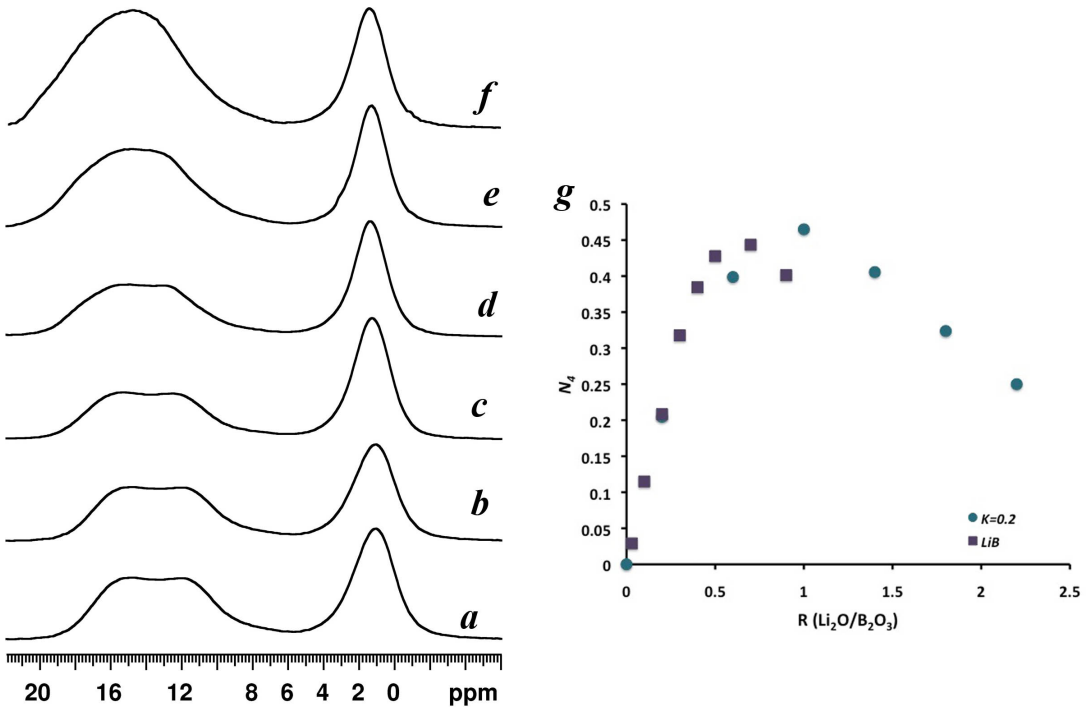

Figure 4.1. ^{11}B MAS NMR spectra of LiBV glasses, (a) R=0.2, (b) R=0.6, (c) R=1, (d) R=1.4, (e) R=1.8 and (f) R=2.2 and (g) fraction of $^{[4]}$B for LiBV (K=0.2) and for pure LiB (K=0.0) glasses.

The four-coordinate resonance located between -1 and +4 ppm exhibits a slightly asymmetric resonance for K=0.2 and R=0.2 (although symmetric for the rest of the K=0.2 glasses), this leads to some suggestion of two sites (~+3 and +1 ppm), indicating some secondary, medium-range order. In addition, the higher loaded glasses show that the $^{[4]}$B linewidth decreases from 600 Hz (R=0.2) to 400 Hz (R=1.4), beyond which a plateau occurs. The chemical shift of this resonance also changes with the associated narrowing, going to higher frequency from 0.8 to 1.4 ppm. This is suggestive of changes in the local symmetry around $^{[4]}$B, that is we speculate two different $^{[4]}$B sites are present at low lithium loadings. An alternative explanation for

the narrowing of the [4]B site is that the variation of [4]B polyhedra becomes less random (i.e., more symmetric environment) as the glass depolymerizes. If the C_Q decreases (as the EFG is sensitive to local structural changes) for the [4]B, this would indicate an increase in local order. As multiple sites are not resolved for K=0.2 glasses it is difficult to conclude further on these results.

4.1.2.1.2. BORON-11 MQMAS

^{11}B 3QMAS of the R=1.8 glass exhibits a very slight asymmetric lineshape in the isotropic dimension (Figure 4.2). The peak position spans 74 - 92 ppm and is characteristic of T^3, T^2 (single NBO) and T^1 (two NBOs) species in borates.[85] The resolution of multiple sites is lacking from the isotropic projection, causing difficulties in determining percentages of NBO species. This is typically seen in high-R lithium borate glasses and is attributed to lithium exhibiting more disorder and lower percentages of NBOs (preference for [4]B) within this glass.[93]

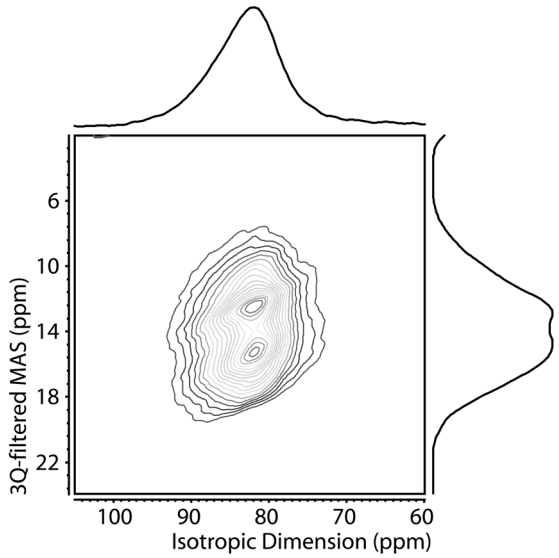

Figure 4.2. ^{11}B 3QMAS NMR for K=0.2, R=1.8 lithium borovanadate glass, suggestive of NBO formation due to asymmetry of the isotropic spectrum.

4.1.2.1.3. LiBV K=0.4 and K=0.6 series

^{11}B MAS NMR spectra for the glasses with K=0.4 and 0.6 (Figure 4.3) show similar behaviour with the onset of $^{[4]}$B forming as R increases. The $^{[3]}$B lineshape does not change throughout the whole series however, indicating that NBOs do not form within the higher vanadia glasses. This is explained by the ability of vanadium to charge-compensate the excess lithium cation charge. Since K=0.4 and 0.6 have double and triple the vanadium concentration, this decreases the need for NBOs on boron. Vanadia in these glasses becomes a major charge compensating oxide, alleviating the need for $^{[3]}$B to depolymerize to species that contain NBOs. The $^{[4]}$B resonance shows a slight asymmetry for compositions R ≤ 0.4 indicative of medium-range order as seen and suggested above. The asymmetric $^{[4]}$B resonance becomes more symmetric and narrows as R is increased, indicating a single $^{[4]}$B site as the glass is depolymerized.

The vanadia concentration seems to affect the population of $^{[4]}$B slightly. This is shown in Figure 4.3, where the $^{[4]}$B maximum is reached at a higher-R composition for elevated K-values (0.4 and 0.6). The three K series have a near-linear behaviour from R=0.2 to 1.2 (1.0 for K=0.2). This behaviour agrees with the changes occurring in the $^{[3]}$B peak shape for K=0.2 (onset of NBOs on boron). The cause of the higher N_4 for K=0.4 and K=0.6 (see below) is the excess vanadium. Higher vanadium concentrations aid in the charge balance and inhibit $^{[4]}$B neighbours (avoidance), allowing higher N_4 as seen in borosilicates.[8,199,200]

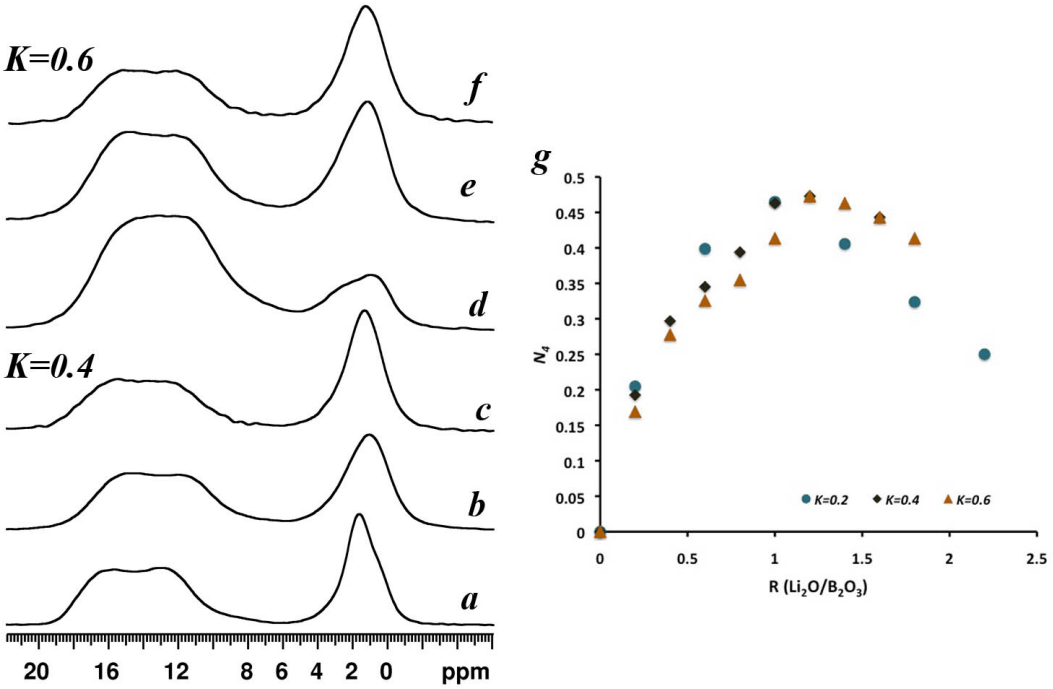

Figure 4.3. ^{11}B MAS NMR of lithium borovanadate glasses (a-c) K=0.4 and (d-f) K=0.6 with alkali loadings of (a,d) R=0.2, (b,e) R=0.8 and (c,f) R=1.6 and (g) N_4 measured from ^{11}B MAS NMR data as R and K increase.

4.1.2.2. VANADIUM-51 MAS NMR

4.1.2.2.1. K=0.2

The ^{51}V (N.A.= 99.75 %, I = 7/2 & Q = -5.2 fm^2) MAS NMR spectra of glasses generally consist of very broad resonances with extensive sideband manifolds. The severe broadening of the CT and ssbs is due to the polarisability of vanadium as the chemical shift for vanadium is very sensitive to changes in bond angle and bond length distortions.[201] These interactions cause the spectra to be complex as the polarisability of vanadium produces broad central transitions. This is alleviated by using fast magic

angle spinning, which is crucial for acquisition of ^{51}V MAS NMR in glasses. The K=0.2 vanadate glasses exhibited linewidths (FWHM) from 5 to 25 kHz (30 to 160 ppm), with the linewidth decreasing as the lithium concentrations increased. The δ_{cgs} also increased to higher frequency as the lithium oxide concentration increased, indicating the onset of depolymerisation, i.e., $^{[5]}V$ breaking down to $^{[4]}V$ (Figure 4.4). This conclusion is based on similar trends seen in crystalline vanadates, where a shift to higher frequency occurs as the $VOO_{3/2}$ (one doubly bound oxygen and three bridging oxygen) polyhedra breaks down into NBOs.[4,202,203]

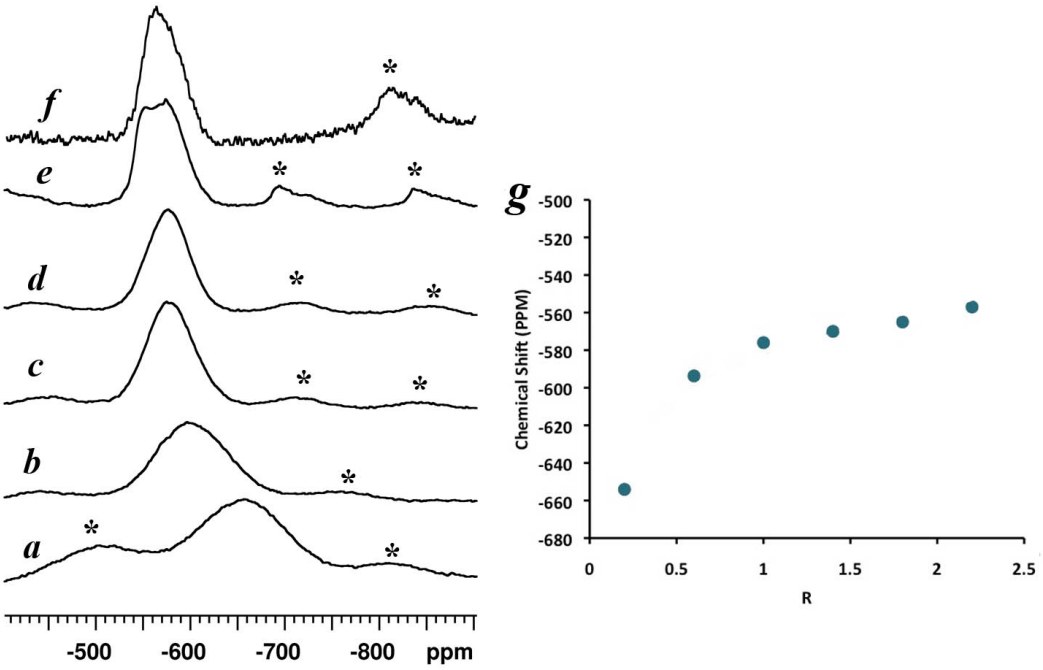

Figure 4.4. ^{51}V MAS NMR of LiBV K=0.2, (a) R=0.2, (b) R=0.6, (c) R=1, (d) R=1.4, (e) R=1.8 and (f) R=2.2 and (g) chemical shifts (δ_{cgs}) measured as R increases. The "*" represent spinning side bands.

It is difficult to extract the quadrupolar parameters from the CT lineshape because ^{51}V has a small quadrupole frequency, υ_Q (where, $\upsilon_Q = 3C_Q/2I(2I-1)$) with

respect to the Larmor frequency and the distribution of parameters inherent in disorder. We obtain estimates of the quadrupole coupling constants using the extent of the ssbs as was done in previous cases for lithium and cesium above. The quadrupolar couplings for the R = 0.6, 1.0 and 1.8 were found to be similar, C_Q = 2.1 ± 0.2 MHz. This indicates that vanadium has a similar EFG throughout the lithium-loading regime. However, the central transition narrows (Figure 4.4) which can be explained by the higher symmetry of the pseudo-tetrahedral environment decreasing the chemical shift distribution. The exception to this is the R=0.2 species which exhibits a larger quadrupolar coupling constant of 3.2 ± 0.4 MHz, due to a different vanadium environment ($^{[5]}$V) at low-R. Nutation experiments, higher field ^{51}V MAS NMR measurements and acquiring vitreous V_2O_5 and vitreous $5B_2O_3$•V_2O_5 provide strong evidence that multiple sites (in quantities > 15%) do not exist. The resonance resembles that seen in *v*-V_2O_5 and is therefore assigned to a $^{[5]}$V unit.

The narrowing at higher loading (K=0.2 and R=2.2) enabled multiple sites (~-547 and ~-580 ppm) to be observed (Figure 4.4). These two resonances were studied further due to the smaller C_Q of one of the sites determined from the extent of the spinning sideband manifold. A nutation array was acquired to better resolve the two vanadium resonances. The nutation behaviour of these two sites was probed by an array of experiments with variable excitation pulse lengths. This is a valuable experiment when two vanadium sites have different quadrupolar interactions as each will have an optimal pulse length as demonstrated earlier for ^{11}B.[204] A longer pulse caused a larger signal intensity for the lower frequency resonance, suggesting a smaller quadrupolar interaction (i.e., < 2.2 MHz).

In an effort to achieve better spectral resolution and further narrowing of the second-order quadrupolar lineshape, higher-field studies were attempted. The ultrahigh field spectrometer (21 T) was used to collect ^{51}V MAS NMR spectra for R=0.6, 1.0, 1.4 and 1.8 samples. Unfortunately, ^{51}V chemical shielding is very sensitive to local structural variations and scales linearly with magnetic field. Since these are disordered, the peak widths reflect inhomogeneous broadening caused by slight variations in bond length and bond angle for each VO_4 polyhedron as vanadium is quite polarisable. In order to obtain comparable resolution at higher field, 32 kHz MAS was required to separate the ssbs from the CT. The high-field ^{51}V data (Figure 4.5) show that a second site exists for borovanadate glasses R= 1.0, 1.4 and 1.8. The higher frequency site can be attributed to a crystalline impurity, which was identified as Li_3VO_4 by chemical shift and powder x-ray diffraction.

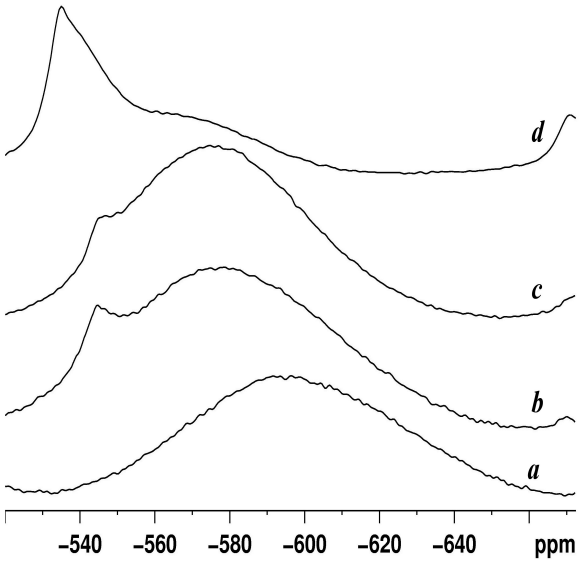

Figure 4.5. ^{51}V MAS NMR ultrahigh field (21 T) for LiBV glasses K=0.2, (a) R=0.6, (b) R=1.0, (c) R=1.4 and (d) R=1.8. The sharper (higher frequency) resonance observed in b-d was determined to be a crystalline impurity of Li_3VO_4.

4.1.2.2.2. K=0.4 & 0.6

The ^{51}V MAS NMR for K=0.4 and 0.6 reveals similar chemical shifts, lineshapes and quadrupolar information as discussed for the K=0.2 glasses. A steady shift from -650 ppm to -550 ppm occurs as R increases, although higher alkali content is required to obtain the same degree of shift as K increases (Figure 4.6). The overall lineshape remains symmetric and decreases in breadth as lithium becomes more prominent. The vanadia concentrations decrease the glass forming region due to the onset of crystallization occurring above R=1.2 (K=0.6) versus R=1.8 (K=0.2).

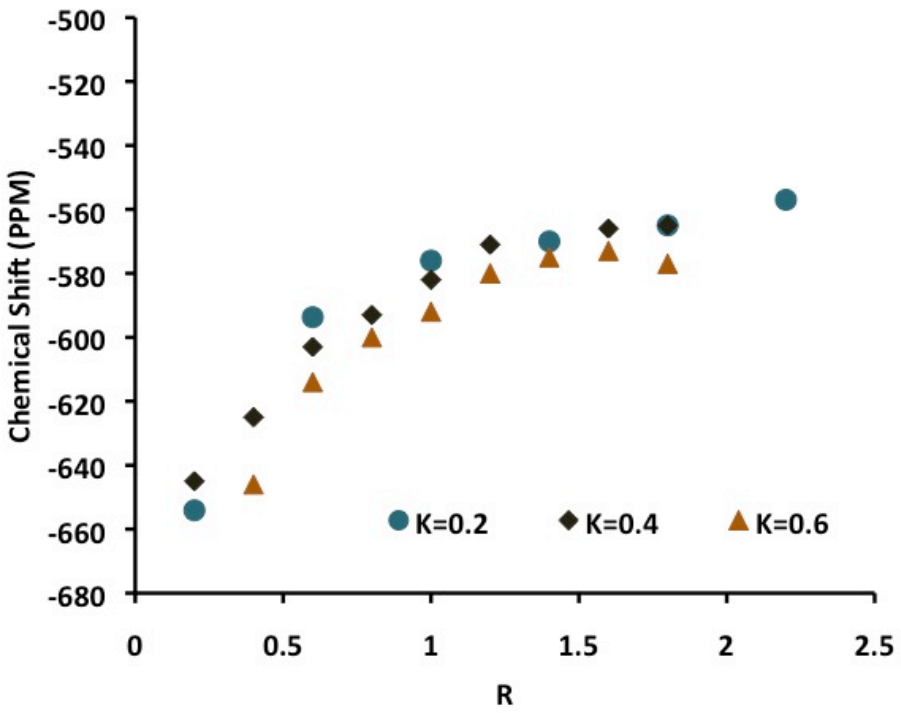

Figure 4.6. ^{51}V MAS NMR δ_{cgs} for lithium borovanadate glasses of K=0.2, 0.4 and 0.6.

4.1.2.3. LITHIUM-7 MAS NMR

^{7}Li MAS NMR reveals characteristic oxide resonances with quadrupolar coupling constants of 160 ± 30 kHz, as determined from the ssb manifold, and FWHM of ~4 ppm (~1000 Hz). The δ_{cgs} were used as isotropic shifts (due to the small SOQE), showing a shift to higher frequency as R increases (as seen in Chapter 3). T_2* were probed by varying the temperature between 15 and 65°C. Linewidths were found to decrease as the temperature increased, which can be attributed to lithium mobility.

Lithium dynamics were studied using exchange spectroscopy on two K=0.2 (R=0.2 and R=2.2) and three K=0.4 (R=0.4, 0.8 and 1.6) glasses. Due to crystallization in the K=0.2, R=2.2 glass, this sample was re-synthesized. This sample was hand

separated into crystalline and vitreous components using a microscope to eliminate crystalline contamination for the EXSY experiment. EXSY revealed dephasing for all compositions at elevated temperatures. Figure 4.7 depicts selected experiments illustrating that cooling the samples and acquiring with the same mixing time for low-R borovanadates show little mixing (a and c) while higher Li-content glasses dephase quickly (b, e, d and f). This can potentially be attributed to lithium hopping (site exchange) during the mixing time.

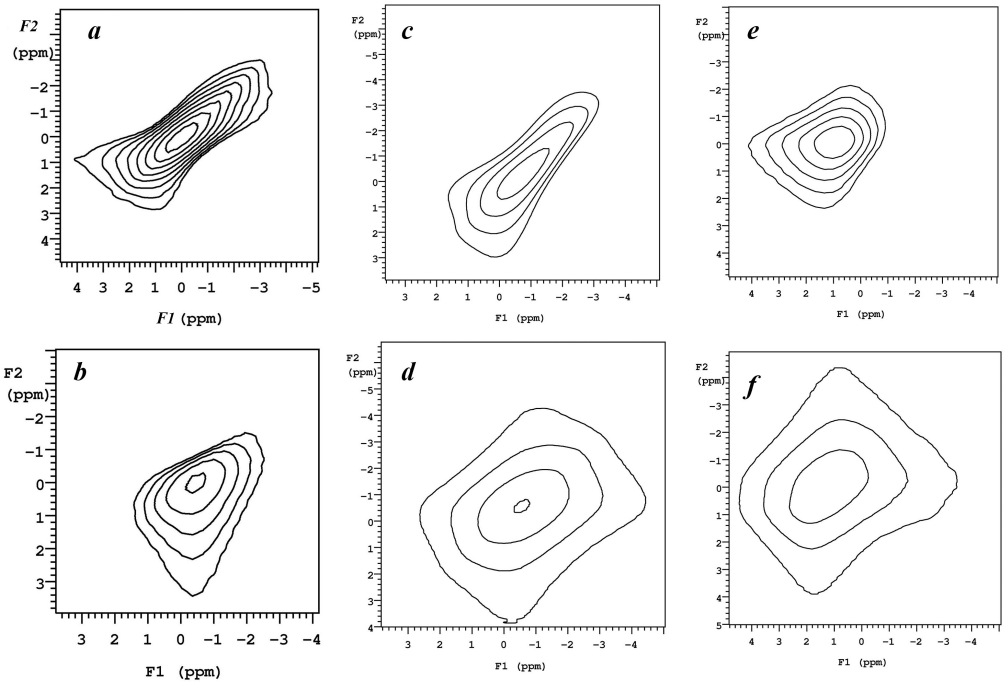

Figure 4.7. ^{7}Li MAS NMR EXSY spectra for select lithium borovanadate glasses. (a and b)R=0.2, K=0.2 at 22 ^{o}C with a mixing time of 2μs and 26ms, respectively, (c) R=K=0.4 (15^{o}C), (d) K=0.4, R=0.8 (15^{o}C), (e) K=0.2, R=2.2 (22^{o}C) and (f) K=0.4, R=1.6 (15^{o}C). Spectra c to f have mixing times of 52 μs.

4.1.3. Discussion

4.1.3.1. Boron speciation

The fraction of four-coordinate boron (0 up to 68.8 mol % lithium oxide), is consistent with the behaviour of other binary and ternary borate-based systems.[2,8,85,86,90,93,119,205] Traditionally, $^{[4]}$B is the only charge-balancing polyhedron until Li_2O loadings reach a point where the probability of $^{[4]}$B-O-$^{[4]}$B is too high, thus causing the formation of NBOs on $^{[3]}$B (i.e., avoidance of $^{[4]}$B neighbouring $^{[4]}$B polyhedron due to the unfavourable build-up of charge). T^2-O-$^{[4]}$B is more favourable than $^{[4]}$B-O-$^{[4]}$B because the negative charge is localized on the oxygen and not on a neighbouring boron, (as is the case with $^{[4]}$B). This allows good separation between the negative charge on the $^{[4]}$B and the one localized on the oxygen. These vanadates show slightly different behaviour, where the vanadium is also contributing in the charge balance by forming NBOs. This enables the maximum of N_4 to occur at higher lithium loadings. The $^{[3]}$B lineshapes and position indicate non-bridging oxygens are formed in the high R, K=0.2 series although this is not the case for K=0.4 and K=0.6. The excess vanadia alleviates the need for NBOs to form on boron. The charge balance behaviour responsible for the trends above is believed to occur due to the similar electronegativities vanadium and boron have per polyhedra building block, sharing charge-compensation.[10,177-179] Borovanadates do not show significant increases in N_4 as K increases, unlike borosilicates.[199] A reasonable explanation for this difference is the ability to share charge, resulting in comparable maxima of N_4. This is further confirmed as vanadium concentration increases, it requires more lithium to reach a similar maximum in N_4. Borosilicates however, cause the boron to contain sole charge balance responsibilities

until a limit is reached and onset of silicate Q^3 occurs.[2,199,205] Binary borate data have a maximum of $N_4 \approx 0.48$, reached at R=0.48. Borovanadates allow $N_4 \sim 0.5$, with a lithium loading of R=1; vanadium effectively doubles the loading limit in $^{[4]}$B formation (Figure 4.1).[198,206] For borosilicates we can estimate the fraction of $^{[4]}$B at a composition of K=0.2 to 0.6 and R=1 to be ~30% (K=0.2) to 45% (K=0.6). Therefore, vanadates enable 5 to 20 % higher concentrations of N_4 than borosilicates. Again this is explained by borovanadates sharing the charge equally between boron and vanadium, allowing for a maximum N_4 to be reached at higher-R loading. Borosilicates on the other hand do not share the charge, thus causing $^{[4]}$B to reach a maximum sooner (lower-R) then breaking down forming NBOs on boron and silicon as alkali loading increases.

The asymmetry present at the $^{[4]}$B resonance is caused by different neighbours (V or B polyhedra) attached to the $^{[4]}$B. This is seen in low-R lithium borovanadates. Similar effects are seen for borates and borosilicates containing sodium to cesium cations and are not typically seen for lithium based glasses, making this a rather unusual system. Further discussion of these assignments will be made in section 4.2, *vide infra*.

4.1.3.2. Crystalline Lithium Vanadates

This is the first study to apply ^{51}V MAS NMR to borovanadate glasses. In order to understand what is occurring within the vanadium polyhedra, a chemical shift 'finger-print' and quadrupolar parameters were required. Although crystalline Li-B-V phases are unknown, two binary Li-V crystalline phases are known to exist. Therefore *c*-V_2O_5, $LiVO_3$ and Li_3VO_4[13,203,207] were acquired and compared to literature values (Figure

4.8). Crystalline V_2O_5 is orthorhombic and comprises VO_5 polyhedra that are square pyramidal in structure and connected via edge- and corner-sharing, creating V_2O_5 sheets. These sheets are connected by weak V-O interactions, where the doubly bound oxygen interacts with the vanadium above it (sitting underneath the square pyramid section).[208] Lithium addition to V_2O_5 in a 1 : 1 ratio forms the metavanadate ($LiVO_3$) which has VO_4^{-1} polyhedra. The VO_4 polyhedra are chain-linked end-to-end while the middle oxygen is a NBO coordinated to Li^+. The lithium cations are six-coordinate octahedra surrounded by oxygens that are bridged to V.[209] Lithium orthovanadate (Li_3VO_4) is orthorhombic and has vanadium in a distorted tetrahedron. The VO_4 units contain three non-bridging oxygens (Q^0) coordinated to Li^+ with a doubly-bound oxygen.[210] The parameters in Table 4.1, provide guidelines for interpreting the glassy ^{51}V MAS NMR spectra.

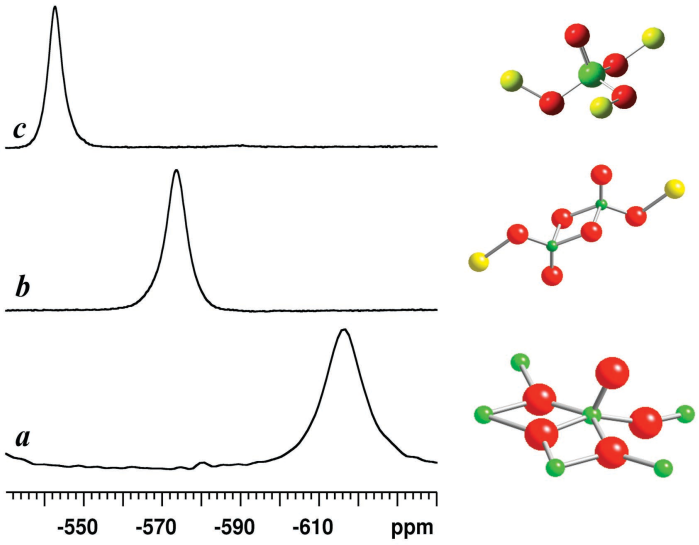

Figure 4.8. ^{51}V MAS NMR of (a) *c*-V_2O_5, (b) $LiVO_3$ and (c) Li_3VO_4, where V (green), O (red) and Li (yellow).

Table 4.1. ^{51}V MAS NMR parameters for select crystalline lithium vanadates[79,207,211]

Crystals	δ_{Iso} (ppm)	C_Q (MHz)
V_2O_5	-610	0.8
$LiVO_3$	-573	3.18
Li_3VO_4	-544	1.52

4.1.3.3. Vanadium speciation

^{51}V MAS NMR is extremely sensitive to its environment, with changes occurring in shift, lineshape and breadth from both CSA and C_Q interactions.[202,207] The linewidths of these borovanadate glasses narrowed as the concentration of lithium increased. Based on the shifts, we can describe the vanadate network as originally structured like *v*-V_2O_5, with a square pyramidal geometry (large CSA interaction) that breaks down into pseudo-tetrahedral meta- and ortho-vanadates due to higher local symmetry (decreasing CSA and C_Q). The shifts in the glasses mirror the modeled crystalline lithium vanadates. The depolymerisation occurring in the vanadium species involves the formation of NBOs on VO_4 units as they break down from $^{[5]}V$ to $^{[4]}V$. This trend is commonly seen in other network formers and modifiers where a decrease in the mean cation-oxygen bond length occurs (i.e., coordination number decrease is related to a shift to higher frequency).[9,13,90,131-133,135,212]

The high-field ^{51}V MAS NMR data revealed a second site for R > 0.6 borovanadates (K=0.2), Figure 4.5 illustrating the sensitivity of higher fields. The peak at higher frequency (~ -544 ± 5 ppm, Li_3VO_4) seems to be in a higher local symmetry

environment (smaller C_Q) than the lower frequency resonance (~ -580 ± 10 ppm, larger C_Q).

The ^{51}V chemical shifts (δ_{cgs}) for all three series eventually reach a plateau at higher lithium loadings (Figure 4.6). This plateau occurs because the vanadium polyhedra possess the maximum number of NBOs, based on composition with the chemical shift of Q^0 in lithium orthovanadate.[201,203,207] ^{51}V chemical shift is sensitive to the number of NBOs on a given VO_4 polyhedron, as NBOs cause a shift to higher frequency, as observed here.[13,177,179,203,207] This relationship is a valuable tool for differentiating speciation in vanadate glasses.

At higher temperatures, redox reactions can occur, bringing into question whether some fraction of the vanadium is present in a paramagnetic state (e.g., V^{4+}), as has been suggested in the literature V^{4+}.[10,175] The strong electron-nucleus interaction can have multiple implications in NMR. The paramagnetic V^{3+} or V^{4+} species would not be physically observable by NMR (this would require EPR). If a significant amount of $V^{3+/4+}$ were present, one could expect significant paramagnetic broadening.[13] To verify that the dominant interactions on the CT are chemical shielding distribution and C_Q, and not paramagnetic broadening, bulk magnetic susceptibility measurements were performed. All six glasses (K=0.2) and two crystalline vanadate species ($NaVO_3$ (diamagnetic) & NH_4VO_3 (paramagnetic), >99.9 % pure) were studied. The results were consistent with previous work by Tian et al.[175] who used electron spin resonance on lithium and sodium borovanadates to measure the concentration of V^{4+} to be < 1%. Our measurements show that the samples are diamagnetic, with no measurable paramagnetic vanadium contribution. These results

are also consistent with the spin-lattice relaxation times observed within these glasses (5 to 15 s), whereas other paramagnetic vanadium systems studied by our group and others have spin-lattice relaxation times on the order of a few hundred ms.[213-216] Furthermore the visual colour of these glasses varied from a brown-yellow to a white colour. Although this does not specifically indicate paramagnetics as a variety of diamagnetic crystalline vanadates are yellow to white in colour, we did consider this.

4.1.3.4. Charge Balance Calculations

Quantification of species can often be confirmed by charge-balance calculations. As shown in Figure 4.9, N_4 reaches a maximum at approximately the same point as the vanadates reach the shift range for Q^1. If we assume that the borate network only forms the $^{[4]}B$ species, and that the associated vanadate network can be determined as Q^1, Q^2 or Q^3, based on their respective chemical shifts (δ_{cgs}), we can determine the number of NBOs expected to occur in the borate matrix. In other words, summing the number of negative charges on $^{[4]}B$ and vanadium, and subtracting this from the total lithium concentration provides an estimate of NBOs on $^{[3]}B$ (Table 4.2). This charge-balance model enables us to estimate whether and to what extent NBOs on boron are likely to exist.

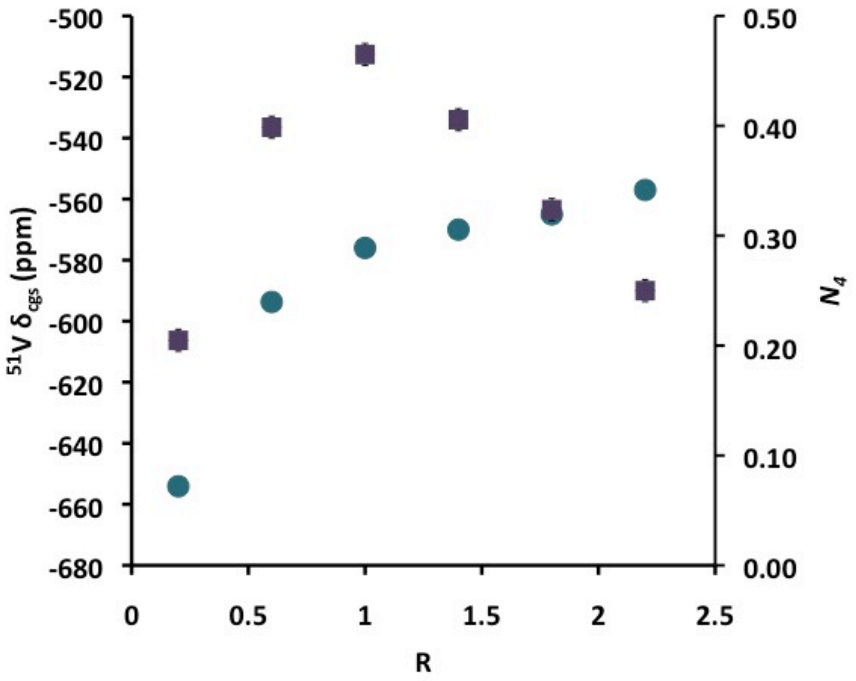

Figure 4.9. Fraction of $^{[4]}B$ (square) determined from ^{11}B MAS NMR and its relation to ^{51}V MAS NMR δ_{cgs} (circle) for lithium borovanadate K=0.2 glass.

Table 4.2. Charge balance calculations for borovanadate glasses.

LiBV	Li Charge	$^{[4]}$B Charge	V Charge/unit	V Species	$^{[3]}$B Charge/unit	$^{[3]}$B Species
K=0.2 R=0.2	4	4	0	$^{[5]}V$	0	T^3
R=0.6	12	8	-1	Q^2	0	T^3
R=1.0	20	9.2	-1	Q^2	-0.55	T^3 / T^2
R=1.4	28	8	-2	Q^1	-1	T^2
R=1.8	36	6.4	-2	Q^1	-1.3	T^2 / T^1
R=2.2	44	5	-2/-3	Q^1,Q^0	-1.8	T^2 / T^1
K=0.4 R=0.2	4	4	0	$^{[5]}V$ & Q^3	0	T^3
R=0.4	8	6	-0.25	$^{[5]}V$/Q^3/<Q^2	0	T^3
R=0.6	12	7	-0.6	$^{[5]}V$/Q^3/<Q^2	0	T^3
R=0.8	16	8	-1	Q^2	0	T^3
R=1.0	20	9.3	-1	Q^2	-0.25	T^3 / T^2
R=1.2	24	9.5	-1.8	Q^1	-0.62	T^3 / T^2
R=1.6	32	9	-2	Q^1	-0.64	T^3 / T^2
R=1.8*	36	9.6	-2	Q^1	-1	T^2
K=0.6 R=0.2*	4	3.4	-0.05	$^{[5]}V$ & Q^3	0	T^3
R=0.4	8	5.5	-0.2	$^{[5]}V$/Q^3 /Q^2	0	T^3
R=0.6	12	6.5	-0.45	Q^3 /Q^2	0	T^3
R=0.8	16	7.1	-0.75	Q^3 /Q^2	0	T^3
R=1.0	20	8.3	-1	Q^2	0	T^3
R=1.2	24	9.5	-1.2	Q^2/Q^1	0	T^3
R=1.4	28	9.3	-1.6	Q^2/Q^1	0	T^3
R=1.6*	32	8.9	-1.9	Q^2/Q^1	0	T^3
R=1.8*	36	8.3	-2	Q^1	-0.2	T^2

*crystalline impurity present

Table 4.2 displays the charge-balance calculations for all lithium borovandate glasses. As seen from the data, the degree of depolymerisation within the borovanadate glass changes as vanadium increases. Both $^{[4]}$B and Q species form as lithium is added. However, the most notable change as K increases is the inhibition of NBOs on boron. As both boron and vanadium share the charge, as one increases the vanadium concentration, the need for NBOs on boron to compensate lithium is no longer required. Although the exact behaviour between $^{[4]}$B and Q-speciation on vanadium cannot be deconvoluted and quantified, it is clear that vanadate polyhedra and $^{[4]}$B provide sufficient anionic behaviour for these glasses, following the trend that is seen in Figure 4.9 and the ^{11}B MAS NMR data.

4.1.3.5. Lithium Mobility

Lithium has a large charge-to-mass ratio and its small size enables high mobility, making it popular for a variety of ionic materials.[171,177,181,189] The linewidths narrowed (T_2* increased) as lithium concentrations increased. This suggests lithium mobility and increases with concentration and temperature observed in the spectra by decreasing the linewidth as it averages the homonuclear dipolar interaction.[84] Exchange spectroscopy on the low-alkali borovanadates (Figure 4.7) show clear, sharp diagonals at short mixing times (<52 μs) for both K=R=0.2(a) and K=R=0.4(c), indicating that no motion is occurring during this time. Increasing the mixing time allows for chemical exchange amongst the lithium sites, causing the observable resonance to form off the diagonal (dephasing).[48,171,217] This also occurs with an increase in sample temperature (d) and an increase in the lithium concentrations (b,

e, f). We can use these data to show that lithium mobility is occurring in these glasses and is on the order of μs to ms. Precise cross peaks commonly seen in crystalline materials do not occur for disordered systems because a distribution of sites exists. Amorphous materials display a "circular" coalescence, indicative of motion.[48,217] EXSY spectra were acquired at variable temperatures for a few of these samples to confirm that the observed dephasing is caused by motion and not spin diffusion which can occur at long mixing times.[48] Spin diffusion can cause similar cross peaks however is not associated with true Li exchange. This can easily be measured by acquiring experiments at variable temperatures as the exchange rates should increase with temperature however spin diffusion will not. ^{11}B and ^{51}V MAS NMR results indicate many possible anionic species where lithium interactions may occur. The faster mobility for the higher-R borovandates is attractive. However, these glasses are more difficult to vitrify as their network becomes increasingly depolymerized (i.e., more ionic).

4.1.4. SUMMARY

A series of lithium borovanadates has been studied in an attempt to understand local structural composition. ^{51}V MAS NMR has not been used to study amorphous based vanadates requiring crystalline model compounds to ascertain information regarding the changes in the vanadia polyhedra. In conjunction with ^{51}V and ^{11}B MAS NMR a complete description of the network forming species was developed, with the fraction of N_4 reaching a maximum between R=1.0-1.2. The rate of NBO formation on boron is retarded by the presence of vanadium, with N_4 maintaining elevated levels in K=0.4 and K=0.6 lithium borovanadate glasses. ^{51}V MAS NMR at moderate fields using fast

MAS is an excellent tool to probe the vanadate environment. In conjunction with isotropic chemical shift, an estimate of NBOs on V can be obtained. Lithium exchange spectroscopy revealed lithium motion for these materials that was affected by temperature and concentration, suggesting a potential use in cathode materials, i.e., as solid electrolytes.

4.2. Cesium Borovanadates

Traditionally, alkali borates and borosilicates have been thought to behave similarly, irrespective of the alkali cation.[2,8,199] However, a difference does occur at higher loadings for borates, where Li^+ behaves differently from Cs^+ in regard to both the alkali environment and borate network.[90] Cs^+ is the largest stable alkali cation and possesses a single positive charge. Cesium has an ionic radius that is approximately three times larger than lithium (1.74 Å versus 0.59 Å) and weighs about 20x more than lithium. This allows its coordination sphere to be large (8 to 12) and causes the charge-to-mass ratio to be a little more than an order of magnitude less than lithium (i.e., 0.14 (Li) vs. 0.0075 (Cs)).[168] The effect of cesium in the same series of borovanadates studied above was probed to determine the effect of vanadium and boron speciation as K=0.2 to 0.6. ^{51}V and ^{11}B MAS NMR were used to determine local environments for cesium borovanadates with the aid of crystalline cesium vanadates. Quantum chemical cluster calculations were used to better understand the evidence of medium-range order present on the $^{[4]}B$ resonance. ^{133}Cs MAS NMR exchange spectroscopy were also acquired using fast MAS and variable temperature to study cesium mobility.

4.2.1. Materials and Methods

4.2.1.1. Synthesis

Cesium borovanadate glasses were synthesized using reagent grade Cs_2CO_3, H_3BO_3 and V_2O_5 (>99%). Boric acid (H_3BO_3) was heated at 500°C for 40 minutes and dehydrated, forming diboron trioxide. Stoichiometric amounts of cesium carbonate were added to divanadium pentoxide and diboron trioxide and mixed for five minutes in an agate mortar and pestle to ensure sample homogeneity. Samples were placed in platinum crucibles and heated to 1000°C for 15 minutes. Crucibles were cooled in air and weighed to confirm decarbonation was complete. Crucibles were placed again in a furnace at 1000°C for five minutes, then the melt was rapidly cooled by plate-quenching ($R < 1.1$) or roller-quenching ($R > 1.1$). Due to the hygroscopic nature of certain cesium borovanadate compositions, high-R samples were quenched in a glove box under a dry nitrogen atmosphere (H_2O content < 2 ppm). The roller quencher was set to a thickness between 25 and 40 microns.

4.2.1.2. Nuclear Magnetic Resonance

^{11}B, ^{51}V and ^{133}Cs MAS NMR spectra were acquired on a Varian ^{UNITY}INOVA 600 (14.1 T) spectrometer using a 3.2 double resonance (H(F)-X) Varian-Chemagnetics or a Fast MAS 1.6 triple resonance (H(F)-X-Y) Varian probe. Spectra were referenced using 0.1M boric acid (19.6 ppm, a secondary reference with respect to $Et_2O{\bullet}BF_3$ (0 ppm)), 0.14M Na_3VO_4 (-574 ppm, a secondary reference with respect to $VOCl_3$ (0 ppm)) and 0.5 M CsCl (0 ppm) for ^{11}B, ^{51}V and ^{133}Cs respectively.

4.2.1.2.1. Boron-11 MAS NMR

^{11}B MAS NMR data (ν_L of 192.4 MHz) were acquired using 64 to 512 co-added transients, recycle delays between 1 and 8 seconds, a spinning frequency of 16.000 ± 0.005 kHz, and a 12^{o} tip angle (ν_{rf} of 70 kHz). 3QMAS for K=0.4, R=0, 0.4, 1 and 1.6 cesium borovanadate glasses were acquired using a z-filtered variant MQMAS pulse sequence, using 32 to 48 increments. The rf nutation frequency for the excitation (4.1 μs) and conversion pulses (1.4 μs) was *ca.* 128 kHz. The soft central-transition selective π-pulse was optimized at 35 μs in duration (ν_{rf} of 12 kHz) and five cycles.

4.2.1.2.2. Vanadium-51 MAS NMR

^{51}V MAS NMR data (ν_L of 157.7 MHz) were acquired with 128 to 2048 co-added transients, recycle delays between 1 and 10 seconds, spinning rates ranging between 18.000 (± 0.008) to 38.000 (± 0.003) kHz, and a 14^{o} tip angle (ν_{rf} of 70 kHz (3.2 mm) and 125 kHz (1.6 mm)). 3QMAS for K=0.2, R=0.3 cesium borovanadate was acquired using a z-filtered fam-MQMAS sequence using 48 increments (fam is the abbreviation for Fast Amplitude Modulation, it is a sequence placed in front of MQMAS to induce a change in the coherence order, it is used to enhance the conversion of triple-quantum to single-quantum coherence).[218,219] The ν_{rf} nutation frequency for the excitation (2.2 μs) and conversion pulses (0.55 μs) was *ca.* 155 kHz. The soft central-transition selective π-pulse was optimized at 35 μs in duration (ν_{rf} of 21 kHz).

4.2.1.2.3. Cesium-133 MAS NMR

^{133}Cs MAS NMR (ν_L of 78.6 MHz) EXSY data were acquired using the 1.6 mm probe. Recycle delays of 10 seconds, spinning speeds of 38 kHz and 16 co-added transients

were collected at mixing times ranging from 50 μs to 770 ms, with 64 increments and an applied rf frequency of 98 kHz, providing a 2.0 μs solid 90°.

4.2.1.3. Quantum Chemical Calculations

Cluster models were built and calculated using Gaussian03 on a SUN X4400 server with 16 cores and 64 GB RAM. This was used to study the effects of nearest neighbours (medium-range order) on $^{[4]}$B, as well as the effect of chemical shift on vanadium and $^{[3]}$B neighbours. Models involved a central polyhedron surrounded by a secondary coordination sphere, which was terminated by hydroxyl groups. Structures were first optimized using a hybrid-DFT level of theory, B3LYP[220-222] and a basis set of 6-31g+. As these systems are disordered, this level of optimization is sufficient and higher levels of optimization were not necessary. These optimized structures were used to perform NMR calculations, in particular looking at the chemical shieldings for boron and vanadium species (only the central atom of each cluster was considered). NMR calculations used a hybrid-DFT level of theory and a pseudo-triple-zeta level basis set of 6-311g(d,p)++.[54] As Gaussian actually calculates shielding a standard ($B(OH)_3$), was also calculated to convert the shieldings into chemical shifts.

4.2.2. Results

4.2.2.1. Boron Speciation

4.2.2.1.1. K=0.2 Borovanadate Series

^{11}B MAS NMR was used to determine the relative ratios of $^{[3]}$B and $^{[4]}$B species (Figure 4.10). The presence of cesium causes the formation of $^{[4]}$B, increasing linearly until R=0.6, when it reaches a plateau. Beyond this plateau (R>0.8), the $^{[4]}$B fraction begins

to decrease with the formation of NBOs on boron. NBOs are also shown by the [3]B resonance that gives evidence of T^2 species at elevated cesium loadings using MQMAS (Figure 4.12). The left-hand edge of the [3]B resonance tends to shift to higher frequency and is associated with a change in peak shape (η>0.6) as cesium loadings increase (Figure 4.10). These data are suggestive of NBO formation, and are commonly observed when T^2 and/or T^1 species form in disordered borates.[93]

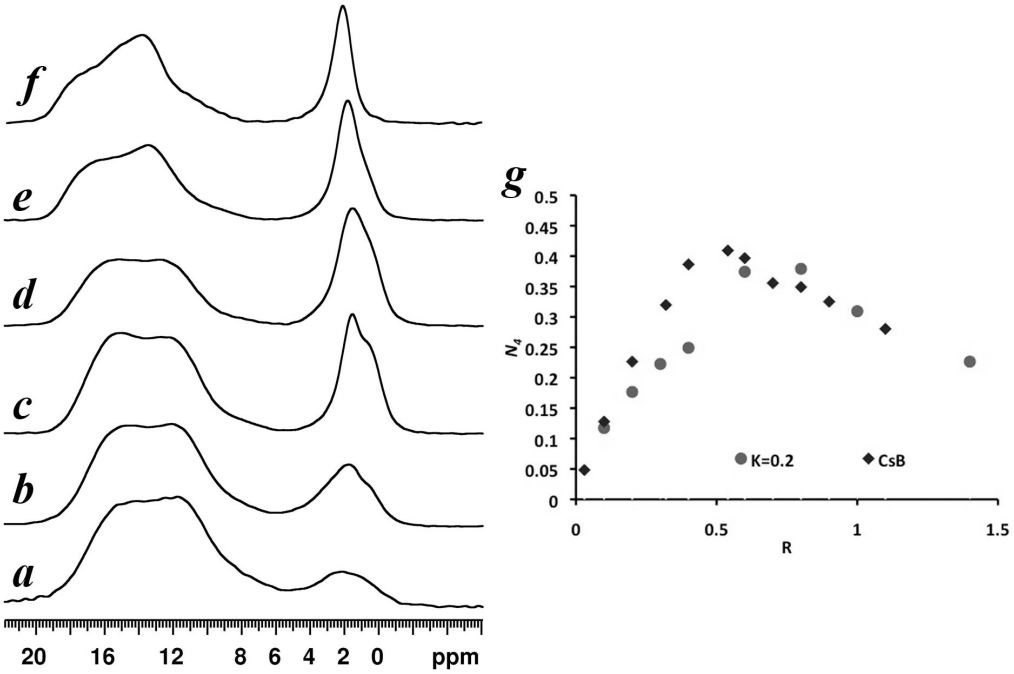

Figure 4.10. [11]B MAS NMR spectra for cesium borosilicate glasses K=0.2 and R of (a) 0.2, (b) 0.6, (c) 1.0, (d) 1.4 and (e) 1.6 and (g) measured N_4 for CsBV K=0.2 and CsB glasses.

The chemical shift regions of 13 to 22 ppm ([3]B) and -4 to +4 ppm ([4]B), and quadrupolar coupling constants of 2.6 ± 0.1 MHz and 400 ± 50 kHz respectively, are

consistent with other borate-based glasses. The four-coordinate boron (-1 to 4 ppm) undergoes a shift to higher frequency with an accompanying narrowing (almost 50% decrease in breadth from R=0.2 to R=1.4) as cesium increases. The lower-R compositions show secondary structure as well at this site. This is presumed to be caused by the varying degree of vanadia polyhedra surrounding $^{[4]}$B as is seen with silicates in borosilicates.[200] The neighbouring aspects will be discussed further using quantum chemical calculations.

4.2.2.1.2. K=0.4 and 0.6 Borovanadate Series

The higher-K series show similar effects as those seen in K=0.2. As seen in the lithium-based glasses, the maximum fraction of $^{[4]}$B is reached at higher-R values (R=1.0 and 1.2) than CsB (R=0.54) as illustrated in Figure 4.13. The degree of depolymerisation on $^{[3]}$B is also inhibited as evidence of NBOs does not appear until R>1.4 (Figure 4.11). This is explained by vanadium charge compensating the Cs^+, limiting the need for NBOs on boron.

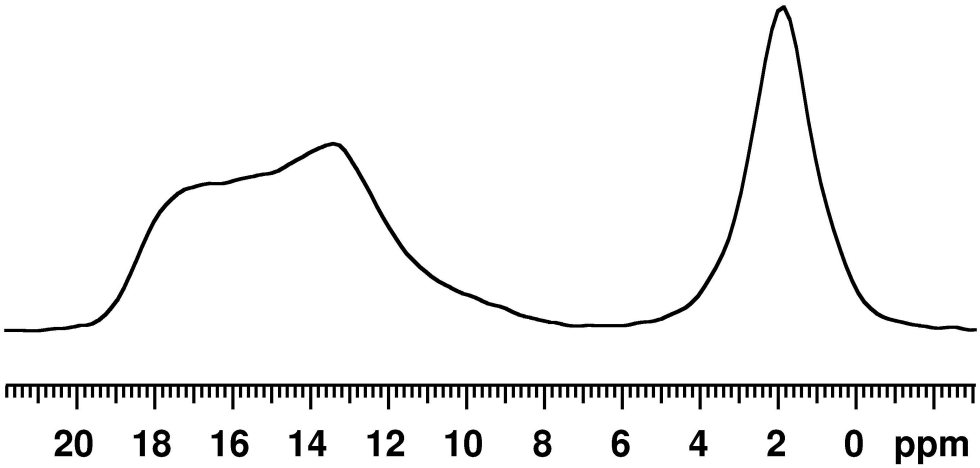

Figure 4.11. CsBV K=0.4 R=1.6, $^{[3]}$B resonance undergoes a slight change in shape as T^2 units begin to form. The taller discontinuity (centred ~13.5 ppm) is caused by the formation of T^2 polyhedra.

The K=0.6 series did not show any indication of T^2, as the higher vanadium concentration compensates the majority of cesium in the system. The $^{[4]}$B resonance does broaden for K=0.6 and R=0.2, indicating an increasing variety of neighbours. This is not surprising, as a large fraction of vanadium is present, inhibiting the breakdown of BO_4 and maintaining polymerization of the borate units, Figure 4.13.

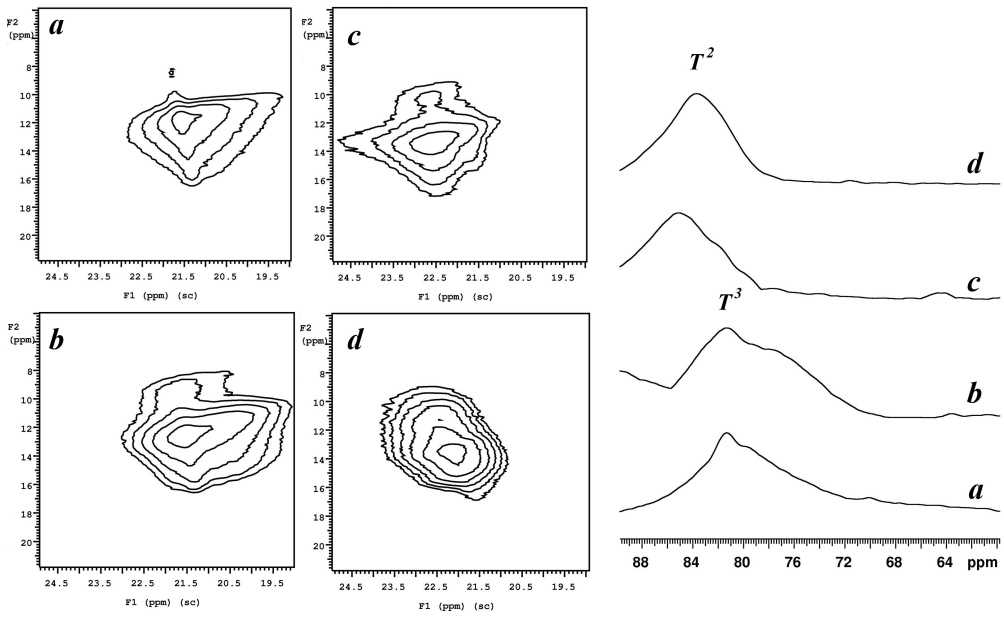

Figure 4.12. ^{11}B 3QMAS for cesium borovanadate K=0.2 and R of (a) 0.0, (b) 0.4, (c) 0.8 and (d) 1.2.

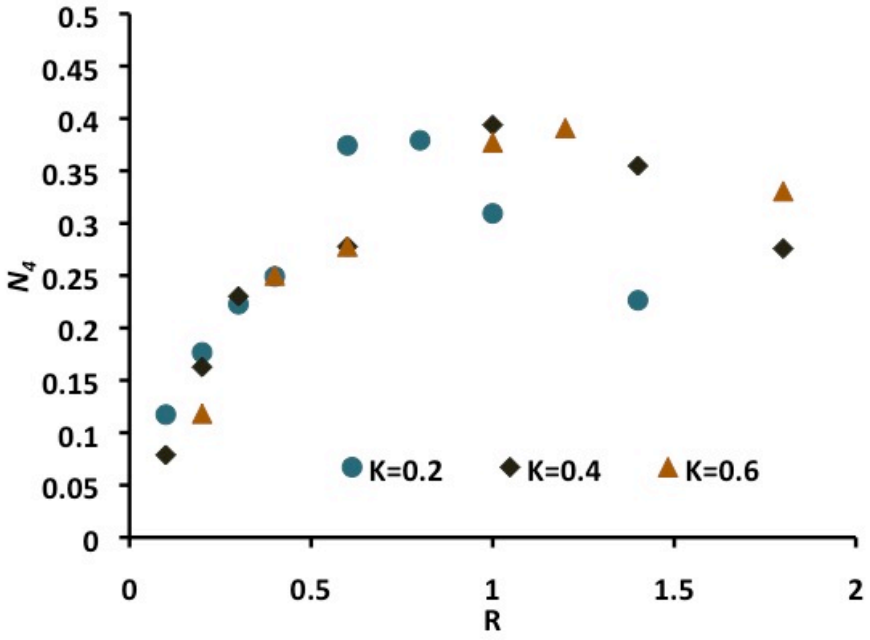

Figure 4.13. Fraction of $^{[4]}$B boron for cesium borovanadates glasses with K=0.2, 0.4 and 0.6.

4.2.2.2. Vanadium-51 MAS NMR

4.2.2.2.1. Crystalline Cesium Vanadate Phases

Three known crystalline cesium vanadate phases were studied in the identical fashion as for the lithium vanadates, where the chemical shifts and interactions from the literature were used to deduce information regarding the cesium borovanadate glasses.[13,202,203] Cesium metavanadate ($CsVO_3$) possesses Q^2 units and has a chemical shift of δ_{iso} of -583 ppm. Cesium pyrovanadate, ($Cs_4V_2O_7$) has two vanadium Q^1 sites located at δ_{iso} of -543 and -567 ppm.[4,202] Cesium orthovanadate (Cs_3VO_4) has a single chemical shift of δ_{iso} of -576 ppm according to the literature[207] but our crystalline phase (confirmed by powder x-ray diffraction) was observed at δ_{iso} of -550 ppm, similar to the lithium orthovanadate shift. In addition, all other alkali orthovanadates are found around this chemical shift range (± 5ppm), perhaps suggesting that the literature value is incorrect or referenced improperly.[202,207]

4.2.2.2.2. K=0.2 Borovanadate Series

^{51}V MAS NMR spectra were collected on vitreous B_2O_3-V_2O_5 and vitreous V_2O_5 in order to determine what type of an effect boron might have on the vanadium shift. The breadths of the CT are similar, with overall peak shapes and δ_{cgs} of -620 ± 15 ppm (borovanadate) and -650 ± 15 ppm (*v*-V_2O_5). The minor shift to higher frequency, together with the same overall shape suggests that vanadium maintains its five-coordinate environment. The shift appears to be caused by boron neighbours and is largely due to the polarisability of vanadium. Addition of Cs^+ caused the ^{51}V resonance to shift to higher frequency in a more pronounced manner (i.e., the shift was not gradual as seen in the LiBV cases but occurred in more discrete units). This suggests

that Cs^+ causes NBOs on vanadium polyhedra to occur sooner than seen using Li^+. This shift is complemented by a decrease in peak width, suggesting an increase in symmetry or a decrease in structural variation, Figure 4.14.

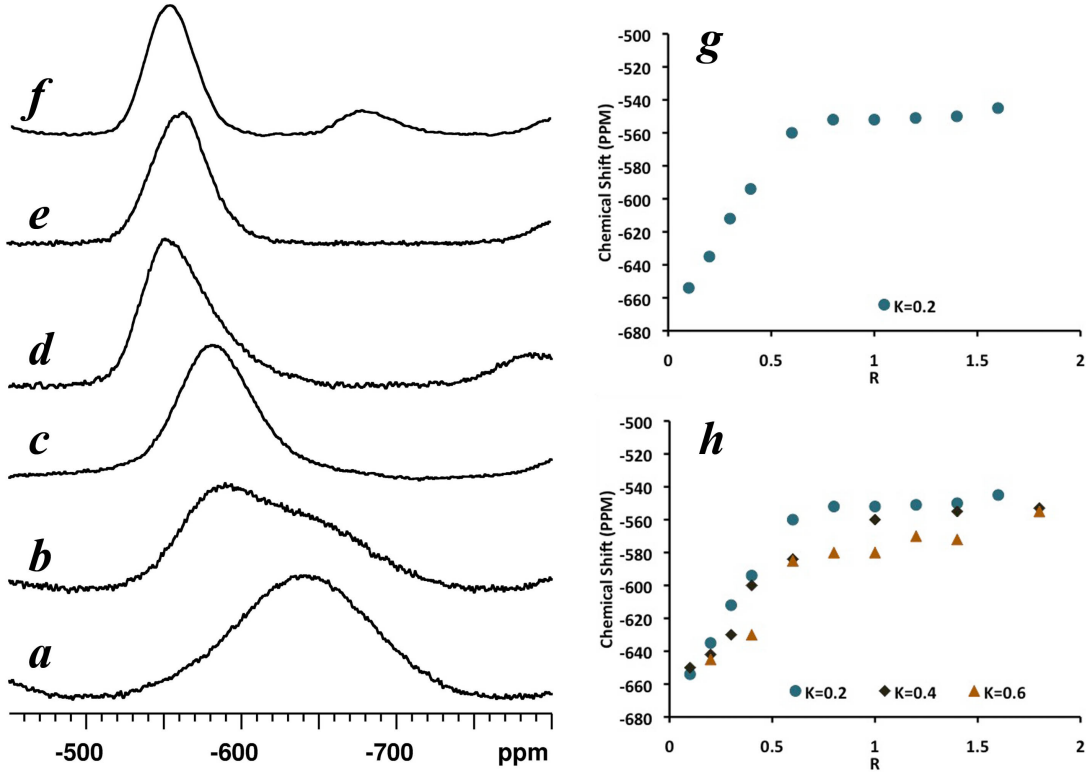

Figure 4.14. ^{51}V MAS NMR spectra of cesium borovanadate glasses, K=0.2 series with R of (a) 0.2, (b) 0.3, (c) 0.4, (d) 0.6, (e) 1 and (f) 1.4. ^{51}V MAS NMR centre of gravity shifts (δ_{cgs}) for (g) K=0.2 and (h) K=0.2, 0.4 and 0.6.

The K=0.2, R=0.3 cesium borovanadate glass (Figure 4.15) shows the presence of a second ^{51}V site (δ_{cgs} of –575 and –640 ppm), indicating both Q^2 and $^{[5]}V$, respectively. ^{51}V 3QMAS (Figure 4.15) of this sample was acquired in an attempt to better resolve these sites. Unfortunately, these resonances did not narrow, indicating

that they were not significantly broadened by the second-order quadrupolar interaction but rather by a distribution in chemical shielding. High-field NMR and fast MAS were also attempted, but produced poorer spectra than those displayed here, for the same reason.

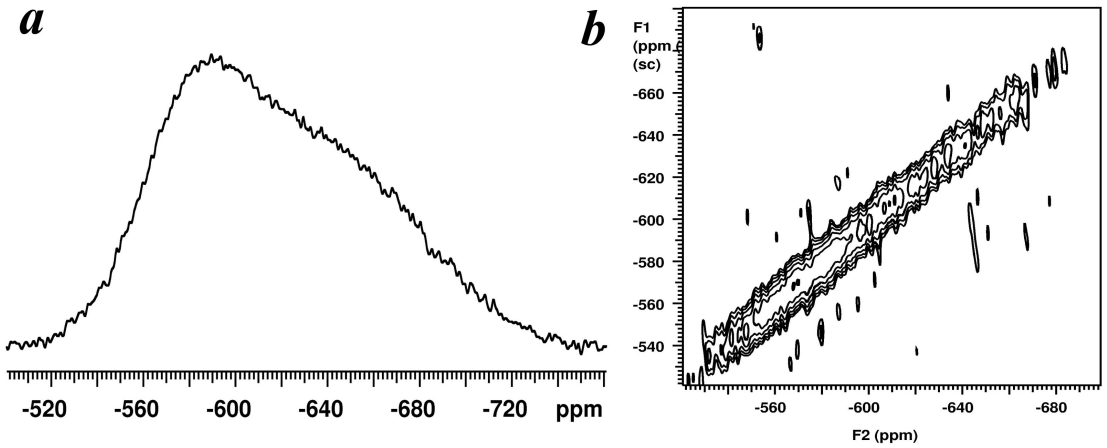

Figure 4.15. ^{51}V MAS NMR of cesium borovanadate K=0.2 R=0.3 glass, (a) 1D MAS spectrum and (b) 3QMAS spectrum at a 38 kHz spinning rate.

4.2.2.2.3. CsBV K=0.4 & 0.6 Glass Series

The cesium borovanadate glasses with K=0.4 and 0.6 behaved similarly to one another, with an increase in chemical shift as R increased. However the overall shift range was smaller than in the case of the K=0.2 glasses. This is rationalized as vanadium is in greater excess thereby requiring higher cesium loadings before Q^2 depolymerize to Q^1 and Q^0 polyhedra occur. These are complementary to the boron data as the $^{[4]}B$ does not break down as fast at higher vanadium concentrations. The ^{51}V chemical shifts proceeded in the same manner (from -650 to -560 ± 10 ppm). An

increase in crystallization tendency was also observed at high cesium and vanadium compositions. This perhaps could be explained by the tendency of Cs^+ cations favouring NBOs, preventing a polymerized, covalently bonding network to form.

4.2.2.3. Cluster Calculations using Gaussian

4.2.2.3.1. Effect on Vanadium as V Depolymerizes

To verify that the shifts are caused by depolymerisation, a variety of vanadium structures (five-coordinate to orthovanadate units) were constructed. These were used to determine the effect on ^{51}V chemical shielding as vanadium depolymerizes. Calculations showed similar effects to those seen in the vanadate crystals ($^{[5]}V$ to $^{[4]}V$) as NBOs formed. The shift to higher frequency propagated as NBOs formed, supporting our interpretation of the experimental results. These calculations also provided a reasonable explanation why multiple vanadium sites from different neighbouring borons were not resolved. If we take the largest difference between the calculated sites (~60 ppm) and we compare this to the experimental breadths of the CT (30 to 160 ppm) resolution will not be easily attainable (Figure 4.16).

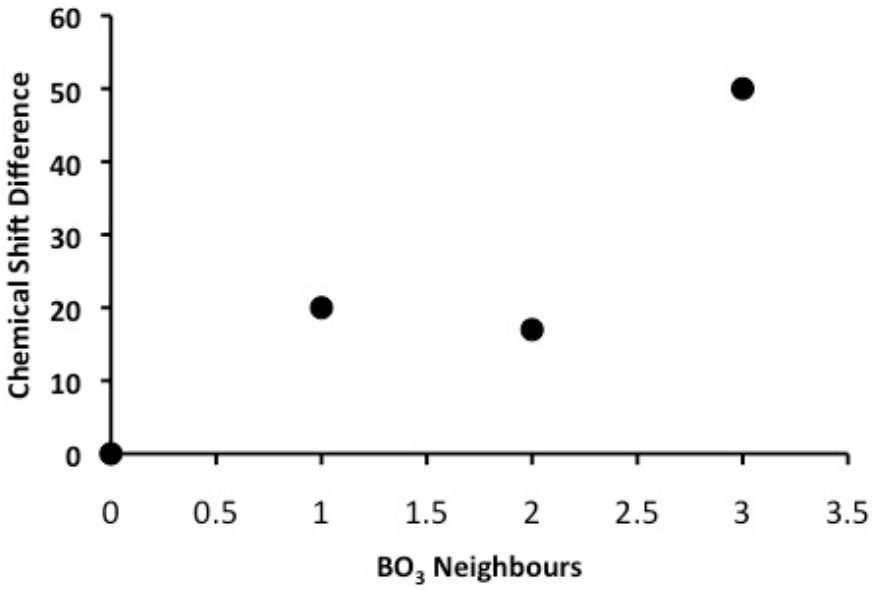

Figure 4.16. Gaussian calculations studying the effect of boron neighbours on a VO_4 polyhedra. These effects explain the difference seen in vitreous V_2O_5 and B_2O_3-V_2O_5.

4.2.2.3.2. Boron Neighbours and their effect on Chemical Shift

Clusters of $^{[4]}B$ species were constructed to determine possible medium-range ordered bridging species. Clusters incorporated the five possible combinations of $^{[4]}B$ neighbours beginning with $^{[4]}B$ with four BO_3 then substituting BO_3 polyhedra for VO_4 neighbours (Figure 4.17 and Figure 4.19). These structures were based on alkali borosilicates, when silicon neighbours cause multiple $^{[4]}B$ resonances to be observed.[4,200,205] Incorporating the vanadium fraction (K-ratio) within these glasses and assuming homogeneous mixing between boron and vanadium, statistically only one to two vanadate polyhedra could be neighbouring $^{[4]}B$ species, limiting the neighbouring possibilities to, all $^{[3]}B$, $1VO_4$:$3^{[3]}B$, $2VO_4$:$2^{[3]}B$ or 3VO4:$1^{[3]}B$. Taking the

K=0.6 series which has 6V for every 10B, if $^{[4]}$B is ~20%, there is a ratio of 6V:2$^{[4]}$B, bringing the total to 3V per $^{[4]}$B. Using these assumptions the likelihood of having more than 3V neighbours is small. Therefore for lower V loadings (i.e., K=0.2 and 0.4) we can estimate an upper limit of vanadium polyhedra surrounding $^{[4]}$B to be around 2V or less.

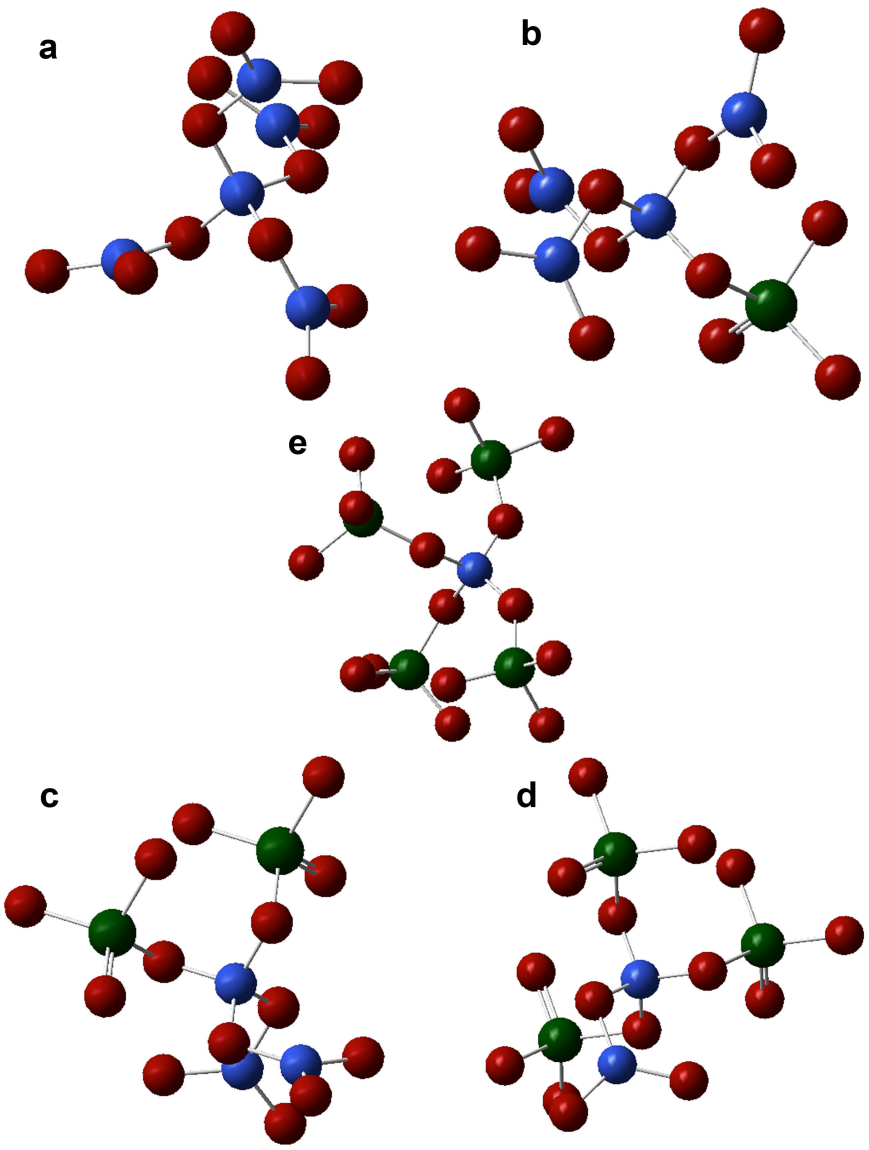

Figure 4.17. Gaussian clusters for $^{[4]}$B neighbours, (a) $^{[4]}$B:4$^{[3]}$B, (b) $^{[4]}$B:3$^{[3]}$B,1$^{[4]}$V, (c) $^{[4]}$B:2$^{[3]}$B,2$^{[4]}$V, (d) $^{[4]}$B:1$^{[3]}$B,3$^{[4]}$V and (e) $^{[4]}$B:0$^{[3]}$B,4$^{[4]}$V. All structures were terminated using hydrogen atoms. The clusters contain vanadium (green), boron (blue) and oxygen (red), while the hydrogen were removed for clarity. There is a -1 charge placed on each of these clusters.

4.2.2.3.3. SUPERSTRUCTURAL UNITS

In the literature superstructural units, which for our purposes will be based on BV ring structures, were not expected to form.[178,179] However, in borates a few ring structures are discussed and could be plausible at low-R values.[223] Ring structures (diborate, di-triborate, pentaborate and triborate) were calculated to determine the $^{[4]}$B isotropic shift for each ring in an all borate, 1V and $2VO_4$ neighbouring environments (Figure 4.19). The triborate and pentaborate contain a single $^{[4]}$B in a ring structure, while the diborate and ditriborate contain two $^{[4]}$B units within a ring. From these 15 structures the diborate and ditriborate (all B and $1VO_4$), triborate (all B and 1V substituted) and pentaborate (all B) would be possible candidates. In crystalline di- and tri-borate species, $^{[4]}$B-O-$^{[4]}$B neighbours (although energetically unfavourable) do exist as the build-up of charge can be partially delocalized over the borate ring(s) that comprise these structures. These are naturally unfavourable in glasses and we would not expect them to occur. To confirm this, ^{11}B 3QMAS NMR data were acquired, as this experiment could show evidence of $^{[3]}$B ring structures if they existed. As borate rings will have $^{[3]}$B and $^{[4]}$B environments, the absence of ring structures from ^{11}B MQMAS provides an indirect measure for the absence of $^{[4]}$B-O-$^{[4]}$B. Gaussian calculations were also carried out on these species in order to provide further support for the MQMAS experimental data. A triborate or a pentadiborate were the only possible calculated structures that could exist based on shift, further confirming that $^{[4]}$B avoidance was occurring.

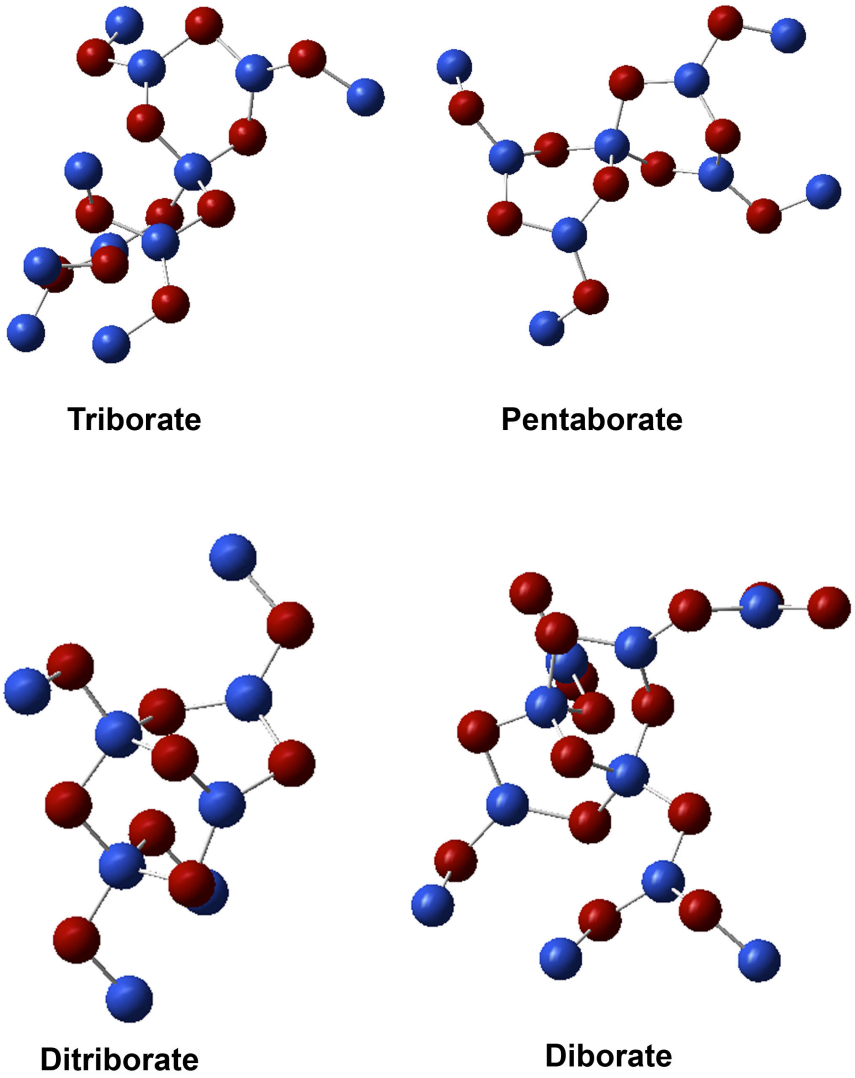

Figure 4.18. Gaussian clusters for ring-based calculations using four different rings. These four rings were also substituted with 1 V neighbour either as part of the ring or as a next nearest neighbour to the borate rings. Each ring has 3 variants (due to V substitution) for a total of 12 rings optimized for NMR calculations. All structures were terminated using hydrogen atoms to fill valency. The clusters contain boron (blue) and oxygen (red), hydrogen atoms were removed for clarity. Each ring contains a negative charge on the $^{[4]}$B polyhedra present within the ring.

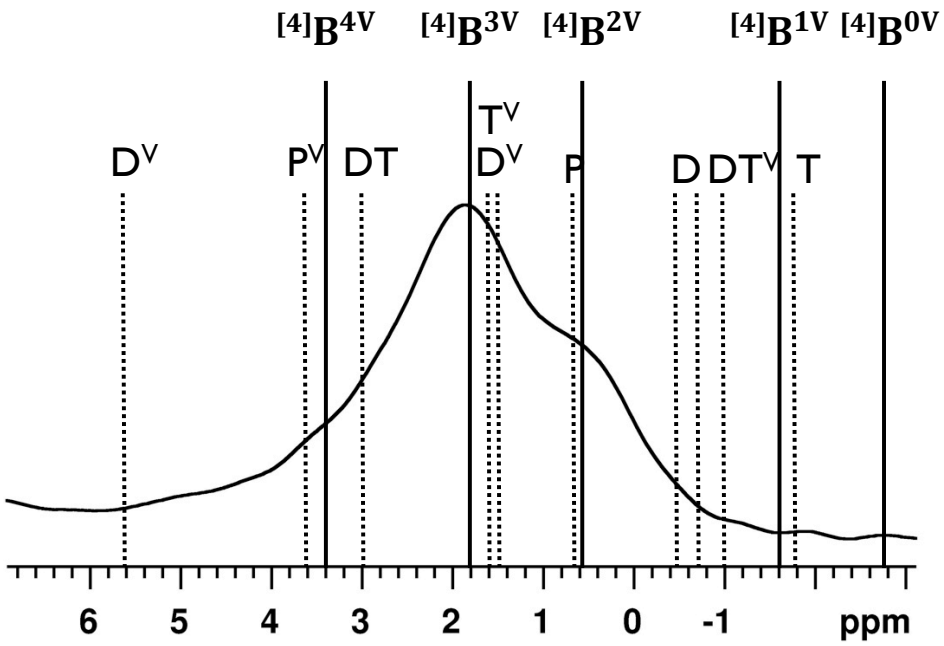

Figure 4.19. Calculated Gaussian03 chemical shifts for ^{11}B of $^{[4]}B$ with different vanadium neighbours and ring environments. The solid lines represent $^{[4]}B$ with different boron and vanadium neighbours (Figure 4.17) while the dotted lines represent $^{[4]}B$ in select ring formations where (D) diborate, (P) pentaborate, (T) triborate and (DT) ditriborate (Figure 4.18). The superscript V simply indicates that the calculated ring structure contained a vanadium substitution within the ring.

4.2.3. Discussion

4.2.3.1. Boron Speciation

^{11}B MAS NMR data show distinct behavioral differences between K=0.2 and K>0.2 (Figure 4.13). The linear behaviour for K=0.2 approaches a maximum N_4 value of 0.38 at R=0.8, whereas the higher K values reach a maximum N_4 of 0.4 at R=1.0. This is different from the lighter alkali borovanadates, where N_4 maxima are reached at ~50% between R=1.0 to 1.2. Cesium requires higher vanadium loadings to retain $^{[4]}B$,

indicating a preference for $^{[3]}$B NBOs as seen for the binary borates.[90] Figure 4.10 clearly illustrates this effect as the second-order quadrupolar shape changes from axial symmetry (T^3) to non-axial asymmetry indicating T^2 formation. Figure 4.12 shows MQMAS data for four K=0.2 CsBV glasses and the chemical shift change that occurs as the T^2 units form.

The narrowing of the $^{[4]}$B resonance as R increases can be understood by the formation of NBOs on vanadium. Low-cesium borovanadates have several possible BO environments ($^{[4]}$B-O-$^{[3]}$B and $^{[4]}$B-O-$^{[4]}V^X$, where X is the number of vanadium neighbours ranging from 0 to 4). As cesium increases, the vanadate units depolymerize to form Q^0 polyhedra, no longer able to participate in bridging oxygens to $^{[4]}$B. Since $^{[4]}$B are still present and need to be bridged, the remaining $^{[3]}$B are next-nearest neighbours, increasing the local order, thus narrowing the resonance. This analysis is similar to that in borosilicates with silicon neighbours on $^{[4]}$B. However, these glasses do show different charge-balancing characteristics than in borosilicates, as both vanadium and boron share the cesium cations which is not typically observed in glass science.[198] This does seem counter-intuitive as the glass becomes more depolymerized (i.e., higher disorder) but the limited species that can bond with $^{[4]}$B decreases, hence our proposal for what is occurring within the $^{[4]}$B resonance.

$^{[4]}$B medium-range order is observed for both cesium and lithium borovanadates, which is absent in lithium borates and borosilicates. We propose that the effect witnessed in these systems is caused by vanadium neighbours on $^{[4]}$B whereas for the lithium borate glass it is the alkali that causes multiple $^{[4]}$B sites (cf. Chapter 3.2). The possible effects on neighbours studied using Gaussian calculations

(see above) agree with the experimental data, suggesting that either superstructures or vanadium neighbours cause the second $^{[4]}$B resonance. We can remove superstructures from the equation as $^{[3]}$B in rings were not seen from MQMAS experiments. The Gaussian calculations indicated that the $^{[4]}$B resonances can be assigned to $^{[4]}$B:1$^{[3]}$B,3$^{[4]}$V and $^{[4]}$B:2$^{[3]}$B,2$^{[4]}$]V. Considering the relative fractions of V:B, it would seem more likely for these to be $^{[4]}$B with 3 $^{[3]}$B and 1 VO_4 and $^{[4]}$B with 4$^{[3]}$B. Based on the calculations and our data we can tentatively assign these resonances as $^{[4]}$B as $^{[4]}$B:4$^{[3]}$B (~ 0.5 ppm) and the higher frequency peak (~2 ppm) containing a single VO_4 neighbour.

4.2.3.2. Vanadium-51 MAS NMR

4.2.3.2.1. K=0.2, 0.4 and 0.6 Borovanadate Series

The crystalline cesium vanadates lay the foundation for assigning the structures in the glasses, as was the case for LiBV. For all glasses studied an increase in R caused a shift to higher frequency. Assuming that the existing literature was incorrect for the crystalline cesium orthovanadate sample, this can be attributed to the formation of NBOs. K=0.2, R=0 has a δ_{cgs} of -650 ± 20 ppm, indicating vanadium in a five-coordinate bridging oxygen species with a moderate quadrupolar interaction (< 3.4 MHz). The addition of Cs^+ also causes the ^{51}V resonance to narrow (Figure 4.14) as a result of a change in local environment (pseudo-tetrahedral) as the conversion from $VO_5 \rightarrow VO_4^{1-} \rightarrow VO_4^{3-}$ occurs; an alternative explanation for this observation is a decrease in structural variation. The ^{51}V 3QMAS experiment unfortunately did not resolve multiple sites, as the spectrum displayed a characteristic glass resonance resulting

from a distribution in shieldings. Ultra-high field and fast MAS (65 kHz) also failed to improve resolution as the resonance increased in breadth at higher fields. This occurred as the dominating interaction is a distribution in shieldings (variation in bond lengths and angles) rather than a distribution of C_Qs. For this reason, Lapina et al. suggest fast spinning and lower fields.[202] A few simple simulations using WSolids® provided some evidence that this could be an option if we used ultra fast MAS at low field (~ 9.4 T). However, MQMAS would be required as the SOQE may need to be contended with at lower fields.[224]

A correlation between the onset of NBOs on boron and the ^{51}V δ_{cgs} plateau occurs at a composition of R=0.8 to R=1. Beyond R=1.0 $^{[4]}B$ break down indicating the formation of NBOs on boron while the vanadium δ_{cgs} are found within the Q^1 and Q^0 regions. This demonstrates clearly the sharing between boron and vanadium species.

The K=0.4 and K=0.6 cesium borovanadate glass series show abrupt changes from R=0.3 to R=0.4, where the CT shifts by 70 ppm and narrows slightly (similar to K=0.2, Figure 4.14). This is followed by another drastic shift of 40 ppm and further narrowing (going from Q^2 to $Q^{1/0}$, Figure 4.20). These structural changes in vanadia units ($^{[5]}V$ to $^{[4]}V$) as a heavy modifier is added suggest more defined local vanadium structures than in the lithium borovanadates, which exhibited smoother vanadium shifts to higher frequency.

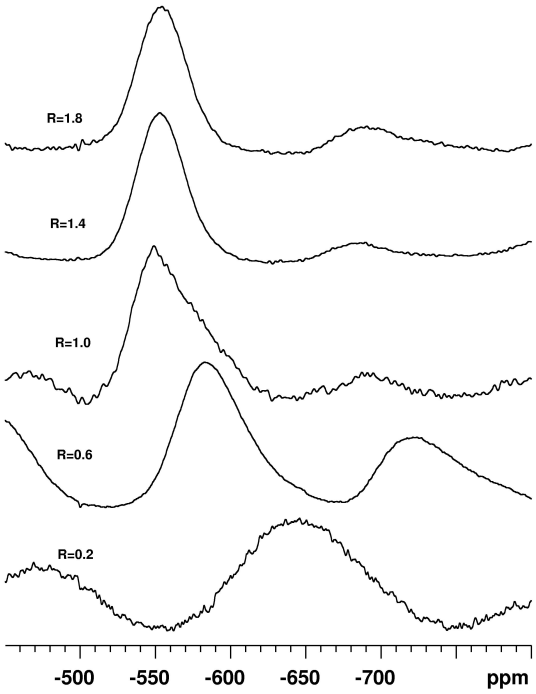

Figure 4.20. ^{51}V MAS NMR of cesium borovanadate K=0.4 (similar effect for K=0.6) glass. Comparing these shifts to comparable LiBV glasses this vanadium shift to higher frequency occurs at lower concentrations.

We speculate that the abrupt changes that occur as the borovanadate glass depolymerizes are caused by the larger size of cesium and its strong preference for NBOs. We can take this idea a step further and suggest cesium sharing between vanadium and boron is not 50/50 as is expected to occur for lithium and sodium borovanadate glasses.[10,178,179] If both vanadium and boron were sharing the Cs^+ evenly, a gradual increase in $^{[4]}B$ accompanied with a breaking down of vanadium (forming NBOs) would be expected, as seen in the case for lithium borovanadate glasses. The cesium borovanadate glasses show a quick breakdown of vanadium

polyhedra, that is preferentially forming Q^1/Q^0 species faster than for lithium, similar to what is seen in lithium and cesium borates.[90]

4.2.3.3. Cesium-133 Exchange Spectroscopy

Cesium EXSY was also attempted to determine whether cesium is mobile within these phases. Mobility should decrease for the heavier Cs^+ and would be expected to be very slow, if at all. Recalling that the lithium borovanadates showed Li^+ mobility with an increase in temperature, an increase in loading or an increase in mixing time occurred (i.e., EXSY dephasing). Using these criteria as a basis, a high-R cesium borovanadate glass was heated and acquired using ^{133}Cs MAS NMR EXSY experiment, as this would be the most likely candidate for cesium dynamics. CsBV K=0.4 and R=1.6 was heated to 60°C (limited by the probe) using mixing times between 100 μs to 700 ms (Figure 4.21). At long mixing times (0.7 s) little dephasing was observed, which is suggestive of little to no motion occurring (perhaps cage rattling). Earlier in Chapter 3, cesium borates glasses were studied and we suggested slow mobility of rattling Cs^+, probed using REDOR. However these binary borates were studied above temperatures of 60°C. Higher temperature would be an asset to further probe and understand possible mobility in cesium borovanadate glasses, as our current probe does not allow for this.

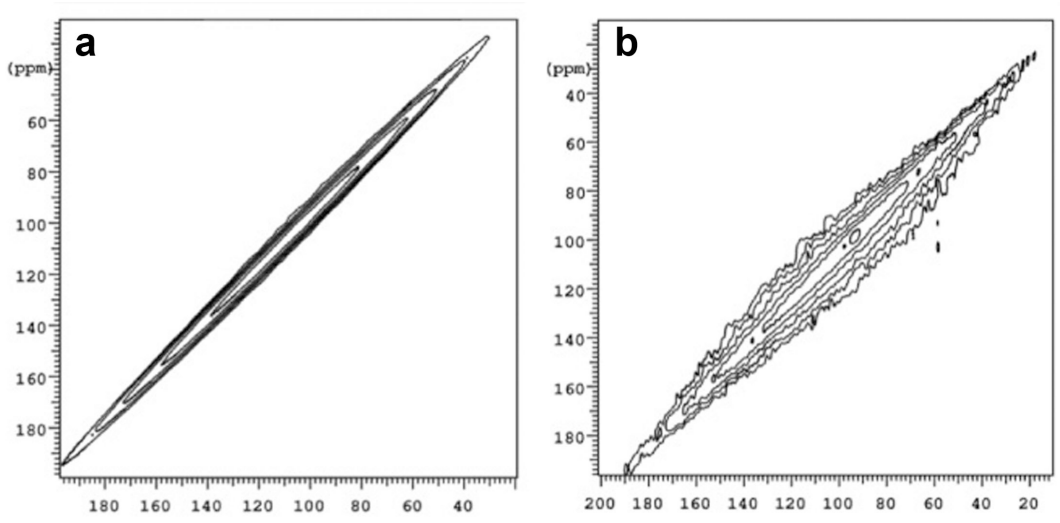

Figure 4.21. ^{133}Cs MAS NMR EXSY spectra of CsBV K=0.4 R=1.6 glass (a) t_{mix} of 100 µs and (b) t_{mix} of 700 ms.

4.2.4. SUMMARY

Cesium borovanadate glasses exhibit similar vanadium speciation, as seen in the lighter lithium borovanadate species. The cesium cations are charge-balanced by both $^{[4]}$B and NBOs on vanadium polyhedra. Vanadium depolymerizes more quickly with cesium addition than with lithium, indicating a stronger preference for Cs-VO_4 interactions and NBOs as seen for binary glasses. The largest differences between the cesium and lithium borovandates are the maximum values of N_4 that are reached. The actual fraction for the cesium borovanadates (K=0.2 to 0.6) are lower (~37% $^{[4]}$B versus ~46% $^{[4]}$B) but the maximum N_4 also occur at lower alkali loadings (R=0.7 to 1.0 versus R=1.0-1.2). This agrees qualitatively with binary borate glasses as cesium prefers BO_3 and VO_4 polyhedra bearing NBOs at higher alkali loadings. As lithium and cesium borovanadate glasses have not been studied using ^{51}V MAS NMR in the past these results contribute in regards to the structural differences that occur in

borovandates. Additionally, this is the first study we are aware of on cesium borovanadates and shows promise for these types of glasses to be studied in the future using MAS NMR. These results are of interest, as it is commonly thought all alkali oxides behave similarly in oxide glasses (i.e., no size effect). In Chapter 3 we showed lithium and cesium cause differences within the borate network as cesium caused a higher fraction of NBOs. This effect is also seen here within the ternary borovanadates. It is prominent in both the ^{11}B and ^{51}V MAS NMR results indicating distinct speciation preferences for cesium and lithium modifiers.

5. Model Nuclear Waste Borosilicates

Nuclear power has been met by an assortment of positive and negative press. It could alleviate the stress of current CO_2 production, enabling agendas set out by the Kyoto protocol to be met, while providing affordable energy to both developing and industrial nations. Other sources such as wind, solar and hydro would also be employed. The safety and waste concerns associated with nuclear power are common downfalls, continually discussed around the world. Canada's role in nuclear power has been significant, in regards to reactor development and uranium supplies, as one of the largest uranium mines in the world is located in the Athabasca Basin, Saskatchewan.[225]

Spent uranium can often be reprocessed so that another fuel cycle can be carried out. The uranium requires reprocessing to remove the fission by-products that occurred as a result of the nuclear reaction. This waste (~30 to 40 kg per ton of loaded fuel) contains a variety of fission products; some that are considered high level waste include ^{135}Cs, ^{137}Cs, ^{93}Zr, ^{90}Sr, etc.[226] Low, medium and high levels of waste are all treated using different methods. Low-level waste is dealt with by the use of retention ponds, allowing fission products with shorter half-lives to decay. These are then purified before the decayed fission products are released into the environment.

Medium-level waste can be handled in a variety of ways, with the current trend being incineration. This method condenses the amount of material, which is then incorporated into cement for long-term storage. The low and medium level waste accounts for most of all nuclear waste created from energy production.[227,228] The remaining waste is designated as high-level liquid waste and represent the deadliest nuclear species, including species possessing half-lives on the order of tens to thousands of years. Waste of this sort is commonly dealt with by mixing the waste stream into a complex melt comprised of borosilicate glass. The borosilicate must be able to incorporate 30 to 50 various oxides while being slowly vitrified into a homogeneous glass. This expensive method has been well studied, is safe and is understood. Our goals for these materials are to improve loading levels, lower melting temperatures and maintain strength and integrity while lowering costs, making this a more attractive process.

5.1. Cesium Vaporization within Borosilicates

Alkali borosilicates can be understood using the same basic principles as alkali borates, except with the added dimension of silicate speciation and reactivity. SiO_2 increases the viscosity and melting point, creating a glass that is more water resistant (most borates are water soluble). An increase in N_4 occurs as silicon dilutes the borate network and decreases the occurrence of the highly unfavorable $^{[4]}$B-O-$^{[4]}$B bridges. Charge balance between B_2O_3 and SiO_2 has been well studied by Bray et al., who developed a charge model describing how the network changes to accommodate the

alkali modifier.[199] Using sodium borosilicate glasses to typify alkali borosilicates, in general Dell and Bray studied the effects on local polyhedra and determined that the borate species undergo conversion to $^{[4]}B$ from $^{[3]}B$. The maximum in N_4 depends on the ratio of SiO_2/B_2O_3, K. As alkali oxide is added, BO_3 converts to BO_4^- to maintain charge compensation from the alkali modifier, in turn increasing the connectivity or degree of polymerization in the glass. At some point a maximum N_4 is reached (depending on alkali and silicon concentration), and silicate units (Q^4) begin to break down, forming NBOs (e.g., Q^3). Further alkali loading causes the formation of NBOs on boron (i.e., $^{[4]}B$ decreases while T^2s form). In the past ten years some aspects of this model have come into question, such as the formation of Q^3 beginning at a lower loading than predicted, however the general trend remains valid.[200,205,229-232]

Cesium borosilicate can be understood as a highly simplified model for nuclear waste glasses. Its study can aid in understanding the nature of Cs^+ (a daughter product from ^{235}U fission) incorporation during vitrification of high-level waste. Two particular isotopes, ^{137}Cs ($t_{1/2}$ ~30 years) and ^{135}Cs ($t_{1/2}$ ~23 x 10^5 years) are long-lived products that decay to barium during long-term storage.[233,234] With recent studies on sodium borosilicates providing evidence of sodium borate species being volatile at typical glass processing temperatures[103,229-231,235,236], concern surrounds cesium incorporation, stability and volatility.

Cesium volatility in a model nuclear waste glass has been studied in a series of cesium borosilicates that were treated for different heating times. Three particular aspects of interest include the structural effects on the borosilicate network as a function of heating time, the effect on ^{133}Cs chemical shift as heating time is increased,

and the echo intensity, as it shows promise in identifying changes in cesium concentrations.

5.1.1. Materials and Methods

5.1.1.1. Sample Preparation

A three gram batch of cesium borosilicate with a composition of K=2 and R=0.5 ($14.3Cs_2O•28.6B_2O_3•57.1SiO_2$ – in mol %) was synthesized from dehydrated boric acid (B_2O_3), SiO_2 and Cs_2CO_3. After extensive mixing of the nominal batch composition in an agate mortar and pestle, the samples were divided equally into seven samples. Each was heated to 600°C within a box furnace to allow for decarbonation, which was verified by mass-loss measurements. These powders were re-ground and placed in ZGS (zirconia grain stabilized) platinum/gold(5%) high-temperature crucibles and heated to 1350°C for the specified time (between 1 and 60 minutes) in an inert argon atmosphere (3 L/hr flow rate). Melts were quenched using deionized water and checked for homogeneity and crystallinity by polarized light microscopy.

5.1.1.2. X-ray Powder Diffraction

Glasses that appeared to have crystalline phases were ground using an agate mortar and pestle and assessed using a PANAlytical X'Pert Pro Bragg-Brentano powder x-ray diffractometer equipped with a Cu K_α radiation source, an X'Celerator detector and a Ni-filter diffracted beam. All data were collected at room temperature using a 2θ range of 5° to 80° at 0.0167° increments with a 75s step time. Powders were mounted using grease on a single-crystal quartz (SiO_2) zero background sample holder.

5.1.1.3. Inductively coupled plasma optical emission Spectroscopy

Three samples (heated for 3, 15 and 60 minutes) were digested (~100 mg) with concentrated HF and analyzed for cesium and boron by inductively coupled plasma optical emission spectroscopy using a Varian Liberty 200. Silicon cannot be analyzed due to the volatility of SiF_4, which is created during digestion with HF, precluding reliable Si measurements.

5.1.1.4. Electron Microprobe Analysis

Powdered samples were mounted on one-inch diameter Perspex disks using heat-activated epoxy. The disks were polished, carbon coated and probed using a Cameca SX-100 EMP. The collection method used the wavelength dispersion mode with an excitation voltage of 15 kV, specimen current of 20 nA, a 10 μm beam size, a background count time of 10 s and a peak count time of 20 s. Each sample was averaged over five sampling points.

5.1.1.5. NMR Spectroscopy

NMR data were obtained on a Varian ^{UNITY}INOVA 600 NMR spectrometer (14.1 T) using a 3.2 mm double resonance Varian-Chemagnetics MAS probe. Sample amounts ranging from 30 to 38 mg were placed in 22 μl (3.2 mm o.d.) ZrO_2 rotors. ^{133}Cs MAS NMR spectra were observed using a Hahn-echo pulse sequence employing the extended phase cycling scheme of Kunwar & Oldfield,[237] with an ν_{rf} of 50 kHz. Sixteen transients were co-added, with recycle delays of 500 to 1,000 s between transients. CsCl (aq, 0.5 M) was used as a primary reference, set to 0 ppm. ^{11}B MAS NMR spectra were collected using a Bloch-decay sequence with short pulses corresponding to a 22°

tip angle and an ν_{rf} of 69 kHz. Sixteen transients were co-added with recycle delays of 10 to 20 s. Boric acid (aq, 0.1 m) was used as a secondary reference, set to 19.6 ppm relative to BF_3-Et_2O (0.0 ppm). ^{29}Si MAS NMR spectra were collected using a Bloch sequence with a short 15° tip angle (ν_{rf} of 50 kHz), recycle delays were set to 60 s with 1024 co-added transients. The ^{29}Si spectra were referenced to 3-(trimethylsilyl)-propanesulfonic at 1.43 ppm relative to the primary TMS reference (0.0 ppm).

5.1.2. Results and Discussion

5.1.2.1. Compositional Change

Final compositions were analyzed by ICP-OES for the 3, 15 and 60 minute samples to determine the absolute molar quantities of cesium and boron (Figure 5.1). The loss of Cs_2O occurs rapidly, within the first three minutes of heating, causing a drop in concentration by 3% absolute, i.e., 14% to 11% Cs_2O. However, the boron concentration remains stable over the three compositions analyzed, indicating that cesium is the volatile component, and not the sodium borate species, as suggested elsewhere.[230,236] The 60 minute cesium borosilicate glass shows a drastic drop in R (nominal composition of R=0.5 to R=0.24 (~50%)), causing a significant change in the borosilicate structure (Figure 5.2). The glass network compensates for cesium boil-off by changing the boron coordination as seen in the ^{11}B MAS NMR, leading to a decrease in N_4, and a corresponding decrease in network connectivity. The decrease in N_4 is caused by the cesium cations being removed.

Although the concentration of silicon cannot be determined from ICP-OES (due to SiF_4 formation), EMPA indicates that the concentration of silicon does not change

with increased heating times. This result is expected given the very high boiling temperatures of SiO_2 (2950°C) and other geologically relevant alkali silicates when compared to cesium oxide (melting temperature, T_m = 490°C).[16] The exact species that is volatile from the cesium borosilicate is difficult to determine. However, it is believed to be in the form of Cs_2O, although elemental Cs has also been observed in the past.[238] Cs_2O is suggested here as at higher temperatures it would be easily oxidized and this is supported by mass-loss measurements recorded after heating the sample, which agree most closely with the loss of Cs_2O.

5.1.2.2. Cesium-133 Spin-Counting

Quantitative ^{133}Cs MAS NMR spectra were acquired on all cesium borosilicate glasses using a spin-echo sequence. The parameters were carefully determined, using appropriate recycle delays, number of scans, spinning speeds and taking the sample mass into consideration. This enabled the tracking of changes in cesium content with the measured echo intensity. Figure 5.1 illustrates the effect of heating time on echo intensity. Although using NMR as an analytical tool to determine concentrations is difficult and is not typical, with careful instrumental setup and treatment a beautiful illustration of its potential for spin-counting may be seen. Quantification requires collection of a standard in order to determine the absolute concentrations of cesium. This can be difficult due to different internal interactions, long recycle delays, etc. Qualitatively, one can see the exponential decay that occurs, mirroring the trend seen in the ICP data.

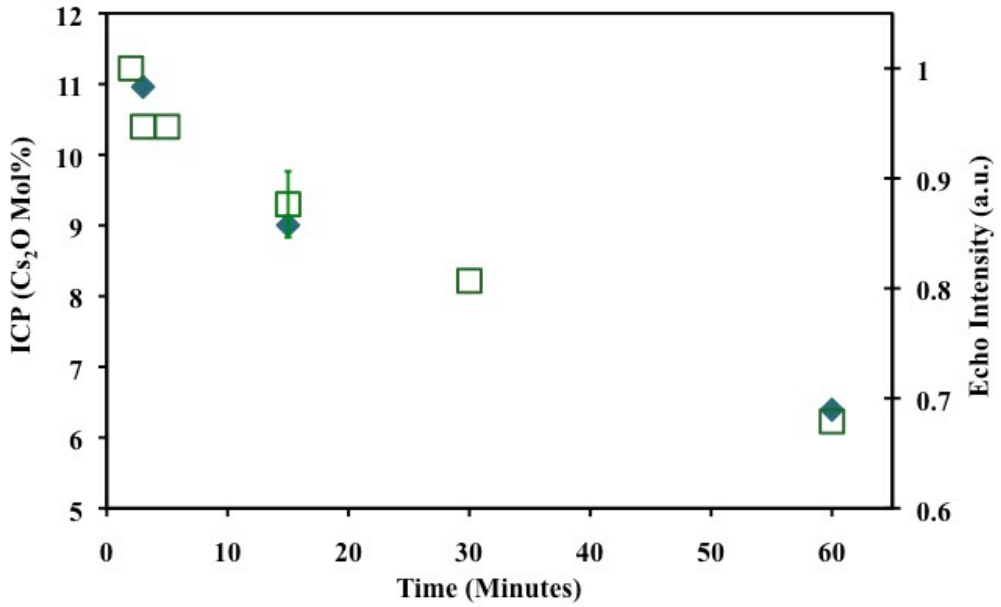

Figure 5.1. ^{133}Cs MAS NMR echo intensities (squares) and ICP (diamonds) results for seven heat treated CsBSi glasses.

5.1.2.3. Boron as a Network Former

In order to determine the N_4, ^{11}B MAS NMR was acquired for all glasses. The moderate magnetic field allows reliable $^{[3]}$B and $^{[4]}$B populations to be measured, where the fraction of $^{[4]}$B can be seen to decrease with increasing heating times (Figure 5.2). This follows the trend observed within ^{133}Cs MAS NMR, ICP-OES and EMPA, which is consistent with a loss of alkali modifier. According to the Dell and Bray model,[199] for an alkali borosilicate glass with a silicate-to-boron ratio K=2, a linear scaling with N_4=R is predicted up to R=0.65.[199] These cesium borosilicates do not reflect this and were determined to have N_4=0.35 at R=0.24 (i.e., 30% more $^{[4]}$B than predicted). This discrepancy could be explained by borate and borosilicate phase separation that may

occur at longer heating times. This can be understood if the ratio of boron changes in the silicate phase (i.e., the concentration of SiO_2, K) as this will affect the behaviour of N_4 for both the borate and borosilicate phases. If boron decreases in the borosilicate phase, this would cause more $^{[4]}B$ species, as removing boron would allow a higher fraction of $^{[4]}B$ and reduce Q^3 in silicon.

The spectra for these different heating times are shown in Figure 5.2, with $^{[3]}B$ (8 to 17 ppm) showing a lineshape commonly observed for T^3 units in ring and non-ring conformations. Elevated heating times cause a shift in the balance between ring and non-ring. This shift to a higher concentration of ring structures at longer heating times would be expected with a lower concentration of alkali modifier, agreeing with all the results reported above.

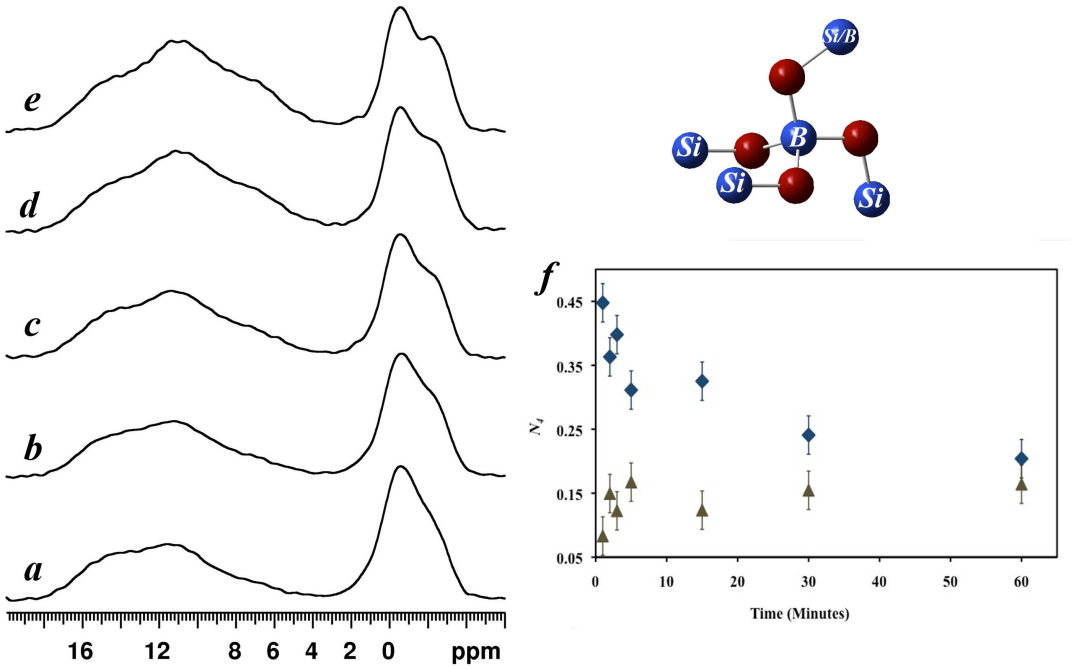

Figure 5.2. ^{11}B MAS NMR spectra of (a) 3 min, (b) 5 min, (c) 15 min, (d) 30 min and (e) 60 min and (f) N_4 for each $^{[4]}$B site (~0ppm and -2 ppm) as a function of heating time. The borosilicate polyhedra above provides an illustration of $^{[4]}$B neighbours, that is silicon or boron.

The $^{[4]}$B region (-4 to +3 ppm) exhibits two distinct resonances, providing information regarding the second coordination sphere (medium-range order). Based on measured chemical shifts and previous studies on sodium borosilicates,[200,205] the resonance at δ≈-2 ppm is attributed to a $^{[4]}$B surrounded by four silicon neighbours, while δ≈0 ppm is a $^{[4]}$B with one $^{[3]}$B and three silicon tetrahedra.

As observed in the spectra, the ratio of these species seems to change as heating times are increased. Careful integration and peak fitting of the ^{11}B MAS NMR data using STARS® and SpinWorks© revealed that the higher frequency four-coordinate

peak decreases ($^{[4]}B^{1B,3Si}$), and the lower frequency peak ($^{[4]}B^{4Si}$) remains essentially constant (see above). This unusual behaviour suggests preferential cesium loss at a site–specific position. An alternative explanation involves some form of rapid equilibrium between the sites that occurs during the melt and volatilization period. As cesium volatilizes it seems to be retained or favoured at a $^{[4]}B$ site surrounded by neighbouring silicates since the concentration stays nearly constant. Cesium located at the $^{[4]}B$ with a $^{[3]}B$ neighbour decreases exponentially, mirroring the ICP and echo data. These observations, (i) onset of ring formation in $^{[3]}B$ and (ii) preferential site retention between $^{[4]}B$ sites differs from what has been seen for sodium borosilicate glasses, suggesting an alkali effect.[200] As the cesium cation is larger than sodium its bonding strength, i.e., ability to form strong bonds, would be reduced, allowing volatilization to occur more easily with a greater effect on the forming network.

Upon closer examination of the $^{[4]}B$ with a $\delta \approx 0$ ppm, a plot of the peak intensity against the R-value (which was experimentally determined from ICP-OES) indicates a linear trend, with a correlation of $R^2=0.997$ and an intercept near zero (0.008), Figure 5.3.

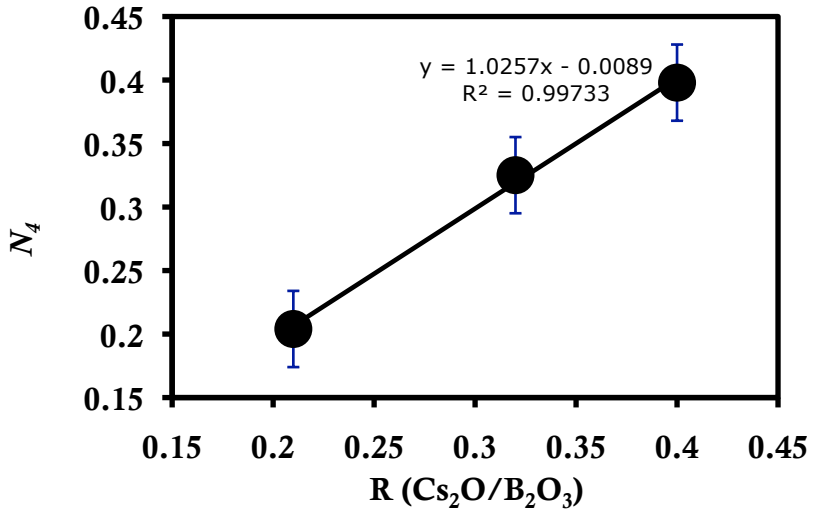

Figure 5.3. Population of [4]B (0 ppm) with R composition determined from ICP for 5, 15 and 60 minute heat treated glasses.

This is the relationship predicted by Dell and Bray, perhaps suggesting one phase is preferentially being affected or modified by the cesium boil-off, while the other glass phase has maintained and incorporated cesium, inhibiting loss. Evidence for phase separation has been studied within our group using ^{17}O MAS NMR (ideal for bonding investigations and different bonding environments) on similar CsBSi glasses. Immiscibility regions have been documented in similar alkali borosilicate systems with similar compositions.[2,200,205]

5.1.2.4. SILICON-29 MAS NMR

^{29}Si MAS NMR for the 3, 15 and 60 minute glasses are presented in Figure 5.4. Chemical shifts move to lower frequency for increased heating times, associated with a decrease of NBOs on silicon. This can be explained by the presence of Q^3 units (-80 to -100 ppm) in the 3 minute sample, but these units are absent at longer heating

times. The formation of Q^4 species at longer heating times can be explained by the loss of cesium which no longer requires NBOs on silicon to compensate for the charge.

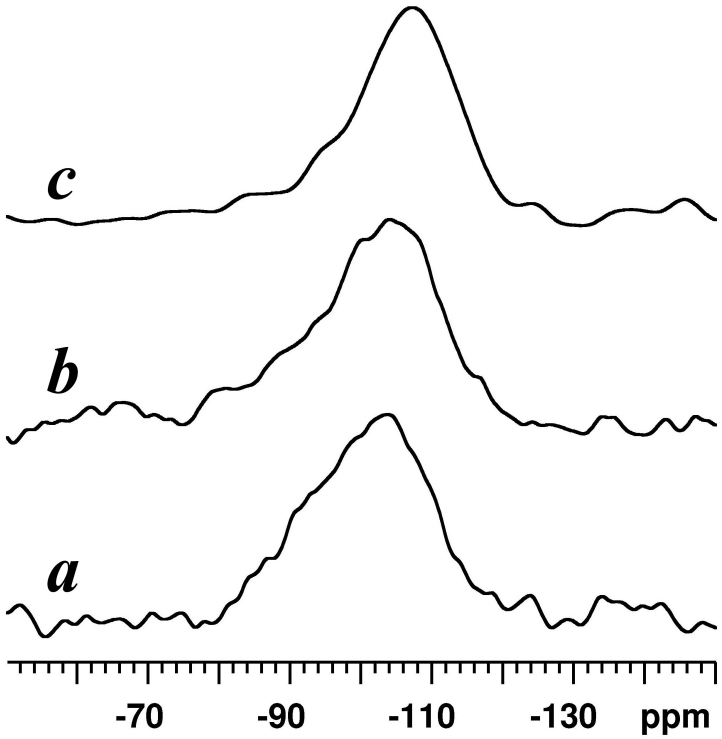

Figure 5.4. ^{29}Si MAS NMR spectra for heating times of a) 3 min, b) 15 min and c) 60 min, Q^3 region (-80 to -100 ppm) and Q^4 region (-100 to -120 ppm)

One complication is that these compositions, according to the Dell and Bray model, should not require Q^3 to maintain the charge balance. An alternative explanation for the ^{29}Si shift into the Q^3 range is that the Cs^+ affects the known chemical shifts of Q^4 speciation. As this has not been observed for any other cation – silicate interaction, we do not believe this to be the case. Therefore, the shift to higher frequency (for low heating times) does indicate the formation of Q^3 species. Resolution of the two sites (Q^3 and Q^4) and reliable peak fitting is not possible from these data and we refrain from quantitative analysis. The Q^3 species could be from a

phase separated, silicate-rich region that contains Cs^+, as only silicate polyhedra would be able to maintain charge balance requiring the formation of Q^3, prior to homogeneous mixing of the melt.

5.1.2.5. Cesium-133 MAS NMR

^{133}Cs is a highly polarisable nucleus (chemical shielding is sensitive to local changes in geometry) therefore it typically exhibits broad peaks that span large chemical shift ranges when in glasses.[92] As seen in Figure 5.5, the linewidths and peak shapes do not change from one heating time to the next, but a chemical shift change (to lower frequency) is observed. This shift correlates to the decrease in N_4 and cesium content. This shift is precisely what has been observed for binary borates (cf. Chapter 3) and is interpreted as a coordination change. The shift to lower frequency for the cesium borosilicate series is thought to be caused by an increase in the average coordination sphere. The addition of SiO_2 as a secondary network former and the possibility of phase separation complicate this relationship, as these effects may also contribute to changes in the ^{133}Cs MAS NMR spectra (Figure 5.5). The shift effect for cesium seems to be more sensitive (larger change in shift over a smaller R range) for these ternary borosilicate than in binary cesium borates. This indicates that silicon has a major effect on the cesium environment, manifested by the observed chemical shift, either as a structural effect, a chemical shielding effect or a combination of both.

Scatter in the ^{133}Cs data within the first 3 minutes (Figure 5.6) may be due to the fact that the starting reagents did not fully melt and mix homogeneously. These samples were found to contain minor amounts of crystalline cesium-containing

compounds. The crystalline impurities were identified both by x-ray diffraction and ^{133}Cs MAS NMR, but the exact phase(s) could not be determined. The amounts were minor (< 3%), and should have no measurable impact on the results. These minor crystalline phases are likely due to incomplete reaction of the starting materials for very short melting times, preventing their fusion. The most actively volatile stage of these glasses according to our data (Figure 5.6) occurs within the first few minutes of heating, suggesting that the cesium vaporizes more rapidly due to incomplete mixing.

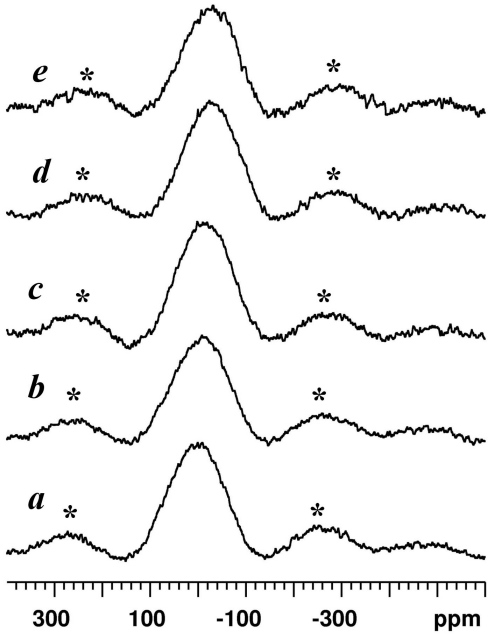

Figure 5.5. ^{133}Cs MAS NMR spectra for (a) 3 min, (b) 5 min, (c) 15 min, (d) 30 min and (e) 60 min.

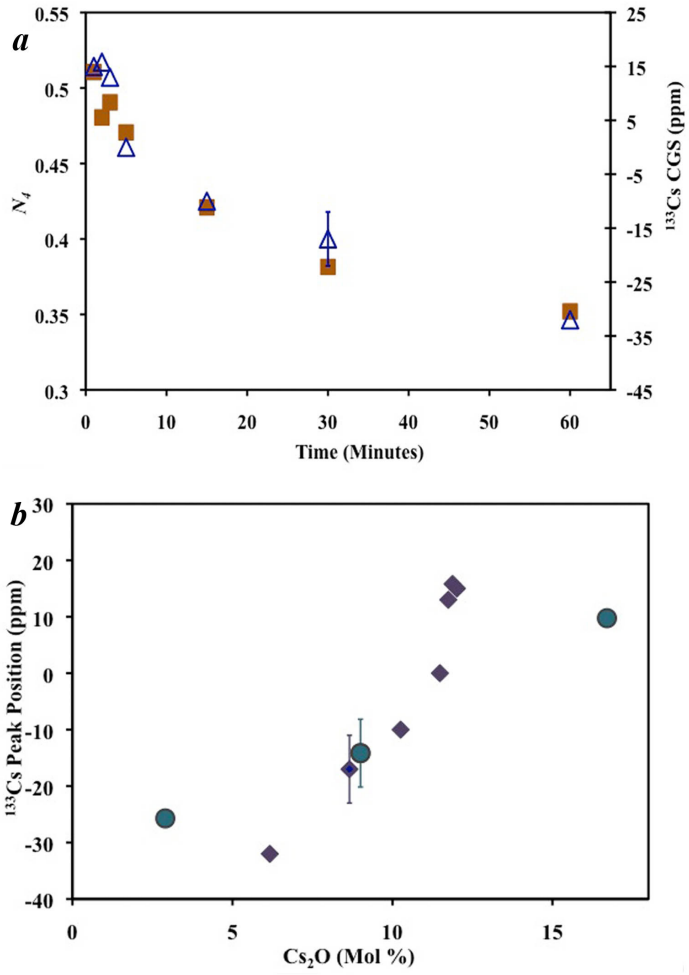

Figure 5.6. (a) Relationship between fraction of $^{[4]}$B (square) and the ^{133}Cs, δ_{cgs} (triangle). (b) ^{133}Cs peak position (δ_{cgs}) and Cs concentration from ICP for CsBSi (circles) and CsB (diamonds).

5.1.3. SUMMARY

These cesium borosilicate glasses show that cesium is a rather volatile element. This should be accounted for when preparing such cesium containing materials, as the nominal batch composition will change during the glass-making procedure. These concentrations of cesium are higher than those found in nuclear waste glasses.

However, industrial heating times are longer and cooling rates are slower, suggesting that volatility may be of concern. The changes observed within the borosilicate (boron (^{11}B) and silicon (^{29}Si) MAS NMR) structure correlate well with ICP, EMPA and ^{133}Cs spin-echo experiments showing that the structural effect on the overall integrity of the glass is significant as the cation concentration decreases. To overcome the effects of cesium volatilization so that one maintains the required cesium concentration, excess loading on the order of ~ 50% is suggested. This additional cesium would enable cesium borosilicates to be synthesized appropriately with proper cesium compositions. As the volatility will fluctuate based on batch composition, heating time and temperature, one should be aware that other amounts may be required in order to obtain proper glass compositions.

5.2. Aluminum and Gallium Modified Sodium Borosilicate

Amorphous silicate and borosilicate materials have a vast range of applications that includes fiber optics,[239] films[240] and nuclear waste storage.[241,242] The balance between silicate and borate units is complex and changes when other modifiers or formers are added (e.g., Al_2O_3).[199] The charge balance within borosilicates was discussed above, where $^{[4]}$B are formed first from $^{[3]}$B. At some point silicate Q^4 breakdown occurs, forming Q^3 species to accommodate the higher alkali loadings.[2,10,243-245] A method to reduce NBOs (on boron and silicon polyhedra) without compromising glass integrity is the addition of an intermediate glass former, such as Al^{3+} or Ga^{3+}. The interaction of aluminum (Al^{3+}) and the larger cation, gallium (Ga^{3+}) in model nuclear waste glasses

has been studied extensively to determine the implications these have on the borosilicate network and how they may increase glass strength, loading and ease of formation.

Solid-state nuclear magnetic resonance is an ideal method of observation for these four network-forming species, probing directly the local environment of ^{11}B, ^{27}Al, ^{29}Si and $^{69/71}Ga$ and allowing effects on the formers and modifiers to be observed. The glass forming species boron and intermediate-former aluminum are attractive due to their favourable NMR interactions (^{11}B: 80% N.A., Q of 4.06 fm^2 and γ of 8.58 × 10^7 rad / T s and ^{27}Al: 100% N.A., Q of 14.7 fm^2 and γ of 6.97 × 10^7 rad / T s) and good spectral resolution of various species can be achieved at moderate to high magnetic fields. The other two network species, silicon and gallium, can be troublesome for NMR. ^{29}Si suffers from low natural abundance (~4%) and longer relaxation times. Gallium has two NMR-active nuclei, both suffering from significant chemical shielding distribution and large quadrupolar moments (^{69}Ga, Q of 17.1 fm^2 and ^{71}Ga, Q of 10.7 fm^2).[4,124] This requires maximizing both field strength and spinning frequency for optimized resolution. The environments are best studied using traditional methods such as Bloch[37] and CPMG[42,44] to determine local structural building units. The glass composition 1:1:3 Na_2O:B_2O_3:SiO_2 was chosen to model the "R7T7" French nuclear waste glass, and was modified by addition of Al_2O_3 or Ga_2O_3 in place of SiO_2.[138] REDOR[50], MQMAS[246] and statistical mechanics[232] were used to determine proximity and connectivity within these systems.

5.2.1. Materials and Methods

5.2.1.1. Synthesis

Reagent grade (> 99%) Na_2CO_3, $B(OH)_3$, Al_2O_3, Ga_2O_3 and $SiO(OH)_3$ were used to prepare the amorphous materials. Boric and silicic acids were heated to 600°C and 950°C, respectively, to dehydrate the species and obtain B_2O_3 (30 minutes) and SiO_2 (16 hours). The remaining starting materials were placed in an oven at 140°C for 24 hours to remove any surface water. Stoichiometric ratios (nominal batch compositions given in Table 5.1) were then placed in platinum/gold(5%) crucibles at 700°C to decarbonate the Na_2CO_3. Samples were kept at this temperature until the mass loss corresponded to the appropriate CO_2 loss (approximately four hours). These decarbonated powders were then ground in an agate mortar and pestle, placed in a Pt/Au(5%) ZGS (zirconia grain stabilized) crucible and heated to 1400°C for 20 minutes, followed by rapid quenching in deionized water. All samples were doped with 0.2 wt% of MnO_2 to reduce relaxation times, resulting in glass disks that were transparent with a slight shade of light purple/blue. Glasses were formed in 500 mg batches (Table 5.1). Glasses were weighed before and after the heat treatments to confirm decarbonation and that no volatilization occurred.

Table 5.1. Nominal batch compositions for NaBSi phases with Al and Ga addition.

Sample	Na_2O (mol%)	B_2O_3 (mol%)	SiO_2 (mol%)	Al_2O_3 (mol%)	Ga_2O_3 (mol%)
NBS	20	20	60	0	0
NBSA-5	20	20	55	5	0
NBSA-10	20	20	50	10	0
NBSA-15	20	20	45	15	0
NBSG-5	20	20	55	0	5
NBSG-10	20	20	50	0	10
NBSG-15	20	20	45	0	15

5.2.1.2. Nuclear Magnetic Resonance

Nuclear magnetic resonance was performed using a Varian ^{UNITY}INOVA 600 spectrometer. The Bloch, CPMG and MQMAS experiments were performed using a 3.2 mm double-resonance Varian-Chemagnetics H(F)-X probe. REDOR experiments used a 3.2 mm triple-resonance Varian-Chemagnetics H(F)-X-Y probe, doubly tuned to 158.6 MHz (^{23}Na), 156.6 MHz (^{27}Al) and 192.4 MHz (^{11}B) for ^{27}Al{^{11}B} and ^{11}B{^{23}Na}. Glass samples were packed into 22 µl zirconia rotors containing 30 to 45 mg of powdered sample. The experimental details for each nucleus studied can be found in Table 5.2. The N_4 values were obtained by integrating the relative intensities between $^{[4]}$B and $^{[3]}$B, and correcting these values as described by Massiot et al.[123] REDOR experiments were carried out using 8 kHz MAS on a 3.2 mm ZrO_2 rotor with optimized pulses ^{11}B(π were $^{[3]}$B (2.8 µs) and $^{[4]}$B (4 µs)), ^{23}Na (5.0 µs π/2) and ^{27}Al (2.5 µs π/2).

The $^{27}Al\{^{11}B\}$ and $^{11}B\{^{23}Na\}$ REDOR spectra were acquired using 128 and 32 co-added transients respectively and processed using SpinWorks.[80] SIMPSON® simulations were carried out on ^{27}Al-^{11}B and ^{11}B-^{23}Na spin pairs in order to estimate the dipolar interaction.[81]

Table 5.2. Experimental parameters for MAS NMR experiments

Nucleus	**^{11}B**	**^{23}Na**	**^{27}Al**	**^{29}Si**	**^{71}Ga**
Sequence	Bloch	Bloch	Bloch	CPMG	Bloch
ν_{rf} (kHz)	65	61	61	55	45
Flip angle	15	12	15	90, 180	22
Spinning Freq. (kHz)	16	16	16	10	20
Scans	128	256	512	64-512	25 000
Recycle Delay (s)	3 – 5	2 – 5	3 – 5	180-300	1 – 3
Reference	0.1M H_3BO_3 (19.6 ppm)	1M NaCl (0.0 ppm)	0.1M $Al(NO_3)_3$ (0.0 ppm)	Hexamethyl -disiloxane (6.68 ppm)	1M $Ga_2(SO_4)_3$ (0.0 ppm)

5.2.1.3. Polarized Light Microscopy and X-Ray Diffraction

Amorphous samples were examined for crystalline phases using polarized light microscopy. All samples were homogeneous and free of crystallinity, except for the

high alumina borosilicate (NBSA-15), which showed small crystalline inclusions (on the order of a few microns). This was later confirmed using powder x-ray diffraction and ^{27}Al MAS NMR, indicating that a small fraction of crystalline γ-Al_2O_3 phase did not completely react with the NaBSi material. It most likely required a longer heating time or a higher melting temperature. The concentration of the crystalline impurity was determined to be an insignificant fraction (<3%) of the total aluminum concentration, and is not expected to affect significantly the measurements.

5.2.2. Results

5.2.2.1. Sodium-23 MAS NMR

Typical ^{23}Na MAS NMR spectra are observed for these sodium borosilicate glasses (Figure 5.7). Peak shapes are symmetric, indicating that breadths are caused by a distribution in chemical shift. The δ_{cgs} for all seven glasses are found in the range -13 ± 1 ppm. Estimates of the maximum quadrupolar couplings for these glasses were measured from the central transition using STARS® and are on the order of 3 ± 0.5 MHz. As seen in other systems,[90,119] this induces a quadrupolar shift on the order of ca. 1 ppm (150 Hz), enabling us to use the δ_{cgs} to determine the effect on sodium as aluminum and gallium are added.

Aluminum addition causes a small shift to higher frequency for the sodium resonance (~1 ppm). If we assume that the coordination environment for sodium does not change for these glasses (valid due to the large sodium shifts seen for sodium borates) this could be caused by aluminum interacting with the Na^+ "directly" as

silicon is being replaced by aluminum. Gallium causes similar effects as the ^{23}Na resonance shifts ~ 3 ppm to a higher frequency as silicon is replaced by gallium.

The cause for the different effects on the ^{23}Na chemical shifts is not currently understood. We can speculate that gallium is larger, thus providing a larger variation for the Na^+ while associating with $^{[4]}Ga$ polyhedra. This is reasonable as gallium allows for more variation for the sodium to sit within (as the GaO_4^- polyhedron are larger than AlO_4^- and BO_4^-). The FWHM in the ^{23}Na spectra for the aluminum and gallium borosilicate show (Figure 5.7) similar behaviour, as the resonance narrows by 550 ± 50 Hz (ca. 14%) as Al(Ga) is added. This decrease in breadth could be caused by a reduction in variation in the sodium geometry (angles and bonds) or a reduction of the quadrupolar coupling. When these interactions decrease, this is often attributed to an increase in order and is thought to occur since most of the sodium cations are being pulled away from borate and silicate polyhedra into aluminum and gallium polyhedra reducing the amount of variability. Although silicon is the most electronegative species, Na^+ will be attracted to polyhedra that contain a negative charge. As the aluminum (and gallium) concentrations increase, NBOs of silicon and the fraction of $^{[4]}B$ decrease (see below) leaving AlO_4^- (GaO_4^-) as the main charge compensator.

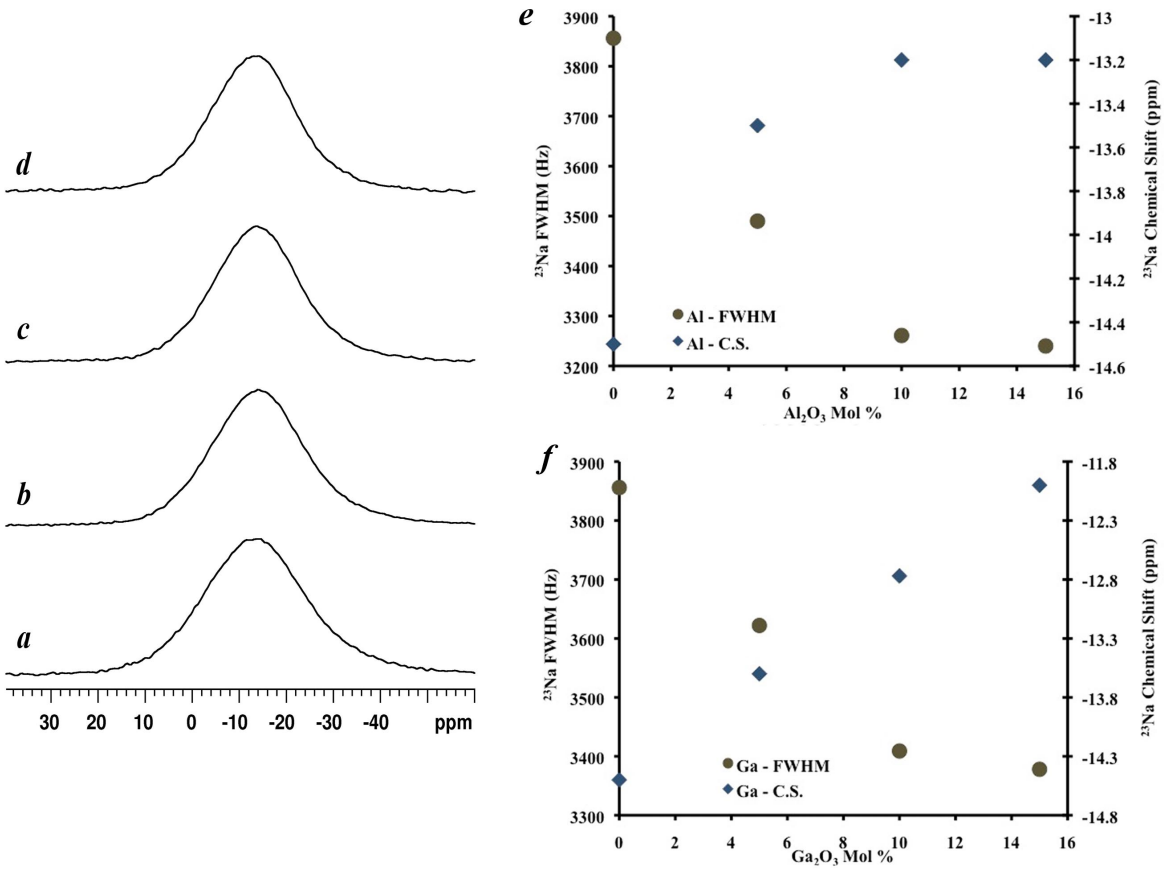

Figure 5.7. ^{23}Na MAS NMR spectra for NBS containing Al, (a) NBS, (b) NBSA5, (c) NBSA10 and (d) NBSA15. Effect on ^{23}Na CT breadth and δ_{cgs} for (e) Al and (f) Ga doped sodium borosilicate glasses.

5.2.2.2. Aluminum-27 MAS NMR

^{27}Al MAS NMR data (Figure 5.8) show symmetric peak shapes again indicating a distribution in chemical shift. An upper bound for the quadrupolar coupling constant was estimated from the central transition to be approximately 5 ± 1 MHz, determined from STARS®. The chemical shift (δ_{cgs}) was 57 ± 2 ppm (FWHM of 15 ppm).[244] These ^{27}Al MAS NMR data indicate that all aluminum atoms are four-coordinate.[2,232] From the estimate of the quadrupolar coupling interaction, the second-order quadrupolar

effect is ~900 Hz, which gives a δ_{iso} of 61 ± 5 ppm (section 1.6.3). The NBSA-15 glass contains a small sharp resonance located at 0 ppm (< 3%), which is assigned to a crystalline phase of γ-Al_2O_3 (starting material). This occurred as a result of incomplete mixing during the melt process, which was also confirmed using powder x-ray diffraction. As the concentration is small, this is not expected to influence the measured trends.

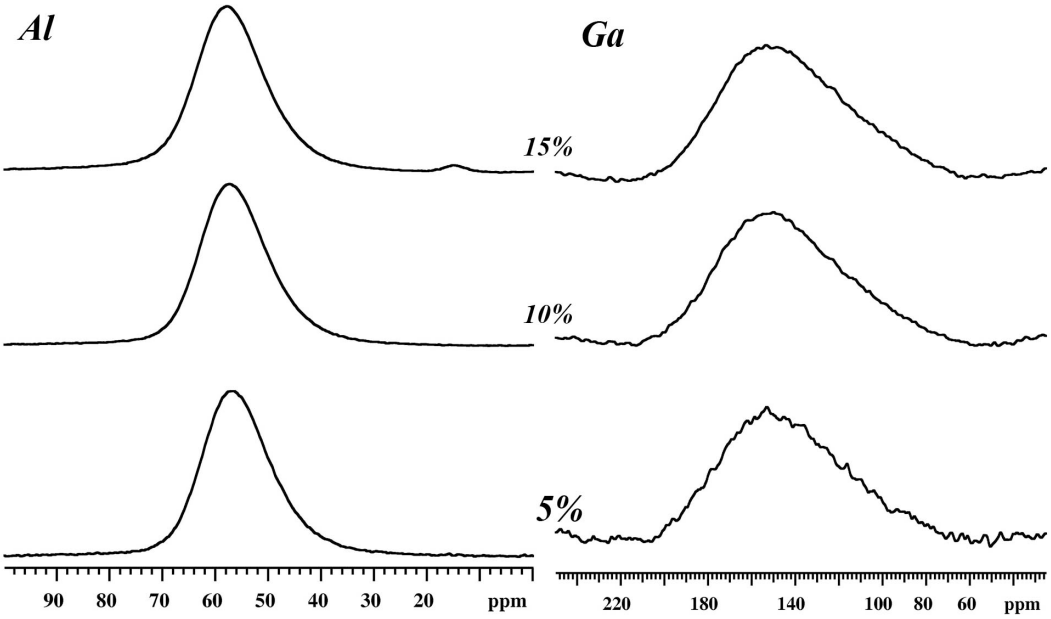

Figure 5.8. ^{27}Al MAS NMR and ^{71}Ga MAS NMR spectra of the doped sodium borosilicates (5 to 15 %).

5.2.2.3. GALLIUM-71 MAS NMR

^{71}Ga MAS NMR spectra (Figure 5.8) show a peak shape that is asymmetric. This asymmetry is attributed to a distribution in quadrupolar couplings, as observed in

other aluminum and gallium containing glasses.[14,247] The large quadrupole moment for gallium prevents true isotropic chemical shifts from being determined. However the δ_{cgs} for all three glasses is 154 ± 7 ppm, with an estimated maximum quadrupolar interaction of 7 ± 1.5 MHz similar to those seen in other gallium containing glasses.[4,14,247] The δ_{cgs} values indicate that the gallium coordination environment contains four oxygens ($^{[4]}$Ga) with a delocalized negative charge (as seen with the aluminum doped glasses). The chemical shift range for $^{[5]}$Ga and $^{[6]}$Ga are 25 ppm to 110 ppm and -100 ppm to 25 ppm respectively, supporting this assignment.[4,248] The second-order quadrupolar effect is on the order of 8 kHz which corresponds to δ_{iso} of 197 ± 30 ppm.

5.2.2.4. Silicon-29 MAS NMR

^{29}Si CPMG MAS NMR spectra are shown for the aluminum- and gallium-containing borosilicates (Figure 5.9). Based on the chemical shift distribution from NBS glass, there is evidence that both Q^4 (-100 to -120 ppm) and Q^3 (-80 to -100 ppm) sites are present with the possibility of Q^2 (-70 ppm to -85 ppm).[4] Fitting the ^{29}Si spectra of glasses is difficult to do reliably, due to significant peak overlap; nevertheless, we used the known ^{29}Si chemical shift ranges for various Q-speciation as a qualitative guide. The overall trend for both aluminum- and gallium-containing glass is that the δ_{cgs} moves to higher frequency as the concentrations of aluminum and gallium are increased, implying net depolymerisation of the silicon network.

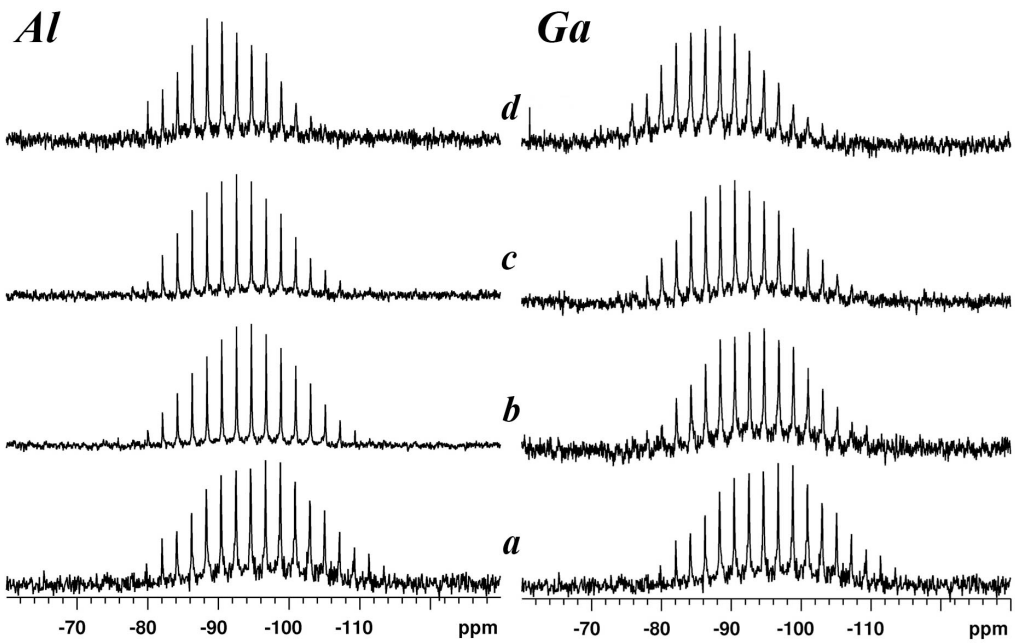

Figure 5.9. ^{29}Si MAS NMR CPMG spectra for Al (left) and Ga (right) doped borosilicates with (a) 0%, (b) 5%, (c) 10% and (d) 15%, Al or Ga respectively.

5.2.2.5. BORON-11 MAS NMR

^{11}B MAS NMR spectra were acquired to quantify the fraction of four-coordinate boron. Figure 5.10 illustrates $^{[3]}$B (8 to 20 ppm) and $^{[4]}$B (4 to -4 ppm) resonances. The quadrupolar couplings for both $^{[3]}$B and $^{[4]}$B were determined from the breadth of the ssb manifold to be 2.6 ± 0.2 MHz and 520 ± 50 kHz, respectively, agreeing with previous studies.[9,90,244] MQMAS spectra indicate no evidence of NBOs on boron. These data however do show an increase in distributions of bridging oxygen species as aluminum and gallium are introduced due to the smearing of the resonance to higher and lower frequencies (Figure 5.11).

The fraction of $^{[4]}$B is shown in Figure 5.10, where a linear decrease occurs for both aluminum and gallium at comparable fractions. As aluminum or gallium is added, the charge balance required for the NBS glass is relieved, causing a decrease in the N_4. This is attributed to the onset of $^{[4]}$Al ($^{[4]}$Ga) whereby a delocalized negative charge neutralizes the sodium cationic charge. Although the behaviour of aluminum and gallium are similar (Figure 5.10) the decrease in $^{[4]}$B is slightly more effective with the addition of aluminum. The exact cause for this occurrence is not currently known as gallium is expected to behave identically. A possible explanation for this discrepancy is that gallium could potentially create an imbalance between silicon NBOs and $^{[4]}$B. Aluminum perhaps pulls sodium from both $^{[4]}$B and Q^3 species as it is incorporated. Gallium may cause NBOs on silicon to be more unfavourable, preventing Na^+ to interact directly with the silicate network. This would cause the higher fraction of $^{[4]}$B since it has to charge compensate the Na^+ that would normally be interacting with silicon. Further studies perhaps using REDOR could be used to probe this more precisely to determine possible environments exhibited by aluminum, gallium, $^{[4]}$B and silicon.

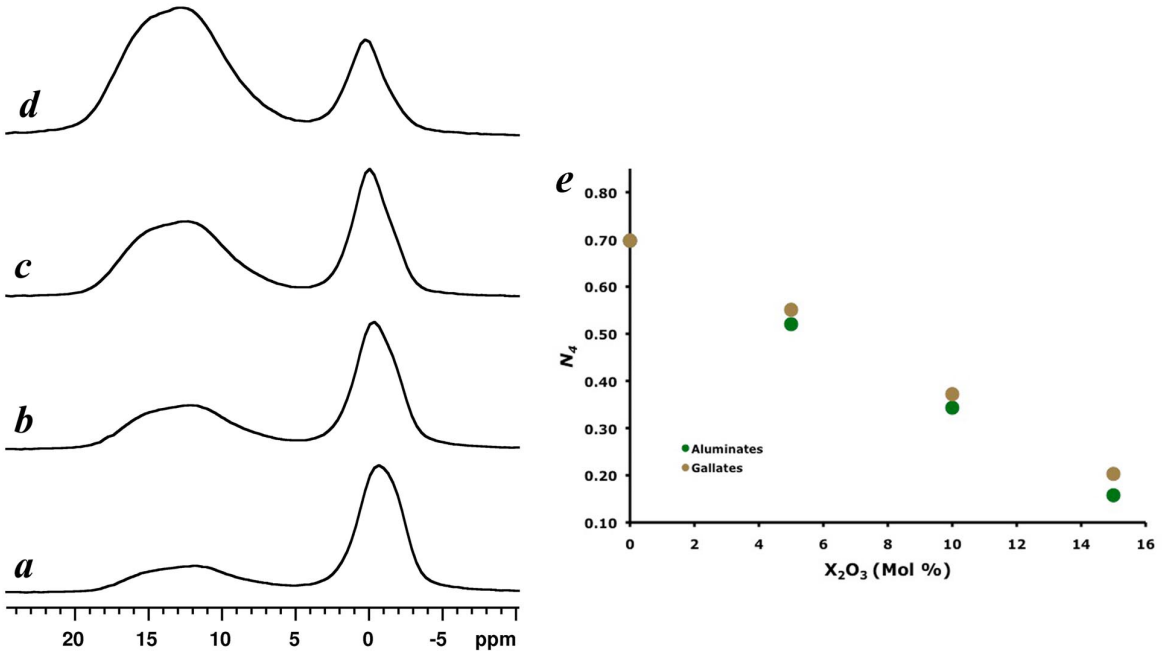

Figure 5.10. ^{11}B MAS NMR spectra of the Ga-doped NaBSi glasses, (a) NBS, (b) NBSG5, (c) NBSG10, (d) NBSG15 and (e) fraction of $^{[4]}B$ as a function of X_2O_3 (X = Al or Ga).

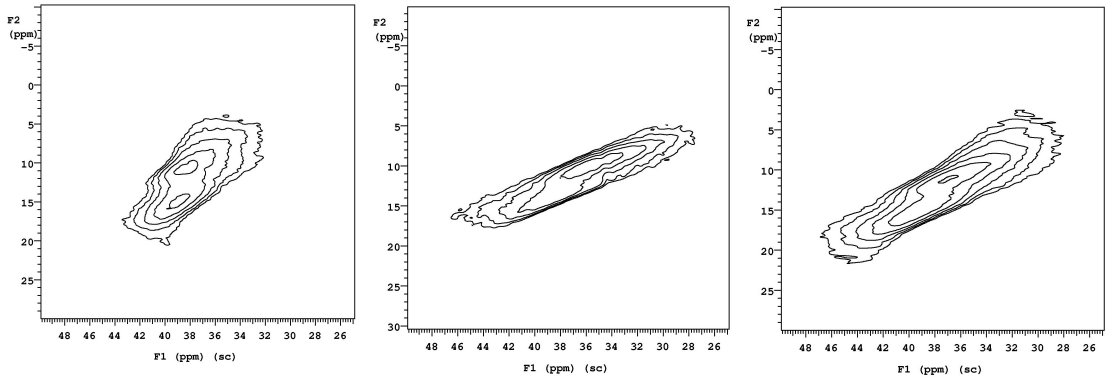

Figure 5.11. ^{11}B 3QMAS for NBS, NBSA15 and NBSG15 glasses, respectively.

5.2.2.6. $^{27}Al\{^{11}B\}$ AND $^{11}B\{^{23}Na\}$ REDOR

5.2.2.6.1. $^{[4]}Al$-O-$^{[4]}B$ AVOIDANCE

In a variety of glass systems four-coordinate avoidance (e.g., $^{[4]}$B-O-$^{[4]}$B, $^{[4]}$B-O-$^{[4]}$Al and $^{[4]}$Al-O-$^{[4]}$Al (analogous with gallium)) is always considered. When high levels of four-coordinate species are present the statistical probability for them to interact will increase, although it is energetically unfavourable. If avoidance occurs this is an indication of ordering which should not occur if a material is defined as a randomly distributed short-range network. This is studied using the statistical mechanics model of Du and Stebbins,[232] where we calculate the fraction of bridging species from a random model and an avoidance model (Table 5.3). The following equations were used to determine the bridging oxygen environments.

$$Y^{[3]}B = 3X(^{[3]}B(T^3)) + 2X(^{[3]}B(T^2)) \quad \textbf{(5.1)}$$

$$Y^{[4]}B = 4X(^{[4]}B) \quad \textbf{(5.2)}$$

$$Y^{[4]}Al = 4X(^{[4]}Al) \quad \textbf{(5.3)}$$

$$Y^{[4]}Si = 4X(^{[4]}Si(Q^4)) + 3X(^{[4]}Si(Q^3)) \quad \textbf{(5.4)}$$

$$Y_{total} = Y^{[3]}B + Y^{[4]}B + Y^{[4]}Al + Y^{[4]}Si \quad \textbf{(5.5)}$$

$$Z = (0.5Y_{total} + X(^{[3]}B(T^2)) + X(^{[4]}Si(Q^3)) \quad \textbf{(5.6)}$$

Random Model:

$$J_{M\text{-}O\text{-}N} = (iY_MY_N/Y)/Z \quad \textbf{(5.7)}$$

Avoidance Model:

$$J_{M\text{-}O\text{-}[4]Al} = [(Y_{[4]Al})(Y_M)/(Y_{[3]B}+Y_{[4]Si})]/Z \quad \textbf{(5.8)}$$

$$J_{M\text{-}O\text{-}[4]Al} = [(Y_{[4]B})(Y_M)/(Y_{[3]B}+Y_{[4]Si})]/Z \quad \textbf{(5.9)}$$

$$J_{M,left} = Y_M - [(Y_{[4]B}+Y_{[4]Al})(Y_M)/(Y_{[3]B}+Y_{[4]Si})] \quad \textbf{(5.10)}$$

$$J_{M\text{-}O\text{-}N} = [i(Y_{M,left})(Y_{N,left})/(Y_{[3]B,left}+Y_{[4]Si,left})] \quad \textbf{(5.11)}$$

Here $X(^{[4]}B)$, $X(^{[3]}B(T^3))$, $X(^{[3]}B(T^2))$, $X(^{[4]}Al)$, $X(^{[4]}Si(Q^4))$ and $X(^{[4]}Si(Q^3))$ represent the mole fraction of $^{[4]}B$, $^{[3]}B$ (0 NBOs and 1 NBO), $^{[4]}Al$, and $^{[4]}Si$ (0 NBOs and 1 NBO) based on the total of B, Al and Si species. The values of each are determined from ^{11}B, ^{27}Al and ^{29}Si MAS NMR. The total number of species linked to bridging oxygens is denoted by Y_M, where M = $^{[3]}B$, $^{[4]}B$, $^{[4]}Al$ and $^{[4]}Si$. The total number of bridging oxygens is given by equation 5.5 and the total number of oxygens is defined as Z (equation 5.6). The fraction of each type of bridging oxygen species is defined by the term, J. The term i, in equation 5.7 can take one of two values, i = 1 for M ≠ N and I = 0.5 for M = N. The probability to find M or N does depend on the model chosen, therefore the random model is calculated using equation 5.7 while the avoidance model (i.e., some degree of ordering) is defined by equations 5.8 to 5.11.[232]

Table 5.3. Statistically determined bonding arrangement for all seven NaBSi glasses, where X is $^{[4]}$Al or $^{[4]}$Ga.

Species	Model	Si-O-Si %	B-O-Si %	X-O-Si %	B-O-B %	X-O-B %	X-O-X %	X-O-^{4}B %	^{4}B-O-^{4}B %
NBS	Random	36.3	44.8	0	5.2	0	0	0	8.6
	Avoidance	29.6	58.3	0	7.1	0	0	0	0
NBSA5	Random	29.9	36.8	11.0	7.1	2.6	1.0	4.3	4.5
	Avoidance	22.9	44.4	16.2	9.2	3.8	0	0	0
NBSA10	Random	23.3	30.0	19.0	7.9	7.0	3.9	5.3	1.8
	Avoidance	17.4	32.2	28.5	9.5	10.5	0	0	0
NBSA15	Random	17.7	24.4	23.9	8.1	13.1	8.1	3.4	0.4
	Avoidance	12.7	21.7	36.5	8.1	20.0	0	0	0
NBSG5	Random	29.2	36.9	11.0	6.7	2.4	1.0	4.5	5.0
	Avoidance	22.2	45.7	16.4	9.0	3.6	0	0	0
NBSG10	Random	23.4	30.3	19.0	7.7	6.6	3.9	5.7	2.1
	Avoidance	17.0	33.2	29	9.5	10.0	0	0	0
NBSG15	Random	18.0	24.7	24.1	7.9	12.2	8.0	4.3	0.6
	Avoidance	12.3	22.5	37.6	8.3	19.1	0	0	0

From these calculations, a fraction of bridging species ($^{[4]}$B-O-X) should exist in a random model (between 3 to 6 %), in regards to bridging species involving $^{[3]/[4]}$B and $^{[4]}$Al ($^{[4]}$Ga) bonding it accounts for 20 to 60% of boron species. To probe bridging

environments by NMR one typically has to isotopically enrich the sample with ^{17}O and acquire ^{17}O MQMAS. An alternative approach, which requires no enrichment and can be applied to probe $^{[4]}B$-O-$^{[4]}Al$ connectivities is $^{27}Al\{^{11}B\}$ REDOR. Within NBSA15 glass a random model predicts that 25% of all bridging borons should be $^{[4]}B$-O-$^{[4]}Al$.

This fraction is large enough that REDOR should be able to determine whether $^{[4]}Al$ are neighbouring $^{[4]}B$ (i.e., breaking the avoidance rule). Figure 5.12 shows $^{27}Al\{^{11}B\}$ REDOR for both $^{[3]}B$ and $^{[4]}B$, with pulses selected to obtain maximum excitation and dephasing for both ^{27}Al and ^{11}B. The two distinct boron species contain drastically different quadrupolar interactions (2.6 MHz ($^{[3]}B$) and 520 kHz ($^{[4]}B$)) and can be selected by using proper pulse widths. This will allow for maximum excitation of $^{[4]}B$ over $^{[3]}B$ and vice versa.[85,249] The $^{[3]}B$ has a much stronger REDOR curve (Figure 5.12) attributed to a stronger interaction, whereas the $^{[4]}B$ is much weaker, being further away. Due to our system being amorphous, is not an isolated spin-pair and involves quadrupolar nuclei, direct bond distances cannot be measured. However, we can use the dipolar interaction between ^{11}B and ^{27}Al, to measure an average B-Al interaction with the aid of SIMPSON® calculations in order to extract information on proximity. We constructed a ^{27}Al – ^{11}B spin-pair with appropriate quadrupolar interactions and varying degrees of dipolar interactions to obtain simulated REDOR curves, on which basis it was determined that the REDOR curve associated with $^{[4]}B$-O-$^{[4]}Al$ is on the order of ~75 (20) Hz, whereas the $^{[3]}B$-O-$^{[4]}Al$ is on the order of ~400 (40) Hz. As the dipolar interaction between $^{[4]}B$ and $^{[4]}Al$ is small this indicated that these two species were not in proximity to one another, thus concluding that some ordering does occur within these disordered species. This also supports the previous

assertion that only Q^4 and T^3 species are surrounding $^{[4]}B$, where the observation of $^{[4]}B$ narrowing suggested a decrease in disorder (i.e., increase in ordering, not randomly mixed).

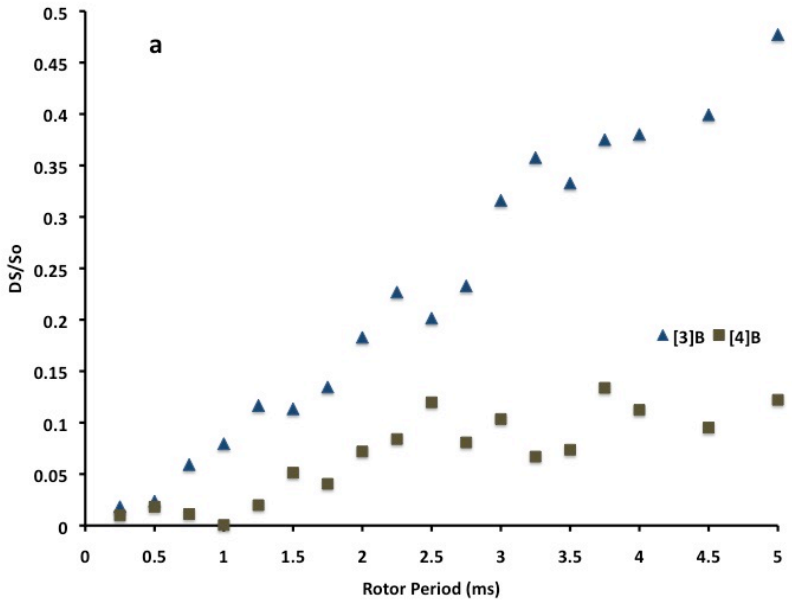

Figure 5.12. $^{27}Al\{^{11}B\}$ REDOR for NBSA15 glass, the $^{[4]}B$ (squares) has a weak dephasing curve, while the $^{[3]}B$ (triangles) illustrates a strong dephasing curve. This provides evidence of Al interacting strongly with $^{[3]}B$, while avoiding $^{[4]}B$

5.2.2.6.2. $^{23}Na^+$ INTERACTING WITH $^{[4]}B/^{[4]}Al$ POLYHEDRA

REDOR was also used to probe modifier proximity within the substituted borosilicate. $^{11}B\{^{23}Na\}$ REDOR can be used to determine where the Na^+ sit within the borosilicate network as has been done with sodium borates.[250] Three glasses (NBS, NBSA15 and NBSG15) were probed with $^{[3]}B$ ($^{11}B\{^{23}Na\}$-REDOR), showing similar behavior (Figure 5.13). This confirms that Na^+ cations interact minimally with $^{[3]}B$, and all boron

species are bridging T^3 units, as predicted by Dell and Bray and in agreement with the ^{11}B MQMAS data. Comparison of the relative Na^+ - $^{[4]}B$ interaction was also done for the same three glasses. The NBS glass has a very strong REDOR curve due to $^{[4]}B$ and Q^3 species maintaining charge balance. However, the NBSA15 and NBSG15 glasses have $^{[4]}B$ REDOR curves showing a weaker dephasing curve (although stronger than for the $^{[3]}B$ glass). This shows that some Na^+ is still within the vicinity of $^{[4]}B$, while the majority has moved to $^{[4]}Al$ ($^{[4]}Ga$), providing evidence that the Na^+ has moved; these results agree with the fraction of $^{[4]}B$ and charge balance model calculations.

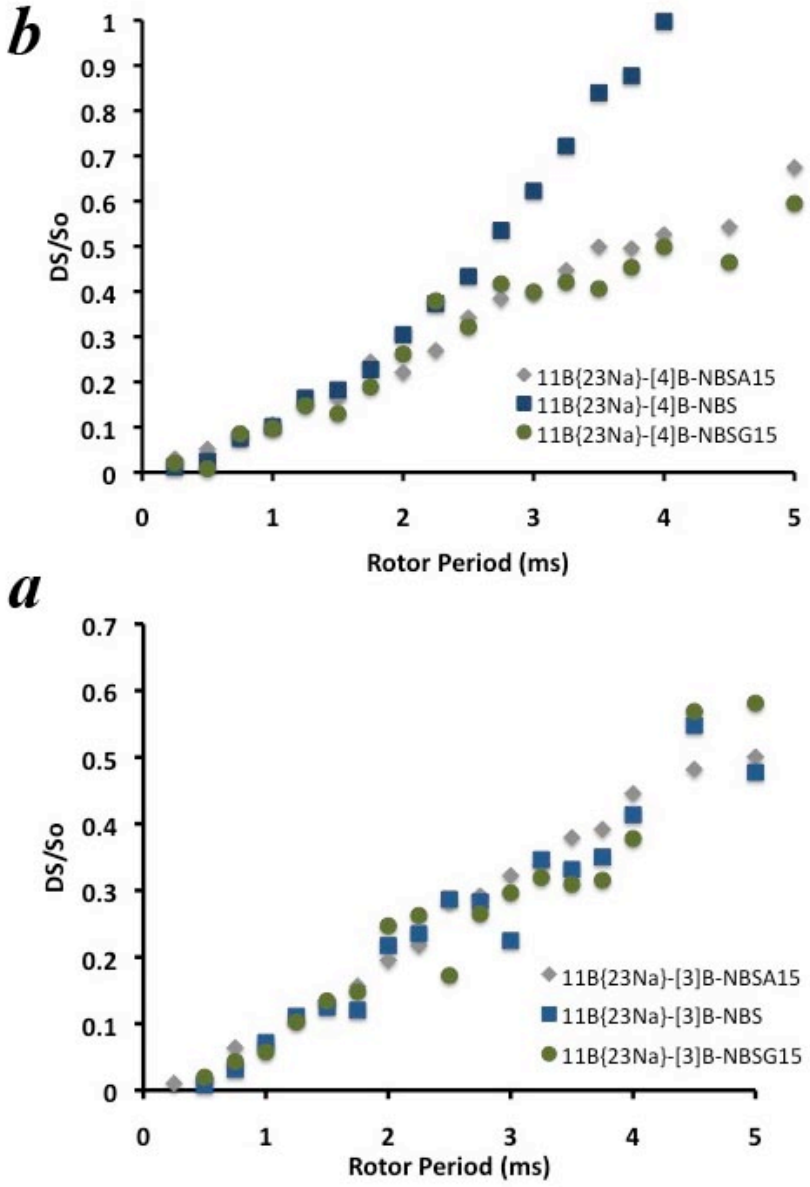

Figure 5.13. $^{[3]}$B and $^{[4]}$B, ^{11}B{^{23}Na} REDOR curves for NBS (squares), NBSA15 (diamonds) and NBSG15 (circles). NBS, NBSA15 and NBSG15 for the Na/$^{[3]}$B all have similar interactions indicating similar $^{[3]}$B-Na^{+} behaviour. For the Na/$^{[4]}$B REDOR curves the NBS glass has the strongest interaction while Al and Ga containing glasses are weaker. These weaker interactions are attributed to Na^{+} preferentially interacting with Al (Ga).

5.2.3. Discussion

5.2.3.1. Borosilicate Modification

Modification of the borosilicate phase occurs by an alkali modifier (Na^+) and the addition of 5, 10, and 15 mol% intermediate glass formers (Al_2O_3 / Ga_2O_3). The ^{23}Na spectra indicate a shift to higher frequency (< 3 ppm total) for both the aluminum and gallium series, accompanied by a narrowing of the central transition (Figure 5.7). The change in shift can be due to either a change in coordination number or local Na^+ environment. As seen for borates[90] and silicates[251], a chemical shift change to higher frequency occurs with the increase in concentration, implying a decrease in the average coordination sphere. The addition of aluminum (gallium) to borosilicate will affect the overall glass network as we maintained a constant ratio of Na_2O/B_2O_3, R=1. These small shifts seem to be caused by the neighbouring polyhedra and not the coordination number. This explanation is reasonable as the sodium cation will interact with the negatively charged $^{[4]}Al$ ($^{[4]}Ga$). Furthermore, the AlO_4^- (GaO_4^-) tetrahedra will be larger than $^{[4]}B$, interacting from a further distance. Although longer interactions allow an increase in coordination, the chemical shift changes seem to be minor relative to those observed above for sodium borates.

The ~15% decrease in width for the sodium resonance can be caused by Na^+ motion or a decrease in the distribution around the Na^+. For these glasses Na^+ mobility generally requires higher temperatures (i.e., >50°C), unlike Li^+.[84,165,212] A decrease in distribution could explain these results as a decrease in silicon concentration and an increase in aluminum (gallium) will shift the balance of charge-containing species. Silicon Q^3s will be decreased as the Na^+ is balanced by $^{[4]}Al$ ($^{[4]}Ga$)

and [4]B. Even though when adding an extra former one would expect an increase in disorder, the local sodium environments would no longer be exposed to NBOs and would be charge-balanced mainly by pseudo-tetrahedral units from group III (i.e., BO_4^-, AlO_4^- or GaO_4^-) with a delocalized negative charge.

Aluminum and gallium are known as 'intermediate' network formers as they cannot form glasses on their own. They will, however, participate in covalent bonding and network connectivity when combined with a network-forming cation.[2,243] Incorporation of aluminum (gallium) into a borosilicate glass typically occurs as a four-coordinate species (identical to [4]B) with a delocalized negative charge over the AlO_4^- (GaO_4^-) unit.[2,4] The glasses studied show no evidence of higher coordination environments as seen in other boroaluminates,[14,252] borogallates,[14] aluminosilicates and borosilicates.[245,253] The broad aluminum and gallium resonances compared to the narrow four-coordinate resonance are caused by a large quadrupole moment and increased sensitivity to distortions in geometry. Gallium-containing sodium borosilicate glasses exhibited broad (~50 ppm) non-Gaussian shaped resonances (unlike [4]Al), with a low frequency tail. The tail was determined to be caused by a distribution in the quadrupolar coupling constants.[34,254] Although not the case presented here, low frequency tails must be treated carefully as they can be caused by higher coordinate species such as [5]Ga or [5]Al as seen in the heavy metal oxide borogallates[14] studied by our group, and also in calcium aluminosilicates.[245]

The crystalline Al_2O_3 phase present in the NBSA15 glass was not observed for the analogue Ga glass (NBSG15). This is not surprising as Ga_2O_3 (T_m=1806°C) has a

lower melting point than Al_2O_3 (T_m = 2046°C), allowing incorporation into the borosilicate network without crystallization.[16]

5.2.3.2. SILICON SPECIATION

^{29}Si MAS NMR spectra were analyzed qualitatively for features relating to the silicon network. The Carr-Purcell-Meiboom-Gill sequence provides these spectra within a reasonable timescale (~1 - 4 hrs), as opposed to traditional Bloch experiments (~ 24 hrs). Basic charge-balance calculations (below) indicate that the NBS glass requires 17% NBOs located on silicon polyhedra. For all glasses, Q^4 will be >80%, while Q^3 will be <20% to maintain charge balance. Q^2 is unlikely to be present, as this would typically require ~50% NBOs on the silicate units and NBOs on boron prior to further breakdown within the silicate polyhedra. Furthermore, we found no evidence for T^2 units (NBOs on boron). The charge balance equations used to determine Q^3 speciation are:

$$C_{[4]B} = N_4 \bullet [B_2O_3] \bullet 2 \quad \textbf{(5.12)}$$

$$C_{NBO} = (1 \bullet T^2) + (2 \bullet T^1) + (3 \bullet T^0) \quad \textbf{(5.13)}$$

$$C_{Cation} = \text{sum}(CC \bullet M) \quad \textbf{(5.14)}$$

$$C_{[4]X} = f_{[4]X} + 2 \bullet X_2O_3 \quad \textbf{(5.15)}$$

$$Q^3 = [C_{[4]B} + C_{NBO} + C_{[4]X}] - C_{Cation} \quad \textbf{(5.16)}$$

$$Q^4 = Si\text{-}Q^3 \quad \textbf{(5.17)}$$

Here N_4 is the fraction of $^{[4]}$B from the NMR data, T^2,T^1,T^0 are the non-bridging oxygen species on boron (if there is only T^3 then this term is zero, as in our case), M is the number of modifying cations, CC is the charge (e.g., 20Na, +1), $f_{[4]X}$ is the fraction of

X (X = $^{[4]}$Al or $^{[4]}$Ga) determined from the NMR spectrum, and Si is the total number of Si units.

Table 5.4. NaBSi glass charge balance speciation based on equations 5.12 - 5.17.

Sample	N_4 (1%)	# $^{[4]}$B	# $^{[4]}$Al	# $^{[4]}$Ga	# Na	Total +'ve	Total –'ve	Q^3	Q^4	% Q^3
NBS	0.70	28	0	0	40	40	28	12	48	20.0
NBSA5	0.52	21	10	0	40	40	31	9	46	16.4
NBSA10	0.34	14	20	0	40	40	34	6	44	12.0
NBSA15	0.16	7	30	0	40	40	37	3	42	6.7
NBSG5	0.55	22	0	10	40	40	32	7	48	12.7
NBSG10	0.37	15	0	20	40	40	35	5	45	10.0
NBSG15	0.20	8	0	30	40	40	38	2	43	4.4

The change in ^{29}Si shifts are caused by $^{[4]}$Al (or $^{[4]}$Ga) next-nearest neighbours substituting into the network as the ratio of Al (Ga) is increased. This substitution (change in second coordination sphere) causes the ^{29}Si δ_{iso} to shift to a higher frequency masquerading as Q^2 formation.[4] The increase in aluminum (gallium) concentration correlates linearly with the δ_{cgs} shift to higher frequency, further confirming this explanation. For the NBS glass, recent molecular orbital calculations suggest similar shifts for boron, whereby a shift to higher frequency occurs as SiO_4 neighbours are replaced by BO_3 and/or BO_4^- units, even if only to a small degree.[255]

The number of aluminum (gallium) neighbours can be estimated by using the observed shift and taking into account the statistical probabilities of having aluminum (gallium) around a silicon species. The results based on chemical shift and ratios of aluminum to silicon (not taking into account boron) suggest 0.5 to 2 aluminum (gallium) neighbours per silicon species. Since boron is also present, the exact distribution of aluminum (gallium) within the borosilicate network is not known, precluding the determination of an exact number. However this provides an upper bounds of 2Al (Ga) neighbours per Si unit.

5.2.3.3. Boron speciation

^{11}B MAS NMR spectra show a drastic reduction of four-coordinate boron as N_4 decreases from 70% (NBS) to 15% (NBSA15) and 20% (NBSG15). This results in a high-R glass composed of a large fraction of $^{[3]}$B (up to 85%). The incorporation of $^{[4]}$Al ($^{[4]}$Ga) shifts the balance of $^{[3]}$B/$^{[4]}$B as these cations serve as charge-balancing polyhedra. The balance shifts because aluminum (gallium) forms four-coordinate tetrahedra, drawing the Na^+ away from boron and silicon as these glass-forming species bridge oxygens and are maintained as neutral species. The breadth of the $^{[4]}$B peak (Figure 5.10) decreases systematically with addition of aluminum (gallium). As seen in the cesium borosilicates, the $^{[4]}$B site is often sensitive to medium range order. This decrease indicates an increase in local ordering around the $^{[4]}$B resonance. Although multiple $^{[4]}$B resonances are not observable, possible coordinating species for NBS include $^{[3]}$B, Q^4 and Q^3 species. As aluminum (gallium) is added to the borosilicate network, Q^3 become Q^4 and a large reduction in N_4 occurs. This causes the environments of the $^{[4]}$B to have only Q^4 silicate or T^3 borate neighbours (note that $^{[4]}$B

is unlikely to be bonded to AlO_4^- (GaO_4^-) neighbours due to the associated charge repulsion that would occur ($^{[4]}$B-O-$^{[4]}$X, X = Al, Ga, $^{[4]}$B)). Additionally, AlO_4^- (GaO_4^-) is substituting for silicon, decreasing its concentration relative to boron and further ordering the second coordination sphere of $^{[4]}$B (as this creates fewer neutral species that can bond with $^{[4]}$B). Although counter-intuitive, the presence of more types of neighbouring species (i.e., B, Al (Ga) and Si) appears to decrease the distribution of neighbours about $^{[4]}$B. In other words causing less distortion of the BO_4 tetrahedron.

The resonance of $^{[4]}$B is affected in a similar manner whether aluminum or gallium is substituted into the glass, agreeing with previous studies that gallates behave similarly to aluminates.[2] However, N_4 is always slightly higher for Ga-containing glasses than in the Al-containing borosilicates indicating some sort of difference in charge balance. Aluminum containing borosilicates appear to be more efficient at minimizing the fraction of four-coordinate boron than gallium-based borosilicates. Although why this may be is not understood; aluminum could be more efficient at substituting for silicon since it is comparable in size (r_{Si} = 111 pm, r_{Al} = 118 pm, r_{Ga} = 126 pm). The difference in behaviour could provide a fine-tuning ability that could be applied to a variety of borosilicate-based materials, using small concentrations of gallium instead of aluminum. The relationship between the N_4 and aluminum (gallium) substitutions ranging between 1 to 20 mol% X_2O_3 is determined to be:

$$N_4^{[Ga]} = 0.915\ N_4^{[Al]} + 0.07 \qquad (5.18)$$

The chemical shift of $^{[4]}$B is assigned to a $^{[4]}$B with one $^{[3]}$B and three silicon polyhedra as determined in other sodium borosilicates.[205] The $^{[3]}$B shift seems to increase in frequency as aluminum (gallium) is added. Although it is the left edge being measured and not the true isotropic chemical shift (difficult due to a distribution of sites and a C_Q of 2.6 (± 0.1) MHz), it does provide weak evidence that aluminum and gallium affect the interaction of the $^{[3]}$B environment. Typically this is associated with the formation of non-bridging oxygens on boron, such as a T^2. For these glasses, charge balance indicates that T^2 units are not required, especially with such a low concentration of Q^3.[199] This was further confirmed by acquiring ^{11}B MQMAS spectra (Figure 5.11), which indicated only T^3 species. However it did reveal a large distribution of sites within the glass when compared with a borate glass. The measured shift to higher frequency is attributed to a decrease in silicon neighbours as aluminum and gallium concentrations are increased.[4]

5.2.4. SUMMARY

Multinuclear magnetic resonance revealed short and medium-range structures for a series of aluminum- and gallium-substituted NaBSi glasses. The measured effect in ^{23}Na MAS NMR measured shifts were small but interesting due to a large effect seen in ^{133}Cs MAS NMR for cesium borosilicates (section 5.1). This suggests that the Na^+ environment is not nearly as sensitive to silicon as the Cs^+ seemed to be. ^{27}Al and ^{71}Ga MAS NMR indicated four-coordinate speciation. The addition of aluminum (gallium) caused measurable effects on the ^{11}B, ^{23}Na and ^{29}Si environments in regards to peak widths, chemical shifts and REDOR measurements. Combining one-dimensional experiments, charge balance calculations, MQMAS and REDOR, the borosilicate

network was determined to be composed of Q^3 and Q^4 polyhedra for silicon, and T^3 and $^{[4]}B$ for boron. We have shown an alternate approach to probe possible avoidance without the need for costly isotopic enrichment. A combination of REDOR and statistical modeling shows that these glasses exhibit $^{[4]}B$-O-$^{[4]}Al$ avoidance. These results indicate that the addition of aluminum (gallium) creates a more "ordered" glass network. This approach could be extended to other materials that are expected to display avoidance or a need to probe the proximity of various cations within a matrix. In regard to structure and strength these small modifications decrease the number of NBOs and increase polymerization potentially providing a stronger based borosilicate material. The distinct behaviour for Ga^{3+} in the ^{11}B MAS NMR data shows that aluminum and gallium behave similarly, although a difference in charge units must occur to account for the difference in N_4.

6. GERMANATES

Certain nuclei suffer from very unfavourable properties, which impede or limit their study by NMR. They may have low natural abundance, low gyromagnetic ratio, large quadrupolar moments or have inefficient relaxation mechanisms. In fact, many nuclei which I will refer to as ultra-low gamma (those whose gamma is ½ that of ^{15}N) suffer from a combination of these issues; they include ^{235}U, ^{197}Au, $^{191/193}$Ir, ^{73}Ge, ^{177,179}Hf, etc.

^{73}Ge NMR is often avoided despite the importance of germanium in glassy, crystalline and mineral forms. Recent increases in magnetic field and the construction of lower-gamma NMR probes have provided the ability to probe crystalline and glassy germanates. We have extensively studied oxides of germanium, laying a foundation of NMR parameters previously unknown for this nucleus.

6.1. CRYSTALLINE GERMANATES

Germanium is used in many materials applications including optical fibers and lenses, catalysts, mesoporous materials, and nanocrystalline semiconductors,[256-259] where the lack of periodic long-range order limits diffraction-based structural investigations. The characterization of germanium in these systems is far from routine, despite the fact that their physical properties are often determined by their local structure.[257,260] In principle, germanium nuclear magnetic resonance (NMR) spectroscopy is ideal for studying such effects, as it is sensitive to the local environment of the nucleus of

interest. However, the only NMR active isotope (^{73}Ge), suffers from unfavourable NMR properties, and has traditionally been considered as an "impossible" nucleus to study in the solid state.[261] The nuclear properties of ^{73}Ge include a nuclear spin, I=9/2, a low resonance frequency (ν_L = 3.498 MHz, relative to ^{1}H in TMS at 100 MHz), large quadrupole moment (-19.6 fm^2) and low natural abundance (7.73%), giving it a receptivity of 1.09×10^{-4} relative to ^{1}H. The quadrupolar interaction in particular can complicate the spectrum, causing significant anisotropic broadening of the lineshape and effectively reducing sensitivity. When the germanium nucleus is at a site of cubic symmetry or undergoes rapid isotropic tumbling, sharper peaks may be observed.[262,263] However, this is rare in solids and only a handful of solid-state ^{73}Ge NMR studies have appeared in the literature.[264-267]

Our study provides a comprehensive series of oxides containing different local structures, coordination environments, and a variety of counter cations (with varying charge). This is required to establish trends in NMR properties and lay the groundwork for the application of ^{73}Ge NMR to oxide materials. This work is complemented by DFT calculations of the structural effects and provides benchmarks for more accurate calculational procedures.

6.1.1. Materials and Methods

6.1.1.1. Synthesis

Crystalline phases were synthesized in 1 g batches from stoichiometric mixtures of their respective components. All starting materials were >99% pure (Li_2CO_3, Na_2CO_3, K_2CO_3, $CaCO_3$, $MgCO_3$, Bi_2O_3, PbO, ZrO_2, Ga_2O_3, and GeO_2) and were ground in an agate

mortar and pestle for five minutes. These samples were placed in platinum/gold (5%) or Al_2O_3 crucibles at 700 ^oC for four hours to remove any surface water and enable decarbonation. Decarbonation was verified by mass-loss measurements. Samples were re-ground and placed in a box or vertical tube furnace for 48 to 230 hours at temperatures in the range of 900^{o}C to 1350^{o}C, according to literature synthesis descriptions.[259,268-279] After the initial heating cycle, samples underwent a second grinding and were heated for 24 hours to improve crystallinity. Amorphous samples were treated similarly, before placing them in a high temperature vertical tube furnace at 1425^{o}C for 30 minutes and subsequent quenching in deionized water.

6.1.1.2. Nuclear Magnetic Resonance

All NMR data were acquired on a Bruker Avance II 900 (21.1T) spectrometer with a 7mm low-gamma MAS probe. ^{73}Ge NMR spectra were acquired using either a solid echo, QCPMG (Quadrupolar-Carr-Purcell-Meiboom-Gill) sequence[280,281] or WURST-QCPMG[45,46,282] with $\pi/2$ and π pulses calibrated using liquid $GeCl_4$. Each spectrum was collected in several (two to seven) pieces, and summed to obtain the overall experimental spectrum. Recycle delays ranged from two to ten seconds and 512 to 4096 co-added transients (per piece) were collected. The number of echoes collected during acquisition (QCPMG and WURST-QCPMG) varied between 32 and 256, depending on T_2. All spectra were referenced to 30.9 ppm using $GeCl_4$, as a secondary reference, relative to $GeMe_4$ (0 ppm). All spectra were simulated using WSolids[283] to obtain isotropic chemical shifts (δ_{iso}), quadrupolar couplings (C_Q) and quadrupolar asymmetry parameters (η).

The spectrum of the quartz-like GeO_2 phase was also acquired on a Bruker AMX 500 (11.7 T) spectrometer using a home-built 5mm probe with a 10-turn copper coil and 400 pF of capacitance, enabling the probe to be tuned at 17.6 MHz, and pulse widths of 2 μs to be achieved (ν_{rf} of 25 kHz). GeO_2 was packed into a modified 5mm quartz NMR tube, with acquisition using a QCPMG sequence over four days.

6.1.1.3. Quantum Chemical Calculations

Electric field gradient and chemical shielding calculations for all crystalline germanates were carried out using CASTEP,[66] a fast and efficient density functional theoretical method which uses a plane-wave basis set to compute properties in periodic systems. The PBE functionals are used in the GGA for the exchange-correlation energy[284,285] on a HP xw4400 Workstation with a single Intel Dual-Core 2.67 GHz processor. The ultrafine basis set was used with the projector-augmented wave method (GIPAW) and relativistic effects using the scalar-relativistic zeroth-order regular approximation (ZORA).[286] Geometry optimizations were attempted for a few structures but the differences were insignificant, so non-optimized structures are included in Table 6.1. The shielding of crystalline $GeCl_4$ was used as a reference to convert calculated shieldings to chemical shifts. CASTEP output was analyzed using a modified version of EFGshield (V2.2) to obtain the EFG tensor principal components.[287] The quadrupolar moment used in CASTEP (-17.3 fm^2) was corrected to the more commonly accepted value of -19.6 fm^2.[124]

Electric field gradients in selected structures were also calculated using WIEN2k, a DFT package for calculating electronic structure in ionic solids which uses a full-potential linearized augmented plane-wave method.[73,288] These calculations

used the PBE functional[68,69], generalized gradient approximation, involving 15k to 100k irreducible k-points, the RKmax basis set size (7 to 9) and a low-charge level convergence criterion ($<10^{-5}$).[284] Calculations were carried out on a SUN X4440 server with 16 cores and 64 GB of RAM. These parameters were adjusted until changes in the EFG were reduced to less than one part per hundred. All CASTEP and WIEN2k input files were constructed from the literature crystal structures.

6.1.1.4. Powder X-Ray Diffraction

Crystalline samples were checked for purity using a PANalytical X'Pert Pro Bragg-Brentano powder X-ray diffractometer with a Cu-Kα radiation source, an X'Celerator detector and a Ni-filter diffracted beam. All data were acquired at room temperature with a 2θ range of 10° – 90° at 0.0167° increments using 60 seconds per step. The samples were mounted with grease on a single-crystal quartz (SiO_2) zero-background sample holder.

6.1.2. Results

A series of crystalline germanium oxides has been studied using ultrahigh field NMR experiments of non-spinning samples. The central transitions (1/2 <–> -1/2) of selected compounds are displayed in Figures 6.1-6.12. Experimental and calculated results are tabulated in Table 6.1.

6.1.2.1. FOUR COORDINATE GERMANIUM

6.1.2.1.1. GeO_2

The germanium oxide quartz-like structure contains a relatively small C_Q of 9.3 ± 0.3 MHz and an asymmetry, η = 0.55 ± 0.05 (Figure 6.1). The spectral width is on the order of 30 kHz at 21.1 T (50 kHz at 11.7 T) and the isotropic chemical shift, δ_{iso} is -100 ± 50 ppm. The germanium centre has a two-fold rotation axis, which lies along the a-axis. The EFG components according to CASTEP lie along the unit cell axes, a (V_{xx}), b (V_{yy}) and c (V_{zz}).

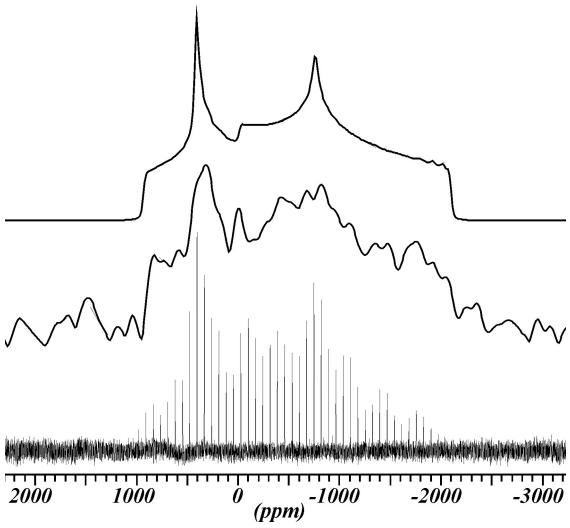

Figure 6.1. ^{73}Ge NMR of Crystalline GeO_2 (quartz-like phase), (top) simulated, (middle) spin-echo and (bottom) experimental QCPMG spectrum collected at 11.7 T.

6.1.2.1.2. $Bi_4Ge_3O_{12}$

This bismuth germanate[268] phase has a C_Q of 11.5 ± 0.5 MHz (Figure 6.2). The asymmetry parameter is zero, as required by symmetry, with the germanium lying on a two-fold rotation-axis and a four-fold inversion centre (S_4).[268] CASTEP

underestimates the C_Q (9.1 MHz) and predicts the EFG tensor principal components to lie along the crystal axes of the cubic cell, as illustrated in Figure 6.2. The isotropic chemical shift is estimated to be -70 ± 50 ppm. A low intensity signal between -750 ppm and -1000 ppm comes from a $Bi_2Ge_3O_9$ impurity, estimated by XRD to be <10%.

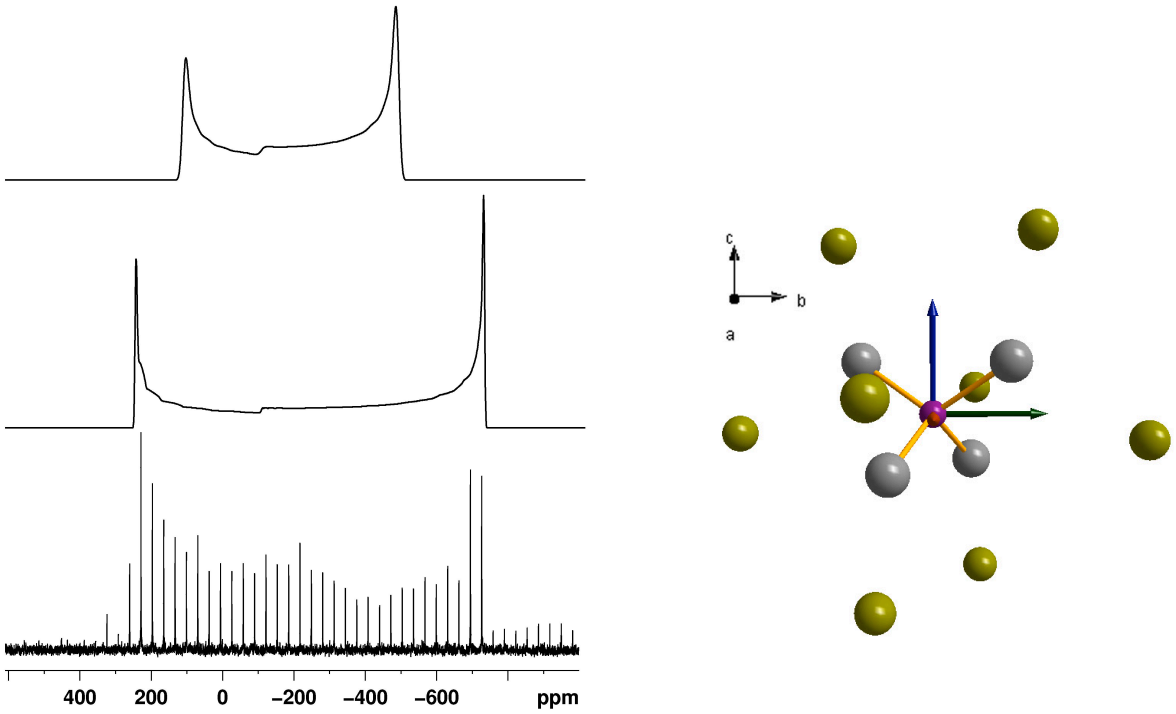

Figure 6.2. ^{73}Ge NMR of $Bi_4Ge_3O_{12}$: (top) CASTEP prediction, (middle) spectral simulation and (bottom) experimental QCPMG data. CASTEP calculated EFG tensor principal components V_{xx} (orange), V_{yy} (green) and V_{zz} (blue), with V_{xx} directed out of the plane of the page. The structure is represented as Ge (purple), O (grey) and Bi (gold) cations, bonds to Bi are omitted for easier visual representation.

6.1.2.1.3. Zr_3GeO_8

Trizirconium germanium oxide[269] has a quadrupolar coupling constant of 24 ± 1 MHz and is axially symmetric (η = 0.0). Figure 6.3 illustrates the experimental spectrum and its simulation, with a central transition spanning ~5,000 ppm (160 kHz). The experimental δ_{iso} is estimated to be -20 ± 100 ppm. CASTEP predicts that the EFG tensor principal components are aligned with the axes of the crystal lattice; V_{xx}=a, V_{yy}=b and V_{zz}=c. The Ge^{4+} cation is situated on a C_2 screw-axis along V_{zz} and a four-fold inversion centre (S_4). While the symmetry implies η = 0.0 at the germanium site, a simulation of η = 0.07 ± 0.05 provides a slightly better fit to the experimental data, hinting at the presence of an additional anisotropic interaction or a small degree of structural disorder.

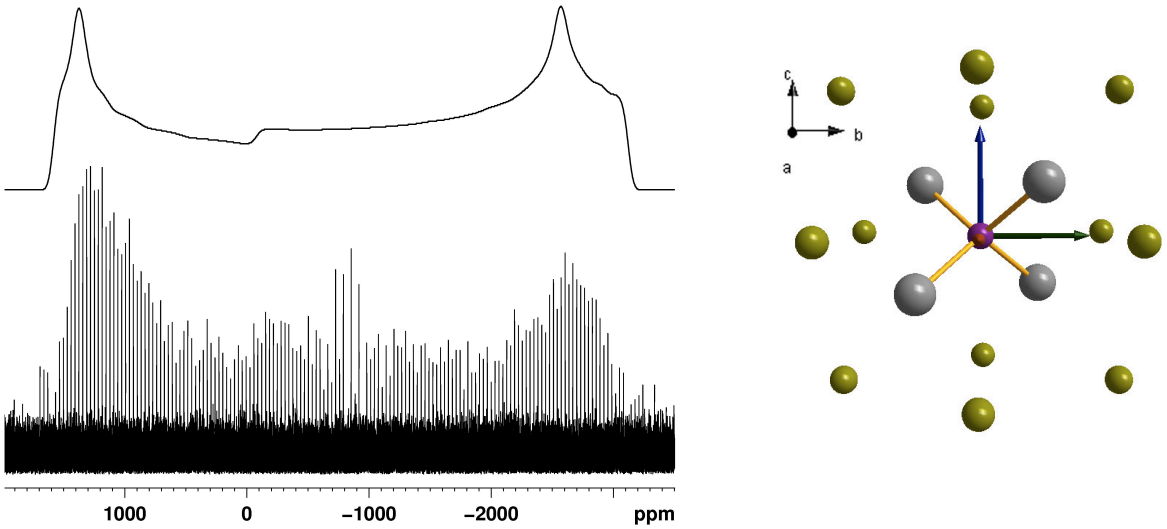

Figure 6.3. ^{73}Ge NMR of Zr_3GeO_8: Experimental simulation (top) and QCPMG spectrum (bottom). Calculated EFG tensor principal components: V_{xx} (orange) directed out of the plane of the page, V_{yy} (green) and V_{zz} (blue) with the crystal structure, Ge (purple), O (grey) and Zr (gold) cations, bonds to Zr are omitted for

easier viewing. The extra intensity observed at ~ -800 ppm is caused by the placement of the transmitter and is not from the sample.

6.1.2.1.4. Ca_2GeO_4

The ^{73}Ge NMR spectrum of the CT of dicalcium germanate[289] (Figure 6.4) spans 5,300 ppm (165 kHz) and has a C_Q of 22 ± 1 MHz, η = 0.65 ± 0.1 and δ_{iso} = 5 ± 60 ppm. The EFG principal components are slightly rotated (~20°) from the three Ge-O bonds. Since the Ge^{4+} cation sits on a mirror plane, V_{yy} is directed normal to this plane.

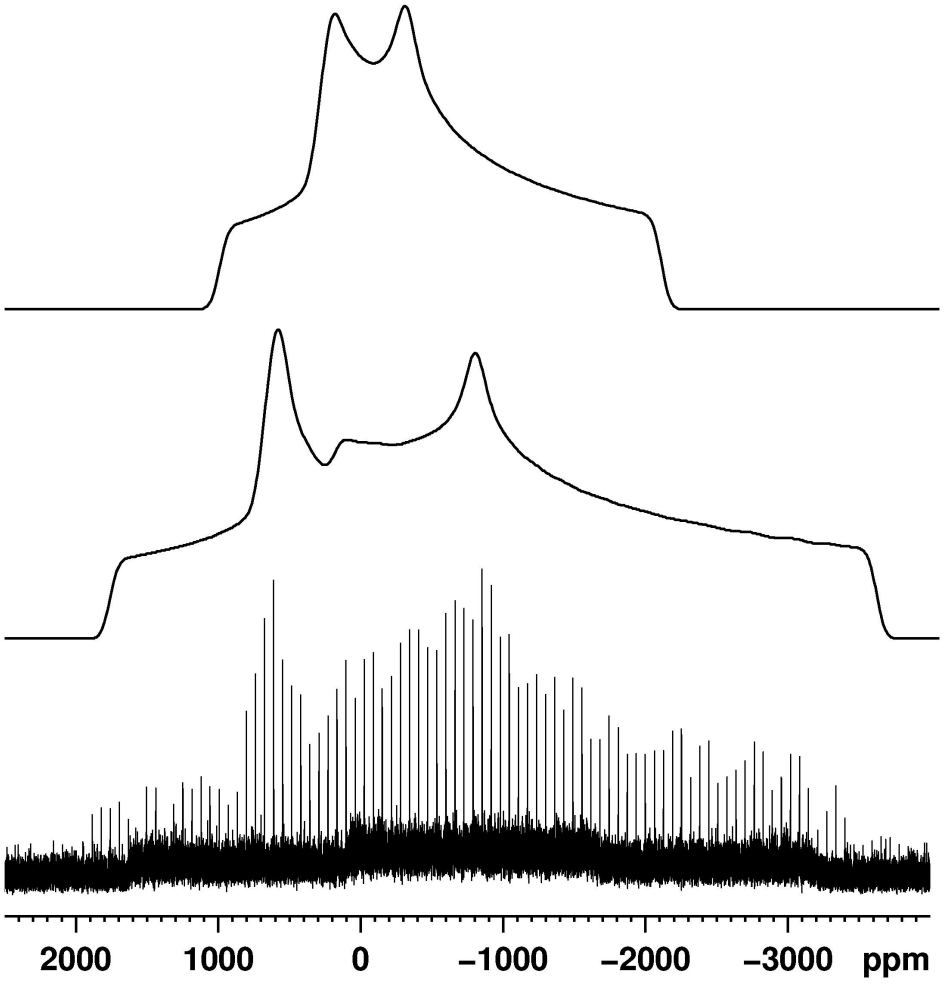

Figure 6.4. ^{73}Ge NMR of Ca_2GeO_4 crystal, (top) CASTEP, (middle) spectral simulation and (bottom) experimental spectrum.

6.1.2.1.5. Mg_2GeO_4

Dimagnesium germanate[279] is isostructural with Ca_2GeO_4 but it possesses a larger quadrupolar interaction of 26.5 ± 1 MHz. The corresponding asymmetry parameter was determined to be η = 0.70 ± 0.05. Figure 6.5 shows a central transition that is almost 9000 ppm broad (270 kHz). The isotropic chemical shift is similar to that of Ca_2GeO_4, -20 ± 100 ppm. The germanium cation sits on a mirror plane, with the V_{xx} perpendicular to it, according to CASTEP.

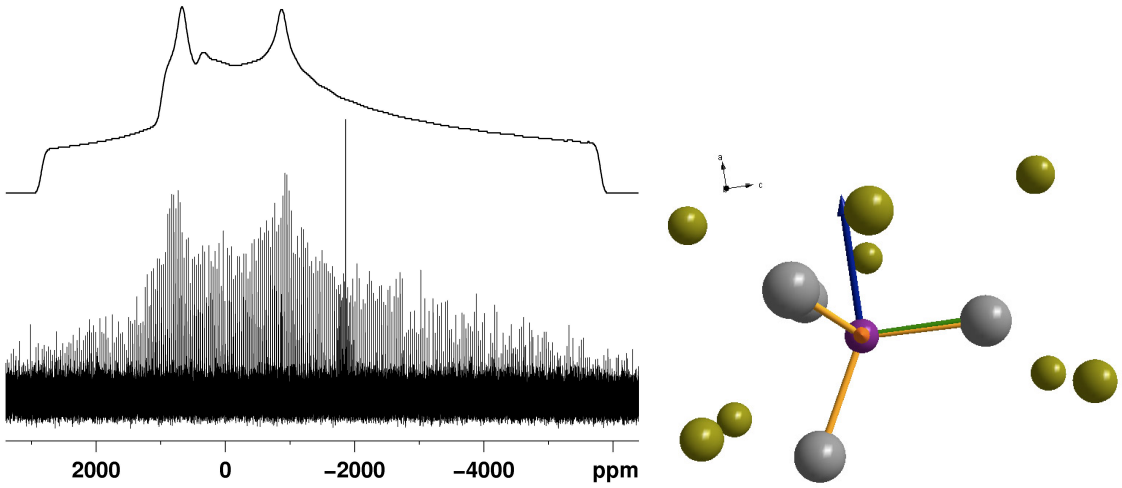

Figure 6.5. ^{73}Ge NMR of Mg_2GeO_4 crystal; (top) simulation and (bottom) experimental WURST-QCPMG. Calculated EFG tensor principal components V_{xx} (orange), V_{yy} (green) and V_{zz} (blue), with V_{xx} being directed out of the plane of the page. The crystal structure is represented as Ge (purple), O (grey) and Mg (gold) cations, with the Mg to O bonds omitted. A "spurious signal" developed outside of the spectrometer (observed at ~-1800 ppm) during acquisition.

6.1.2.1.6. Li_4GeO_4

The ^{73}Ge NMR spectrum of lithium orthogermanate[275] is about 1900 ppm (60 kHz) broad (Figure 6.6), corresponding to $C_Q < 12 \pm 1$ MHz, and an isotropic shift of 0 ± 100 ppm. The unusual lineshape suggests some kind of structural disorder that is not obvious from the powder x-ray diffraction.

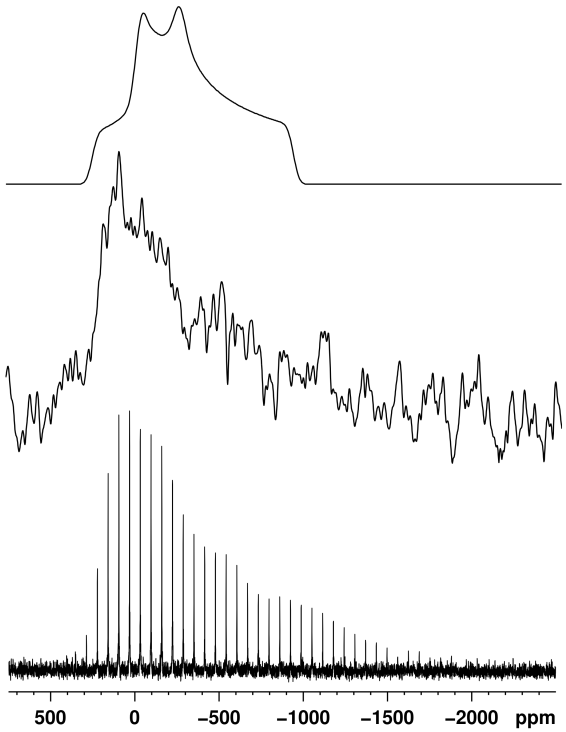

Figure 6.6. ^{73}Ge NMR of Li_4GeO_4, (top) CASTEP, (middle) solid-echo and (bottom) experimental QCPMG.

6.1.2.1.7. $PbGeO_3$

Lead germanium oxide[277] has a CT spectral width of 11,200 ppm (350 kHz), corresponding to C_Q = 29 ± 1 MHz, η = 1.0 ± 0.05 and δ_{iso} = -90 ± 150 ppm (Figure 6.7). This germanium centre is also one of the most distorted four-coordinate sites in this collection, with no special symmetry elements at the germanium centre.

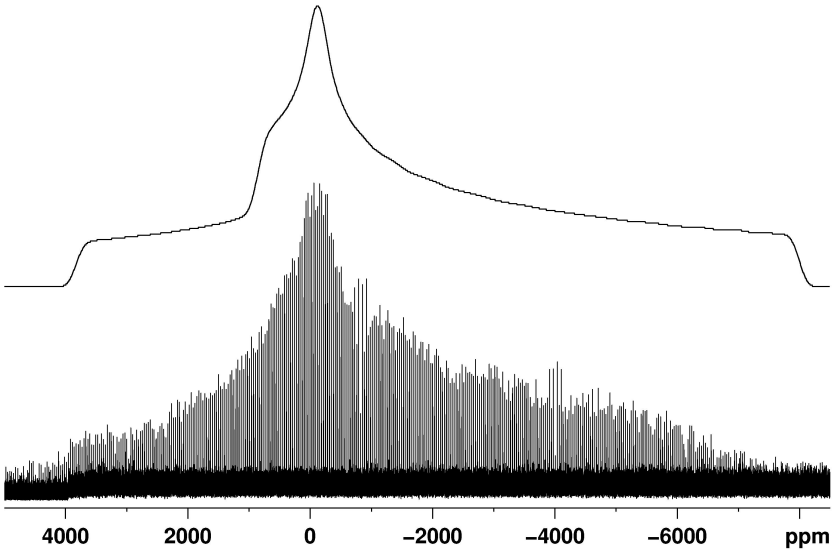

Figure 6.7. ^{73}Ge NMR of crystalline $PbGeO_3$, (top) simulation and (bottom) experimental.

6.1.2.1.8. $Bi_2Ge_3O_9$

Dibismuth germanium oxide[272] (Figure 6.8) contains the largest quadrupolar coupling of any of the four-coordinate germanium sites observed. The experimental C_Q is 32 ± 2 MHz, η = 0.4 ± 0.2 and δ_{iso} = -95 ± 100 ppm. An impurity of $Bi_4Ge_3O_{12}$ is present between 500 ppm and -800 ppm, confirmed by XRD and accounting for approximately

20% of the sample. The medium-range structure within this germanate comprises three GeO_4 units that form a three-member ring.

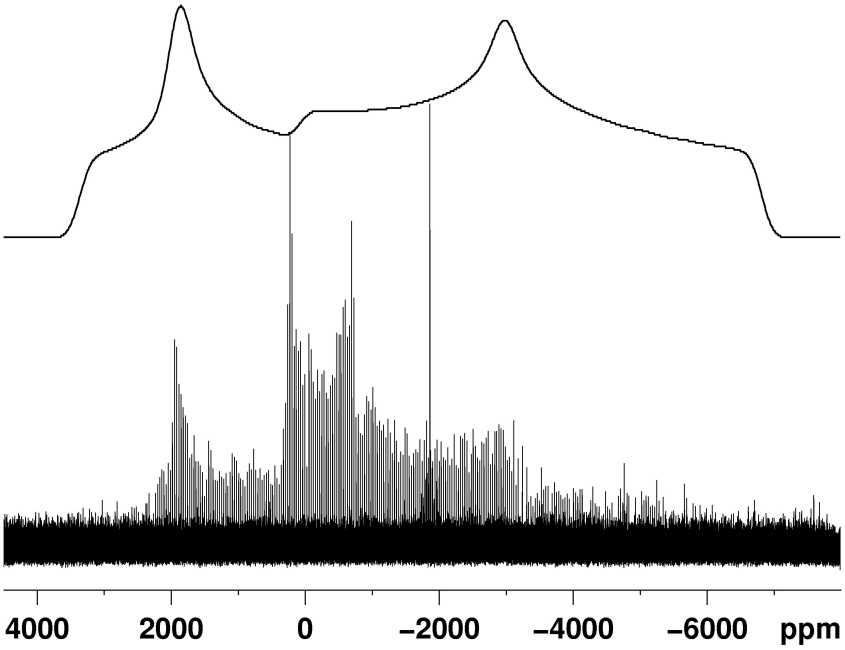

Figure 6.8. ^{73}Ge NMR of $Bi_2Ge_3O_9$, (top) simulation and (bottom) experimental WURST-QCPMG spectrum. A ~20% impurity of the $Bi_4Ge_3O_{12}$ phase is located in the centre of the spectrum (400 ppm to -800 ppm, Figure 6.2). The sharp peak at -1800 ppm is caused by a signal outside of the spectrometer that appeared during acquisition, confirmed using an empty rotor.

6.1.2.1.9. Other Four-Coordinate Germanates

Other crystalline germanates were calculated, but not experimentally observed. K_4GeO_4,[290] Rb_4GeO_4,[291] $Al_2Ge_3O_9$,[292] and $In_2Ge_3O_9$[293] proved difficult to synthesize in sufficiently high purity. Li_2GeO_3[274] is predicted to have a C_Q = 50 MHz; preliminary

experiments indicated it will require seven days of data acquisition due to a long T_1 and short T_2. Likewise, calculation of $SrGeO_3$[294] suggested the largest C_Qs known to date for a four-coordinate Ge: 62.4 and 64.4 MHz for the two sites. Moreover, neither site is expected to be axially symmetric, rendering the overall spectrum impractically challenging to collect and interpret. Finally, Na_2GeO_3[278] suffered from severe probe ringing which is believed to be caused by a piezo-electric effect.[295] The calculated parameters are included in Table 6.1 for completeness.

6.1.2.2. Five-Coordinate Germanium, $K_2Ge_8O_{17}$

The only (alkali) germanate with a well-defined five-coordinate germanium site is dipotassium octagermanate.[270] The structure contains four distinct germanium sites, three of which are four-coordinate. As such, the ^{73}Ge spectrum contains overlapping contributions from all four sites in a 1:1:1:1 ratio, making for a very complex appearance (Figure 6.9) from which no experimental parameters for the $^{[5]}$Ge site can be reasonably obtained. While it is impossible to attempt deconvolution of these data, the spectrum predicted by CASTEP, shown as reference, bears some resemblance to the experimental spectrum.

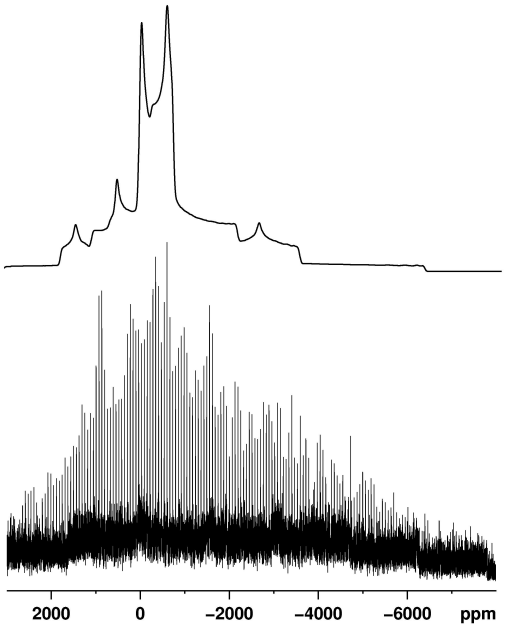

Figure 6.9. ^{73}Ge NMR of $K_2Ge_8O_{17}$ (four Ge sites) with (top) CASTEP predicted parameters and (bottom) experimental QCPMG spectrum.

6.1.2.3. Six-Coordinate Germanium

6.1.2.3.1. GeO_2

The NMR spectrum of germanium oxide with a rutile-type crystal structure is illustrated in Figure 6.10 and has a quadrupolar coupling of 19.3 ± 0.5 MHz and η = 0.55 ± 0.05. The spectral span is just over 4,000 ppm at 21.1 T (~ 130 kHz) and the isotropic shift is -300 ± 40 ppm. The six-coordinate Ge lies at the centre of a distorted octahedron with axial elongation causing local symmetry (D_2h) at the GeO_6 site. The germanium site sits on an inversion centre and the calculated EFG components V_{XX}, V_{YY} and V_{ZZ} lie between the a, b, and c axes.

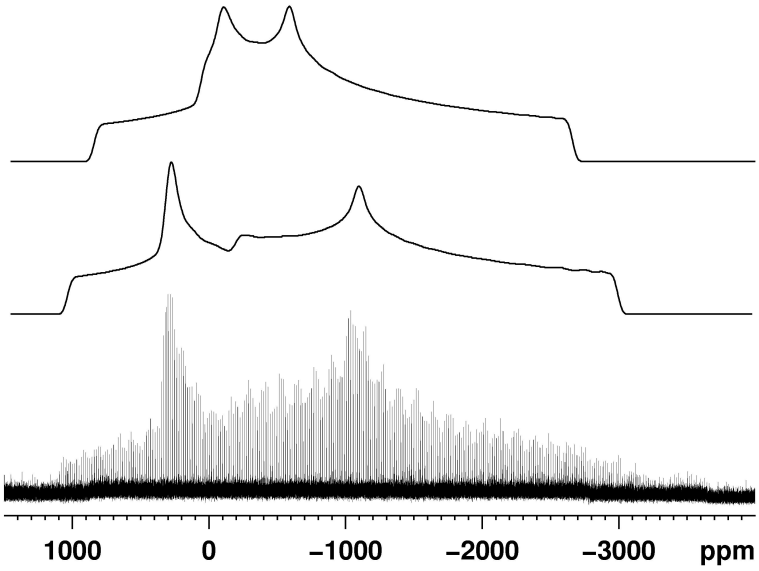

Figure 6.10. ^{73}Ge NMR spectrum of crystalline GeO_2 (rutile-like phase), (top) CASTEP, (middle) spectral simulation and (bottom) QCPMG spectrum

6.1.2.3.2. Ga_4GeO_8

Tetragallium germanate (α-phase)[273] contains a six-coordinate germanium centre with a spectrum spanning some 13,000 ppm (410 kHz). Simulations reveal an experimental C_Q of 35 ± 2 MHz, η = 0.95 ± 0.05 and δ_{iso} = -420 ± 200 ppm (Figure 6.11). The six-coordinate Ge^{4+} sits in a axially-compressed octahedron, forming chains.[273] The high asymmetry parameter is not surprising because the germanium cation contains only the identity symmetry element. CASTEP predicts that the V_{zz} EFG principal component lies between the axial and equatorial oxygens, while the V_{xx} and V_{yy} sit within the equatorial plane, splitting the oxygens. Upon closer inspection of the

left edge of the spectrum, it appears that a portion of a satellite transition is observable (3/2 <–> 1/2), due to the high asymmetry parameter.

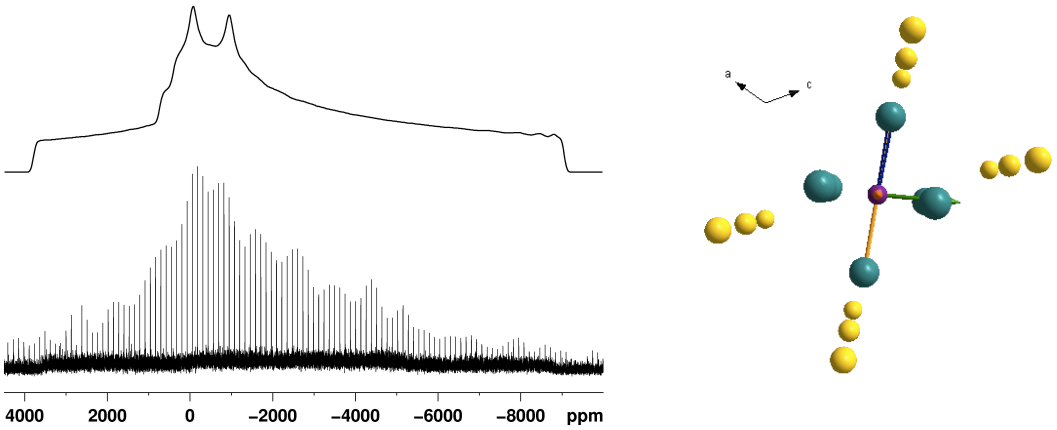

Figure 6.11. ^{73}Ge NMR of Ga_4GeO_8; (top) simulation and (bottom) experimental WURST-QCPMG. Calculated EFG tensor principal components V_{xx} (orange) being directed out of the plane of the paper, V_{yy} (green) and V_{zz} (blue). The crystal structure is represented as Ge (purple), O (teal) and Ga (gold), Ga-O bonds are omitted for visualization.

6.1.2.3.3. $Na_4Ge_9O_{20}$

Sodium enneagermanate[271] contains three Ge sites with coordination numbers of 4, 4, and 6 in a ratio of 1:4:4. The spectrum is shown in Figure 6.12, but cannot be simulated due to the extensive spectral overlap.

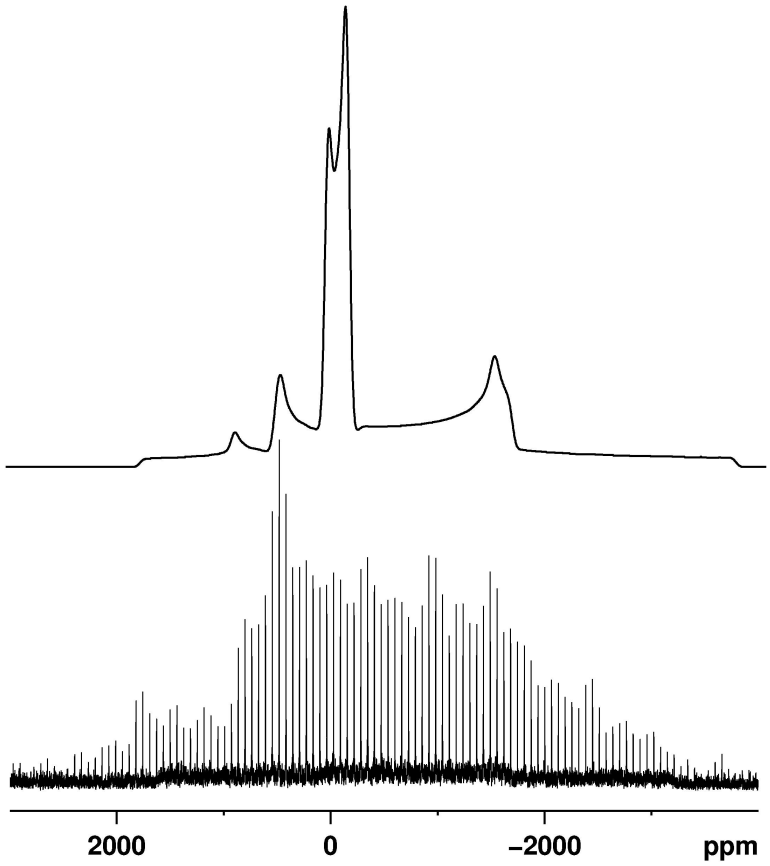

Figure 6.12. ^{73}Ge NMR of $Na_4Ge_9O_{20}$ with 3 Ge sites, (top) CASTEP and experimental QCPMG spectrum (bottom)

6.1.3. Discussion

6.1.3.1. ^{73}Ge Chemical Shift Behaviour

The dependence of NMR chemical shifts on local structure is one of the most fundamental relations defining the utility of NMR in structural studies. The data indicate about a 200 ppm difference between the $^{[4]}$Ge and $^{[6]}$Ge species. This oxide series indicates that four-coordinate germanium are found to have δ_{iso} between ~5 and -120 ppm, whereas the six-coordinate germanium (rutile-GeO_2 and Ga_4GeO_8) are

found between ~-300 and -420 ppm (Figure 6.13, Figure 6.14 and Table 6.1). Scatter within the four-coordinate samples is most likely due to local distortions, different charge-balancing cations and the presence of rings, but there are too few data to delineate any clear trends. CASTEP calculations are somewhat shifted from the experimental values, but agree with the relative trend. Although no experimental value for the five-coordinate germanium could be obtained due to spectral overlap, the calculated value is -293 ppm, directly between the calculated four- and six-coordinate regions.

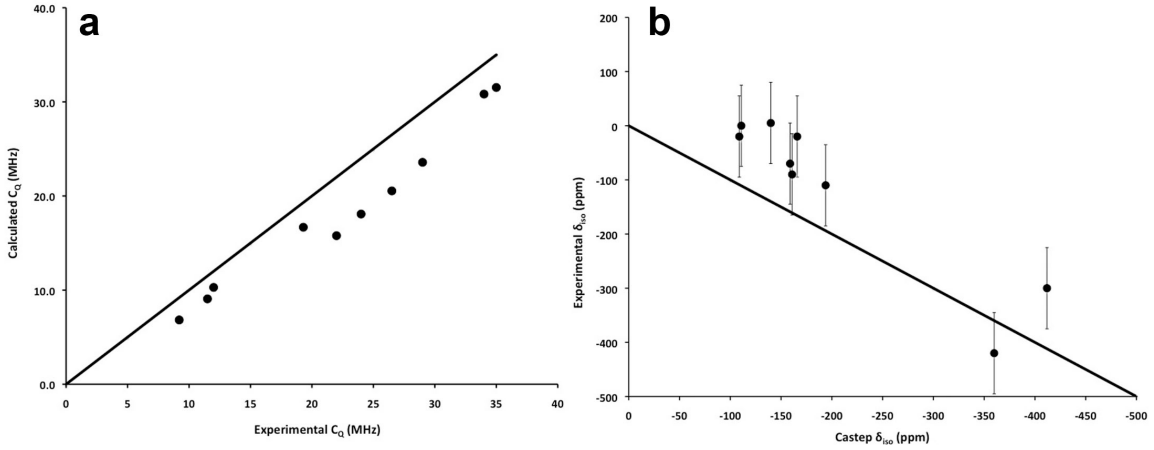

Figure 6.13. Relationship between the experimental and CASTEP-calculated quadrupolar coupling constant (a) and isotropic chemical shift (b). The bold black line is the expected 1:1 relation between experimental and calculated results

This general relationship has been found for many network-forming cations (e.g. Si, B, Al, Cs, etc.),[9,13,90,121,131-135] where increasing coordination number is positively correlated with increased nuclear shielding. Despite confirmation of this trend, the large uncertainties in measured δ_{iso} values due to the very broad peaks

compromises its usefulness in structural studies. With significantly higher resolution, however, this relationship may become useful for ^{73}Ge NMR.

6.1.3.2. ^{73}Ge Chemical Shift Anisotropy

Chemical shielding anisotropy has the potential to provide electronic and structural insight but the present series of germanates does not exhibit measurable CSAs due to the very large C_Qs. Despite CASTEP calculations indicating shielding spans of 19 to 380 ppm (Table 6.1), lineshape simulations incorporating shielding effects were indistinguishable from those without CSA. This contrasts with a recent study in which a CSA of 30 ppm was measured due to an anomalously small C_Q which did not interfere with observation of the CSA.[266] More generally, it is often found that CSA and quadrupolar interactions increase in concert, and are related to the degree of local geometric distortions. Although the CASTEP CSA calculations have not been experimentally verified, it is worth noting that the largest CSAs correlate with the largest C_Q's (K_4GeO_4: C_Q = 7.5 MHz, Ω = 25 ppm; Li_2GeO_3: C_Q = 50.1 MHz, Ω = 319 ppm, Figure 6.14). In general, reliable measurements of CSA will require even higher magnetic fields to reduce the influence of the quadrupolar interaction on the spectral appearance and increase that of the anisotropic shielding.

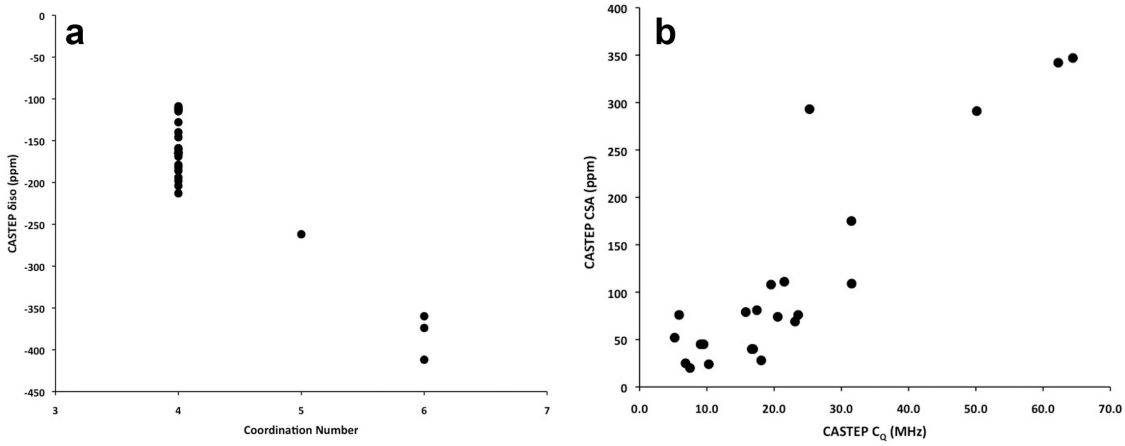

Figure 6.14. (a) CASTEP calculated isotropic chemical shifts with Ge coordination sphere and (b) CASTEP calculated CSA with quadrupolar coupling constants

6.1.3.3. ^{73}Ge Quadrupolar Interactions

The second-order quadrupolar lineshape of the CT can be used to infer structural features in the vicinity of germanium. For example, the quadrupolar asymmetry parameter reports on the local symmetry of the germanium nucleus: $Bi_4Ge_3O_{12}$ and Zr_3GeO_8 have η-values near zero because the local environment is highly symmetric about the c-axis. By contrast, $PbGeO_3$ and Ga_4GeO_8 have η-values near 1 and possess no special point symmetry elements. The measurement of this parameter is straightforward in single-site systems and provides direct insight into the local symmetry.

The magnitude of C_Q also reflects the local germanium environment. Cubic symmetry eliminates the electric field gradient and results in a single sharp peak. For nuclei with a large quadrupole moment like ^{73}Ge, even small deviations from cubic

symmetry result in large second-order quadrupolar effect, which can provide a sensitive measure of local structure. However, the magnitude of the C_Q can be related to tetrahedral and octahedral distortions. Robinson et al.[296] and Fleet[297] have studied distortions in polyhedra and octahedral systems in minerals. These distortion parameters can be calculated for both octahedral and tetrahedral polyhedra:

$$\sigma_{oct} = \frac{1}{11}\sum_{i=1}^{12}\left(\theta_i - 90^0\right)^2 \tag{6.1}$$

$$\lambda_{oct} = \frac{1}{6}\sum_{i=1}^{6}\left(\frac{l_i}{l_o}\right)^2 \tag{6.2}$$

$$\sigma_{tet} = \frac{1}{5}\sum_{i=1}^{6}\left(\theta_i - 109.47^0\right)^2 \tag{6.3}$$

$$\lambda_{tet} = \frac{1}{4}\sum_{i=1}^{4}\left(\frac{l_i}{l_o}\right)^2 \tag{6.4}$$

where σ represents the angular variance, λ is the mean quadratic elongation parameter, θ_i is the angular distortion from ideal octahedral or tetrahedral geometry, l_i is the strained or crystal length between germanium and oxygen and l_o is length of the non-strained crystal.

The mean quadratic elongation parameters hint at a correlation with experimental quadrupolar couplings (Figure 6.15a). Figure 6.15b shows the C_Qs calculated from CASTEP to provide a larger sampling. The relationship is suggestive but clearly imperfect. Interestingly, a simplified version of the model, correlating the differences between the longest and shortest bond lengths with C_Q, appears to perform better than the distance distortion parameter (Figure 6.15c). The variance observed from the 1:1 linear fit may be caused by the different cation sizes and field

strengths in the systems. These models illustrate the sensitivity of the ^{73}Ge C_Q to the Ge-O bond distances.

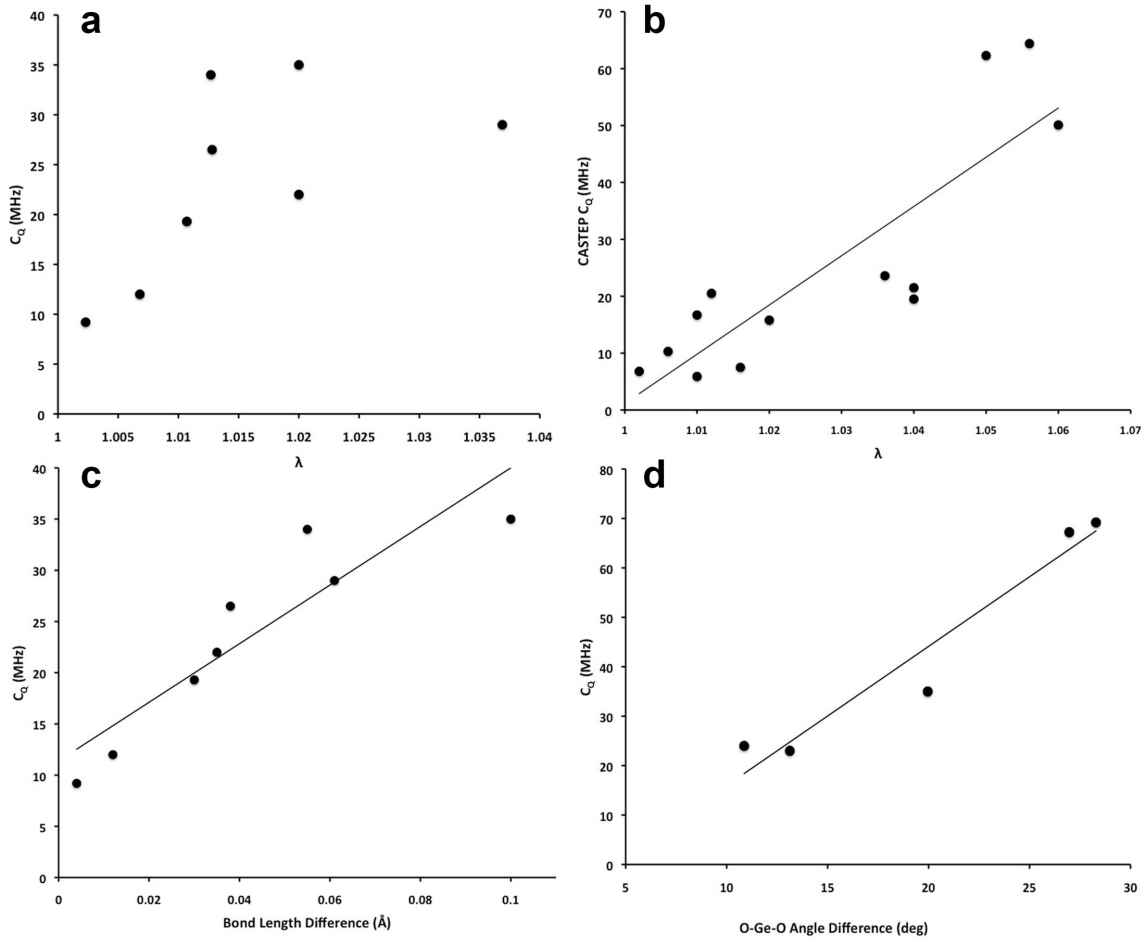

Figure 6.15. (a) Experimental and (b) CASTEP calculated quadrupolar coupling constant with mean distance distortion parameter. The experimental C_Q relationship with either (c) bond length or (d) O-Ge-O angle difference are also shown. The solid lines are linear fits.

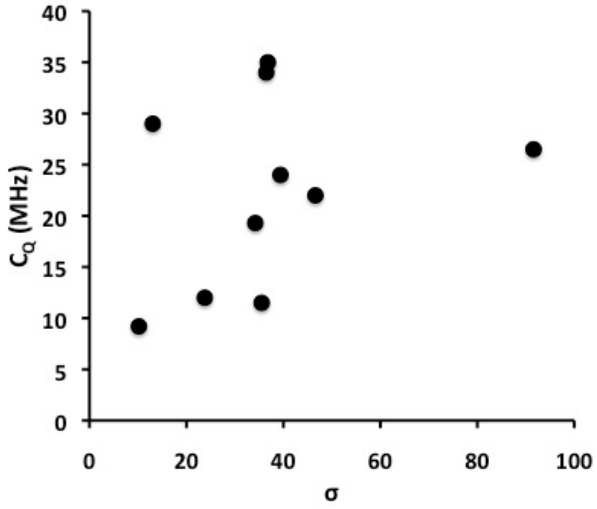

Figure 6.16. Experimental quadrupolar coupling constant as a function of calculated angle distortion parameter, σ.

On the other hand, some compounds do not obey the observed trends. Zr_3GeO_8 and $Bi_4Ge_3O_{12}$ have identical bond lengths (λ = 1) but different, non-zero C_Q's. Thus the quadrupolar interaction must be caused by an angular distortion. Two species Ga_4GeO_8 and $SrGeO_3$ have similar bond lengths, but bond angles that are rather distorted. Figure 6.15d illustrates a reasonable relationship between C_Q and the difference between the largest and smallest O-Ge-O bond angle for these four compounds. A plot of the full data set using the polyhedral angular variance parameters yields no obvious trend (Figure 6.16), suggesting that the Ge-O distance distribution dominates the EFG, with O-Ge-O angles a secondary influence.

Table 6.1. Experimental and calculated NMR parameters for germanium oxides

Material	CN	C_Q (MHz)	η	δ_{iso} (ppm)[b]	Ω (ppm)	κ
$Bi_4Ge_3O_{12}$	4	11.5 ± 0.5	0.0 ± 0.05	-70 ± 50	n.d.	n.d.
CASTEP		9.1	0.0	-159	45	-1
Zr_3GeO_8	4	24 ± 1	0.0 ± 0.05	-20 ± 100	n.d.	n.d.
CASTEP		18.1	0.0	-166	28	-1
WIEN2k		22.1	0.0	n.d.	n.d.	n.d.
Ca_2GeO_4	4	22 ± 1	0.65 ± 0.1	5 ± 60	n.d.	n.d.
CASTEP		15.8	0.77	-140	100	-0.13
WIEN2k		16.8	0.85	n.d.	n.d.	n.d.
Mg_2GeO_4	4	26.5 ± 1	0.7 ± 0.05	-20 ± 100	n.d.	n.d.
CASTEP		20.5	0.46	-109	96	-0.07
WIEN2k		22.8	0.38	n.d.	n.d.	n.d.
Li_4GeO_4	4	12 ± 1	0.9 ± 0.1	0 ± 100	n.d.	n.d.
CASTEP		10.3	0.74	-111	27	-0.52
WIEN2k		12.8	0.91	n.d.	n.d.	n.d.
$PbGeO_3$	4	29 ± 1	1.0 ± 0.05	-90 ± 150	n.d.	n.d.
CASTEP		23.6	0.67	-161	93	-0.27
WIEN2k		24	0.88	n.d.	n.d.	n.d.
$Bi_2Ge_3O_9$	4	28 ± 1	0.15	-95 ± 100	n.d.	n.d.
CASTEP		30.8	0.52	-179	158	-0.27
GeO_2[b]	4	9.2 ± 0.5	0.5	-110 ± 30	n.d.	n.d.
CASTEP		6.8	0.85	-194	30	-0.35
K_4GeO_4[a]	4	7.5	0.8	-111	25	-0.21
Rb_4GeO_4[a]	4	5.9	0.42	-113	90	-0.36
$Al_2Ge_2O_7$[a]	4	21.5	0.25	-198	115	-0.85
$In_2Ge_2O_7$[a]	4	19.5	0.31	-204	19	-0.72
Li_2GeO_3[a]	4	50.1	0.65	-128	319	-0.65

Na_2GeO_3	4	48.6	0.7	-130	336	-0.68
$SrGeO_3$ Site1[a]	4	62.3	0.38	-165	378	-0.61
Site 2[a]	4	64.4	0.41	-169	380	-0.65
$K_2Ge_8O_{17}$	5	n.d.	n.d.	n.d.	n.d.	n.d.
CASTEP		25.3	0.15	-262	340	-0.44
Site 2	4	n.d.	n.d.	n.d.	n.d.	n.d.
CASTEP		9.5	0.16	-182	46	-0.88
Site 3	4	n.d.	n.d.	n.d.	n.d.	n.d.
CASTEP		31.5	0.99	-213	198	-0.54
Site 4	4	n.d.	n.d.	n.d.	n.d.	n.d.
CASTEP		17.4	0.49	-186	94	-0.46
Ga_4GeO_8	6	35 ± 2	0.95 ± 0.05	-420 ± 200	n.d.	n.d.
CASTEP		31.5	0.41	-360	138	-0.15
$Na_4Ge_9O_{20}$	4	n.d.	n.d.	n.d.	n.d.	n.d.
CASTEP		23.1	0.45	-164	84	-0.28
WIEN2k		26.4	0.39	n.d.	n.d.	n.d.
Site 2	6	n.d.	n.d.	n.d.	n.d.	n.d.
CASTEP		16.9	0.06	-374	48	-0.31
WIEN2k		18.5	0.17	n.d.	n.d.	n.d.
Site 3	4	n.d.	n.d.	n.d.	n.d.	n.d.
CASTEP		5.2	0.0	-146	52	-1
WIEN2k		9. 9	0.0	n.d.	n.d.	n.d.
GeO_2	6	19.3 ± 1	0.55	-300 ± 50	n.d.	n.d.
CASTEP		16.7	0.81	-412	40	-0.97
WIEN2k		15.6	0.61	n.d.	n.d.	n.d.
GeO_2	Vitreous	<10.5	n.d.	-30 ± 40	n.d.	n.d.
$Li_2O•GeO_2$	Vitreous	<22	n.d.	-120 ± 100	n.d.	n.d.
$Na_2O•GeO_2$	Vitreous	<23	n.d.	-140 ± 100	n.d.	n.d.

a) Calculated values from CASTEP, note: all CASTEP C_Q values have been corrected to reflect the commonly accepted quadrupolar moment of -19.6 fm^2,[40] b) Referenced to $GeCl_4$ at 30.9 ppm and n.d. is an abbreviation for 'not determined'.

6.1.3.4. Quantum Chemical Calculations

The CASTEP C_Q results (Figure 6.13, Figure 6.17 and Table 6.1) show good agreement with the experimental quadrupolar coupling constants. The C_Qs are consistently underestimated, even after correction from the quadrupole moment used by the software to the commonly accepted quadrupole moment of -19.6 fm^2.[124] This CASTEP underestimation has also been reported by Kibalchenko et al. with the C_Q of crystalline-GeO_2 being underestimated by ~11%.[298] One possibility for this systematic discrepancy is that even the most recent quadrupole moment determination is low. Another possibility is that the germanium pseudo-potential is poorly optimized for these calculations. However, WIEN2k also underestimates the C_Q values (Figure 6.17). Since the latter is an all-electron DFT method, this suggests that the origin of the deficiency is the exchange-correlation functional.

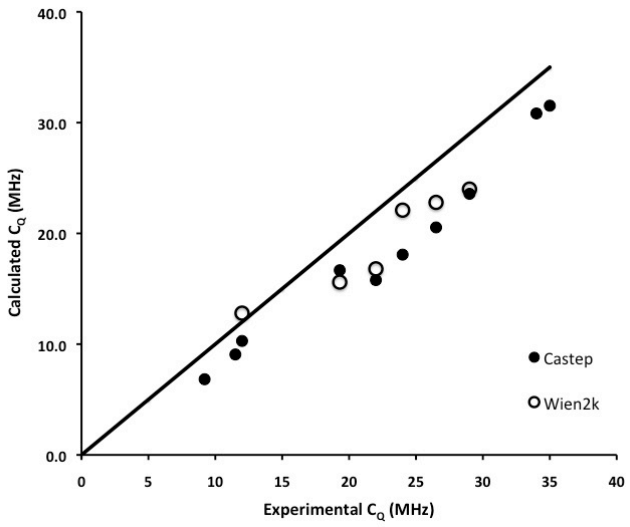

Figure 6.17. Experimental quadrupolar coupling constant compared to WIEN2k and CASTEP calculated C_Q's. The solid line is the 1:1 relation between experimental and calculated results. Errors are found within the size of the plotted points.

The asymmetry parameters are poorly predicted by CASTEP and WIEN2k. Only in the case of near-axial symmetry do the theoretical results produce reasonable results, as would be expected due to symmetry restrictions. Likewise, the isotropic chemical shifts calculated from CASTEP do not agree with the experimental data, falling systematically at lower frequency, however little can be made of this due to the large experimental uncertainties in the isotropic chemical shifts. Nevertheless, the calculations accurately reproduce the relative ordering of chemical shifts for different germanium coordination numbers (Figure 6.14).

6.1.3.5. ^{73}Ge Setup Standard

Experimental and theoretical chemical shifts were externally referenced to $GeCl_4$ at 30.9 ppm, with respect to the traditional reference sample, $Ge(CH_3)_4$.

Tetramethylgermanium suffers from a low boiling point, extreme flammability and high cost.[16] Germanium tetrachloride, by contrast, is more stable, is readily available at a more reasonable price, and produces a single sharp peak (13 Hz at 9.4 T, 5mm non-spinning probe) after a single scan with fast recycle delays (1 second).

6.1.4. SUMMARY

We have presented a comprehensive investigation of ^{73}Ge NMR properties in a variety of typical germanates to evaluate its potential for structural studies. Despite its unfavourable NMR properties, interpretable spectra were obtained in almost all cases, demonstrating that ^{73}Ge NMR is no longer an inaccessible nucleus. The electric field gradient at germanium is generally straightforward to measure in terms of C_Q and η, where the former appears to be dominated by the variation in Ge-O bond lengths, while the latter reflects the germanium local symmetry. While isotropic chemical shifts are difficult to measure with high precision due to broad peak widths, they show a clear correlation with coordination number, with increasing coordination resulting in a shift to lower frequencies.

Density-functional theory calculations using CASTEP and WIEN2k give mixed results. The magnitudes of the quadrupole coupling constants are reliably predicted, albeit systematically underestimated, suggesting that the exchange-correlation functional is unsuitable for these calculations. Quadrupolar asymmetry parameters are in generally poor agreement with experiment, except when axial symmetry is imposed by the crystal symmetry. Isotropic chemical shifts are systematically underestimated, but mirror the experimental trend with coordination number. Complementing the experimental data with calculations proves to be a powerful

approach to establish useful relationships between NMR observables and germanium structural environments.

Although ^{73}Ge NMR spectra can usually be readily acquired with good sensitivity using QCPMG, large quadrupolar interactions generally yield poor site resolution in oxides and this will limit its applicability in materials characterization where multiple germanium environments are expected to be present. This is illustrated by the multi-site $K_2Ge_8O_{17}$. In alkali germanate glasses, where inherent structural disorder broaden peaks and erodes lineshape features, these problems are compounded, making the identification and quantification of short-range order exceedingly challenging. Nevertheless, this study represents the first systematic investigation of ^{73}Ge NMR in typical oxides, and the trends established herein will prove useful when improved spectral resolution can be achieved, making NMR central to the study of Ge-bearing materials. With this information we now turn to the more difficult task of using ^{73}Ge to analyze amorphous materials, and we attempt to address the long-standing question of what causes the "germanate anomaly"?

6.2. Germanate Glasses

6.2.1. The Germanate Anomaly

Industrial applications involving germanate glasses include fiber optics,[299] optical applications[300,301] (lenses, infrared, etc.) and solar cells.[302,303] The local structure of these glasses, however are poorly understood. Germanium is found within group 14, beneath silicon and in theory should behave similarly where Q^4 units in GeO_2 will break down forming NBOs as alkali oxide is added. Silicate glasses have linear

property trends with alkali loading due to depolymerisation (i.e., SiO_2 (Q^4) + Li ➔ $LiSiO_4$ (Q^3) + Li ➔ Li_2SiO_4 (Q^2), etc.). Germanate glasses however behave differently from silicates, as shown in Figure 6.18.

This unique behaviour implies that depolymerisation of the germanate network is not the only structural change that is occurring. The basis for this behaviour was proposed in the 1960's by two groups suggesting that at lower alkali loadings a coordination change occurs.[15,304] These groups suggested that vitreous GeO_2 ($^{[4]}Ge$, Q^4) converts to a higher coordinate germanium polyhedron ($^{[5]}Ge/^{[6]}Ge$) as alkali oxide is added. This high-coordinate model was proposed on the basis of the borate "anomaly" and thus named the germanate anomaly. Despite a variety of experimental results supporting this model[2,11,260,305-312] some inconsistencies suggest the situation is not so simple.

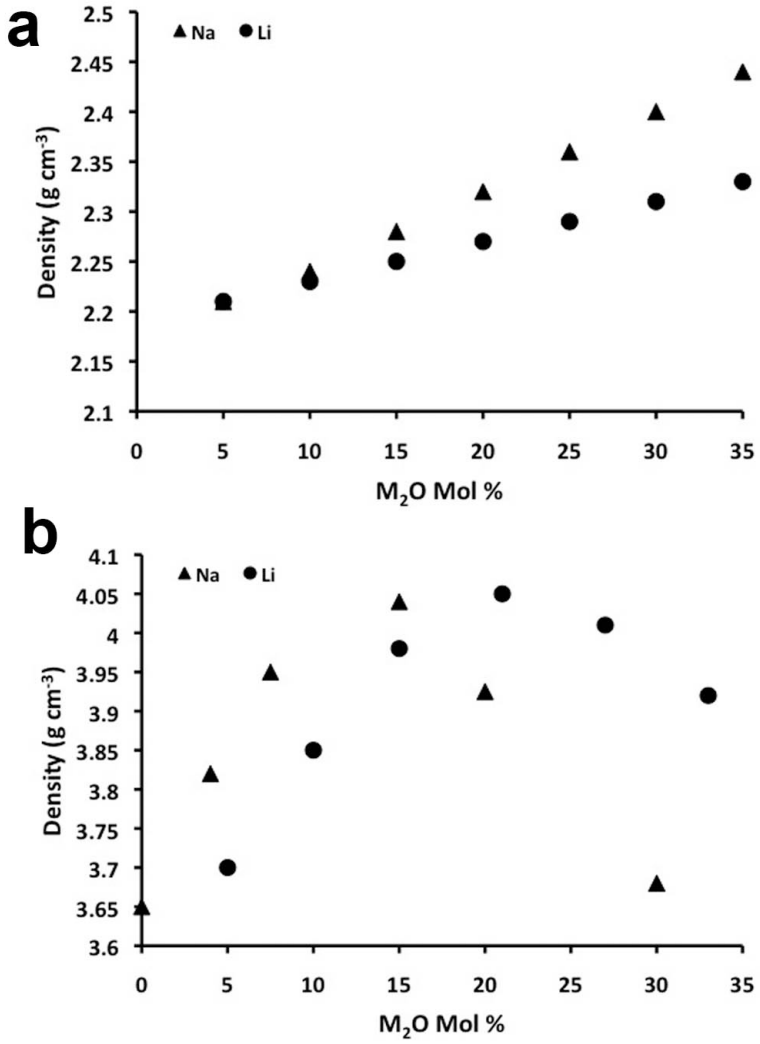

Figure 6.18. Density behaviour for (a) silicate and (b) germanate glasses as Li and Na modifier is added.[2,304]

An alternate model was proposed in the early 1990's by Henderson and Fleet.[313] They proposed a combination of three-member GeO_4 rings and depolymerisation. Henderson argues that the original model has two major faults, one being no evidence of NBOs forming at early alkali loadings.[260,314] The other involves the lengthening of the Ge-O distance being associated with a higher coordination

environment. He states that NBOs are observed with the onset of alkali loadings and the bond lengthening at the early onset (attributed to high coordination) is not supported at higher loadings because the Ge-O bond length does not decrease (as one would expect to occur when higher-coordinate species break down into four-coordinate NBOs) after the maximum is reached in the physical properties (Figure 6.18).[260] Henderson does acknowledge that neutron diffraction data suggest a $^{[5]}$Ge species is present in small amounts but this increase in coordination is not associated with the behavior of the glass.[260] For 20 years the scientific community has been unable to agree on a single model.[315] NMR should be able to address what causes the germanate anomaly. NMR is the obvious choice as it probes locally and can reveal structural information such as bonding arrangement and local coordinating environment. For germanates, solid-state NMR can probe germanium directly (^{73}Ge) or indirectly (^{17}O). We will focus on the direct method here, but will provide a few details in regards to what has been done using ^{17}O MAS NMR.

6.2.2. ^{17}O MAS NMR Studies

^{17}O NMR has become very important in the past decade with over 75 publications (vs. ~160 since the 1950's) in solid-state NMR. To probe the germanate anomaly, ^{17}O MAS NMR has been used as an indirect method for determining local coordination environments on germanium. ^{17}O is a I=5/2 nucleus with a moderate gyromagnetic ratio (-3.628 rad/Ts) and a quadrupolar moment of -2.56 fm^2. However, it is only 0.037% naturally abundant, inhibiting NMR observation without enrichment. To overcome these issues, one typically isotopically enriches the sample (~$1000/g of 90% $H_2{}^{17}O$; ~ 500 mg of starting material enriched between 40 to 60%; i.e., $500 per

sample). ^{17}O enrichment is done rather than ^{73}Ge enrichment, as it is less expensive, has a higher receptivity, a smaller quadrupolar moment and better understood NMR parameters. Therefore, studies have focused on this nucleus. Bridging oxygens can be observed to determine different bonding interactions. Oxygen's quadrupolar interaction (^{17}O) is sensitive and can distinguish BOs ($C_Q \sim$ 4-7 MHz) and NBOs ($C_Q \sim$ 2-3 MHz).[316] The chemical shift is also sensitive, where the difference between BO and NBO is on the order of ~100 ppm.[316] This is precisely the method that has been applied to study a series of crystalline and amorphous glasses. A series of crystalline compounds with four- and six-coordinate germanium were studied by Du and Stebbins:[317] namely $^{[4,6]}GeO_2$, $Na_4{}^{[4,6]}Ge_9O_{20}$ and $Na_2{}^{[4]}GeO_3$. They selected these species as a variety of BO and NBO species are present and can be used to map out the chemical shifts for these environments. Using these parameters as a fingerprint, a series of sodium germanate glasses ranging from 0 to 27 mol% Na_2O were studied using ^{17}O MQMAS. Regions for germanates were determined: $^{[4]}$Ge-O-$^{[4]}$Ge (-25 to -50 ppm), $^{[4]}$Ge-O-$^{[6]}$Ge (-50 to -100 ppm) and $^{[6]}$Ge-O-$^{[6]}$Ge (-110 ppm to -150 ppm), aiding the identification of similar environments within the germanate glasses. Although peak widths within glasses are broadened by a distribution of sites, the MQMAS data were quite clean, yielding a minimum of two sites and providing evidence of higher-coordinating species.

However, Henderson's model[260] predicts both higher-coordinate species (as seen by neutron diffraction) and rings. Rings cause bond lengthening similar to higher-coordinate species, potentially creating issues in the interpretation of the ^{17}O NMR results, such as whether these oxygens are from $^{[4]}$Ge in rings or $^{[5,6]}$Ge units.

Other studies using ^{17}O[318-321] have concluded that an increase in coordination occurs but none have studied the ^{17}O spectral signature of a three-member ring. Although the higher-coordination model is widely accepted, debate continues regarding the true cause of the germanate anomaly.

^{73}Ge NMR is a direct probe that could be used to decide between these models. Using the crystalline series above, three glasses were studied in an attempt to provide further structural information.

6.2.3. Materials and Methods

6.2.3.1. Synthesis

Amorphous germanates were synthesized at 1450°C in a vertical-tube high-temperature furnace in ZGS platinum/gold(5%) crucibles. Quartz-phase GeO_2 was heated for 60 minutes then quenched (in deionized water) to form vitreous GeO_2. Lithium and sodium germanate glasses were made with appropriate fractions of Li_2CO_3 or Na_2CO_3 and mixed with crystalline GeO_2 in an agate mortar and pestle. These mixtures were decarbonated at 650 – 750°C for two hours, reground, and placed into the high-temperature furnace for 60 minutes, followed by quenching. Glasses were analyzed using polarized light microscopy and indicated no visual signs of inclusions or crystallization.

6.2.3.2. Nuclear Magnetic Resonance

Non-spinning ^{73}Ge NMR spectra of the glasses were acquired on a Bruker Avance II 900 (21.1 T) spectrometer with a 7mm MAS low-gamma probe. Samples were packed within 7mm (o.d.) cylindrical sample holders, and pulse widths were calibrated to 2

μs (solid π/2). ^{73}Ge spectra were acquired using either a solid echo or QCPMG (Quadrupolar-Carr-Purcell-Meiboom-Gill) sequence.[280,281] Each spectrum was collected in several (two to four) pieces, then summed to obtain the overall experimental spectrum. Recycle delays were two seconds and collections involved 1024 to 4096 co-added transients (per piece). The number of collected echoes during acquisition (QCPMG) varied between 32 and 128. Magic-angle spinning NMR was done on *v*-GeO_2 at a spinning speed of 7.000 (±0.002) kHz. All spectra were referenced to $GeCl_4$ at 30.9 ppm relative to $Ge(CH_3)_4$ (0 ppm).

6.2.4. RESULTS

6.2.4.1. VITREOUS-GERMANATE, GeO_2

Vitreous-GeO_2 (Figure 6.19 and Figure 6.20) has a Gaussian shaped resonance indicative of a distribution of germanium sites and a spectral width of 1,500 ppm (47 kHz, FWHM of 600 ppm) comparable to the quartz-like crystalline phase. The resonance is about half the breadth of the rutile-like GeO_2 phase bearing a six-coordinate germanium. An upper bound on the C_Q can only be estimated from fitting the breadth of the central transition as < 10.5 MHz using WSolids. These data agree with previous predictions by others and our MAS data.[265] The echo and QCPMG reveal a centre-of-gravity shift of about 220 ppm. Accounting for the second order quadrupolar shift, this implies a $\delta_{iso} \approx -30 \pm 30$ ppm.

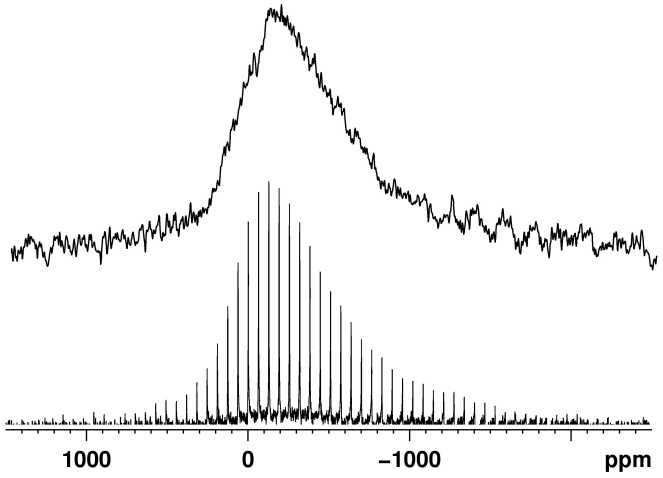

Figure 6.19. ^{73}Ge NMR of vitreous GeO_2 (top) echo and (bottom) QCPMG.

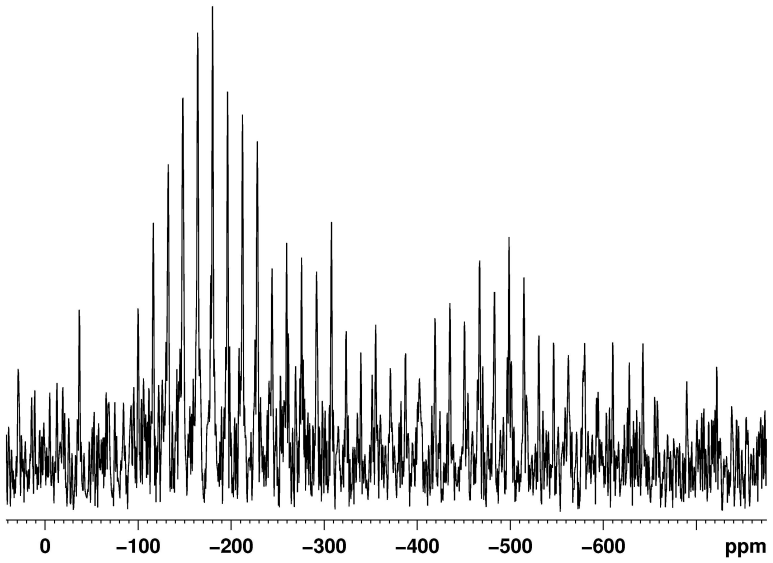

Figure 6.20. ^{73}Ge QCPMG MAS NMR spectrum of *v*-GeO_2 at 8 kHz spinning frequency, intensity at ~-500 ppm is a spinning side band.

6.2.4.2. LITHIUM GERMANATE GLASS

The ^{73}Ge NMR spectrum of lithium germanate (9.3 mol% Li_2O) is shown in Figure 6.21. The spectral width at the base is ~4,500 ppm, with a FWHM of 1,900 ppm. An estimate of the quadrupolar interaction from the central transition is ~ 21 ± 2 MHz. Adding a small amount of Li_2O causes the spectral width (at the base) to more than triple when compared to *v*-GeO_2 suggesting that the quadrupolar interaction increased. The δ_{cgs} ≈-280 ± 50 ppm; incorporating the quadrupolar interaction, an estimate of the isotropic shift is determined to be ~-120 ± 70 ppm. This is a shift to lower frequency relative to *v*-GeO_2.

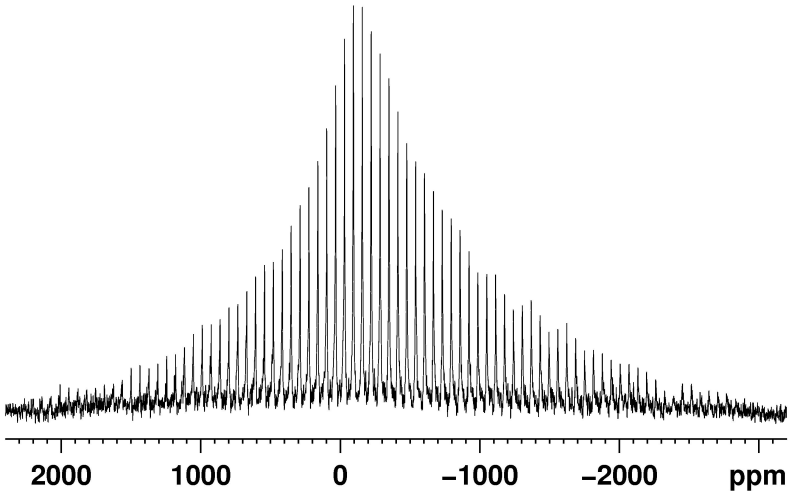

Figure 6.21. ^{73}Ge QCPMG NMR spectrum of 9.3 mol% lithium germanate glass.

6.2.4.3. Sodium Germanate Glass

The ^{73}Ge NMR spectrum of sodium germanate (13.8 mol%) glass is shown in Figure 6.22. As observed for lithium, the spectral breadth increases to ~5,000 ppm and has a δ_{cgs} = ~-300 ± 50 ppm. The quadrupolar interaction determined from the breadth of the central transition is ~23 ± 2 MHz and provides an estimate of the $\delta_{iso} \approx$ -140 ± 70 ppm.

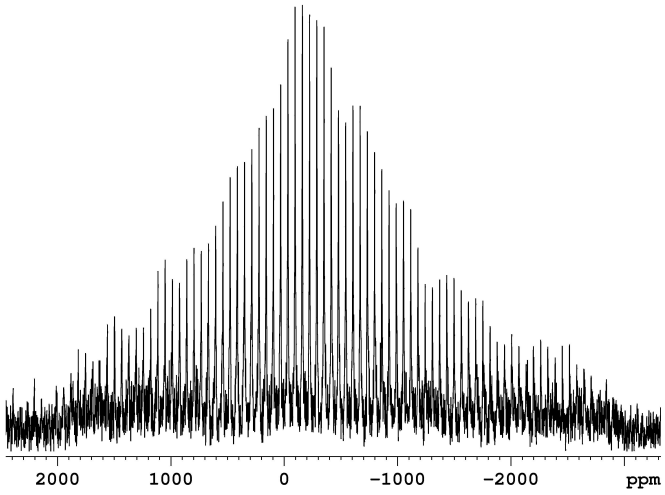

Figure 6.22. ^{73}Ge NMR spectrum of 13.8 mol% sodium germanate glass

6.2.4.4. Alkali Germanates Glasses

An additional four amorphous germanates were synthesized ($32Na_2O•100GeO_2$, $33 K_2O•100GeO_2$, $42K_2O•100GeO_2$ and $56Cs_2O•100GeO_2$) and NMR data acquired at high field. According to the observed physical property trends and models, these species should be pseudo-tetrahedral $^{[4]}$Ge structures and should show similar behaviour to alkali silicate glasses. They are ideal to study, as all $^{[6]}$Ge or rings should not be present in appreciable amounts and only Q^4 and $Q^{3(or2)}$ should be present. Unfortunately, all

four glasses suffered from unfavourable T_2 relaxation rates (as we have seen in silicates with NBOs) preventing successful QCPMG acquisition. Echoes could have been attempted but the length of the experiments and low excitation precluded such an attempt for these glasses.

6.2.5. Discussion

The ^{73}Ge NMR spectra (Figure 6.23) show that significant spectral changes are induced by the addition of alkali oxides. However, the lack of spectral resolution makes the interpretation of such spectra difficult. Based on the foregoing results from the crystalline compounds, all of four-, five- and six-coordinate germanium may possess large C_Qs and they are capable of producing broad spectra. The asymmetry is typically seen when there is a distribution of quadrupolar couplings constants.

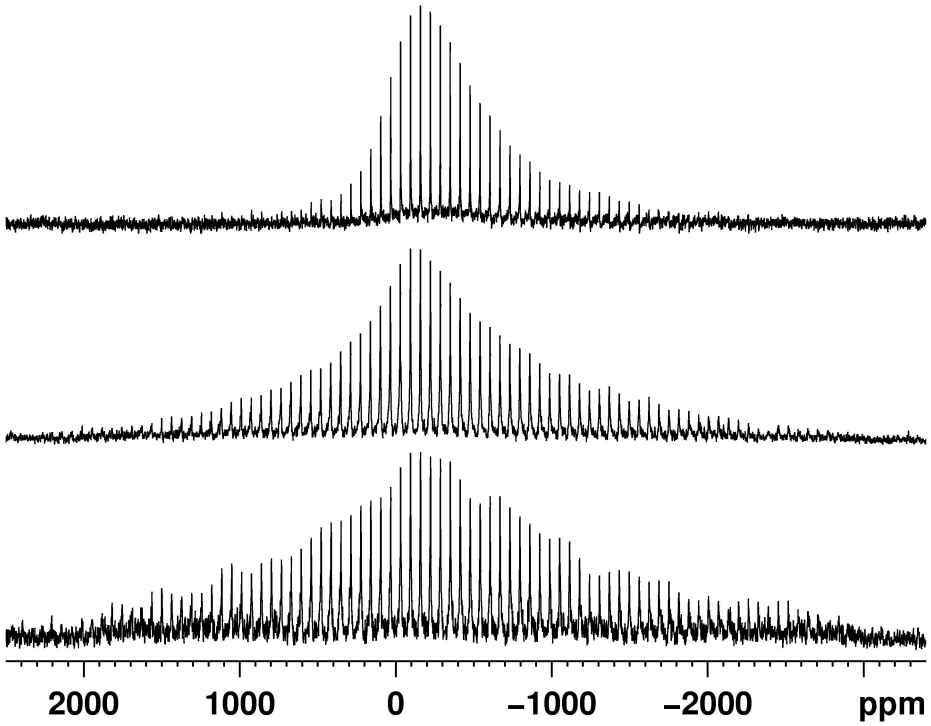

Figure 6.23. ^{73}Ge NMR of (top) *v*-GeO_2, (middle) 9.3 mol% lithium germanate glass and (bottom) 13.8 mol% sodium germanate glass.

However, the ring structures present in both $Bi_2Ge_3O_9$ and $SrGeO_3$ produce comparable quadrupolar interactions of 32 to > 60 MHz, so there may not be a well-defined spectroscopic signature for high-coordinate germanium and rings, especially if non-bridging oxygens are also involved. While the peak maxima shift by about 100 ppm to lower frequency of the GeO_2 glass, the breadth of the peaks make it difficult to assert that this is a true change in isotropic chemical shift. Finally, the likely presence of multiple distinct germanium local environments in a given glass means that low levels of broad overlapping peaks would be undetectable. Possible solutions include higher magnetic fields (>1.8 GHz) and fast magic-angle spinning (>40 kHz) to improve resolution, along with isotopic enrichment to enhance sensitivity.

What we do know is that *v*-GeO_2 occurs in four-coordinate polyhedra (Q^4) and contains a small C_Q resembling quartz-like crystalline GeO_2 and lithium orthogermante (Li_4GeO_4, Q^0).[315] Addition of alkali oxide (lithium and sodium) causes the breadth of the central transition to increase (by two to three times at its base). This indicates a significant change in the local structure based on the crystalline germanates and the sensitivity of C_Q and bond length distortion parameter. The structural changes cannot be conclusive, a higher coordination ($^{[5],[6]}Ge$), rings or both could cause these changes. One important aspect from this study involves NBOs which, as stated by Henderson, form immediately and could explain broadening of the lithium and sodium germanate spectra (formation of Q^3 species could have larger quadrupolar interactions). Fortunately, ^{17}O MAS NMR data are excellent for finding BO and NBOs. NBOs were not observed for the ~14 mol% sodium and ~9 mol% lithium germanate glasses, eliminating as a possible effect in lineshape and breadth.[317] If these glasses contained significant concentrations of rings, we would expect the breadths of the spectrum to be at least 50% larger than measured here, *vide supra*. Since ring structures have large quadrupolar interactions and are expected to be found in small concentrations (<20%), this could be difficult to prove and probe with the currently available technology. Further work will need to be done to further understand what is occurring.

6.3. SUMMARY

The origin of the germanate anomaly remains elusive, however ^{17}O and ^{73}Ge NMR provide evidence that the original theory of Murthy and Ip[15] may be correct. Studying other ring based germanates such as zeolites may provide a good foundation relating chemical shift, quadrupolar interaction and ring structures for these species. ^{73}Ge NMR is possible, although limitations exist, such as short T_2s and low percent of Ge in the sample. Due to the low natural abundance, severe quadrupolar interaction and low gyromagnetic ratio, we are still at the frontiers of ^{73}Ge NMR in germanium containing solids. Higher magnetic fields and improvements in probes (to handle higher powers) will pave the way for future ^{73}Ge NMR work, and the study of other low-gamma nuclei in materials, such as ^{43}Ca, ^{87}Sr and perhaps even ^{197}Au.

7. 1500 Days of Glass and NMR

7.1. Synergy of Oxide Materials

One's research cannot be defined as a unique piece of work, it is a collection of ideas, experiments, hard hours, and at certain times blood, sweat and tears (the latter is especially true when working at high temperatures). Each factor contributes a piece to a puzzle. This puzzle is solved as one discusses, understands and relays the results in a thesis or publication for others to read, learn and move on. The Greeks called this "syn-ergos"; today it is known as synergy, where a collection of pieces placed together provide a more concrete picture with greater understanding.

This thesis is my contribution to the community that studies ordered and disordered oxide materials. The thesis provides a comprehensive discussion on borate-containing glasses ranging from simple binary systems to complex quaternary glasses. The sixth chapter extends these studies by returning to a binary system that has troubled both glass scientists and NMR spectroscopists for more than 50 years, in an attempt to determine alternate methods of studying germanates. The crafting of this thesis was designed to illustrate a variety of NMR methods particularly focused on disordered systems, although these methods can be applied to solids in general. It

also lays a foundation for future studies for others within our group to build upon. Below, I discuss further three recurring aspects within the thesis and present an overview of possible avenues for future exploration of these materials.

The debate over the best method for structure determination of solids may never finish, nor is this the place for such a discussion. However, NMR is indeed a nice complementary tool that is available to provide further information that is sometimes difficult to diagnose solely from x-ray diffraction experiments. Examples of this are apparent in the literature and this area of research is often referred to as 'NMR Crystallography', where a combination of calculations and NMR are used to determine a crystal structure whereas ambiguity exists when using x-ray techniques alone.[322-328] This reinforces why NMR is advantageous especially in disordered materials as it probes local short-range order that is, the *speciation*. X-ray and neutron diffraction are used typically to study the bulk of a sample. NMR is nucleus-specific, that is it is a *selective* probe of a particular nucleus or set of nuclei depending on the experiment, enabling short- and medium-range information. The final recurring theme that will be discussed is *resolution*. The lack of resolution can often limit interpretation. We show that a variety of methods such as high fields, fast MAS and isotopic depletion are ways to improve resolution in NMR of solids.

7.1.1. Speciation

The ability to identify local structure with a variety of NMR methods is critical for determining short- and medium-range order in glasses. Understanding structure-property relationships enables us to design better materials, avoiding any unwanted properties. A good example of this is the study of lithium environments in $LiCoO_2$. As

this material is the industrial standard for battery based applications, understanding the environment and dynamics of lithium has enabled other metals to be considered (manganese, nickel and vanadium).[172,181] High-level radioactive waste is a well studied and understood field, but the inhibition of crystallization and increased loading capacity are areas which could be improved upon for lowering processing costs. NMR is one particular approach that is being used to study these aspects due to its ability to probe local structure.[329,330]

In regards to speciation, the effects of aluminum in alkali borosilicates have been studied. ^{27}Al MAS NMR has demonstrated a change in coordination of Al_2O_3 ($^{[6]}$Al) to $^{[4]}$Al within the borosilicate glass. The effects of aluminum are also seen in ^{29}Si and ^{11}B MAS NMR, as silicon Q^3 polyhedra decrease as aluminum is added. The fraction of $^{[4]}$B was shown to decrease with the incorporation of aluminum. This was attributed to Na^+ moving to aluminum polyhedra, decreasing the need for $^{[4]}$B. Lead boroaluminates, borogallates and boroaluminosilicates have also been studied by our group to determine aluminum and gallium speciation. These systems were shown to contain three different coordination environments for both aluminum and gallium.[14,91] NMR of tourmalines has also been done for its ability to identify small amounts (~1 to 9 %) of $^{[4]}$B and $^{[4]}$Al that are present within these minerals.[88,89,331,332]

NMR is an attractive tool for studying coordination environments in solids. It has been shown that for a variety of nuclei (e.g., B, Si, Al, Na, Li, Mg, etc.) an increase in chemical shift to higher frequency is typically associated with a decrease in coordination number. We have noted this trend with our studies of ^{39}K, ^{87}Rb, ^{133}Cs, ^{51}V and ^{73}Ge. This was proven to be the case for both ^{51}V and ^{73}Ge containing oxides.

However, further work is still required on ^{39}K, ^{87}Rb and ^{133}Cs crystalline oxides to confirm this trend in declining coordination number.

The ability to identify speciation in NMR does not depend solely on chemical shift. Over 70% of the NMR active nuclei within the Periodic Table are quadrupolar. These nuceli can exhibit a quadrupolar interaction that can be used to identify speciation. An excellent example is ^{11}B speciation. The $^{[3]}B$ resonance possesses a second-order quadrupolar lineshape, whereas $^{[4]}B$ does not. The higher local symmetry of the $^{[4]}B$ inhibits second-order broadening of the resonance. Vanadium environments display a similar scenario as ^{11}B. The various four-coordinate vanadates have similar quadrupolar coupling constants < 2 MHz (FWHM of ~5 to 10 kHz). In comparison the $^{[5]}V$ has a lower local symmetry, resulting in a larger quadrupolar interaction, ~3.2 MHz (FWHM of ~25 kHz). A very well known example that uses the quadrupolar interaction for speciation is ^{17}O MAS NMR. ^{17}O NMR of oxides has been shown to be sensitive to whether the oxygen is in a bridging (C_Q ~ 4 - 7 MHz) or non-bridging (C_Q < 3 MHz) environment. We have used this well documented phenomenon for our studies of cesium borosilicate glass.[200,232,316]

High fields (>14 T) and double-resonance methods (i.e., REDOR, CP, etc.) have been used to investigate short-range speciation. High fields have been used to study the neighbouring environments of $^{[4]}B$, while REDOR was shown to aid in identifying where cation species reside within the borate network. REDOR was also shown to be a useful tool for determining site-specific dynamics, rather than global dynamics in cesium borate glasses. REDOR has been used extensively by our group and others to

study speciation, alkali and network-former proximity and connectivity within alkali borosilicates, borovanadates and borophosphate glasses.[85,119,169,250,333]

7.1.2. Selectivity

Most chemically relevant systems are composed of many elements in different arrangements. Choosing the proper method to study these systems can be difficult. X-ray diffraction provides information initially by displaying diffraction peaks that are refined into a specific crystalline space group, irrespective of the elements within the material. This enables one to determine an appropriate structure. However, some knowledge of the elements within that structure is required if mixing occurs. X-rays provide an average of the electron density, which is used to assign elemental positions in the lattice. If there are many elements with similar electron densities or some mixing occurs, these averages could be assigned to inappropriate ions in the lattice. NMR can reveal information regarding fully ordered materials, fully disordered or a mixture of both.[325-327,329] NMR is more selective in that it can specifically probe a particular nucleus of interest. The advantage of selectivity may not be apparent at first but is readily demonstrated in many materials. For example, x-ray diffraction can have difficulty differentiating between materials composed of similar electron densities such as, C / N or Mg / Al / Si. X-ray diffraction also has limitations in identifying species containing hydrogen, lithium and four-coordinate boron. An example of x-ray diffraction having difficulty in differentiating between similar electron densities occurs in the study of cyanide bearing materials (carbon versus nitrogen). This creates difficulties in determining the ordering from x-ray diffraction alone. NMR enables the environment(s) of the nucleus to be probed directly, providing structural

ordering for these cyanide containing materials, i.e., cyanide groups that are terminal, bridging or nitrogen bound using ^{13}C and ^{15}N.[334-337]

Double-resonance NMR methods selecting two spin-pairs (e.g., $^{11}B\{^{133}Cs\}$, $^{11}B\{^{23}Na\}$ and $^{11}B\{^{27}Al\}$) were used to probe the interactions between both $^{[3]}B$ and $^{[4]}B$ environments with sodium and cesium and provide evidence of $^{[4]}B$-O-$^{[4]}Al$ avoidance. Double-resonance NMR enables the study of two interacting nuclei and the determination of how they affect each other's environments. Cross-polarization is a double-resonance method that involves polarization transfer from one nucleus to another. This is commonly used as a tool for sensitivity enhancement; however, we have used this method as a selective technique to differentiate between phosphates containing hydrogen neighbours and those that do not. Recently, a Canadian NMR group (Zwanziger NMR group) at Dalhousie University has demonstrated the ability to probe network connectivity between isotopes of the same element using REDOR. $^{11}B\{^{10}B\}$ REDOR can be implemented to understand how $^{[4]}B$ interacts with other $^{[3]}B$ and $^{[4]}B$. REDOR enabled selectivity for different boron environments and therefore led to a better understanding of its local- and medium-range order.

7.1.3. Resolution

Resolution in any spectroscopic method is always a challenge, NMR being no exception. Resolution is difficult to obtain when dealing with quadrupolar nuclei in disordered environments due to their typically broadened peaks. In the past decade, faster MAS and higher magnetic fields have contributed greatly to improving resolution.

An NMR probe has been developed to increase its spinning speed from

~30 kHz to 70 kHz. This increase in speed has provided better resolution for materials bearing multiple sites. The improvement in resolution is related to the reduction of anisotropic interactions. Faster MAS further provides a means to study nuclei with large quadrupolar interactions. It enables the study of large quadrupolar interactions as it allows the central transition to be observed without the overlap of ssbs. An indirect advantage related to increased resolution from faster MAS is increased sensitivity. The increased sensitivity is related to the reduction in ssbs and the averaging of the anisotropic interactions.

In NMR's infancy, iron-based electromagnets provided field strengths of <2 T. With the introduction of superconducting magnets (starting at 2.35 T) significant improvements for both I=1/2 and I>1/2 nuclei have been accomplished. Recently a superconducting magnet of 23.4 T (1 GHz, ultra-high field) has been introduced by the NMR industry. This increase in field strength is beneficial for resolution. An increase in spectral resolution occurs as the resonance frequency is increased per ppm (e.g., ^{1}H at 4.7 T vs. 23.4 T, the resonance frequency is five-times larger per ppm at the higher field, enabling better resolved sites, resolve higher order J-coupling, etc.). For quadrupolar nuclei, the high field decreases the second-order quadrupolar broadening component of the central transition, thereby increasing resolution.

The reduction of SOQE at high field was used in the study of ^{73}Ge as it reduces the breadth of the CT. Other groups have studied nuclei such as ^{33}S, ^{49}Ti, $^{117/119}$In, ^{209}Bi, etc. because of the advantage related to the reduction of SOQE at higher fields.[338-342] We have also used this increase in resolution at high-fields to study ^{23}Na in crystalline samples. At moderate fields (14 T) evidence of two sodium sites was

obtained. MQMAS provided evidence of a third sodium site. This was later determined to be three different crystalline phases co-existing in the material of interest. Acquiring these data at 21 T using a single-pulse (Bloch decay) experiment provided resolution of the three sites. High-field NMR proved advantageous as it increased resolution, while decreasing the acquisition times (21 T Bloch, ~10 minutes whereas 14 T MQMAS, ~36 hours). The reduction in second-order quadrupole broadening was also used for both potassium and rubidium borate glasses, with ^{39}K potentially displaying evidence of a second site at higher fields and faster MAS (Section 3.2). High-field ^{17}O MAS NMR was used by our group in a cesium borosilicate glass to resolve multiple oxygen sites at 21 T, with comparable resolution to the ^{17}O MQMAS acquired at 14 T. Again, an advantage in time (8 hrs (21 T) vs. 7 days (14 T)) and resolution was achieved.

Three aspects: *speciation*, *selectivity* and *resolution* have been a common theme, aiding in answering questions about borate and germanate based materials. A variety of examples has been mentioned to highlight how speciation, selectivity and resolution have been achieved within this thesis, in other materials studied within the group and by others. Thinking critically about a material, physical properties and ways of using these three aspects will enable the proper experiments to be used in order to answer the underlying questions. Understanding the tools laid out here should enable one to pose a question and choose an appropriate experiment that can answer it.

7.2. Future Studies of Borate-Based Glasses and Low-Gamma Nuclei

The various studies outlined above on borate- and germanate-bearing systems have provided a great detail of information regarding speciation, modifier-former relationship, some insight into alkali mobility, etc. I will now discuss possible extensions for these studies into a 'future works' section, to provide a glimpse of possible avenues one could take. While, some of these may require specialized equipment, most could be attempted with the tools at hand.

7.2.1. Binary Borates

Borate-based glasses have been studied extensively in NMR. Modern high field instruments (≥ 11.7 T) provide resolution between three- and four-coordinate boron. However, medium-range order within heavier alkali borates could be studied further in order to understand the physical origin of the second $^{[4]}$B site. A series of heavy alkali borate based crystalline materials containing a variety of ring structures could be probed by NMR, as vibrational spectroscopy experiments have suggested ring-based species exist. In particular, ^{11}B{^{10}B} REDOR or other multi-dimensional NMR methods such as ^{11}B{^{10}B} HETCOR (HETeronuclear CORrelation experiment, relates species that are connected by a two-dimensional experiment), could be used to probe the B-B interactions. Theoretical cluster calculations could be carried out and used in conjunction with the experimental results to determine the effects on chemical shift and C_Q of rings in various crystalline materials. The data surrounding the

characterization of crystalline borates could then be applied to glasses in the hope of understanding the local- and medium-range structural components.

^{7}Li and ^{133}Cs variable temperature NMR of borate glasses was performed to measure dynamics within the borate framework. These studies were limited by the probe, as the maximum experimental temperature was ~120^{o}C. ^{133}Cs high temperature NMR on cesium borate glasses is a natural choice for future studies. This could provide information on three areas of interest: activation energies, type(s) of mobility and the onset of crystallization as cesium borate glasses are annealed within the spectrometer. Binary borates may seem basic but high temperature ^{133}Cs MAS NMR for glasses has not been well characterized in the existing literature. Borates would provide a system that is well characterized structurally in which one could better understand the measured effects and eventually move to more complex systems such as borosilicates. These results could also provide insight into nuclear waste glasses that typically have internal temperatures of 200 to 300^{o}C during storage. A combination of saturation recovery and EXSY experiments using ^{7}Li and ^{133}Cs would allow characterization of the potential dynamics and perhaps providing evidence of percolation channels.

Crystalline borates and borosilicates involving potassium, rubidium and cesium have not been studied extensively by alkali NMR. The expected chemical shifts and quadrupolar couplings for ^{39}K, ^{87}Rb and ^{133}Cs have focused around simple salts, leaving the opportunity to study glass and mineralogically relevant specimens. As all three spectroscopic probes suggested a decrease in coordination number as alkali loading increased, determining the average coordination environment would be

helpful, possibly leading to a determination of the coordination number(s) in glasses. A systematic study involving a series of potassium, rubidium and cesium containing borate and borosilicate crystals with varying alkali coordination environments could be probed by NMR to better define the quadrupolar couplings and chemical shift ranges expected for these species. These could then be related to borate and borosilicate glass compositions to further the modifying roles of alkali cations. Alkali NMR has been done in this manner in the past for lithium and sodium borosilicates.[121,132] Both potassium and rubidium would benefit from higher fields as ^{39}K is a low-γ nucleus while ^{87}Rb has been shown to contain large quadrupolar couplings. Rubidium also has two NMR active isotopes (^{85}Rb and ^{87}Rb), which could both be probed to extract more accurate C_Qs and possibly chemical shielding interactions. Selection criteria of the crystals would also be important so that a good sampling of coordination environments can be studied (6 to 12, depending on the alkali cation).

Lithium isotope substitution was shown to be an alternative method for acquiring high-resolution ^{7}Li MAS NMR. Isotopic dilution of ^{7}Li could be attempted for lithium borates, borosilicates and borovandates at lower (< 100 K) temperatures. The lower temperatures would inhibit lithium mobility, reducing any chance of spectral coalescence. Choosing borates, borosilicates and borovanadates would provide three different networks that would have a variety of charge-compensating network-forming polyhedra. These differences in speciation with isotopic depletion could potentially reveal different lithium sites. If multiple sites were resolved, the study could be furthered by determining which anionic polyhedron (e.g., T^2, Q^3, $^{[4]}$B)

preferentially interact with the Li^+. Variable temperature EXSY could be used to determine approximate time-scales for alkali-hopping within these glasses and potential activation energies, etc.

7.2.2. Borovanadates

NMR of alkali borovanadate glasses has only been done recently, with a great amount of information being extracted as shown (Chapter 4). However, a few areas of interest include further characterization of alkali and network-forming environments. Understanding the cause of medium-range order observed on $^{[4]}B$ was accomplished using an argument based on borosilicates and quantum chemical calculations. To further confirm our assignments, $^{11}B\{^{51}V\}$ REDOR could be used to probe the proximity between vanadium and boron network formers, in particular, the two $^{[4]}B$ resonances that are observed. One would expect to see stronger dephasing curves for the $^{[4]}B$-site neighbouring a vanadium polyhedron, aiding in assignments. Crystalline and glass samples possessing different degrees of vanadium substitution on $^{[4]}B$ could also be probed, providing a chemical shift 'fingerprint' for medium-range order effects in borovanadates. An alternative approach could be $^{11}B\{^{51}V\}$ CP-HETCOR, where the $^{[4]}B$ site interacting with ^{51}V would produce a cross-peak. These experiments could allow for further structural details to be measured in borovanadates.

Alkali borovanadates are of interest as conductive materials that display an increased conductivity with temperature. High temperature NMR of $^{6/7}Li$, ^{23}Na and ^{133}Cs borovanadates would be beneficial in the study of alkali activation energies, alkali mobility and possible crystalline phase transitions. Although not discussed above, the cesium borovanadate glasses have displayed very low glass transition

temperatures. The crystalline-glass transition temperatures for the borovanadate glasses could be further studied by high temperature NMR as a way to determine the onset of crystallization either by alkali or $^{11}B/^{51}V$ MAS NMR.

7.2.3. Borosilicates

Cesium incorporation in glasses and its effect in limiting volatilization is an ongoing interest for nuclear waste glasses as $^{135\ \&\ 137}Cs$ are common waste products. In Chapter 5 we made reference to $Cs_2O_{(g)}$ being a possible volatilized product. Although we stated that the exact phase is unknown, some further studies in determining this would be fundamental. This may be accomplished by using mass spectrometry (MS). As the sample is heated, the volatilized gas may pass through a MS, enabling the identification of the exact species that leaves the melt. Based on the EMPA, ICP and past[238] results, we are confident that cesium is leaving, thus designing an approach for minimizing cesium loss should be considered. There are three different ways, in which this could be attempted. First, one could add certain oxides that react with cesium quickly. This could potentially cause the cesium to be incorporated into a phase(s) that has a higher boiling point, therefore inhibiting boil-off. Alternatively, one could add other oxides such as P_2O_5, which lower the working temperatures, thus enabling cesium capture without boil-off. A more sophisticated approach might involve synthesizing materials that could incorporate volatile cesium species such as a zeolite, or a lower melting-point oxide, or perhaps a caged structure, prior to the borosilicate vitrification stage. One could use borate, borophosphates or lead-based material to encapsulate cesium cations in one of these low-temperature precursors. These melts (depending on boiling temperatures) could then be introduced into the more robust

borosilicate matrix. These templates could inhibit volatilization while maintaining good glass-forming characteristics and strength as these are added into a borosilicate melt. Glass transition temperatures and electron microprobe analysis would be essential tools for determining the optimal materials. NMR would be used to identify the possible crystalline phases and also as a probe of homogeneous mixing.

In the study of nuclear waste glasses, phase separation in borosilicates is an issue. Our group has moved into this area recently and one can extend this to include molybdenum, zinc, zirconium, lanthanum and titanium which are commonly found in borosilicate waste glasses and act as nucleation sites, promoting crystallization of potentially water-soluble phases. X-ray crystallography can be used to identify certain major phases such as ZrO_2 and $CaMoO_4$, but it often fails to identify other more complex, minor phases that contain cesium such as $NaCsMoO_4$, $NaCs_3Mo_2O_8$ and $Cs_2ZrSi_6O_{15}$.[329] ^{133}Cs MAS NMR can be used to study these devitrified products in model nuclear waste. Areas of interest include identifying devitrified species using alkali NMR, and materials design to inhibit the onset of crystallization or the formation of non-soluble crystalline phases, which can also be characterized by NMR. To study the inhibition of crystalline materials, the addition of phosphorus, aluminium, gallium and indium based oxides could be good starting oxides for such a project. These oxides participate in the glass network, increasing connectivity and aiding glass mixing. The four elements listed above typically form four-coordinate polyhedra, bearing a negative delocalized charge (Al, Ga, In) or form NBO (P).

These changes would relieve the charge balance from $^{[4]}B$, $^{[3]}B$ NBO, and Q^3 as the alkali cations will preferentially interact with aluminum, gallium and indium. This

would enable potentially better mixing and inhibit the alkali cations from interacting with the nucleating agents. Many network-forming and modifying species are NMR active so using Bloch decay or spin echo pulse sequences should be ideally suited to identifying small amounts of crystallinity. Double-resonance NMR methods could be applied to determine glass homogeneity and measure the degree of interaction between alkali modifier/glass former and glass former/glass former, e.g., $^{11}B\{^{23}Na,^{133}Cs\}$, $^{27}Al\{^{133}Cs\}$, $^{29}Si\{^{11}B\}$, etc.).[169,329]

Medium-range order involving $^{[4]}B$ species was seen in borosilicates. These data showed $^{[4]}B(^{1}B,^{3}Si)$ species decreasing while the $^{[4]}B(^{0}B,^{4}Si)$ environment was maintained over the various heating times. This result is interesting in that it indicates some sort of preferential interaction or balance in kinetics. This could be an interesting area to study by synthesizing a series of lithium, sodium, potassium, rubidium or cesium borosilicates and adjusting the melt times. Analyzing the ^{11}B MAS NMR data for relative fractions of the two sites as a function of heating time could provide insight into the kinetic behaviour between the two $^{[4]}B$ resonances. In other words, determining the site preferences of the alkali cations. As the cation size shrinks, the volatility also decreases. Understanding the impact of field strength and volatility on the $^{[4]}B$ resonance(s) could provide structural information on which alkali cations prefer certain $^{[4]}B$ environments. REDOR could also be used to probe modifier and former effects, determining where the cations such as cesium and sodium prefer to interact with the anionic polyhedra (BO_3^-, BO_4^-, SiO_4^-).

Medium-range order in silicon environments has a shift effect on neighbouring species. As seen in the aluminoborosilicate mentioned above, aluminum neighbours

cause a shift to higher frequency. The Grandinetti group has recently shown a two-dimensional ^{29}Si experiment that contains a MAS "1D" spectrum in one dimension, while the other dimension provides a site-specific powder pattern for each Q-species found in the glass (e.g., Q^4, Q^3, etc.).[343] This method could be extended to borosilicates, aluminosilicates and borophosphates to extract the CSA components of ^{29}Si and ^{31}P. Silicon or phosphorus species may be identifiable by their characteristic CSA patterns that occur when substitution of boron or aluminum is involved. The substitution will cause the Q^4, Si-O-Si environment to change with aluminum, with a consequent change in the local symmetry of the site. The effects of aluminum on a silicon polyhedron however, may be undetectably small. To enhance the CSA interaction one would need to attempt these experiments at high-field. This would be attractive and could be further applied to other I=1/2 species such as ^{31}P, ^{89}Y and ^{209}Pb.

Annealing effects in amorphous materials are of interest in some systems. Glasses are maintained around T_g for extended periods of time, which allows certain species to begin to crystallize. The effects are studied by a variety of annealing and sample acquisition steps so that one can track how the glass changes from a disordered solid to an ordered solid. The degree of crystallization is typically determined by combining both x-ray diffraction and NMR on the various heat-treatments the sample undergoes. With a high-temperature MAS probe these glasses could be annealed in the spectrometer and NMR data collected in-situ. This allows a real-time measurement of what is occurring in the glass during the annealing process. If done properly, not only can one stop the experiment at the correct annealing point,

but also the onset of crystallization could be measured as a function of time, therefore enabling the measurement of reaction kinetics.

7.2.4. Germanium-73

^{73}Ge NMR is still in its infancy, although it has been used more this past year than in the previous five years by our group and others.[264,267,344] The increased use of ^{73}Ge NMR has been facilitated by the developing ability to now study this nucleus at high fields.[264] However, limitations still exist, particularly in higher magnetic fields and probes capable of handling higher powers and complex pulse sequences that could aid in population enhancements are required. The significance of higher fields should not be underestimated. Simulations show that fields of 45 T and spinning speeds of 50 kHz will be required to resolve resonances for typical $^{[4]}$Ge and $^{[6]}$Ge sites. While sufficiently fast MAS can be achieved at present, the reduced sample size causes a significant sensitivity issue. The ability for probes to incorporate more sample and spin quickly is not possible as the MAS rate is usually limited by Physics and not mechanically. To put it simply, the rotor cannot break the speed of sound, which is approached earlier as the rotor size increases, limiting the speed at which it can spin. The speed of sound is 343,200 mm/s, as the rotor decreases in size the rotor speed can increase due to the distance traveled decreases (i.e., rotor circumference (π•d(mm)) decreases). However, obtaining higher rf powers could be developed, enabling other techniques such as MQMAS or STMAS (satellite Transition Magic Angle Spinning) to be used. MQMAS or STMAS would enable one to resolve multiple sites that suffer from overlap due to second-order broadening of the CT. Methods such as DAS (dynamic angle spinning) and DOR (double rotation) would be difficult. DOR

would cause large amounts of ssb overlap while DAS requires longer T_2*s*, than normally found in these materials. To increase sensitivity, population transfer methods could be employed. These methods have been used often for I=3/2 and 5/2 nuclei, providing a basis for attempting these techniques on similar nuclei. As only a handful of nuclei have I=9/2, these have not been attempted to any real extent and some 'trial and error' is required to optimize these sequences. Three sequences of particular interest include RAPT[345,346] (rotor-assistance-population transfer), which would be ideal for MAS conditions; DFS[347,348] (double-frequency sweep) and HS[349,350] (hyperbolic secant) which are methods that can be used for spinning and non-spinning samples. Optimization of these three methods could be done using ^{93}Nb NMR, as it is an easier and more receptive I=9/2 nucleus than ^{73}Ge. The optimized parameters should transfer efficiently, provided similar quadrupolar interactions and rf powers are used. The gain in S/N would be on the order of three to four times, which, for ^{73}Ge NMR, would allow more routine observation at high field and widen the potential applications at lower fields.

We have studied germanium oxide and halide materials, with an opportunity to extend our studies to organo-germanium compounds. As organics typically contain many hydrogen or fluorine nuclei, cross-polarization could potentially be used to study them by NMR. CP involves transferring the polarization from a high-gamma nucleus (e.g., ^{1}H) to a lower gamma nucleus (e.g., ^{73}Ge), thereby causing an increase in sensitivity. Cross-polarization for low frequency quadrupolar nuclei is difficult in practice as finding the appropriate match conditions is not trivial. To alleviate this, we could begin by selecting samples with little to no quadrupolar interaction. These

species behave like I=1/2 nuclei and make it easier to find the Hartman-Hahn match. In the presence of quadrupolar interactions or MAS, pulse calibrations begin to change making the match conditions more difficult to find. For low gamma quadrupolar nuclei the contact times (i.e., the time required to efficiently transfer ^{1}H spin-polarization to germanium) are longer (~20 to 60 ms). These longer times create excess heating and potentially damage the probe. The wide-bore magnet installed earlier this year in our laboratory is ideal for an attempt at CP, as the corresponding probes are more robust. A series of samples with a range of small to moderate quadrupolar couplings would be ideal for optimizing this method. This would provide comprehensive parameters that could be further implemented into a large range of characterization tools for solid organic-bearing germanium compounds.

MQMAS would be a natural choice to attempt resolution of multiple sites in systems containing more than one germanium site. These experiments would be best accomplished at the ultrahigh field facility. The current probe (7mm MAS) spins slowly (<8 kHz) and has a rather poor ν_{rf} (17 kHz), inhibiting the ability to perform MQMAS. A faster MAS probe (~20 kHz) would allow certain ^{73}Ge samples to be studied without overlap of ssb within the CT, further increasing resolution and sensitivity. The reduction in coil size (which is required to spin faster) provides better filling factors and the ability to obtain higher rf pulses. These two changes are ideal for enabling MQMAS as a possible two-dimensional method for resolving multiple sites.

The decrease in sample volume limits the amount of ^{73}Ge in the rotor. To circumvent this and improve sensitivity for the MQMAS method, enriching with ^{73}Ge would need to be considered. Isotopic enrichment would alleviate many of the

difficulties in acquiring a ^{73}Ge NMR spectrum. As MQMAS is not trivial for spin 9/2 nucleus, optimization on ^{93}Nb could be attempted, with parameters used as starting conditions for ^{73}Ge. If these experiments proved to be fruitful on basic systems such as GeO_2, a variety of the samples studied in Chapter 6 could be resolved without the need for 40+ T magnets, and may possibly provide insight into the germanate anomaly. A drawback is the cost of enrichment. The cost of ^{73}Ge enrichment was approximately \$12 USD / mg for GeO_2 as of late-2010. A 4 mm rotor can accommodate ~100 mg oxide: as an example, for GeO_2 with 95% ^{73}Ge, would cost around \$1200. Single resonance experiments such as QCPMG and spin echo would not require such high enrichment, lowering the average cost per sample, however for MQMAS to be a viable option, maximum enrichment (95%) would be essential. If the crystalline systems are successful, we would require ~ 1 g (four samples at 300 mg) to attempt to solve the germanate anomaly. A crude estimate for these samples is ~ \$14 000, which is in part why no attempt has been made.[x]

Off-angle (or variable angle) experiments have been used with some success.[351-353] As our group searches for a way to reduce the large second-order quadrupolar effect on the CT for ^{73}Ge, some thought has gone into off-angle experiments. As discussed in Chapter 1, all major anisotropic interactions contain a term $(3\cos^2\theta-1)$ that goes to zero if one spins "infinitely fast" at the magic angle (54.7°). However, the second-order interaction is subject to an additional spatial relation ($P_4(\cos\theta)$) described by the fourth-order Legendre polynomial. The magic

[x] For reference, other isotopes used or considered were, ^{6}Li at ~ \$0.03 / mg, ^{17}O at ~\$1.37/ mg, ^{95}Mo at ~\$3.50/mg, ^{33}S at ~\$4.30 / mg and ^{29}Si at ~\$8.00 / mg.

angle deals with the $P_2(\cos\theta)$ but the $P_4(\cos\theta)$ term only partially averages out as mentioned in Chapter 1:

$$P_4(\cos\theta) = 0.125(35\cos\theta^4 - 30\cos\theta^2 + 3) \quad (7.1)$$

For this interaction to be averaged it must be rotated at either 30.6° or 70.1°. Unfortunately, there is not a single angle that averages both of these polynomials simultaneously but we can change the probe angle to minimize both.[4] It has been observed that variable angle spinning of ^{133}Cs NMR at an angle of 52.25° provided efficient minimization of the quadrupolar and CSA contributions.[354] Although ^{73}Ge will have a larger quadrupolar interaction similar experiments could be attempted. If this were achievable, the significant reduction in the breadth of the central transition could potentially allow resolution of multiple sites, as the off-angle axis minimizes further the second-order quadrupolar interaction while maintaining efficient averaging of the chemical shielding and first-order quadrupolar interaction. If certain specialty probes were available such as DOR or a DAS probe, these would be worth attempting as they spin at two angles, the magic angle (54.7°) and the angle at which the second-order quadrupolar interaction is averaged (30.6°). These probes do have limitations, as slow spinning of the outer rotor in DOR will produce a 'nightmare' of ssbs, inhibiting resolution. DAS provides faster spinning which can prove to be beneficial but it requires the sample to have longer T_2s (>1000 μs), which is not typically the case for our samples.

A variety of avenues have been suggested for borate-based glasses and germanium-bearing systems. Many of these would have been ideal to try while studying these materials, however most will not be amenable within our laboratory

setting until early next year. The most interesting systems to investigate further include borosilicates, as these materials are the most industrially relevant glasses with a variety of directions worth pursuing. Our group has studied ^{73}Ge NMR and has made major contributions to this area however a few key areas are still worth pursuing. In particular, the ability to obtain more highly resolved spectra and attempting cross-polarization for organic-bearing germanium.

8. References

(1) Müller-Warmuth, W.; Eckert, H. *Physics Reports* **1982**, *88*, 91-149.

(2) Shelby, J. E. *Introduction to Glass Science and Technology*; 2 ed.; RSC: Cambridge, 2005.

(3) Zachariasen, W. H. *Journal of the American Chemical Society* **1932**, *54*, 3841.

(4) Mackenzie, K. J. D.; Smith, M. E. *Multinuclear Solid-State NMR of Inorganic Materials*; 1 ed.; Pergamon, 2002.

(5) Dupree, R.; Holland, D.; Mortuza, M. G. *Nature* **1987**, *328*, 416.

(6) Stebbins, J. F.; Farnan, I.; Xue, X. *Chemical Geology* **1992**, *96*, 371.

(7) Youngman, R. E.; Haubrich, S. T.; Zwanziger, J. W.; Janicke, M. T.; Chmelka, B. F. *Science* **1995**, *269*, 1416.

(8) Bray, P. J. *Inorganica Chimica Acta* **1999**, *289*, 157.

(9) Kroeker, S.; Stebbins, J. F. *Inorganic Chemistry* **2001**, *40*, 6239.

(10) Rao, K. J. *Structural Chemistry of Glasses*; Elsevier: New York, 2002.

(11) Hoppe, U.; Kranold, R.; Weber, H. J.; Hannon, A. C. *Journal of Non-Crystalline Solids* **1999**, *248*, 1.

(12) Ketelaar, J. A. A. *Zekgax* **1936**, *95*, 9.

(13) Mackenzie, K. J. D.; Smith, M. E. *Multinuclear Solid-State NMR of Inorganic Materials*; Pergamon: London, 2002; Vol. 6.

(14) Wren, J. E. C.; Michaelis, V. K.; Kroeker, S. *In Preparation* **2010**.

(15) Murthy, M. K.; Ip, J. *Nature* **1964**, *201*, 285-286.

(16) Lide, D. R. *CRC Handbook of Chemistry and Physics*; 82 ed.; CRC Press: Florida, 2001.

(17) Hawthorne, F. C. *Spectroscopic Methods in Mineralogy and Geology*; Mineralogical Society of America: Chelsea, 1988; Vol. 18.

(18) Skoog, D. A.; Holler, F. J.; Nieman, T. A. *Principles of Instrumental Analysis*; 5 ed.; Brooks/Cole: USA, 1998.

(19) Maniu, D.; Iliescu, T.; Ardelean, S.; Cinta-Pinzaru, S.; Tarcea, N.; Kiefer, W. *Journal of Molecular Structure* **2003**, *651*, 485.

(20) Cramer, C. J. *Essentials of Computational Chemistry: Theories and Models*; Wiley: West Sussex, 2005.

(21) Slichter, C. P. *Principles of Magnetic Resonance*; Harper & Row: New York, 1963.

(22) Fukushima, E.; Roeder, S. B. *Experimental Pulse NMR*; Addison-Wesley: London, 1981.

(23) Levitt, M. H. *Spin Dynamics: Basics of Nuclear Magnetic Resonance*; Wiley & Sons Ltd: Chichester, 2001.

(24) Larmor, J. *Philosophical Magazine* **1897**, *44*, 503.

(25) Orendt, A. M. *Chemical Shift Tensor Measurement in Solids*; Wiley, 2007.

(26) Duer, M. J. *Solid-State NMR Spectroscopy*; Blackwell Science: Cambridge, 2002.

(27) Wasylishen, R. E. *Encyclopedia of NMR*, 1996; Vol. 3.

(28) Cohen, M. H.; Reif, F. *Solid State Physics* **1957**, *5*, 321.

(29) Man, P. P. *Encyclopedia of Analytical Chemistry*; John Wiley and Sons: Chichester, 2000.

(30) Man, P. P. *Quadrupolar Interactions*; WILEY, 2007.

(31) Schaefer, T.; Kroeker, S.; McKinnon, D. M. *Canadian Journal of Chemistry* **1995**, *73*, 1478.

(32) Andrew, E. R., Bradbury, A. and Eades, R.G. *Nature* **1959**, *183*, 1802.

(33) Lowe, I. J. *Physical Review Letters* **1959**, *2*, 285-287.

(34) Czjzek, G.; Fink, J.; Gitz, F.; Schmidt, H.; Coey, J. M. D.; Rebouillat, J. P.; Lienard, A. *Physical Review B* **1981**, *23*, 2513.

(35) Michaelis, V. K.; Marat, K., **2008**, Construction and Application of a Single Channel Low-Gamma Broadband Solids Probe.

(36) Bloch, F. *Physical Review* **1946**, *70*, 460.

(37) Bloch, F.; Hansen, W. W.; Packard, M. *Physical Review* **1946**, *70*, 474.

(38) Hahn, E. L. *Physical Review* **1950**, *80*, 580.

(39) Mansfield, P. *Physical Review* **1965**, *137*, A961.

(40) Davis, J. H.; Jeffrey, K. R.; Bloom, M.; Valic, M. I.; Higgs, T. P. *Chemical Physics Letters* **1976**, *42*, 390.

(41) Farrar, T. C. *NMR Spectroscopy*; Ferragut Press: Madison, 1997.

(42) Carr, H. Y.; Purcell, E. M. *Physical Review* **1954**, *94*, 630.

(43) Larsen, F. H.; Jakobsen, H. J.; Ellis, P. D.; Nielsen, N. C. *Journal of Physical Chemistry A* **1997**, *101*, 8597.

(44) Meiboom, S.; Gill, D. *Review of Scientific Instruments* **1958**, *29*, 688.

(45) O'Dell, L. A.; Rossini, A. J.; Schurko, R. W. *Chemical Physics Letters* **2009**, *468*, 330-335.

(46) O'Dell, L. A.; Schurko, R. W. *Journal of American Chemical Society* **2009**, *131*, 6658-6659.

(47) Jeneer, J.; Meier, B. H.; Bachmann, P.; Ernst, R. R. *Journal of Chemical Physics* **1979**, *71*, 4546.

(48) Bain, A. D. *Progress in Nuclear Magnetic Resonance Spectroscopy* **2003**, *43*, 63.

(49) Gullion, T. *Concepts in Magnetic Resonace* **1998**, *10*, 277.

(50) Gullion, T.; Schaefer, J. *Journal of Magnetic Resonance (1969)* **1989**, *81*, 196-200.

(51) Frydman, L.; Harwood, J. S. *Journal of the American Chemical Society* **1995**, *117*, 5367-5368.

(52) Koch, W.; Holthausen, M. C. *A Chemist's Guide to Density Functional Theory*; 2nd ed.; Wiley-VCH: Weinheim, 2007.

(53) Kohn, W.; Sham, L. J. *Physical Review* **1965**, *140*, A1133.

(54) Frisch, M. J.; Trucks, G. W.; Schlegel, H. B.; Scuseria, G. E.; Robb, M. A.; Cheeseman, J. R.; Montgomery, J., J.A.; Vreven, T.; Kudin, K. N.; Burant, J. C.; Millam, J. M.; Iyengar, S. S.; Tomasi, J.; Barone, V.; Mennucci, B.; Cossi, M.; Scalmani, G.; Rega, N.; Petersson, G. A.; Nakatsuji, H.; Hada, M.; Ehara, M.; Toyota, K.; Fukuda, R.; Hasegawa, J.; Ishida, M.; Nakajima, T.; Honda, Y.; Kitao, O.; Nakai, H.; Klene, M.; Li, X.; Knox, J.; Hratchian, H. P.; Cross, J. B.; Bakken, V.; Adamo, C.; Jaramillo, J.; Gomperts, R.; Stratmann, R. E.;

Yazyev, O.; Austin, A. J.; Cammi, R.; Pomelli, C.; Ochterski, J. W.; Ayala, P. Y.; Morokuma, K.; Voth, G. A.; Salvador, P.; Dannenberg, J. J.; Zakrzewski, V. G.; Dapprich, S.; Daniels, A. D.; Strain, M. C.; Farkas, O.; Malick, D. K.; Rabuck, A. D.; Raghavachari, K.; Foresman, J. B.; Ortiz, J. V.; Cui, Q.; Baboul, A. G.; Clifford, S.; Cioslowski, J.; Stefanov, B. B.; Liu, G.; Liashenko, A.; Piskorz, P.; Komaromi, I.; Martin, R. K.; Fox, D. J.; Keith, T.; Al-Laham, M. A.; Peng, C. Y.; Nanayakkara, A.; Challacombe, M.; Gill, P. M. W.; Johnson, B.; Chen, W.; Wong, M. W.; Conzalez, C.; Pople, J. A.; G03 ed.; Gaussian: 2003.

(55) Becke, A. D. *Journal of Chemical Physics* **1996**, *107*, 8554.

(56) Binkley, J. S.; Pople, J. A.; Hehre, W. J. *Journal of American Chemical Society* **1980**, *102*, 939.

(57) Gordan, M. S.; Binkley, J. S.; Pople, J. A.; Pietro, W. J.; Hehre, W. J. *Journal of American Chemical Society* **1982**, *104*, 2791.

(58) Dunning, T. H. *Journal of Chemical Physics* **1989**, *1990*, 1007.

(59) Hay, P. J. *Journal of Chemical Physics* **1977**, *66*, 4377.

(60) Kendall, R. A.; Dunning, T. H.; Harrison, R. J. *Journal of Chemical Physics* **1992**, *96*, 6796.

(61) McLean, A. D.; Chandler, G. S. *Journal of Chemical Physics* **1980**, *72*, 5639.

(62) Raghavachari, K.; Binkley, J. S.; Seeger, R.; Pople, J. A. *Journal of Chemical Physics* **1980**, *72*, 650.

(63) Wachters, A. J. H. *Journal of Chemical Physics* **1970**, *52*, 1033.

(64) Frisch, M. J.; Pople, J. A.; Binkley, J. S. *Journal of Chemical Physics* **1984**, *80*, 3265.

(65) Clark, T.; Chandrasekhar, J.; Spitznagel, G. W.; Schleyer, P. v. R. *Journal of Computational Chemistry* **1983**, *4*, 294.

(66) Profeta, M. M.; Mauri, F.; Pickard, C. J. *Journal of the American Chemical Society* **2003**, *125*, 541.

(67) Segall, M. D.; Lindan, P. J. D.; Probert, M. J.; Pickard, C. J.; Hasnip, P. J.; Clark, S. J.; Payne, M. C. *Journal of Physics: Condensed Matter* **2002**, *14*, 2717.

(68) Perdew, J. P.; Burke, K.; Ernzerhof, M. *Physical Review Letters* **1996**, *77*, 3865.

(69) Perdew, J. P.; Burke, K.; Ernzerhof, M. *Physical Review Letters* **1998**, *80*, 891.

(70) Yates, J. R.; Pickard, C. J.; Payne, M. C.; Mauri, F. *Journal of Chemical Physics* **2003**, *118*, 5746.

(71) Pickard, C. J.; Mauri, F. *Physical Review B* **2001**, *63*, 245101.

(72) Yates, J. R.; Pickard, C. J.; Mauri, F. *Physical Review B* **2007**, *76*, 024401.

(73) Blaha, P.; Schwarz, K.; Madsen, G. K. H.; Kvasnicka, D.; Luitz, J.; Karlheinz Schwarz: Techn. Universität, Austria, 2001.

(74) Eichele, K.; 1.18.8 ed. Tübingen, 2007.

(75) Alderman, D. W.; Solum, M. S.; Grant, D. M. *Journal of Chemical Physics* **1986**, *84*, 3717.

(76) James, F.; Ross, M. *Computer Physics Communications* **1975**, *10*, 343.

(77) Skibsted, J.; Nielsen, N. C.; Bildsoe, H.; Jakobsen, H. J. *Journal of Magnetic Resonance* **1991**, *95*, 88.

(78) Skibsted, J.; Nielsen, N. C.; Bildsoe, H.; Jakobsen, H. J. *Chemical Physics Letters* **1992**, *188*, 405.

(79) Skibsted, J.; Nielsen, N. C.; Bildsoe, H.; Jakobsen, H. J. *Journal of American Chemical Society* **1993**, *115*, 7351.

(80) Marat, K.; 3.16 ed.; University of Manitoba: Winnipeg, 2009.

(81) Bak, M.; Rasmussen, J. T.; Nielsen, N. C. *Journal of Magnetic Resonance* **2000**, *147*, 296.

(82) Liu, S. M.; Huang, J. Y.; Jiang, Z. J.; Zhang, C.; Zhao, J. Q.; Chen, J. *Journal of Applied Polymer Science* **2010**, *117*.

(83) Miwa, K.; Kamiya, T.; Fujiwara, T. *Current Opinion in Plant Biology* **2009**, *12*.

(84) Bohmer, R.; Jeffrey, K. R.; Vogel, M. *Progress in Nuclear Magnetic Resonance Spectroscopy* **2007**, *50*, 87.

(85) Aguiar, P. M.; Kroeker, S. *Solid State Nuclear Magnetic Resonance* **2005**, *27*, 10.

(86) Kroeker, S.; Aguiar, P. M.; Cerquiera, A.; Clarida, W. J.; Doerr, J.; Olesiuk, M.; Ongie, G.; Affatigato, M.; Feller, S. A. *European Journal of Glass Science and Technology* **2006**, ***47***, 393.

(87) Kroeker, S.; Feller, S. A.; Affatigato, M.; O'Brien, C. P.; Clarida, W. J.; Kodama, M. *Physics and Chemistry of Glasses* **2003**, *44*, 54.

(88) Lussier, A. J.; Aguiar, P. M.; Michaelis, V. K.; Kroeker, S.; Hawthorne, F. C. *American Mineralogist* **2009**, *94*, 785.

(89) Lussier, A. J.; Aguiar, P. M.; Michaelis, V. K.; Kroeker, S.; Herwig, S.; Abdu, Y.; Hawthorne, F. C. *Mineralogical Magazine* **2008**, *72*, 747.

(90) Michaelis, V. K.; Aguiar, P. M.; Kroeker, S. *Journal of Non-Crystalline Solids* **2007**, ***353***, 2582.

(91) Saini, A.; Khanna, A.; Michaelis, V. K.; Kroeker, S.; Gonzalez, F.; Hernandez, D. *Journal of Non-Crystalline Solids* **2009**, *355*, 2323-2332.

(92) Mason, J. *Multinuclear NMR*; Springer, 1987.

(93) Aguiar, P. M.; Kroeker, S. *Journal of Non-Crystalline Solids* **2007**, *353*, 1834.

(94) Zachariasen, W. H. *Acta Crystallographica* **1964**, *17*, 749.

(95) Lithium borate, $Li_4B_2O_5$, ICDD; Technisch Physische Dienst, p 2.

(96) Hahn, T. *Space-Group symmetry*; International Union of Crystallography, 2006; Vol. A.

(97) Stewner, V. F. *Acta Crystallographica* **1971**, *B27*.

(98) Granger, P.; Harris, R. K. *Multinuclear Magnetic Resonance in Liquids and Solids - Chemical Applications*; Kluwer Academic London, 1988; Vol. 322.

(99) Akai, T. *Journal of Non-Crystalline Solids* **2000**, *262*, 271.

(100) Rhee, C.; Bray, P. J. *Physics and Chemistry of Glasses* **1971**, *12*, 156.

(101) Imre, A. W.; Voss, S.; Berkemeier, F.; Mehrer, H.; Konidakis, I.; Ingram, M. D. *Solid State Ionics* **2006**, *177*, 963.

(102) Müller, W.; Kruschke, D.; Torge, M.; Grimmer, A.; Schutt, H. *Solid State Ionics* **1987**, *23*, 53.

(103) Parkinson, B. G.; Holland, D.; Smith, M. E.; Howes, A. P.; Scales, C. R. *Journal of Non-Crystalline Solids* **2005**, *351*, 2425.

(104) Donald, I. W.; Metcalfe, B. L.; Taylor, R. N. J. *Journal of Materials Science* **1997**, *32*, 5851.

(105) Bray, P. J. *Inorganica Chimica Acta* **1999**, *289*, 158 - 173.

(106) Bray, P. J.; Peterson, G. L. *Zeitschrift für Naturforschung* **1998**, *53a*, 273 - 284.

(107) Silver, A. H.; Bray, P. J. *Journal of Chemical Physics* **1958**, *29*, 984.

(108) Ratai, E.; Janssen, M.; Epping, J. D.; Eckert, H. *Physics and Chemistry of Glasses* **2003**, *44*, 45.

(109) Youngman, R. E.; Zwanziger, J. W. *Journal of the American Chemical Society* **1995**, *117*, 1397.

(110) Clarida, W. J.; Berryman, J. R.; Affatigato, M.; Feller, S. A.; Kroeker, S.; Ash, J.; Zwanziger, J. W.; Meyer, B.; Borsa, F.; Martin, S. W. *Physics and Chemistry of Glasses* **2003**, *44*, 215-217.

(111) Janssen, M.; Eckert, H. *Solid State Ionics* **2000**, *136-137*, 1007.

(112) Kroeker, S.; Aguiar, P. M.; Cerquiera, A.; Clarida, W. J.; Doerr, J.; Olesiuk, M.; Ongie, G.; Affatigato, M.; Feller, S. A. *European Journal of Glass Science and Technology* **2006**, ***47***, 393.

(113) Jellison, G. E.; Feller, S. A.; Bray, P. J. *Physics and Chemistry of Glasses* **1978**, *19*, 52.

(114) Mackenzie, K. J. D.; Smith, M. E. *Multinuclear Solid-State NMR of Inorganic Materials*; Pergamon: Cambridge, 2002.

(115) Gan, Z.; Gor'kov, P.; Cross, T.; Samoson, A.; Massiot, D. *Journal of the American Chemical Society* **2002**, *124*, 5634.

(116) Stebbins, J. F.; Du, L.-S.; Kroeker, S.; Neuhoff, P.; Rice, D.; Frye, J.; Jakobsen, H. J. *Solid State Nuclear Magnetic Resonance* **2002**, *21*, 105.

(117) Kroeker, S.; Neuhoff, P.; Stebbins, J. F. *Journal of Non-Crystalline Solids* **2001**, *293-295*, 440.

(118) Ratai, E.; Janssen, M.; Eckert, H. *Solid State Ionics* **1998**, *105*, 25 - 37.

(119) Epping, J. D.; Strojek, W.; Eckert, H. *Physical Chemistry Chemical Physics* **2005**, *7*, 2384.

(120) Gee, B.; Janssen, M.; Eckert, E. *Journal of Non-Crystalline Solids* **1997**, *215*, 41.

(121) Xu, Z.; Stebbins, J. F. *Solid State Nuclear Magnetic Resonance* **1995**, *5*, 103.

(122) Stebbins, J. F. *Solid State Ionics* **1998**, *112*, 137.

(123) Massiot, D.; Bessada, C.; Coutures, J. P.; Taulelle, F. *Journal of Magnetic Resonance (1969)* **1990**, *90*, 231-242.

(124) Harris, R.; Becker, E. *Journal of Magnetic Resonance* **2002**, *156*, 323.

(125) Skibsted, J.; Jakobsen, H. J. *Journal of Physical Chemistry A* **1999**, *103*, 7958.

(126) Vosegaard, T.; Byriel, I. P.; Jakobsen, H. J. *Journal of Physical Chemistry B* **1997**, *101*, 8955.

(127) Kroeker, S.; Aguiar, P. M.; Cerquiera, A.; Clarida, W. J.; Doerr, J.; Olesiuk, M.; Ongie, G.; Affatigato, M.; Feller, S. A. *European Journal of Glass Science and Technology* **2006**, ***47***, 393.

(128) Varsamis, C. E.; Vegiri, A.; Kamitsos, E. I. *Physics and Chemistry of Glasses* **2004**, *46*, 72.

(129) Vegiri, A.; Varsamis, C. E.; Kamitsos, E. I. *Journal of Chemical Physics* **2005**, *123*, 014508.

(130) Shannon, R. D. *Acta Crystallographica A* **1976**, *32*, 751.

(131) Engelhardt, G.; Michel, D. *High-Resolution Solid-State NMR of Silicates and Zeolites*; John Wiley & Sons, 1987.

(132) George, A. M.; Sen, S.; Stebbins, J. F. *Solid State Nuclear Magnetic Resonance* **1997**, *10*, 9.

(133) Fiske, P. S.; Stebbins, J. F. *American Mineralogist* **1994**, *79*, 848.

(134) Kroeker, S.; Stebbins, J. F. *American Mineralogist* **2000**, *85*, 1459.

(135) Cherry, B. R.; Nyman, M.; Alam, T. M. *Journal of Solid State Chemistry* **2004**, *177*, 2079.

(136) Mason, J. *Multinuclear NMR*; Plenum Press, 1987.

(137) Frugier, P.; Martin, C.; Ribet, I.; Advocat, T.; Gin, S. *Journal of Nuclear Materials* **2005**, *346*, 194.

(138) Frugier, P.; Gin, S.; Minet, Y.; Chave, T.; Bonin, B.; Godon, N.; Lartigue, J. E.; Jollivet, P.; Ayral, A.; De Windt, L.; Santarini, G. *Journal of Nuclear Materials* **2008**, *380*, 8-21.

(139) Werbelow, L. G. *Relaxation Theory for Quadrupolar Nuclei*; Wiley, 2002.

(140) Traficante, D. D. *Relaxation: An Introduction*; Wiley, 2002.

(141) Bohmer, R.; Qi, F. *Solid State Nuclear Magnetic Resonance* **2007**, *31*, 28.

(142) Gobel, E.; Muller-Warmuth, W.; Olyschlager, H. *Journal of Magnetic Resonance* **1979**, *36*, 371.

(143) Kim, C.; Hwang, Y.; Kim, H. K.; Kim, J. N. *Physics and Chemistry of Glasses* **2003**, *44*, 166.

(144) Nagel, R.; Grob, T. W.; Gunther, H.; Lutz, H. D. *Journal of Solid State Chemistry* **2002**, *165*, 303.

(145) Sen, S.; Stebbins, J. F. *Physical Review B* **1997**, *55*, 3512.

(146) Shantz, D. F.; Lobo, R. F. *Journal of Physical Chemistry B* **1998**, *102*, 2339.

(147) Malyarenko, D. I.; Vold, R. L.; Hoatson, G. L. *Macromolecules* **2000**, *33*, 7508.

(148) Meyer, B.; Borsa, F.; Martin, D. M.; Martin, S. W. *Physical Review B: Condensed Matter and Materials Physics* **2005**, *72*, 144301.

(149) Wilkening, M.; Amade, R.; Iwaniak, W.; Heitjans, P. *Physical Chemistry Chemical Physics* **2007**, *9*, 1239.

(150) Lee, Y. J.; Wang, F.; Grey, C. P. *Journal of the American Chemical Society* **1998**, *120*, 12601.

(151) Bloembergen, N.; Purcell, E. M.; Pound, R. V. *Physical Review* **1948**, *73*, 679.

(152) Massiot, D.; Bessada, C.; Echegut, P.; Coutures, J. P.; Taulelle, F. *Solid State Ionics* **1990**, *37*, 223.

(153) Stebbins, J. F. *Chemical Review* **1991**, *91*, 1353.

(154) Stebbins, J. F.; Farnan, I. *Science* **1992**, *255*, 586.

(155) Winter, R.; Jones, A.; Shaw-West, R.; Wolff, M.; Florian, P.; Massiot, D. *Applied Magnetic Resonance* **2007**, *32*, 635.

(156) Greaves, G. N.; Fontaine, A.; Lagarde, P.; Raoux, D.; Gurman, S. J. *Nature* **1981**, *293*, 611-616.

(157) Bielecki, A.; Burum, D. P. *Journal of Magnetic Resonance* **1995**, *116*, 215.

(158) Massiot, D.; Bessada, C.; Coutures, J. P.; Taulelle, F. *Journal of Magnetic Resonance* **1990**, *90*, 231.

(159) Voigt, U.; Lammert, H.; Eckert, H.; Heuer, A. *Physical Review B* **2005**, *72*, 064207.

(160) Vogel, M.; Brinkmann, C.; Eckert, H.; Heuer, A. *Journal of Non-Crystalline Solids* **2006**, *352*, 5156.

(161) Aguiar, P. M.; Kroeker, S. C. *Solid State Nuclear Magnetic Resonance* **2005**, *27*, 10 - 15.

(162) Matsuo, T.; Shibasaki, M.; Saito, N.; Katsumata, T. *Journal of Applied Physics* **1996**, *79*, 1903.

(163) Waugh, J. S.; Fedin, E. I. *Soviet Physics. Solid State* **1963**, *4*, 1633.

(164) Matsuo, T.; Shibasaki, M.; Katsumata, T. *Solid State Ionics* **2002**, *154-155*, 759.

(165) George, A. M.; Stebbins, J. F. *Physics and Chemistry of Minerals* **1996**, *23*, 526.

(166) Stebbins, J. F. *Reviews in Mineralogy* **1988**, *18*, 405.

(167) Brinkmann, D. *Progress in NMR Spectroscopy* **1992**, *24*, 527-552.

(168) Stebbins, J. F.; McMillan, P. F.; Dingwell, D. B. *Structure, dynamics and properties of silicate melts*; Mineralogical Society of America, 1995; Vol. 32.

(169) Martineau, C.; Michaelis, V. K.; Schuller, S.; Kroeker, S. *Chemistry of Materials* **2010,** *22*, 4896.

(170) Cho, J.; Kim, Y. J.; Park, B. *Chemistry of Materials* **2000**, *12*, 3788.

(171) Cahill, L. S.; Chapman, R. P.; Britten, J. F.; Goward, G. R. *Journal of Physical Chemistry B* **2006**, *110*, 7171.

(172) Muller, C.; Valmalette, J. C.; Soubeyroux, J. L.; Bourée, F.; Gavarri, J. R. *Journal of Solid State Chemistry* **2001**, *156*, 379-389.

(173) El-Desoky, M. M.; Hassaan, M. Y. *Physics and Chemistry of Glasses* **2002**, *43*, 1.

(174) Murugesan, S.; Wijayasinghe, A.; Bergman, B. *Solid State Ionics* **2007**, *178*, 779.

(175) Tian, F.; Zhang, X.; Pan, L. *Journal of Non-Crystalline Solids* **1988**, *105*, 263.

(176) Ichinose, N.; Nakai, Y. *Journal of Non-Crystalline Solids* **1996**, *203*, 353.

(177) Muthupari, S.; Lakshmi Raghavan, S.; Rao, K. J. *Journal of Physical Chemistry* **1996**, *100*, 4243.

(178) Muthupari, S.; Prabakar, S.; Rao, K. J. *Journal of Physical Chemistry* **1994**, *98*, 2646.

(179) Muthupari, S.; Lakshmi Raghavan, S.; Rao, K. J. *Journal of Materials Research* **1995**, *10*, 2945.

(180) Tarascon, J. M.; Armand, M. *Nature* **2001**, *414*, 359.

(181) Fu, R.; Ma, Z.; Zheng, J. P.; Au, G.; Plichta, E. J.; Ye, C. *Journal of Physical Chemistry B* **2003**, *107*, 9730.

(182) Zhang, S.; Li, W.; Li, C.; Chen, J. *Journal of Physical Chemistry B* **2006**, *110*, 24855.

(183) Baudrin, E.; Laruelle, S.; Denis, S.; Touboul, M.; Tarascon, J. M. *Solid State Ionics* **1999**, *123*, 139.

(184) Ostroushko, A. A.; Mogil'nikov, Y. V.; Ostroushko, I. P. *Inorganic Materials* **2000**, *36*, 1256.

(185) Scrosati, B.; Selvaggi, A.; Fausto, C.; Wang, G. *Journal of Power Sources* **1988**, *24*, 287.

(186) Breger, J.; Meng, Y. S.; Hinuma, Y.; Kumar, S.; Kang, K.; Shao-Horn, Y.; Ceder, G.; Grey, C. P. *Chemistry of Materials* **2006**, *18*, 4768.

(187) Kang, K.; Meng, Y. S.; Breger, J.; Grey, C. P.; Ceder, G. *Science* **2006**, *311*, 977.

(188) Veluchamy, A.; Ikuta, H.; Wakihara, M. *Solid State Ionics* **2001**, *143*, 161.

(189) Wang, S.; Huang, X.; Chen, L. *Journal of Materials Chemistry* **2000**, *10*, 1465.

(190) Aguiar, P. M.; Kroeker, S. *Journal of Non-Crystalline Solids* **2007**, *353*, 1834.

(191) Kroeker, S.; Aguiar, P. M.; Cerquiera, A.; Clarida, W. J.; Doerr, J.; Olesiuk, M.; Ongie, G.; Affatigato, M.; Feller, S. A. *European Journal of Glass Science and Technology, Part B* **2006**, *47*, 393.

(192) Hoppe, U.; Kranold, R.; Gattef, E. *Solid State Communications* **1998**, *108*, 71.

(193) Shelby, J. E. *Introduction to Glass Science and Technology*; 2 ed.; Royal Society of Chemistry: Cambridge, 2005.

(194) Hoppe, U.; Kranold, R.; Lewis, J. M.; O'Brien, C. P.; Feller, H.; Feller, S. A.; Affatigato, M.; Neuefeind, J, Hannon, A.C. Physics and Chemistry of Glasses **2003**, *44*.

(195) Massiot, D.; Bessada, C.; Coutures, J. P.; Taulelle, F. *Journal of Magnetic Resonance* **1990**, *90*, 231.

(196) Eichele, K.; WSolids, 1.17.30 ed. 2001.

(197) Kriz, H. M.; Bray, P. J. *Journal of Magnetic Resonance* **1971**, *4*, 76.

(198) Du, L. S.; Stebbins, J. F. *Journal of Non-Crystalline Solids* **2003**, *315*, 239.

(199) Dell, W. J.; Bray, P. J.; Xiao, S. Z. *Journal of Non-Crystalline Solids* **1983**, *58*, 1-16.

(200) Du, L. S.; Stebbins, J. F. *Journal of Physical Chemistry B* **2003**, *107*, 10063.

(201) Mackenzie, K. J. D.; Smith, M. E. *Multinuclear Solid State NMR of Inorganic Materials*; Pergamon, 2002.

(202) Lapina, O. B.; Khabibulin, D. F.; Shubin, A. A.; Terskikh, V. V. *Progress in NMR Spectroscopy* **2008**, *53*, 128.

(203) Lapina, O. B.; Shubin, A. A.; Khabibulin, D. F.; Terskikh, V. V.; Bodart, P. R.; Amoureux, J. P. *Catalysis Today* **2003**, *78*, 91.

(204) Samonson, A.; Lippmaa, E. *Journal of Magnetic Resonance* **1988**, *79*, 255.

(205) Du, L. S.; Stebbins, J. F. *Journal of Non-Crystalline Solids* **2003**, *315*.

(206) Dell, W. J.; Bray, P. J.; Xiao, S. Z. *Journal of Non-Crystalline Solids* **1983**, *58*, 1.

(207) Lapina, O. B.; Mastikhin, V. M.; Shubin, A. A.; Krasilnikov, V. N.; Zamaraev, K. I. *Progress in NMR Spectroscopy* **1992**, *24*, 457.

(208) Enjalbert, R.; Galy, J. *Acta Crystallographic C* **1986**, *42*, 1467-1469.

(209) Shannon, R. D.; Calvo, C. *Canadian Journal of Chemistry* **1973**, *51*, 265.

(210) Lim, A. R.; Park, S. H.; Kim, J. N.; Jang, M. S. *Journal of the Physical Society of Japan* **2003**, *72*, 419.

(211) Gornostansky, S. D.; Stager, G. V. *Journal of Physical Chemistry* **1967**, *46*, 4959.

(212) Xu, Z.; Stebbins, J. F. *Science* **1995**, *270*, 1332.

(213) Shafi, S. P.; Kotyk, M. W.; Cranswick, L. M. D.; Michaelis, V. K.; Kroeker, S.; Bieringer, M. *Inorganic Chemistry* **2009**, *48*, 10553-10559.

(214) Breger, J.; Kang, K.; Cabana, J.; Ceder, G.; Grey, C. P. *Journal of Materials Chemistry* **2007**, *17*, 3167.

(215) Breger, J.; Dupre, N.; Chupas, P. J.; Lee, P. L.; Proffen, T.; Parise, J. B.; Grey, C. P. *Journal of the American Chemical Society* **2005**, *127*, 7529.

(216) Cahill, L. S.; Chapman, R. P.; Kirby, C. W.; Goward, G. R. *Applied Magnetic Resonance* **2007**, *32*, 565.

(217) Lapina, O. B.; Terskikh, V. V.; Shubin, A. A.; Mastikhin, V. M.; Eriksen, K. M.; Fehrmann, R. *Journal of Physical Chemistry B* **1997**, *101*, 9188.

(218) Ball, T. J.; Wimperis, S. *Journal of Magnetic Resonance* **2007**, *187*, 343.

(219) Madhu, P. K.; Goldbourt, A.; Frydman, L.; Vega, S. *Journal of Chemical Physics* **2000**, *112*, 2377.

(220) Becke, A. D. *Journal of Chemical Physics* **1993**, *98*, 5648.

(221) Lee, C.; Yang, W.; Parr, R. G. *Physical Review B: Condensed Matter* **1988**, *37*, 785.

(222) Miehlich, B.; Savin, A.; Stoll, H.; Preuss, H. *Chemical Physics Letters* **1989**, *157*, 200.

(223) Berkowitz, J.; McConnell, M. R.; Tholen, K.; Feller, S.; Affatigato, M.; Martin, S. W.; Holland, D.; Smith, M. E.; Kemp, T. F. *Physics and Chemistry of Glasses-European Journal of Glass Science and Technology Part B* **2009**, *50*, 372.

(224) Lapina, O. B.; Khabibulin, D. F.; Shubin, A. A.; Terskikh, V. V. *Progress in Nuclear Magnetic Resonance Spectroscopy* **2008**, *53*, 128.

(225) CNA; Canadian Nuclear Association: Ottawa, 2010; Vol. 2010.

(226) Roth, G.; Weisenburger, S. *Nuclear Engineering and Design* **2000**, *202*, 197.

(227) WNA; Association, W. N., Ed. Ottawa, 2010; Vol. 2010.

(228) Bickford, D. F.; Hrma, P. *Journal of the American Ceramics Society* **1990**, *73*, 2903.

(229) Parkinson, B. G.; Holland, D.; Smith, M. E.; Howes, A. P.; Scales, C. R. *Journal of Physics: Condensed Matter* **2007**, ***19***, 415144.

(230) Parkinson, B. G.; Holland, D.; Smith, M. E.; Howes, A. P.; Scales, C. R. *Journal of Non-Crystalline Solids* **2007**, ***353***, 4076.

(231) Parkinson, B. G.; Holland, D.; Smith, M. E.; Larson, C.; Doerr, J.; Affatigato, M.; Feller, S. A.; Howes, A. P.; Scales, C. R. *Journal of Non-Crystalline Solids* **2008**, *354*, 1936.

(232) Du, L.-S.; Stebbins, J. F. *Journal of Non-Crystalline Solids* **2005**, *351*, 3508-3520.

(233) Flynn, K. F.; Glendenin, L. E.; Harkness, A. L.; Steinberg, E. P. *Journal of Inorganic and Nuclear Chemistry* **1965**, *27*, 21.

(234) *Radiation Source Use and Replacement*; The National Academies Press: Washington, 2008.

(235) Archakov, I., Y.; Stolyarova, V. L.; Shultz, M. M. *Rapid Communications in Mass Spectrometry* **1998**, ***12***, 1330.

(236) Delorme, L. *Méchanismes de volatilité des verres et des fontes borosilicates d'intérêt nucleaire, Influence de la structure, Thesis, Université d'Orléans* **1998**.

(237) Kunwar, A. C.; Turner, G. L.; Oldfield, E. *Journal of Magnetic Resonance* **1986**, *69*, 124.

(238) Mukerji, J. *Transactions of the Indian Ceramic Society* **1971**, 57.

(239) Kogelnik, H. *Science* **1985**, *228*, 1043-1048.

(240) Barron, A. R. *Advanced Materials for Optics and Electronics* **1996**, *6*, 101-114.

(241) Bevilacqua, A. M.; Messi de Bernasconi, N. B.; Russo, D. O.; Audero, M. A.; Sterba, M. E.; Heredia, A. D. *Journal of Nuclear Materials* **1996**, *229*, 187-193.

(242) Vernaz, E.; Gin, S.; Jègou, C.; Ribet, I. *Journal of Nuclear Materials* **2001**, *298*, 27-36.

(243) Peng, L.; Stebbins, J. F. *Journal of Non-Crystalline Solids* **2008**, *354*, 3120-3128.

(244) Sen, S.; Xu, Z.; Stebbins, J. F. *Journal of Non-Crystalline Solids* **1998**, *226*, 29.

(245) Wu, J.; Stebbins, J. F. *Journal of Non-Crystalline Solids* **2009**, *355*, 556-562.

(246) Medek, A.; Harwood, J. S.; Frydman, L. *Journal of the American Chemical Society* **1995**, *117*, 12779-12787.

(247) Massiot, D.; Vosegaard, T.; Magneron, N.; Trumeau, D.; Montouillout, V.; Berthet, P.; Loiseau, T.; Bujoli, B. *Solid State Nuclear Magnetic Resonance* **1999**, *15*, 159.

(248) Bradley, S. M.; Howe, R. F.; Kydd, R. A. *Magnetic Resonance in Chemistry* **1993**, *31*, 883.

(249) Chan, J. C. C.; Bertmer, M.; Eckert, H. *Journal of the American Chemical Society* **1999**, *121*, 5238-5248.

(250) Janssen, M.; Eckert, H. *Solid State Ionics* **2000**, *136-137*, 1007-1014.

(251) Xue, X.; Stebbins, J. F. *Physics and Chemistry of Minerals* **1993**, *20*, 297-307.

(252) Saini, A.; Khanna, A.; Michaelis, V. K.; Kroeker, S.; Gonzalez, F.; Hernandez, D. *Journal of Non-Crystalline Solids* **2009**, *355*, 2323-2332.

(253) Kelsey, K. E.; Stebbins, J. F.; Singer, D. M.; Brown Jr, G. E.; Mosenfelder, J. L.; Asimow, P. D. *Geochimica et Cosmochimica Acta* **2009**, *73*, 3914-3933.

(254) Le Caër, G.; Bureau, B.; Massiot, D. *Journal of Physics: Condensed Matter* **2010**, *22*, 065402.

(255) Nanba, T.; Asano, Y.; Benino, Y.; Sakida, S.; Miura, Y. *Physics and Chemistry of Glasses: European Journal of Glass Science and Technology B* **2009**, *50*, 301.

(256) Armatas, G. S.; Kanatzidis, M. G. *Science* **2006**, *313*, 817-820.

(257) Henderson, E. J.; Veinot, J. G. C. *Chemistry Materials* **2007**, *19*, 1886-1888.

(258) Zou, X.; Conradsson, T.; Klingstedt, M.; Dadachov, M. S.; O'Keeffe, M. *Nature* **2005**, *437*, 716-719.

(259) Zyubin, A. S.; Mebel, A. M.; Lin, S. H. *Journal of Physical Chemistry A* **2007**, *111*, 9479-9485.

(260) Henderson, G. S. *Journal of Non-Crystalline Solids* **2007**, *353*, 1695-1704.

(261) Takeuchi, Y.; Nishikawa, M.; Yamamoto, H. *Magnetic Resonance in Chemistry* **2004**, *42*, 907-909.

(262) Takeuchi, Y.; Nishikawa, M.; Hachiya, H.; Yamamoto, H. *Magnetic Resonance in Chemistry* **2005**, *43*, 662-664

(263) Takeuchi, Y.; Takayama, T. *Annual Reports on NMR spectroscopy* **2005**, *5*, 155-200.

(264) Michaelis, V. K.; Aguiar, P. M.; Terskikh, V. V.; Kroeker, S. *Chemical Communications* **2009**, *31*, 4660-4662.

(265) Stebbins, J. F.; Du, L. S.; Kroeker, S.; Neuhoff, P.; Rice, D.; Frye, J.; Jakobsen, H. J. *Solid State Nuclear Magnetic Resonance* **2002**, *21*, 105-115.

(266) Sutrisno, A.; Hanson, M. A.; Rupar, P. A.; Terskikh, V. V.; Baines, K. M.; Huang, Y. *Chemical Communications* **2010**, *46*, 2817.

(267) Sen, S.; Gan, Z. *Journal of Non-Crystalline Solids* **2010**, *356*, 1519.

(268) Durif, A.; Averbuch-Pouchot, M. T. *Comptes Rendus Hebdomadaires des Seances de l'Academie des Sciences, Series C* **1982**, *295*, 555-556.

(269) Ennaciri, A.; Michel, D.; Perez Y Jorba, M.; Pannetier, J. *Materials Research Bullitin* **1984**, *19*, 793-799.

(270) Fáy, E.; Völlenkle, H.; Wittmann, A. *Kurze Originalmitteilungen* **1971**, *58*, 455.

(271) Fleet, M. E. *Acta Crystallographica C* **1990**, *46*, 1202-1204.

(272) Grabmaier, B. C.; Haussühl, S.; Klüfers, U. P. *Zeitschrift für Kristallographie* **1979**, *149*, 261-267.

(273) Kahn, A.; Agafonov, V.; Michel, D.; Perez Y Jorba, M. *Journal of Solid State Chemistry* **1986**, *65*, 377-382.

(274) Voellenkle, H. *Zeitschrift für Kristallographie* **1981**, *154*, 77-81.

(275) Vollenkle, H.; Wittmann, A. *Zeitschrift fur Kristallographie* **1969**, *128*, 66-71.

(276) Von Dreele, R. B.; Navrotsky, A. *Acta Crystallographica B* **1977**, *33*, 2287-2288.

(277) Xu, Y.; Cheng, L.; Zhou, G.; Wang, Y. *Acta Crystallographica E* **2006**, *62*, 135-137.

(278) Cruickshank, D. W. J.; Kalman, A.; Stephens, J. S. *Acta Crystallographica B* **1978**, *34*, 1333-1334.

(279) Will, G.; Bellotto, M.; Parrish, W.; Hart, M. *Journal of Applied Crystallography* **1988**, *12*, 182.

(280) Cheng, L. T.; Ellis, P. D. *Journal of Physical Chemistry* **1989**, *93*, 2549.

(281) Larsen, F. H.; Jakobsen, H. J.; Ellis, P. D.; Nielsen, N. C. *Journal of Physical Chemistry A* **1997**, *101*, 8597.

(282) Bhattacharyya, R.; Frydman, L. *Journal of Physical Chemistry* **2007**, *127*, 194503.

(283) Eichele, K.; 1.18.8 ed. 2007, Wsolids NMR Simulation Package.

(284) Perdew, J. P.; Burke, K.; Ernzerhof, M. *Physical Review Letters* **1996**, *77*.

(285) Perdew, J. P.; Burke, K.; Ernzerhof, M. *Physical Review Letters* **1998**, *80*.

(286) Yates, J. R.; Pickard, C. J.; Payne, M. C.; Mauri, F. *Journal of Chemical Physics* **2003**, *118*, 5746.

(287) Adiga, S.; Aebi, D.; Bryce, D. L. *Canadian Journal of Chemistry* **2007**, *85*, 496.

(288) Hohenberg, P.; Kohn, W. *Physical Review B* **1964**, *136*, 864.

(289) Redhammer, G. J.; Roth, G.; Amthauer, G.; Lottermoser, W. *Acta Crystallographica B* **2008**, *64*, 261-271.

(290) Halwax, E.; Voellenkle, H. *Monatshefte fur Chemie* **1985**, *116*, 1367.

(291) Hoch, C.; Roehr, C. *Zeitschrift fuer Naturforschung* **2001**, *56*, 1256.

(292) Agafonov, V.; Kahn, A.; Michel, D.; Perez Y Jorba, M. *Journal of Solid State Chemistry* **1986**, *62*, 402.

(293) Gaewdang, T.; Chaminade, J. P.; Gravereau, P.; Garcia, A.; Fouassier, C.; Pouchard, M.; Hagenmuller, P.; Jacquier, B. *Zeitschrift für Anorganische und Allgemeine Chemie* **1994**, *620*, 1965.

(294) Nishi, F. *Acta Crystallographica C* **1997**, *53*, 399-401.

(295) Mignon, C.; Millot, Y.; Man, P. P. *Comptes Rendus Chimie* **2004**, *7*, 425-430.

(296) Robinson, K.; Gibbs, G. V.; Ribbe, P. H. *Science* **1970**, *172*, 567-570.

(297) Fleet, M. E. *Mineralogical Magazine* **1976**, *40*, 531-533.

(298) Kibalchenko, M.; Yates, J. R.; Pasguarello, A. *Journal of Physics: Condensed Matter* **2010**, *22*, 145501.

(299) Jiang, X.; Lousteau, J.; Shen, S.; Jha, A. *Journal of Non-Crystalline Solids* **2009**, *355*, 2015.

(300) Petrov, G. I.; Yakovlev, V. V.; Minkovski, N. I. *Optics Communications* **2004**, *229*, 441.

(301) Torres, F.; Narita, K.; Benino, Y.; Fujiwara, T.; Komatsu, T. *Journal of Applied Physics* **2003**, *94*, 5265.

(302) Wang, J.; He, Y.; Tao, J.; He, J.; Zhang, W.; Niu, S.; Yan, Z. *Chemical Communications* **2010**, *46*, 5250.

(303) Kitiyanan, A.; Kato, T.; Suzuki, Y.; Yoshikawa, S. *Journal of Photochemistry and Photobiology A: Chemistry* **2006**, *179*, 130.

(304) Ivanov, A. O.; Evstroopiev, K. S. Dokl. Akad. Nauk SSSR **1962**, *145*, 797

.

(305) Murthy, M. K.; Kirby, E. M. *Physical chemistry of Glasses* **1964**, *5*, 144.

(306) Henderson, G. S.; Wang, H. *European Journal of Mineralogy* **2002** *14*.

(307) Kamiya, K.; Sakka, S. *Physical Chemistry of Glasses* **1979**, *20*, 60.

(308) Kamiya, K.; Yoko, T.; Itoh, Y.; Sakka, S. *Journal of Non-Crystalline Solids* **1987**, *95*, 209.

(309) Ueno, M.; Misawa, M.; Suzuki, K. *Physica B* **1983**, *120*, 347.

(310) Huang, W. C.; Jain, H.; Meitzner, G. *Journal of Non-Crystalline Solids* **1996**, *196*, 155.

(311) Itie, J. P.; Polian, A.; Calas, G.; Petiau, J.; Fontaine, A.; Tolentino, H. *Physical Review Letters* **1989**, *63*, 398.

(312) Jain, H.; Kamitsos, E. I.; Yiannopoulos, Y. D.; Chryssikos, G. D.; Huang, W. C.; Kucher, R.; Kanert, O. *Journal of Non-Crystalline Solids* **1996**, *203*, 320.

(313) Henderson, G. S.; Fleet, M. E. *Journal of Non-Crystalline Solids* **1991**, *134*, 259-269.

(314) Henderson, G. S.; Wang, H. M. *European Journal of Mineralogy* **2002**, *14*, 733.

(315) Micoulaut, M.; Cormier, L.; Henderson, G. S. *Journal of Physics: Condensed Matter* **2006**, *18*, R753-R784.

(316) Ashbrook, S. E.; Smith, M. E. *Chemical Society Reviews* **2006**, *35*, 718-735.

(317) Du, L. S.; Stebbins, J. F. *Journal of Physical Chemistry B* **2006**, *110*, 12427-12437.

(318) Clark, T. M.; Grandinetti, P. J. *Journal of Non-Crystalline Solids* **2000**, *265*, 75-82.

(319) Hussin, R.; Holland, D.; Dupree, R. *Journal of Non-Crystalline Solids* **1998**, *232-234*, 440-445.

(320) Lee, S. K.; Lee, B. H. *Journal of Physical Chemistry B* **2006**, *110*, 16408-16412.

(321) Peng, L.; Stebbins, J. F. *Journal of Non-Crystalline Solids* **2007**, *353*, 4732-4742.

(322) Widdifield, C. M.; Bryce, D. L. *Physical Chemistry Chemical Physics* **2009**, *11*, 7120.

(323) Othman, A.; Harris, R. K.; Hodkinson, P.; Christopher, E. A.; Lancaster, R. W. *New Journal of Chemistry* **2008**, *32*, 1796.

(324) Harris, R. K.; Wasylishen, R. E.; Duer, M. J. *NMR Crystallography*; Wiley, 2010.

(325) Aharen, T.; Greedan, J. E.; Bridges, C. A.; Aczel, A.; Rodriguez, J.; MacDougall, G.; Luke, G. M.; Imai, T.; Michaelis, V. K.; Kroeker, S.; Zhou, G.; Wiebe, C. R.; Cranswick, L. M. D. *Physical Review B* **2010**, *81*, 224409.

(326) Aharen, T.; Greedan, J. E.; Bridges, C. A.; Aczel, A.; Rodriguez, J.; MacDougall, G.; Luke, G. M.; Michaelis, V. K.; Kroeker, S.; Wiebe, C. R.; Zhou, H.; Cranswick, L. M. D. *Physical Review B* **2010**, *81*, 064436.

(327) Aharen, T.; Greedan, J. E.; Ning, F.; Imai, T.; Michaelis, V. K.; Kroeker, S.; Zhou, H.; Wiebe, C. R.; Cranswick, L. M. D. *Physical Review B* **2009**, *80*, 134423.

(328) Brouwer, D. H. *Journal of American Chemical Society* **2008**, *130*, 3095.

(329) Kroeker, S.; Higman, C. S.; Michaelis, V. K.; Svenda, N. B.; Schuller, S. *Scientific Basis for Nuclear Waste Management XXXII* **2010**.

(330) Michaelis, V. K.; Kroeker, S. *Physical Chemistry in Glasses: European Journal of Glass Science and Technology B* **2009**, *50*, 249.

(331) Lussier, A. J.; Abdu, Y.; Hawthorne, F. C.; Michaelis, V. K.; Aguiar, P. M.; Kroeker, S. *Canadian Mineralogist* **2010,** *accepted*.

(332) Lussier, A. J.; Hawthorne, F. C.; Herwig, S.; Abdu, Y.; Aguiar, P. M.; Michaelis, V. K.; Kroeker, S. *Mineralogical Magazine* **2008**, *75*, 999.

(333) Chen, B.; Werner-Zwanziger, U.; Nascimento, M. L. F.; Ghussn, L.; Zanotto, E. D.; Zwanziger, J. W. *Journal of Physical Chemistry C* **2009**, *113*, 20725.

(334) Kroeker, S.; Wasylishen, R. E.; Hanna, J. V. *Journal of American Chemical Society* **1999**, *121*, 1582.

(335) Harris, K. J.; Wasylishen, R. E. *Inorganic Chemistry* **2009**, *48*, 2316.

(336) Aguiar, P. M.; Katz, M. J.; Leznoff, D. B.; Kroeker, S. *Physical Chemistry Chemical Physics* **2009**, *11*, 6925.

(337) Geisheimer, A. R.; Wren, J. E. C.; Michaelis, V. K.; Kobayashi, M.; Sakikai, K.; Kroeker, S.; Leznoff, D. B. *Inorganic Chemistry* **2010**, *Submitted*.

(338) Hamaed, H.; Ye, E.; Udachin, K.; Schurko, R. W. *Journal of Physical Chemistry B* **2010**, *114*, 6014.

(339) Chen, F.; Ma, G.; Bernard, G.; Cavell, R.; McDonald, R.; Ferguson, M.; Wasylishen, R. E. *Journal of American Chemical Society* **2010**, *132*, 5479.

(340) Widdifield, C. M.; Bryce, D. L. *Journal of Physical Chemistry A* **2010**, *114*, 2102.

(341) Moudrakovski, I.; Lang, S.; Patchkovskii, S.; Ripmeester, J. *Journal of Physical Chemistry A* **2010**, *114*, 309.

(342) Hamaed, H.; Laschuk, M.; Terskikh, V. V.; Schurko, R. W. *Journal of the American Chemical Society* **2009**, *131*, 8271.

(343) Davis, M. C.; Kaseman, D. C.; Parvani, S. M.; Sanders, K. J.; Grandinetti, P. J.; Massiot, D.; Florian, P. *Journal of Physical Chemistry A* **2010**, *114*, 5503.

(344) Sutrisno, A.; Hanson, M. A.; Rupar, P. A.; Terskikh, V. V.; Baines, K. M.; Huang, Y. *Chemical Communications* **2010**, In Press.

(345) Prasad, S.; Kwak, H. T.; Clark, T.; Grandinetti, P. J. *Journal of American Chemical Society* **2002**, *124*, 4964.

(346) Yao, Z.; Kwak, H. T.; Sakellariou, D.; Emsley, L.; Grandinetti, P. J. *Chemical Physics Letters* **2000**, *327*, 85.

(347) Kentgens, A. P. M.; Verhagen, R. *Chemical Physics Letters* **1999**, *300*, 435.

(348) Van Veenendal, E.; Meier, B. H.; Kentgens, A. P. M. *Molecular Physics* **1998**, *93*, 195.

(349) Siegel, R.; Nakashima, T. T.; Wasylishen, R. E. *Chemical Physics Letters* **2004**, *388*, 441.

(350) Silver, M. S.; Joseph, R. J.; Hoult, D. J. *Physical Review A* **1985**, *31*, 2753.

(351) Ash, J. T.; Trease, N. M.; Grandinetti, P. J. *Journal of American Chemical Society* **2008**, *130*, 10858.

(352) Amoureux, J. P.; Trebosc, J. *Journal of Magnetic Resonance* **2006**, *179*, 311.

(353) Luga, D.; Morais, C.; Gan, Z.; Neuville, D. R.; Cormier, L.; Massiot, D. *Journal of American Chemical Society* **2005**, *127*, 11540.

(354) Kroeker, S.; Eichele, K.; Wasylishen, R. E.; Britten, J. F. *Journal of Physical Chemistry B* **1997**, *101*, 3727.